NASA CR- 152454

15 DECEMBER 1976

EXPERIMENT DEFINITION PHASE
SHUTTLE LABORATORY

LDRL-10.6 EXPERIMENT

•

FINAL REPORT
SHUTTLE SORTIE
TO
GROUND RECEIVER TERMINAL

NASA Contract NAS 5-20018

F.E. Goodwin
T.A. Nussmeier
L.S. Stokes
E.J. Vourgourakis

MAR 1977
RECEIVED
NASA STI FACILITY
INPUT BRANCH

HUGHES

15 DECEMBER 1976

EXPERIMENT DEFINITION PHASE

SHUTTLE LABORATORY

LDRL-10.6 EXPERIMENT

●

FINAL REPORT
SHUTTLE SORTIE
TO
GROUND RECEIVER TERMINAL

NASA Contract NAS 5-20018

F.E. Goodwin
T.A. Nussmeier
L.S. Stokes
E.J. Vourgourakis

HUGHES

CONTENTS

iii

1. INTRODUCTION

The objectives of the Shuttle Sortie LDRL-10.6* Experiment are
1) to demonstrate a high performance laser communication link capable of
one-way transmission of wideband (400 Mbps) data from a low earth orbit
Shuttle to a high altitude satellite or to a ground station, and 2) to make
engineering measurements required for the design of future operational sys-
tems. Figure 1-1 illustrates the LDRL-10.6 Experiment link configuration
for 1) a Shuttle to elliptical orbit satellite link, and 2) a Shuttle to ground link.
This volume deals exclusively with the Shuttle to ground station link. The
Shuttle to elliptical orbit satellite link is treated in a separate volume.
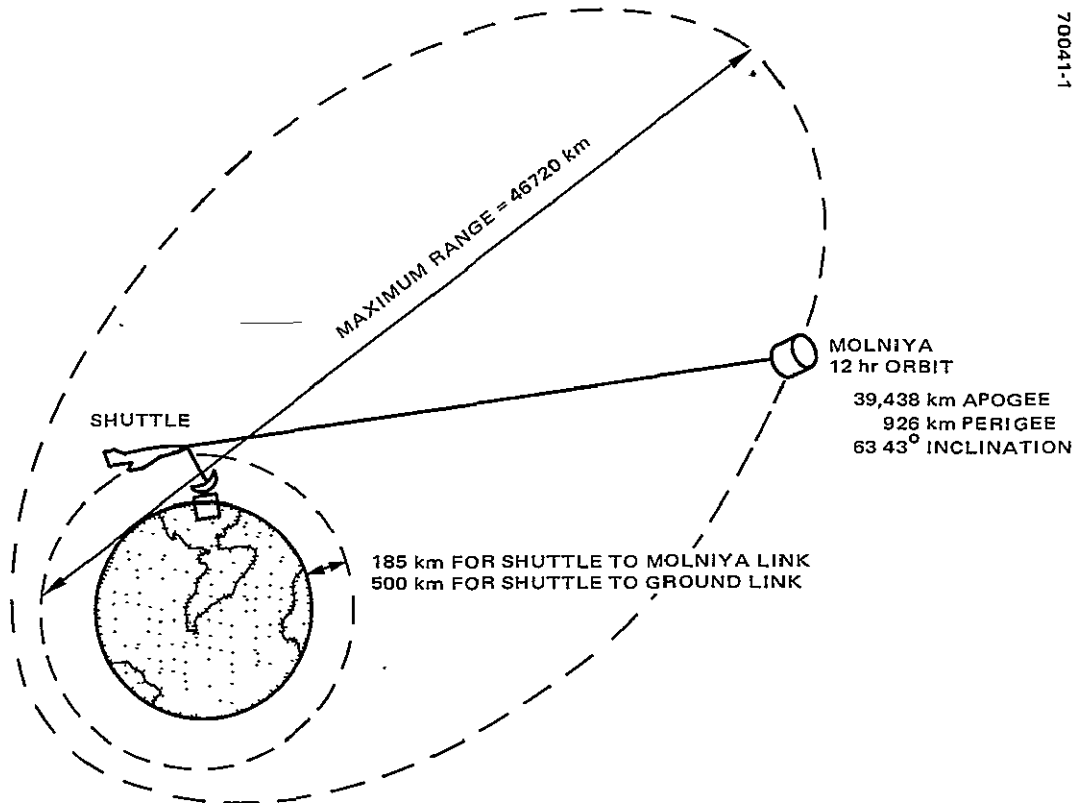
FIGURE 1-1. LDRL-10.6 EXPERIMENT LINK GEOMETRY

---

*LDRL-10.6 is an acronyn for laser data relay link at a wavelength of
10.6 μm (CO_2 laser).

2. EXPERIMENT OBJECTIVES

2.1 INTRODUCTION

The LDRL-10.6 Experiment objectives concern both communication system performance and system development. The communication objective is to achieve a specified quality and quantity of data transmitted over a CO_2 laser link. The system development objective is to resolve problems critical to the implementation of a laser communication system, e.g., doppler tracking, beam point-ahead, and mutual terminal acquisition and tracking using extremely high gain antennas.

2.2 COMMUNICATION OBJECTIVE

As data transmission rate requirements increase, laser communication systems become increasingly attractive because of the large data transmission capability that results from their inherently high antenna gains. In order to evaluate the potential of laser communications, the LDRL-10.6 Experiment has been conceived as a first-generation spaceborne laser communication system. The LDRL-10.6 Experiment communication requirement is to transmit 400 Mbps over both a Shuttle to elliptical orbit satellite link and a Shuttle to ground link.

2.3 SYSTEM OBJECTIVE

The second objective of the LDRL-10.6 Experiment is to explore the operational conditions of a practical spaceborne optical communication system and to assess the hardware development that will be required for its implementation. These problems include accommodation of doppler shift, mixer cooling, link acquisition, antenna pointing and tracking with extremely high gain antennas, the application of laser and modulation technology, and attendant problems peculiar to the integration of a laser communications terminal into a spacecraft. For example, the extreme doppler shift at CO_2 wavelengths (as great as ±942 MHz in the Shuttle to Molniya satellite link) must be compensated by local oscillator tuning. Sensitive mixers which operate at 10.6 μm must be cooled to approximately 110°K. Adequate long-term performance of radiation doolers in a space environment must be assured. Finally, the technology of pointing and tracking with high gain antennas must be demonstrated in a space environment. This will require both precise optical

alignment and accommodation of transmit-receive beam offset (point-ahead) due to velocity aberration. A further problem associated with high antenna gains is the initial acquisition with actual orbital positional uncertainties and LOS angular rates. This must be accomplished with a maximum angular tracking rate of 48 deg/min in conjunction with a 1° field of view (FOV) requirement.

3. DESIGN OPTIONS FOR THE SHUTTLE TERMINAL

For economy, simplicity, and reliability, it is desirable to utilize the Shuttle crew capabilities to the greatest degree possible in performing experiments with the LDRL-10.6 Experiment equipment. This general philosophy has been followed in formulating the LDRL-10.6 design while exploiting the automation capabilities inherent to the LDRL hardware design. The experiment implementation that has evolved is a composite of the automated pallet mode and the man-tended pallet mode options. The composite mode has been termed the quasiautomated man-tended mode. Its key features are as follows:

1) The LDRL-10.6 Experiment transmitter terminal will be mounted on the Shuttle forward swing table.

2) Shuttle position data will be supplied by the guidance and navigation subsystem.

3) The payload specialist will place the terminal in operation and monitor its performance via the payload specialist's control console.

The principal control functions required for the experiment are noted in Table 3-1.

TABLE 3-1. PAYLOAD SPECIALIST'S CONTROLS
FOR THE LDRL-10.6 EXPERIMENT

- Main bus power
- Transmitter laser power
- Beacon receiver power
- Acquisition circuits power
- Manual/automatic gimbal control
- Lens cover control
- Initial search/roll
- Initial search/pitch
- Data signal generator/source

3-1

Several other payload specialist/crew preparatory operations are required prior to LDRL-10.6 Experiment operation. For instance, the Shuttle is to be positioned such that the ground station receiver terminal is centered within the transmitter gimbal field of view. Initial LDRL-10.6 transmitter gimbal positioning signals are derived from Shuttle guidance and navigation inputs by onboard computation.

After the Shuttle terminal has been activated and its telescope manually pointed so that the ground station is centered within its acquisition field of view, LDRL-10.6 acquisition and tracking will follow automatically. Should this fail, the payload specialist will attempt to determine the cause and take corrective action. Once tracking has been established, the experiment may continue under payload specialist control or under monitoring and control of an onboard computer. The major transmitter terminal performance parameters to be monitored by the payload specialist or the monitor computer and to be recorded for subsequent analysis are given in Table 3-2. In addition to the monitored parameters, specific experiment results will be recorded simultaneously as discussed in Section 6.

TABLE 3-2. LDRL-10.6 TRANSMITTER TERMINAL
PARAMETER TO BE MONITORED

- Telescope angle, pitch
- Telescope angle, roll
- IMC angle, pitch
- IMC angle, roll
- Laser output power
- Laser current
- Laser stability control signal
- Beacon receiver steering pitch
- Beacon receiver steering roll
- Laser temperature
- Structure temperature
- Power supply currents
- Power supply voltage

4. SYSTEM DESIGN

4.1 SYSTEM REQUIREMENTS

4.1.1 Orbital Parameters

The LDRL-10.6 Shuttle to ground experiment link assumes a 500 km altitude Shuttle circular orbit rather than the 185 km altitude circular orbit of the Shuttle to Molniya link. (The 500 km Shuttle orbit was chosen because the higher tracking angle rates associated with lower altitude orbits exceed Shuttle terminal acquisition capabilities.) For all possible ground station locations and orbit orientations, the worst case operational environment is closely approximated by that of a circular equatorial orbit Shuttle with the ground station located on the equator, since the earth rotational velocity contribution is relatively small. The Shuttle to ground link acquisition is planned to occur for ground station to Shuttle line of sight (LOS) zenith angles from 80° to 60°; communication is assumed to be restricted to zenith angles less than 60° because of atmospheric degradation. Based upon these assumptions, the following operational environment parameters are determined:

1) doppler frequency

2) point-ahead angle

3) communication range

4) zenith (ground station to Shuttle LOS, measured relative to local zenith)

5) zenith angle rate

6) tracking angle (Shuttle to ground station LOS, measured relative to earth-Shuttle radius)

7) tracking angle rate

4.1.2 Doppler Frequency History

The doppler frequency history for the 500 km circular orbit Shuttle to ground link is plotted in Figure 4-1 as a function of time from Shuttle zenith passing. For the communication period (zenith angle less than 60°), the doppler frequency range is ±540 MHz.
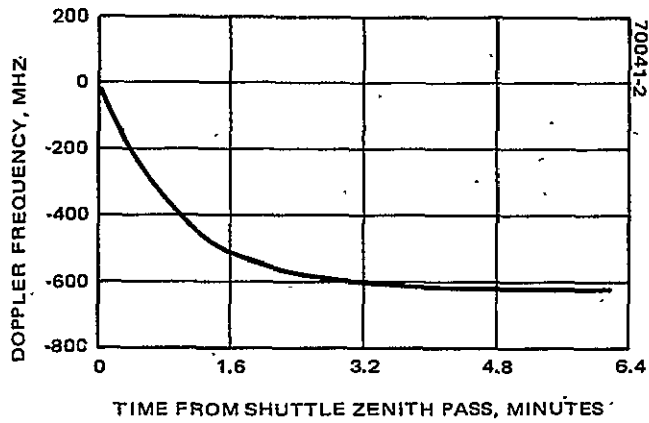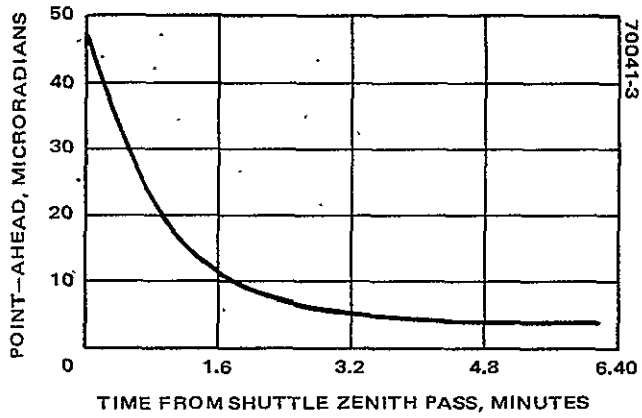
FIGURE 4-1. DOPPLER FREQUENCY HISTORY
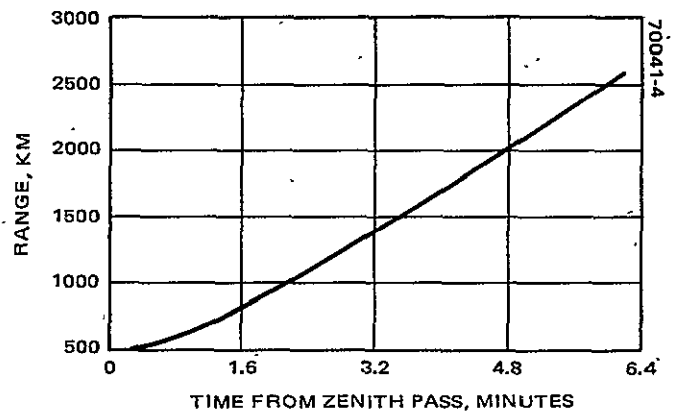

FIGURE 4-2. POINT-AHEAD ANGLE HISTORY

FIGURE 4-3. RANGE HISTORY
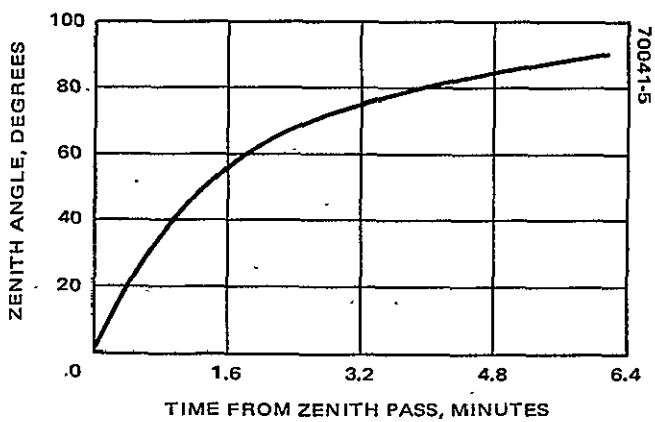
FIGURE 4-4. ZENITH ANGLE HISTORY
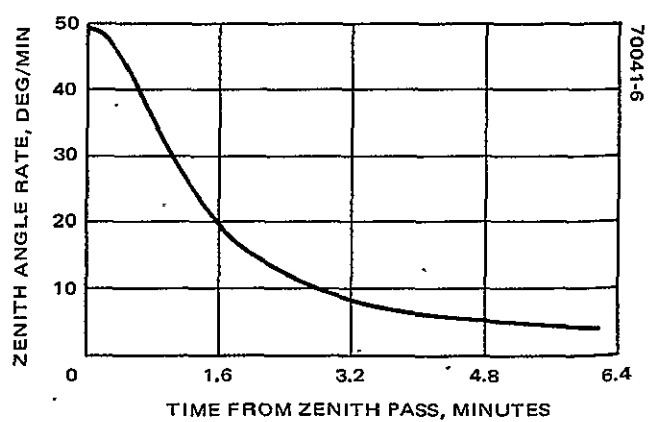
FIGURE 4-5. ZENITH ANGLE RATE HISTORY

4-2

4.1.3 Point-Ahead Angle History

Point-ahead angle is plotted in Figure 4-2 as a function of time from Shuttle zenith passing. The extreme point-ahead angle is 48 μrad and occurs at Shuttle zenith (maximum tangential velocity).

4.1.4 Other Communication and Tracking Parameters

Communication range, zenith angle, and zenith angle rate are plotted in Figures 4-3 through 4-5 as a function of time from zenith angle passing. Tracking angle and tracking angle rate are given in Figure 4-6 as a function of Shuttle time in ground station FOV. These parameters lie within the ranges of values given in Table 4-1. Complete ground station azimuth coverage (0 to 360°) is required. Azimuth rates are always less than the worst case zenith rates specified above.

4.1.5 Time in View for Typical Station Locations

The time in view for Space Shuttle to three ground stations (Goldstone, Greenbelt, and Cloudcroft) is summarized in Table 4-2. The Space Shuttle orbital parameters assumed are as follows:

Altitude	500.0 km circular
Inclination	28.5°
Longitude of ascending node	17°
Sample orbit time	13 days
Zenith angle limit	80° + 0.1 − 0.0

TABLE 4-1. MISSION PARAMETERS AFFECTING SHUTTLE TO GROUND STATION DATA TRANSMISSION, 500 KM ORBIT

Parameter	Acquisition	Communication
Time from zenith	-4 to -1.85 min	-1.85 to 1.85 min
Point-ahead angle	4.5 to 9.5 μrad	9.5 to 48 μrad
Range	1700 to 922 km	922 to 500 km
Zenith angle (ground to Shuttle LOS)	80° to 60°	60° to 0°
Zenith angle rate	0.10 to 0.27 deg/sec	0.27 to 0.80 deg/sec
Tracking angle (Shuttle to ground LOS)	65° to 52°	52° to 0°
Tracking angle rate	0.02 to 0.24 deg/sec	0.24 to 0.80 deg/sec
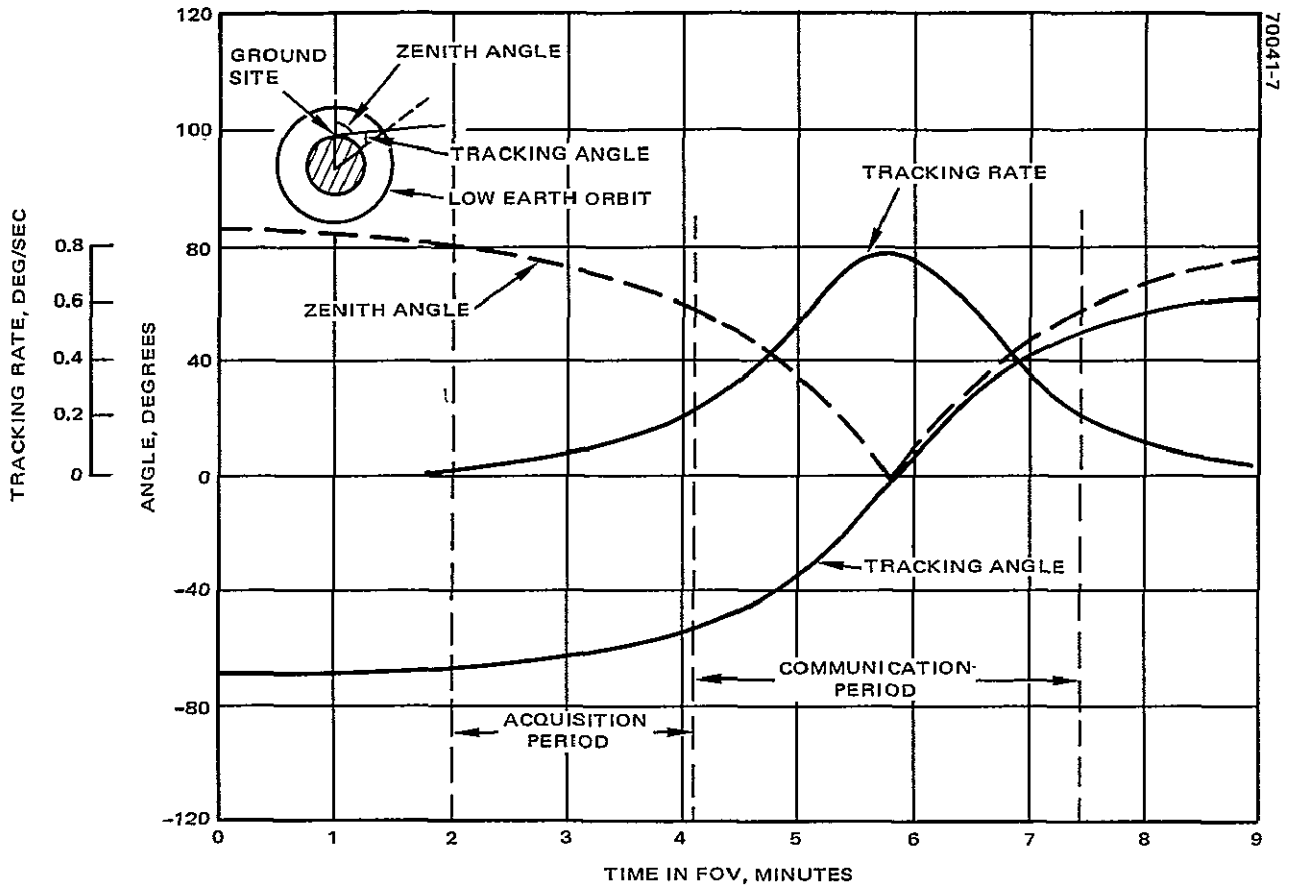
FIGURE 4-6. ACQUISITION PARAMETERS AS FUNCTION OF SATELLITE
TIME IN FIELD OF VIEW

TABLE 4-2. SPACE SHUTTLE TIME IN VIEW SUMMARY*

Station	Latitude °N	Longitude °N	Number of Passes	Total TIV, min	Average TIV, min	Standard Deviation TIV, min	Estimated TIV for 30 Day Mission, min
Goldstone							
Average	35.33	116.90	49	273.7	5.585	1.364	632
95% CL					5.18		586
99% CL					5.07		573
Greenbelt							
Average	39.0	76.53	36	147.8	4.105	1.174	341
95% CL					3.72		309
					3.60		299
Cloudcroft							
Average	32.58	105.40	56	353.2	6.306	1.413	814
95% CL					5.92		765
99% CL					5.81		751

*Sample time = 1.0 min

Table 4-2 presents the ground station coordinates and several results of calculations. These results are calculated for a 13 day mission and provide:

1) The number of passes (the total number of times the satellite was in view)

2) The total time in view (TIV) (the integrated time that the satellite was in the view cone)

3) The average time in view (the total TIV per number of passes)

4) The standard deviation of TIV (computed from the TIV per pass)

5) Lower 95 percent and 99 percent confidence limits (CL) (computed from the average TIV, standard deviation, and student distributions)

6) The estimated time in view for a 30 day mission (ETIV = number of passes x 30/13 x average TIV)

Figure 4-7 shows the time on view per pass frequency distributions for the three ground stations. Note the definite skewing to the left.

Figures 4-8 and 4-9 show variations of average and total time in view with latitude.
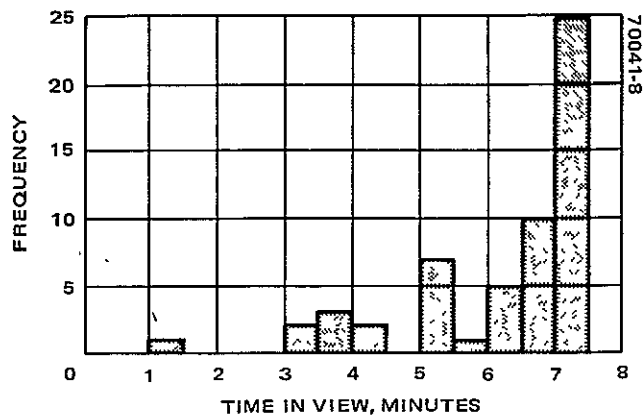
a) CLOUDCROFT
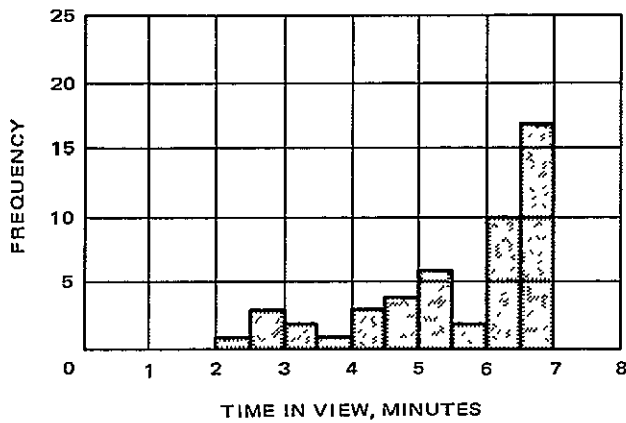
b) GOLDSTONE
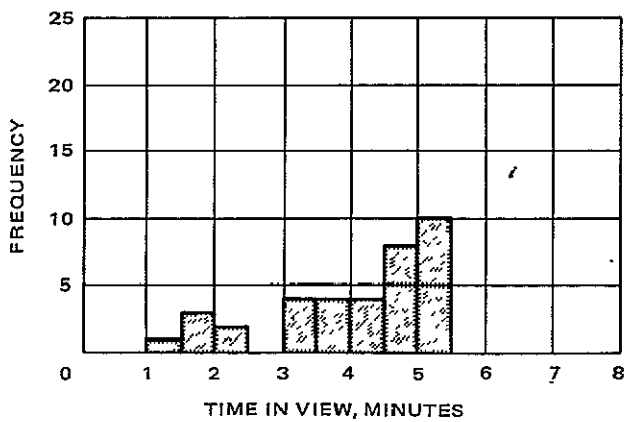
c) GREENBELT

FIGURE 4-7. TIME IN VIEW PER PASS FREQUENCY
DISTRIBUTION (13 DAY SAMPLE)

4-6
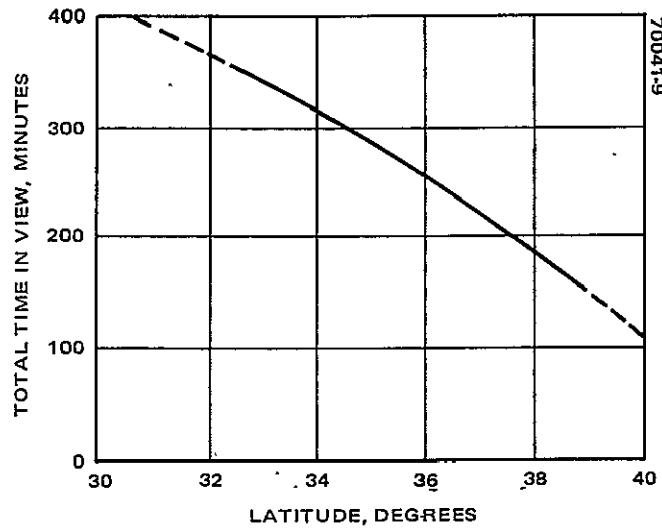
FIGURE 4-8. VARIATION OF TIME IN VIEW WITH LATITUDE

13 DAY MISSION
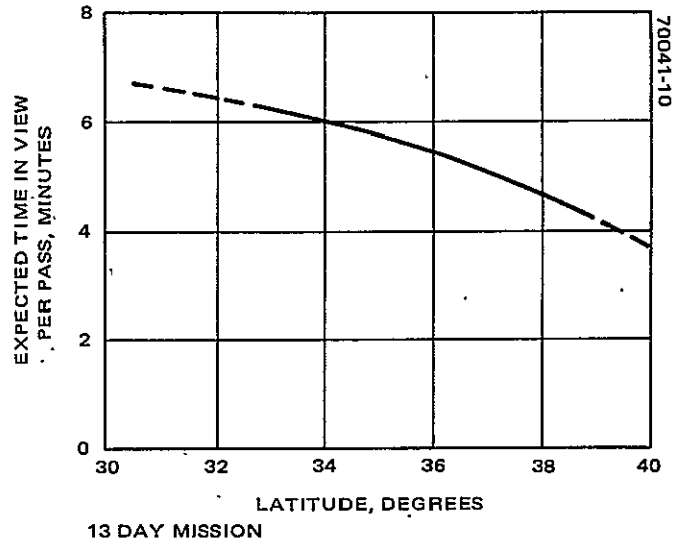
FIGURE 4-9. VARIATION OF AVERAGE TIME
IN VIEW WITH LATITUDE

4.1.6 Lead Angle

Because of the finite velocity of light and the relative tangential velocities, V_T, of the receiving and transmitting vehicles, the transmit line of sight (LOS) and the receive line of sight are displaced. This angular displacement is the point-ahead angle, α, and is given by:

$$\alpha = \frac{2V_T}{c}$$

In order to maintain small pointing losses, it is necessary to compensate for the point-ahead angles whenever that angle is comparable to the transmitting beamwidth. If the point-ahead angle is small compared to the transmit beamwidth the point-ahead function may be unnecessary.

Three basic techniques for accommodating the point-ahead angle are:

1) Onboard computation (no LOS reference used)

2) Onboard sensing and computation (LOS reference used)

3) Beam scanning with position feedback (LOS reference used).

The first method is completely open loop positioning; it is used in situations where no LOS reference is available. The second and third methods use as a reference the LOS between the vehicles provided by the beacon. Each method is discussed briefly in the following paragraphs.

### Direct Onboard Computation

Direct onboard computation requires: accurate ephemeris data for both terminals, spacecraft attitude known to 1/10 of the transmitted beamwidth, accurate position control within the spacecraft attitude reference, and computation to determine the necessary angular position. The onboard computation method appears to be impractical for laser communication on the Space Shuttle.

Onboard Sensing and Computing

An onboard sensing and computing concept may be implemented in two distinct ways, both use the established LOS as a reference. The first calculates the magnitude and direction of the point-ahead angle from the known ephemeris data, and open-loop points the transmitter beam relative to the LOS. The second measures range and angle rate and calculates the point-ahead angle by the relation $V_T = R\dot{\alpha}$, where R is the range between vehicles and $\dot{\alpha}$ is the LOS rotation rate in the transmitting vehicle's inertial coordinate system. The transmit/receive telescope can be instrumented using small, force-restrained, rate gyros to measure the telescope inertial $\dot{\alpha}$. The range

can be obtained by transponding an appropriate pseudonoise sequence or known ephemeris data.

The point-ahead angle, α, is shown as the angle between the tracking LOS and transmit beam LOS in Figure 4-10. The accuracy required of the direction angle is determined by assuming worst case conditions. The worst case point-ahead angle magnitude, α, was 40 μrad. The pointing error ΔP is defined as:

$$\Delta P^2 \cong \Delta\alpha^2 = \Delta\beta^2\alpha^2$$

The factors $\Delta\alpha$ and $\Delta\beta\alpha$ are the error contributions due to errors in the point-ahead angle magnitude and direction. Assume that the point-ahead angle α is approximately 40 μrad and that it is known with an error $\Delta\alpha$ of 1 μrad. In order for the second error term, $\Delta\beta \cdot \alpha$, to be no larger than the first, the direction angle, β, must be known to an accuracy $\Delta\beta$ of 1.4° or less a reasonable value for the Space Shuttle. The point-ahead direction, β, can be determined to within 0.5°; therefore the pointing errors are within reasonable bounds. This method of point-ahead angle compensation is proposed for the Shuttle Sortie LDRL-10.6 Experiment.

Consideration of boresight and mechanical alignment errors is necessary in determining the overall error in beam pointing for each of the point-ahead techniques. Spacecraft motion must be taken into account. Motions having periods very large with respect to the smoothing time of the angle data processing may be assumed negligible, since the computed angular position will be updated several times per second. When the transmit beam positioning with respect to the receive tracking boresight is accomplished after the secondary lens of the system, advantage can be taken of the magnification, M. Two types of errors will be introduced by the point-ahead mechanism, magnitude errors in α and a boresight/alignment error between the mechanism and the receive LOS. The overall error in point-ahead angle and direction can be shown to be

$$\Delta P^2_{\text{pointing}} = \Delta\alpha^2 + \frac{1}{M^2}\left(\epsilon^2_{\text{alignment}} + \epsilon^2_{\text{point-ahead servo}}\right)$$

The alignment and servo errors will be on the order of 10 to 20 μrad or less while the magnification is 41. Thus, the expected point-ahead error due to alignment and boresighting should be 2 μrad or less.

Beam Scanning With Position Feedback (LOS Reference Used)

Initial performance evaluations show the scanning concept to be workable and practical to implement. Various ways to accomplish scanning with position feedback are given below.

One scan technique to determine point-ahead angles and directions is utilized by the viewing satellite to sense the transmitted beam energy while the beam is being spiral scanned about the receive beam LOS. The signals transmitted on the narrow scanning beam are coded with position information as shown in Figure 4-11. The receive satellite may normally detect only two or three of the position coded transmissions. Since scanning the narrow beam opens the tracking loop, this requires either an attitude position memory capability of approximately 0.5 second, or an auxiliary beacon that permits track-while-scanning, or short term vehicle stability of the order of one transmitting beamwidth.

Once the transmit beam has been sensed by a satellite at two or three of the positions (e.g., positions 24, 25, and 26 of Figure 4-11) this position information is relayed to the transmitting servo. The transmitting beam then moves directly to position 25, thus pointing toward the receiving satellite. In order to maintain the pointing, the narrow transmitting beam is nutated about the correct position (e.g., position 25). Again the receiver senses the error in pointing from the position coded nutation and relays the error signal back to the transmitter pointing servo.

·An alternate scanning concept utilizing a conical scan about the tracking LOS is shown in Figure 4-12. This concept utilizes quadrant coding of the transmit beam that tells the point-ahead angle system which quadrant to program the pointing vector. The system would require a programming or logic to reduce the rate of change of the point-ahead angle, $\dot{\alpha}$, as the correct point-ahead angle and direction are approached. The conical scan geometry and quadrant signal position modulation detected at terminal B are shown in Figure 4-12. The beam scanning concept of Figure 4-12a illustrates the beam motion about the axis of the receive beam or tracking line of sight. Figures 4-12b and c show the scan geometry and received signal; when there is no relative motion between terminals, no modulation results, and no point-ahead is required. Figures 4-12 d and e show the scan geometry
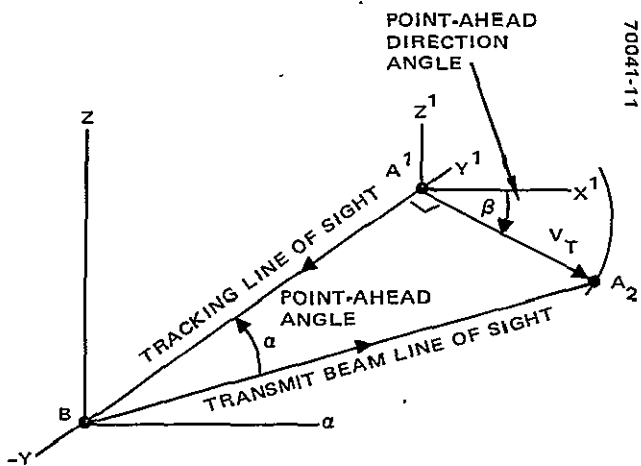
FIGURE 4-10. POINT-AHEAD ANGLE GEOMETRY
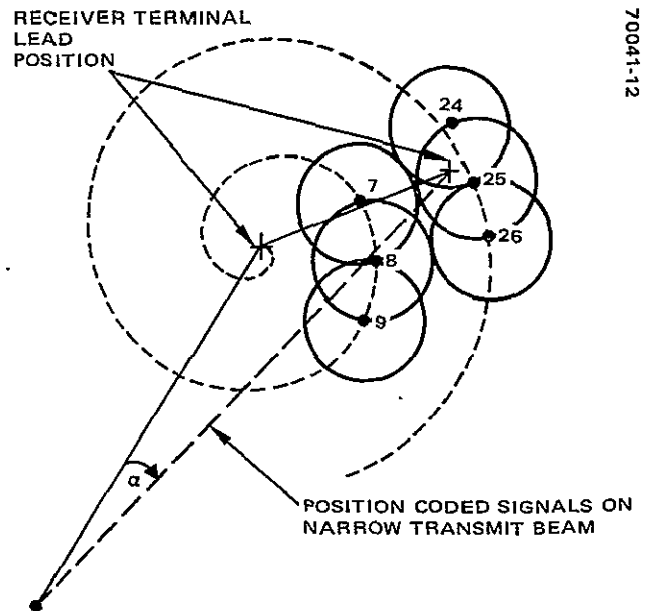
FIGURE 4-11. SPIRAL SCAN GEOMETRY AND BEAM CODING CONCEPT

with relative motion between terminals. The point-ahead angle may be seen by considering the point B' which is displaced from the receive LOS. This represents the apparent offset position of the B terminal due to the tangential velocity between B and A. This displacement and the resulting modulation is a measure of the required point-ahead angle and direction. The modulation and quadrant information is phase-compared at B and transponded to A. This allows A to point ahead with the proper magnitude and direction. This process is continued while the A transmitter beam is narrowed in a controlled manner until the required beamwidth is achieved.
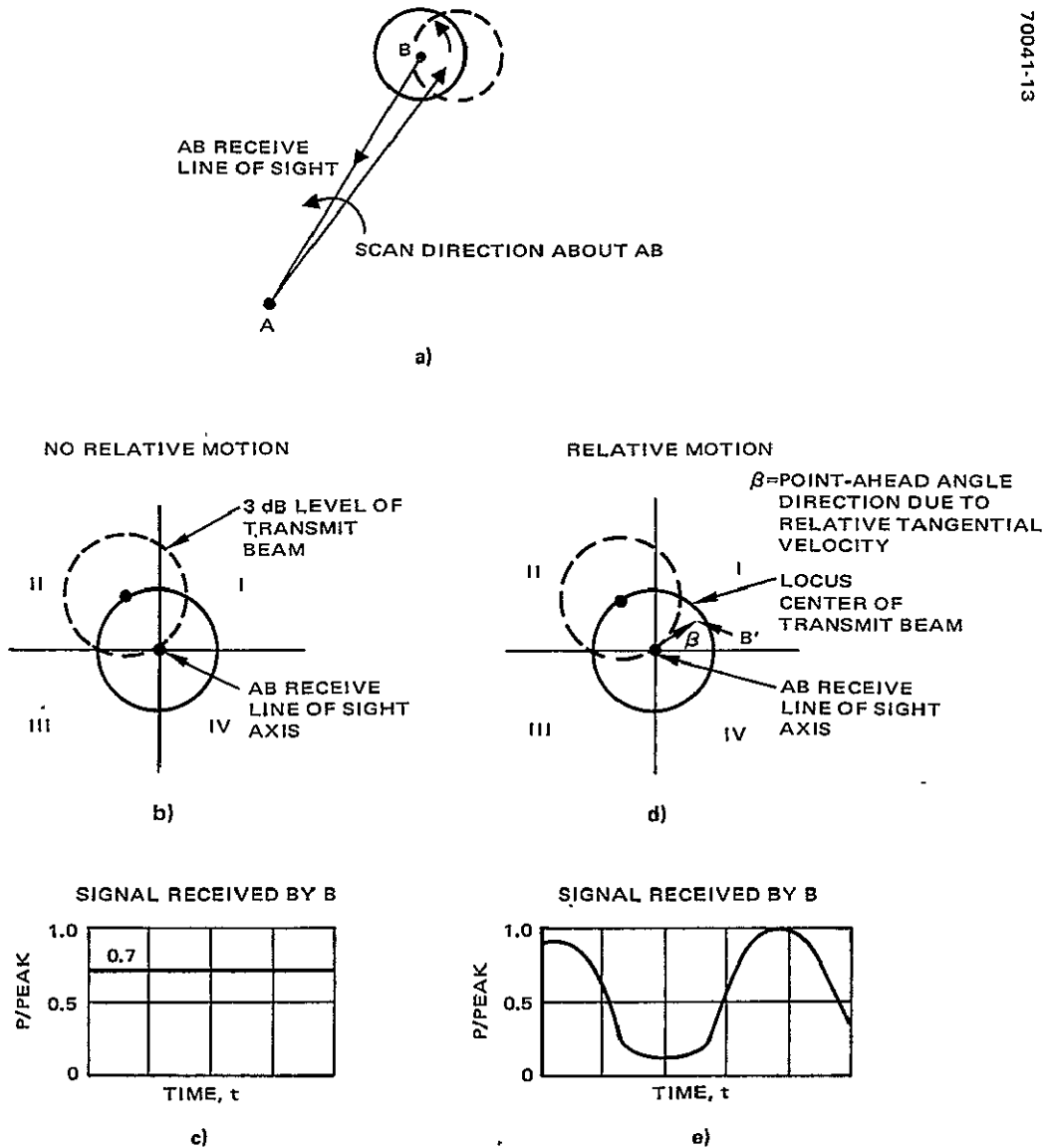
FIGURE 4-12. CONICAL SCAN POINT AHEAD GEOMETRY AND BEAM MODULATION

TABLE 4-3. SHUTTLE TERMINAL
POWER REQUIREMENTS

	Power, W
Transmitter laser input	100.00
Transmitter electronics	76.00
Pointing subsystem	8.25
Beacon receiver	1.00
Control panel	10.00
Total power	195.25
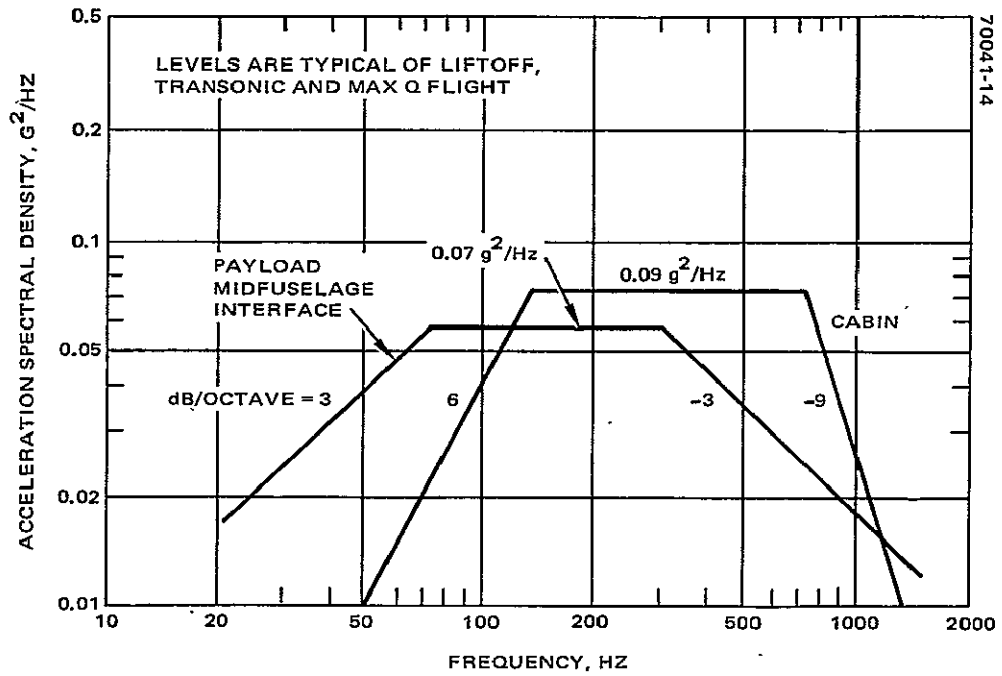
FIGURE 4-13.   RANDOM VIBRATION AT PAYLOAD MIDFUSELAGE
INTERFACE AND IN CABIN

4.1.7 Shuttle Terminal Interface

Vibration Environment

Flight. The Shuttle vehicle will be subjected to fluctuating pressure loading on its exterior surfaces by engine exhaust, Shuttle generated acoustic noise, and airflow generated aerodynamic noise during powered ascent through the atmosphere. These fluctuating pressure loads are the principle sources of structural vibration.

The estimated random vibration for the cabin and midfuselage payload interface due to the fluctuating pressure loads is shown in Figure 4-13. These vibration levels exist for approximately 29 seconds per mission. The reentry vibration environment is negligible. Actual vibration input to payloads will depend on the transmission characteristics of the midfuselage, the payload support structure, and interactions with each payload's weight, stiffness, and center of gravity.

Transient vibration. Events such as gust loading, engine ignition and cutoff, and separation and docking will induce low frequency transient responses in the Shuttle vehicle. The response for each event for various locations will be calculated. However, for the interim, the overall effect of these transient events is accounted for by a swept sinusoidal vibration environment imposed in the frequency range from 5 to 35 Hz at an acceleration amplitude of ± 0.25 g peak.

Ground. The ground vibration spectrum that the payloads are expected to experience is a minimum of four sweeps at 1/2 octave per minute at the following levels (sinusoidal motion):

2 to 5 Hz at 1.0 inch double amplitude

5 to 26 Hz at 1.3 g peak

26 to 500 Hz at 0.36 inch double amplitude

500 to 1000 Hz at 5 g peak

Power Requirement. The LDRL-10.6 Laser Experiment for Shuttle will require 195 watts of conditioned prime input power. A power requirement breakdown is given in Table 4-3.

Shuttle Base Motion (Stabilization). The LDRL-10.6 Shuttle Experiment terminal stabilization and pointing design is predicated on a Shuttle short term motion of 0.01 deg/sec and a long term motion of 0.1 deg/sec (about an arbitrary axis).

4.2 SYSTEM DESCRIPTION

4.2.1 Shuttle Terminal

Operational Characteristics

The Shuttle transmitter must acquire, track, and transmit to either the Molniya orbit receiver or the ground receiver. Figure 4-14 illustrates a typical LDRL-10.6 transmitter installation in the Shuttle space laboratory.

The specified 400 Mbps data bit rate and 10^{-6} probability of bit error (with a 6 dB design margin) is maintained for both links. A maximum doppler tracking range of ±942 MHz is required for the Shuttle to Molniya link. The maximum acquisition and tracking LOS angular rates of 0.24 deg/sec and 0.80 deg/sec, respectively, occur for the (500 km orbit) Shuttle-to-ground link as does the maximum point-ahead angle of 48 μrad.

Operation of the Shuttle terminal utilizes astronaut payload specialist capabilities to maximize reliability and economy. Figure 4-14 illustrates the Shuttle installation. The lifetime of the Shuttle transmitter terminal is defined to be a maximum of 30 days.

LDRL-10.6 Functional Block Diagram

The functional block diagram for the LDRL-10.6 is divided into three major blocks as indicated in Figure 4-15. The first block, the optical mechanical portion of the terminal, is the structural portion of the terminal that contains the large optics and contains the portions of the terminal that move in order to achieve the required pointing and tracking.

The second portion of the terminal contains the transmitter and local oscillator lasers. The transmitting laser will carry the 400 Mbps high data rate. Laser stabilization and control using Stark cell frequency control with the laser power supplies complete the laser subsystem.

The signal processing subsystem includes receive and transmitting electronics and includes the electronics that make up various servocontrol loops for both angle and frequency tracking.

Schematic Block Diagram

Figure 4-16 is the schematic block diagram of the Shuttle terminal. This diagram indicates the implementations the major functions given in Figure 4-15. Several implementations will be mentioned briefly here. For details, see Section 4.4.

The coarse optical pointing and tracking is accomplished using the first optical flat of the optical chain. Inner gimbal axis rotation rotates this mirror through 360°. The outer gimbal motion rotates this same mirror through the second axis to achieve near 2π sr coverage. The energy is directed through an afocal Gregorian telescope through the fine pointing assembly to the transmitter/receiver diplexing.

SHUTTLE COORDINATES

+Z

+Y

+X

−X

−Y

−Z

AFT

FWD

LASER EXPERIMENT

UMBILICAL

1128 TYPICAL TRUNNION STATION

SPACELAB PALLET

CONSOLE

SPACELAB MODULE
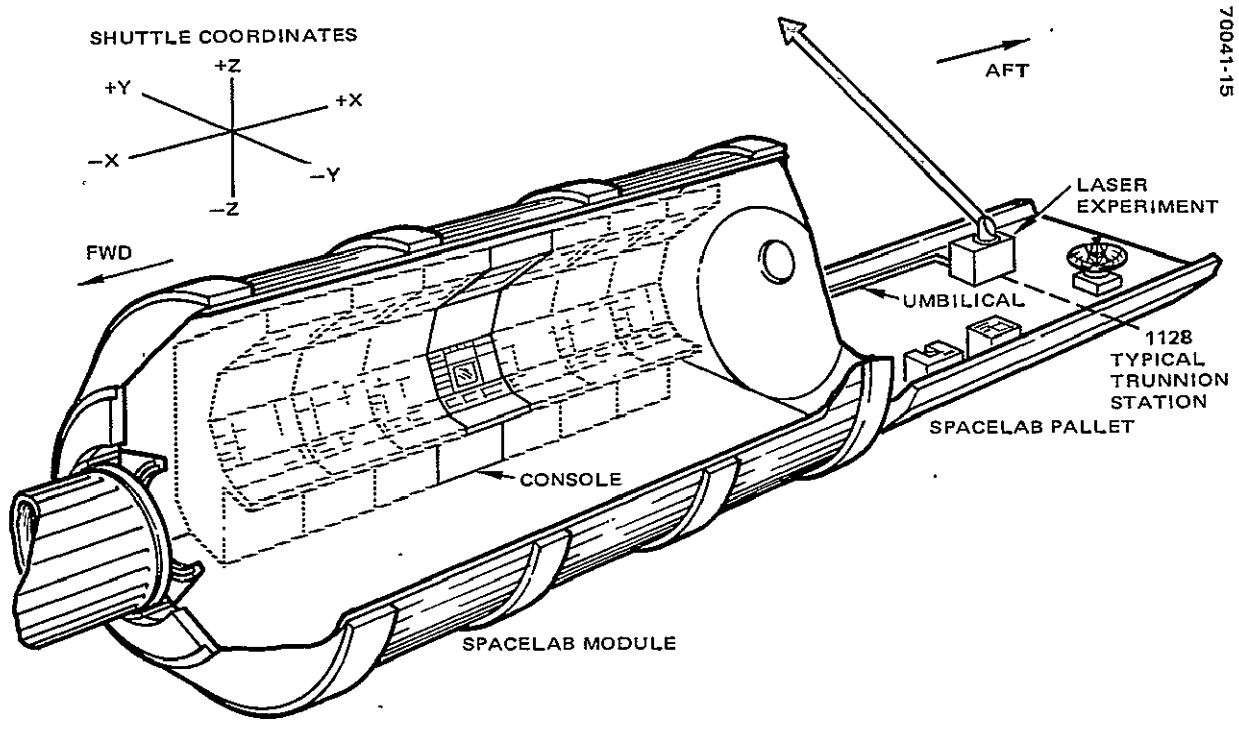
FIGURE 4-14. LDRL-10.6 INSTALLATION IN SHUTTLE SPACE LABORATORY

OPTICAL-MECHANICAL SUBSYSTEM
- POINTING AND TRACKING TELESCOPE
- FINE POINTING AND TRACKING OPTICS
- POINT AHEAD OPTICS
- SERVICE MOTORS
- SEARCH GENERATOR
- PACKAGING INTEGRATION

OPTICAL BEAM

OPTICAL BEAM

LASER SUBSYSTEM
- TRANSMITTER
- TRANSMITTER MODULATOR
- DIPLEXER
- TUNABLE LOCAL OSCILLATOR
- LASER FREQUENCY CONTROL
- LASER POWER SUPPLIES
- DETECTOR AND COOLER

CONTROL AND MONITOR PANEL INTERFACE

SIGNAL PROCESSING SUBSYSTEM
- BEACON TRACKING RECEIVER
- TRACKING SERVOS
  - COURSE
  - FINE
  - POINT AHEAD
  - DOPPLER
- SEARCH GENERATORS
- DATA INPUT AMPLIFIER
- MODULATOR DRIVER

POWER CONDITIONING

400 Mpbs

FIGURE 4-15. SHUTTLE TERMINAL FUNCTIONAL BLOCK DIAGRAM

4-15

FIGURE 4-16. SHUTTLE LASER TRANSMITTER TERMINAL BLOCK DIAGRAM

Transmitter/receiver diplexing is achieved through orthogonal polarization with the orthogonal linear polarization present at the receiver detector and at the transmitter laser and with orthogonal circular polarization from the quarter-wave plate to the output aperture. Separation is achieved by a polarizer such as a wire grid polarizer at a point where the polarizations are orthogonal linear. (Note: In addition to the isolation achieved by polarization diversity, about 30 dB; different transmitter and receiver laser frequencies are used to provide further isolation.)

Stark cell frequency stabilization is used for both the transmitter and local oscillator lasers. Such control circuits not only provide excellent frequency stability but also accommodate the doppler tuning control signals very well.

Point-ahead optics will eventually be placed in series with the transmitter beam. This allows the transmitter beam to have a boresight that is different from the received signal while allowing both the transmitter and receive energy to be directed by the main optics.

·Some form of active cooling of the detector will be used in the Space Shuttle terminal. This could for instance be in the form of a Joule-Thompson cryostat.

IF frequency tracking will be used for doppler tracking in conjunction with local oscillator frequency stepping. The main function of the received signal is to generate angle tracking signals for the coarse, fine, and point-ahead angle controls. The preferred point-ahead control for the Shuttle is an open loop control generated from the Shuttle ephemeris data.

The high data rate modulation is amplified to approximately 100 volts in order to drive the modulator. Thus the modulator drive electronics are a significant task.

Conceptual Design

Although the Shuttle terminal design was largely dictated by its transmitter function, the transmitter and beacon receiver share common optics so as to reduce package weight and volume. System parameters considered in the Shuttle terminal design included:

1) FOV, primary mirror diameter, primary and secondary mirror f-numbers, magnification ratios, and obscuration loss

2) Optimal laser beamwidth for maximum far-field gain

3) Power losses due to vignetting

A discussion of the design rationale follows including a comparison of alternative design options and their relative advantages.

Optical Design Considerations. The size and shape of the primary aperture determine the maximum antenna gain or on-axis peak intensity achievable for a given optical communication system. Because of this, large aperture optics are theoretically attractive for their high antenna gain values. However, practical considerations persuade one to utilize only as large an aperture as is necessary. In addition, smaller aperture optical communication systems lend themselves to simpler and more reliable point and track instrumentation as well as being less sensitive to vibration and distortions due to temperature gradients. Most importantly, the size of the aperture of the optical system must be compatible with achieving a system whose weight and cost are minimized.

A very important design consideration which determines how much energy is transferred through the optical train is the obscuration ratio. It is defined to be the fraction of area of the entrance pupil that is blocked by the image of the central hole in the small folding mirror. This obscuration has a marked effect on the transmitted energy output because the Gaussian beam profile of a CO_2 laser has its highest energy concentration in the center of the beam. The central obscuration of the Gregorian telescope is essentially determined by the inside aperture of the small folding mirror. The size of this aperture is in turn determined by the telescope acquisition FOV ($\pm 0.5°$); this situation occurs because the inside aperture must be sufficiently large so that no part of the image field of the incoming beacon beam is obscured during acquisition. The size of the image field, η, at the focal plane of the primary mirror is given by

$$\eta = f \cdot \theta$$

where f is the focal length of the primary mirror. For the LDRL-10.6 laser transmitter, $\theta = 17.45$ mr ($1°$). Thus, for a given θ and primary mirror diameter, D, the central obscuration can be minimized only if f is minimized. This implies that the f-number (=f/D) of the primary must be small if the power loss resulting from central obscuration is to be minimized. Based on practical experience, the f-number of the primary should not fall much below f/1.5, or the misalignment tolerances will become extremely small. Here the advantage of having a fast primary could easily be canceled by the performance degradation resulting from residual misalignments.

The actual obscuration is slightly larger than the calculated value to allow for manufacturing tolerances in centering and aligning the optical system. For the LDRL-10.6 design, 1 mm of decentration tolerance was allowed in calculating the obscuration ratios.

Another consideration is the configuration of the beam expander optics. This configuration can be either refractive, reflective, or catadioptric, in any of the possible combinations or modifications of classical telescope designs (i.e., Cassegrainian, Schmidt, Gallilean, etc.). The function of the telescope beam expander is to expand the signal beam from a laser source to a size compatible with an aperture based on the antenna gain requirements

of the system. Beam expanders usually consist of all-reflective elements due to the possible use of widely different wavelengths for the transmitter and receiver channels. Also there are greater lightening possibilities with all-reflective designs.

Optical features. The following general design features were considered in the LDRL-10.6 space communication system:

1) The transmitter must be designed to be diffraction limited and is always pointed at the receiver with an angular pointing error which is small in comparison to the diffraction beam spread.

2) The alignment error between the transmitter and receiver must be small compared to the diffraction angle of the transmitter antenna. This requirement usually leads to the practice of having the transmitter and receiver share the same antenna.

3) A deliberate offset or point-ahead angle must be added to the boresight adjustment between the transmitter and receiver.

The following paragraphs discuss these and other features that are incorporated into the design.

Beam expander optics. The beam expander is an afocal telescope that transforms a small diameter, collimated laser beam into a beam of larger diameter with less divergence. Beam expander optics are considered to be common to both the transmitter and the beacon receiver. The size of the beam expander output aperture determines the maximum achievable antenna gain for both the beacon receiver and transmitter. The FOV of the beam expander will be determined primarily by the IMC and acquisition requirements. These FOV requirements in combination with thermal and mechanical constraints determine the f-number of the components of the beam expander. Another restriction on the beam expander design is that it provides a pupil location that is accessible to the IMC function.

Image motion compensation. Success of a laser communication system necessitates that the aimpoint of the narrow beamwidths of these systems be maintained with great stability. The output pointing direction must be isolated from the angular motions of the Shuttle platform to a small fraction of the transmitter beamwidth. To achieve the necessary mirror response bandwidths with a minimum of power, it is desired that the optical element of the IMC that performs this task have as low an inertia as possible. The preferred location for this function is at (or very close to) the telescope stop position where the diameter of the optical aperture is smallest. The pointing angle range of the IMC device must be wide enough to accommodate the largest residual angular motions.permitted by the gimbal pointing or Shuttle stabilization requirements. Initial acquisition between the Shuttle and receiver station can also utilize the IMC components to provide a search/scan function.

Initiation of acquisition sequence.   The acquisition sequence of the transmitter receiver linkup can be initiated by injecting a suitably small diameter laser beam into the transmitter optics.   The corresponding output beam serves as a transmitter beacon, and the initial acquisition sequence . then consists of the receiver searching for this beacon beam.   Now, if the axis of this beam is accurately aligned parallel to the output axis of the transmitter, and if the angular diffraction spread of this beam is matched to the desired FOV for the initial acquisition, a beacon lock-on by the receiver establishes the relative angular position between the receiver and the transmitter to within the acquisition tolerance.

Point-ahead optics.   Due to the relative orbital velocity of the Shuttle and the receiver station and the finite velocity of light, the pointing direction of the receiver beacon does not automatically provide the exact indication of the location of the receiver.   Therefore, it is not appropriate to direct the transmitter's output beam in the apparent direction of the beacon but rather aim it toward the receiving station location at the time the light travels that distance.   Thus, a point-ahead correction must be introduced between the pointing direction of the receiver and transmitter.   For the LDRL-10.6 system the point-ahead correction will be achieved using a second set of IMCs that are in the receiving optical path only.   Control signals will be received from the Space Shuttle to open loop direct the receive beam relative to the transmit beam.

Energy redistribution technique.   The Gaussian profile TEM_{00} basic laser mode has its highest energy concentration in the center of the beam. Yet this central portion of the beam is lost in an aperture beam expander. Several methods have been devised for reconstituting the intensity profile of laser beams to reduce loss due to central obscurations.

One technique is to suitably expand the beam to overfill the aperture stop of the telescope.   By broadening the beam profile, the high energy central region will be spread more, and consequently a given obscuration ratio will cut off a smaller portion of the laser energy.   The increase in the output power is achieved by truncating the lower power, $1/e^2$, regions of the beam profile and passing more of the high power regions.   This technique was optimized and utilized in the LDRL-10.6 transmitter design.

Laser beam parameters.   The laser output beam is a diffraction limited truncated Gaussian beam from a 1.5 mm square laser bore.   Output from the laser is taken as the specular component from the diffraction grating used for P-line selection.   The Littrow angle of the grating is 52.5°; thus the specular output beam from the laser will exit at 105° measured from the laser longitudinal axis.   The grating will be located 0.75 inch from one end of the tube and it may be assumed that the Gaussian beam waist is located at the grating.

The Gaussian radius of the fundamental mode coupled from a waveguide is $w_0 = 0.6435a$, where a is the waveguide radius.   Assuming a negligible difference for a square waveguide, $w_0 = 0.48$ mm, and the truncation ratio $a/w_0 = 1.55$.

Using these values and some unpublished data derived for the propagation parameters of truncated Gaussian beams, the following beam divergence values are estimated:

3 dB beamwidth = 0.009 rad (0.53°)

2w beamwidth $(1/e^2)$ = 0.00159 rad (0.91°)

Truncation diameter beamwidth = 0.0255 rad (1.46°)

To form a 1° 3 dB beamwidth beacon a demagnification of the beam waist of 0.53 is required. This means that the laser beam waist location must be treated as an object and magnified 0.53 times through the entire optical train. The location of the magnified image is immaterial; it may be relayed several times to keep the limit ray within specified bounds.

The truncation beamwidth of 1.46° may be used to estimate necessary clear apertures along the beam path. (This angle is subject to ray trace optics treatment.) Note that once the final beacon image location is established, this all-inclusive angle becomes 1.46/0.53 = 2.75°.

An approximation to the range where a laser remains "collimated" (nondivergent) may be established by dividing the beam waist diameter $(2 w_0)$ by the angular divergence, yielding a value of about 6 cm. This range is a good location to avoid, as the source is in the process of changing from a collimated source to a point source. Since it would be physically difficult to locate optical elements much closer than 6 cm to the beam waist, it is better to extend the optical path and treat the source as a point source. This requires the beam expander telescope to operate with a finite conjugate. To allow some latitude in the optical path length from the source to the beam expander, a single lens was placed a fixed distance from the laser to create a second beam waist which now becomes the source. As the diameter of this source is larger, the beam is now collimated for a significantly longer range; thus the remainder of the beam expander optics will operate in the afocal mode.

Optical back-end diagram. A schematic layout of the optical system is shown in Figure 4-17. The transmitter laser is located directly above the local oscillator laser, with the nutator and detector located in the plane of the local oscillator.

The transmitter beam is reflected by a partially transparent beam-splitter. The transmitter portion of the beam is used for stabilization and power monitoring. The reflected beam (refer to side view) is recollimated by a lens located about 11 inches from the beam waist; thus the Gaussian diameter (2w) at this point is 0.7 inch (4.4 mm). This is sufficiently large to propagate to the beam expander primary without significant divergence.
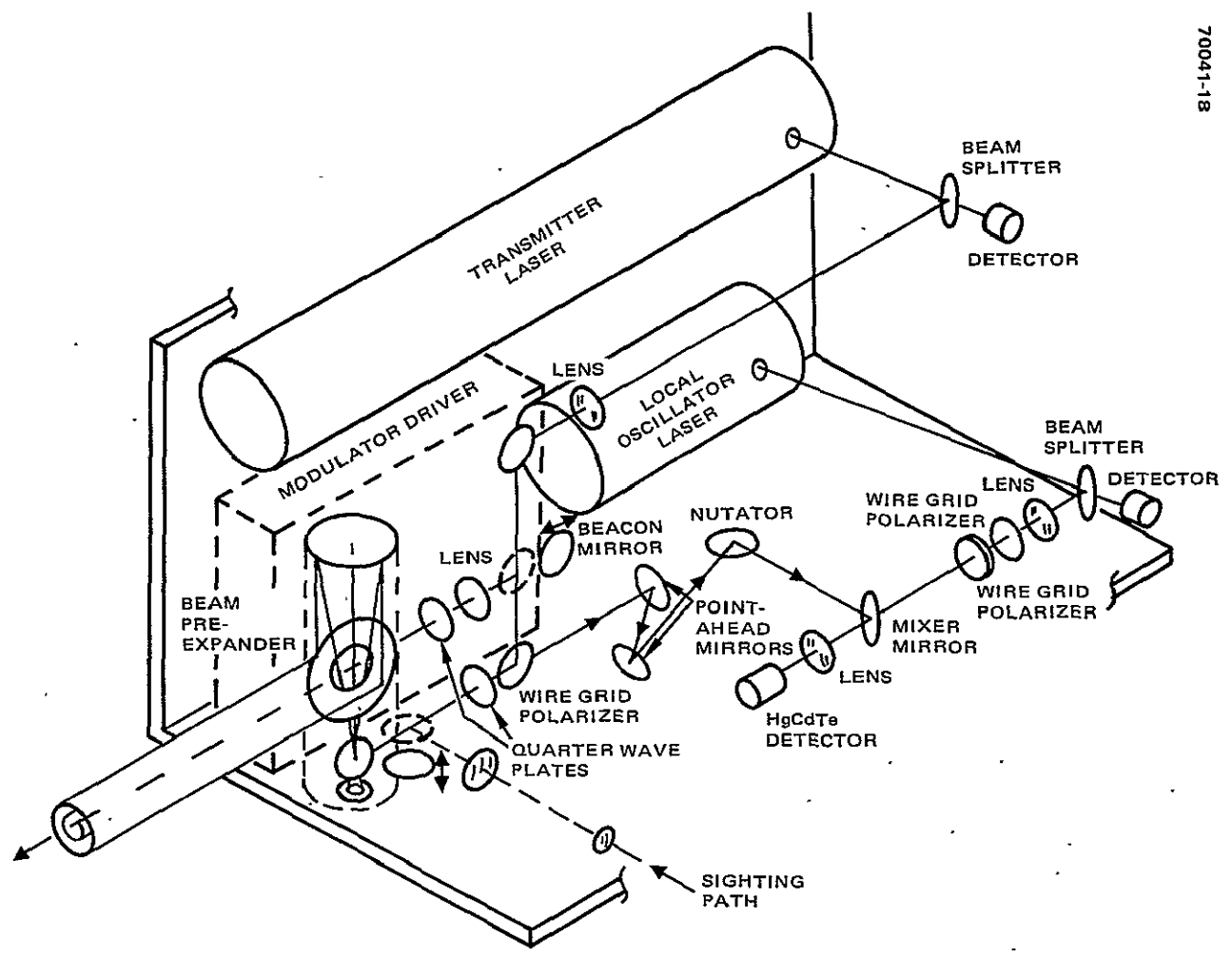
FIGURE 4-17. CONCEPTUAL SHUTTLE TERMINAL BASE COMPARTMENT
AND ARRANGEMENT

From Klein and Degnan,* the best filling factor for an obscuration of 0.42 is a/w - 0.955; thus, assuming a beam expander output diameter is 1 inch, the required beam expander magnification is 6.03, or ~6. The drawing assumes a primary f-number of 4.2; the maximum allowable for this configuration is f/5.17 assuming a 0.42 obscuration ratio. Slower optics are possible but increased length would be required.

The beacon path is shown with a 5.8 inch lens. This lens produces a beam waist of 0.51 mm which, since the beam is still diffraction-limited, propagates with a 3 dB beamwidth of 1°.

The received beam is separated from the common transmit/receive path at the wire grid polarizer. This beam is passed through the point-ahead mirrors and is reflected by the nutator, which is assumed to be a two-axis device. If two single-axis devices must be used, this portion of the path must be modified. The beam continues to the mixing mirror, where the local oscillator is injected through the central obscuration. A lens focuses an f/8 beam onto the detector.

The local oscillator path duplicates the transmitter configuration, but is displaced both vertically and horizontally. After collimation, the beam has a Gaussian diameter of 0.12 inch (3.0 mm). Wire grid polarizers are used for power and polarization control.

An important element not included in previous designs is a provision for visual sighting. This is provided in the present design by incorporating a removable mirror at the location shown. This mirror will couple an afocal sighting scope into the reflective portion of the optical train. The small hole in the first folding mirror of the beam expander will act as a field stop and beam locating aperture. This feature is essential for ground-based communication testing.

Payload Weight Chargeable Items

Table 4-4 lists weights of components in the Shuttle laser communication terminal. This table was based on individual hardware weights that were scaled to the LDRL-10.6 design. The table is a computer output which was used in the selection process for the terminal aperture and transmitted power. The table includes a 10 pound margin.

Systems Parametric Summary

The major LDRL-10.6 terminal parameters are given in Table 4-5. These parameters define the overall performance, aperture and power, optical losses, and overall weight and power.

---

*B. M. Klein and J. J. Degnan, Appl. Opt., Vol. 13, No. 9, September 1974, pp 2134-2141.

TABLE 4-4. SHUTTLE TERMINAL WEIGHT BREAKDOWN

	Weight, lb
Structure	24.37
Optical telescope with mountings	8.15
Gimbals, motors, and steering mirror	9.72
Servo electronics	4.42
Laser, modulator, and modulator driver (1)	25.00
Servo power conditioning	7.33
Other power conditioning	12.50
Diplexer and miscellaneous optics	3.06
Laser stabilization electronics	0.40
Beacon detector and power supply (1)	0.58
Beacon receiver optics and electronics	0.66
Image motion compensation subsystem	2.62
Cables and connectors	1.71
Miscellaneous	10.05
Total weight	110.57

TABLE 4-5. SHUTTLE TERMINAL PARAMETERS SUMMARY

Antenna diameter	0.18 m
Transmitter output power	1 W
Transmitter efficiency	1%
Beam splitter loss	5%
Collimating lens loss	2%
Diplexer loss	9%
Beam preexpander loss	9.6%
Image motion compensator loss	4.9%
Relay mirrors loss	4.9%
Beam expander loss	9.6%
Pointing mirror loss	2.5%
Pointing error	0.0 μrad
Pointing loss	0.0%
Terminal weight	110.6 lb
Terminal power	195 W

4.2.2 Ground Station for 500 km Orbit Shuttle Terminal Test

The ground stations to be employed in testing the elliptical orbit receiver are the existing stations of the Goddard Optical Research Facility. The 48 inch aperture, precision tracking telescope located near Greenbelt, Maryland is shown in Figure 4-18. A transportable 30 inch aperture facility, shown in Figure 4-19, may be moved to achieve the best possible operational environment. For the purpose of testing the elliptical orbit receiver, the LDRL-10.6 transmitter engineering model will be mated to either of these ground station telescopes.
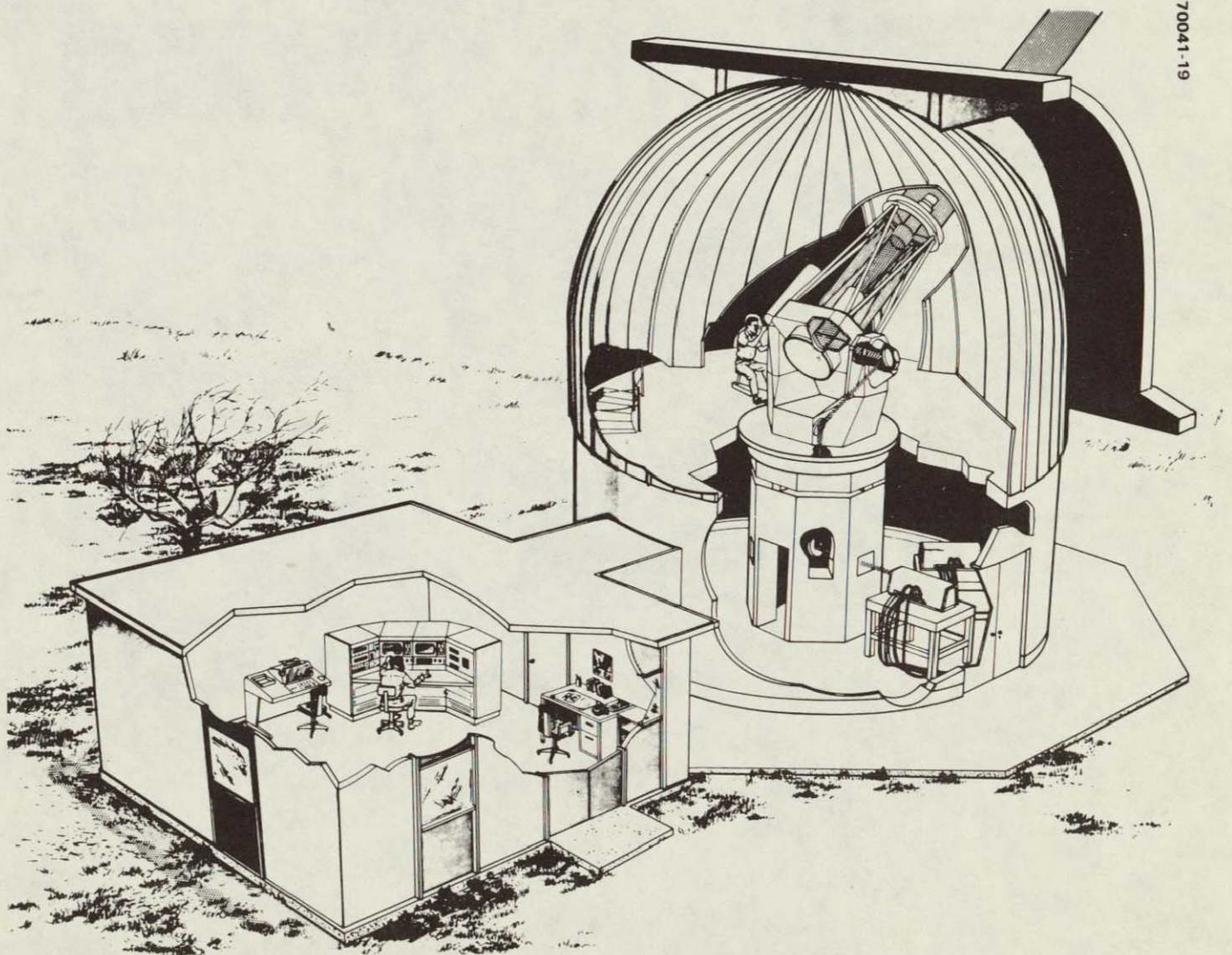
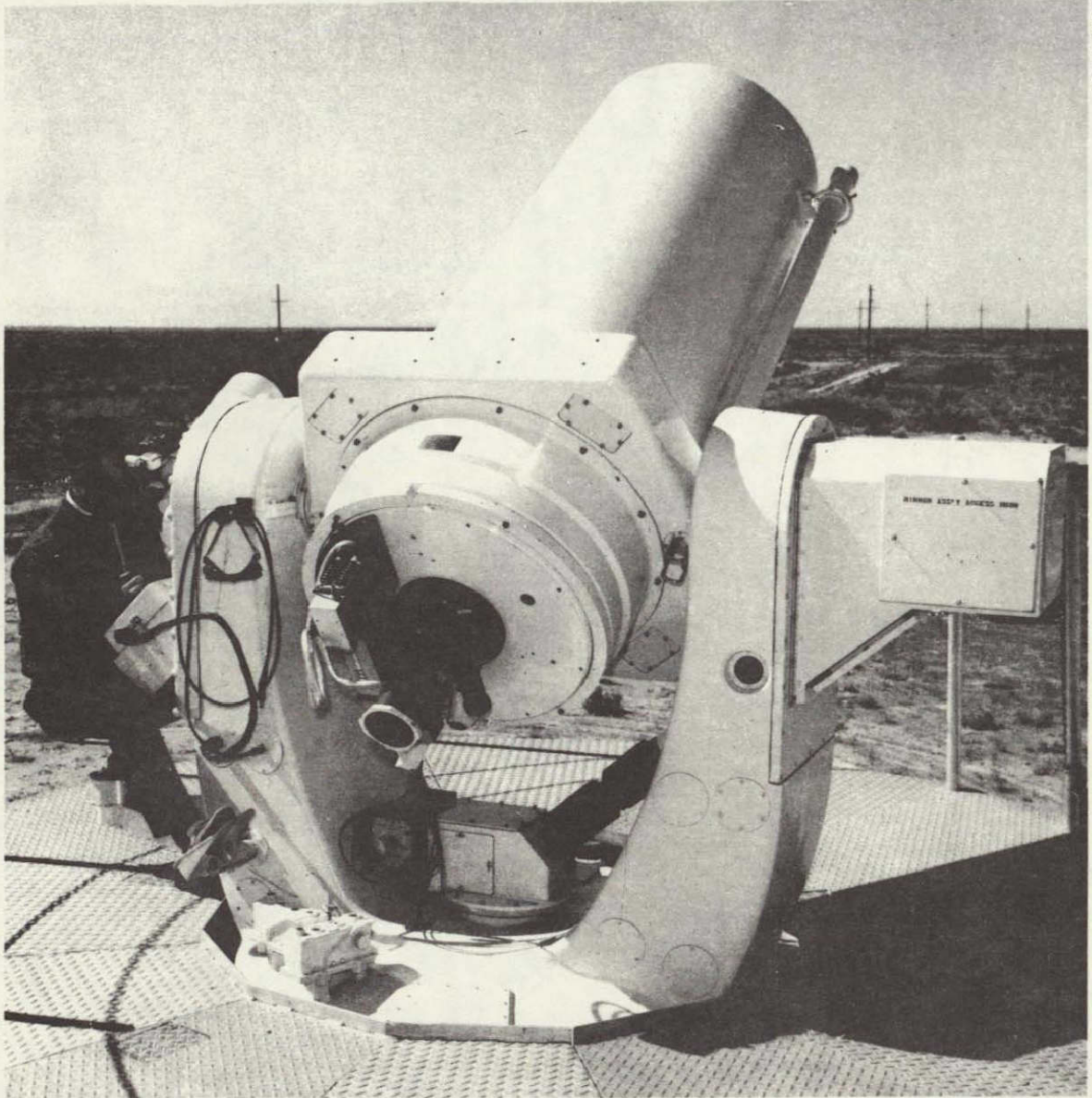FIGURE 4-18. FORTY-EIGHT INCH (1.22 METER) GROUND STATION

FIGURE 4-19. THIRTY INCH (76 CENTIMETER) MOBILE GROUND STATION

Operational Characteristics

The LDRL-10.6 Experiment ground receiver terminal must acquire the 500 km orbit Shuttle transmitter during the approximately 2 minute period when LOS zenith angle is between 80° and 60° (any azimuth) at LOS angular rates to 0.27 deg/sec. After acquisition, it must track the transmitter for zenith angles up to 60° (any azimuth) at peak LOS angular rates up to 0.8 deg/sec. During this approximately 4 minute communication and tracking period, the ground station must maintain the 400 Mbps Shuttle to ground telemetry downlink with a probability of bit error no greater than 10^{-6}.

If the tracking ability of the chosen telescope is adequate to meet the ground station requirements, it will not be necessary for the engineering model LDRL-10.6 to participate in the tracking function. The transmitter IMC output may then be relayed directly to the telescope secondary through appropriate transfer optics without using the large LDRL-10.6 optical head.

It is desirable to be able to optically stop down the ground telescope to as small an effective aperture as possible in order to reduce atmospheric turbulence degradation and to broaden the transmitter beamwidth (thereby relaxing the transmitter pointing requirement). Using the 1 watt LDRL-10.6 transmitter output, the nominal ground aperture requirement for 30° elevation angle and a corresponding maximum range (909) is 16.5 cm.

The ground transmitter station will consist of two main parts, a model of the LDRL-10.6 transmitter and a ground optical facility. LDRL-10.6 transmitter used need not have a complete optical telescope but only the optics necessary to couple into the ground terminal.

The ground terminal which is currently available is the Goddard Optical Research Facility (GORF) shown in functional block diagram form in Figure 4-20. This figure indicates the peripheral equipment, the main 48 inch telescope and the LDRL-10.6 transmitting terminal. A summary of the characteristics of GORF is given in Table 4-6.

The precision tracking GORF telescope has a fixed focus that facilitates experimentation by permitting all equipment to be mounted on tables in the base of the dome. This is illustrated schematically in Figure 4-21.

TABLE 4-6. GODDARD 48 INCH TELESCOPE CHARACTERISTICS

Telescope type	Alti-azimuth mount with Cassegrain and Coudé focal positions
Optical system	48 in. clear aperture Cassegrain with two secondaries which provide f/8 focus, and an f/30 Coudé focus, respectively
Tracking accuracy	20 arcsec, in any alti-azimuth position
Repeatability	5 arcsec each position
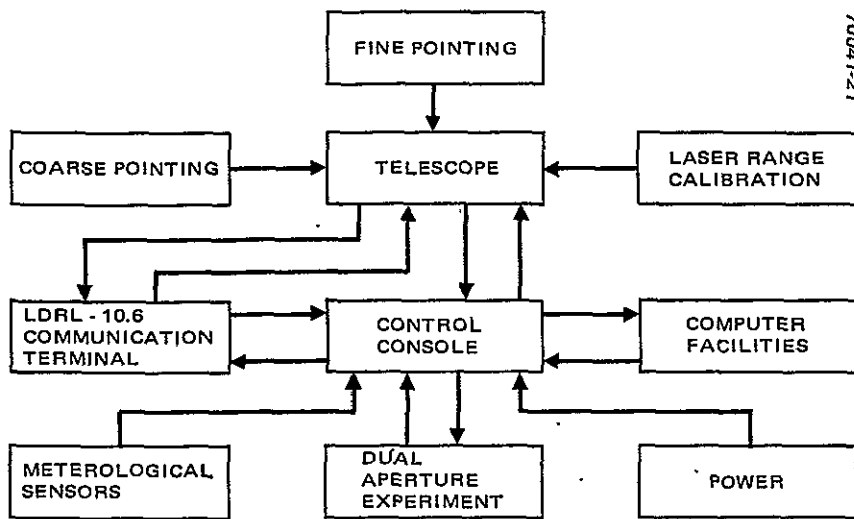
70041-21

FIGURE 4-20. LDRL-10.6 LASER TERMINAL INCORPORATED INTO GODDARD OPTICAL RESEARCH FACILITY
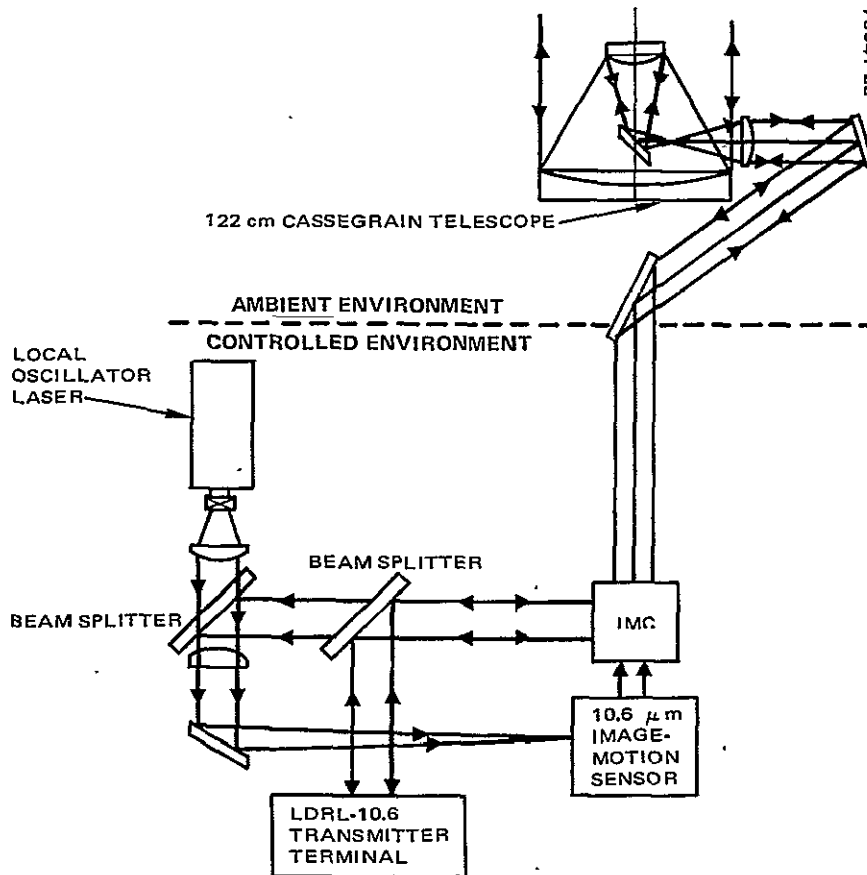
70041-22

FIGURE 4-21. SCHEMATIC ARRANGEMENT OF GORF AND LDRL-10.6 TRANSMITTER USED IN SHUTTLE/GROUND LINK

For the purpose of testing the 400 Mbps Shuttle terminal, the LDRL-10.6 transmitter engineering model is to be mated with the GORF ground station telescope. The transmitter output may then be relayed to the telescope secondary by appropriate transfer optics (to be designed). It is desirable to stop down the ground telescope to as small an effective aperture as possible in order to reduce atmospheric turbulence degradation and broaden the transmitter beamwidth (thereby relaxing the transmitter pointing requirement). Using the 1 watt LDRL transmitter output, the ground aperture requirement is 16.5 cm.

A summary of the ground station parameters is given in Table 4-7.

Conceptual Design

The ground station receiver terminal consists of a 16.5 cm aperture optomechanical subsystem, the receiver front end (detector and wideband preamplifier), the receiver back end (IF stage, doppler tracking, and data demodulation electronics), and the detector radiation cooler. The optomechanical subsystem utilizes the existing 16.5 cm experimental prototype built by Hughes, suitably modified to accommodate the gimbal field of view and tracking rate requirements imposed by the 500 km orbit Shuttle to ground link geometry. The receiver back and front ends were built by the Airborne Instruments Laboratory; the cooler was developed by the A. D. Little Company. These components are to be integrated by Hughes into a receiver meeting the LDRL-10.6 Experiment requirement of a 400 Mbps data rate with a bit error probability of 10^{-6}.

The 16.5 cm aperture experimental receiver provides over 20 dB performance margin (beyond the specified 6 dB) for the 500 km Shuttle to ground link communication requirement (see Section 4.3). Its gimbal field of view and acquisition rate capabilities, however, must be upgraded to meet the requirements of the Shuttle to ground link. The present 20° by 20° gimbal field of view will be effectively enlarged to permit coverage of zenith angles from 0° to 80° (at any azimuth). The actual maximum target rate during acquisition will be approximately 0.27 deg/sec compared to the maximum presently permissible rate of 0.03 deg/sec. These requirements can be most readily accommodated by the addition of an external two-axis gimbaled

TABLE 4-7. GROUND STATION SYSTEM
PARAMETERS SUMMARY

Transmitter data rate	400 Mbps
Transmitter power	1 W
Output aperture (maximum)	48 in.
Tracking accuracy	
• GORF telescope	100 μrad
• LDRL-10.6 telescope	5 μrad
Tracking of elliptical orbit ephemeris	Available
Transmit wavelength (P-20)	10.6 μm
Receive wavelength (P-18)	10.6 μm

pointing mirror to be command controlled (in zenith, azimuth, and respective rates) based on Shuttle ephemeris data. The pointing accuracy, rate, and field of view requirements of the added pointing system would be such as to render its output compatible with the respective capabilities of the existing experimental receiver. The details of this scheme have yet to be finalized; however, it is conceptually straightforward.

Apart from the additional pointing system, the conceptual design of the ground receiver terminal is as follows: the incoming laser beam is received by the Goddard Optical Research Facility; it is then fed into the all reflecting Gregorian telescope, the image motion compensation (IMC) mirror, and an optical detector.

The communication data on the incoming beam are recovered in several steps. First, the optical beam is mixed with a local oscillator beam to produce a difference signal, still carrying the data, whose frequency lies in the RF portion of the spectrum. Second, the RF signal is processed as in a conventional microwave receiver to recover the data. Following the RF detection circuitry are automatic gain control (AGC) circuits and beam-presence logic. The RF signal also contains an amplitude modulation which is impressed by the conical scan of the IMC device, which circularly sweeps the beam on the detector. This amplitude modulation contains the servo error information, which is recovered in a synchronous demodulator. After suitable shaping, the error signal is applied to the IMC drive loop in the phase and magnitude required to reduce the detected error[1]

The IMC drive loop consists of a piezoelectric actuator, a high voltage driver amplifier, a strain gage pickoff and associated instrumentation amplifier, and the shaping network necessary to give the desired servo response. The stepper motor driving the GORF is actuated by a threshold circuit operating on the strain gage signal, which energizes the GORF when the IMC exceeds a preset higher threshold and turns the GORF off when the IMC position is forced back below a low threshold. The GORF motor can also be energized manually to drive the gimbals to any desired position within their range.

4.3 LINK ANALYSIS

4.3.1 Introduction

The objective of the link analysis task has been to itemize sequentially all link signal power gains and losses from the modulated transmitter output to the detector output. These correspond to a specified (or determined) received data bandwidth signal to noise ratio (S/N). The link analysis is performed by a computer program which has as one of its outputs the Design Control Table (link power budget) for the maximum range (i.e., 60° LOS zenith angle) 500 km circular orbit Shuttle to ground, 400 Mbps downlink. In general, the link analysis program optimizes the transmitter and receiver aperture diameters and transmitter power to minimize total system weight. In the case of the LDRL-10.6 Experiment, however, the transmitter aperture diameter (18 cm) was established by cost considerations (with little additional weight penalty), while the 10.6 μm transmitter output power is constrained to no more than 1 watt by present CO_2 laser technology. A minimum received data bandwidth S/N of 18.90 dB is required to achieve the specified bit error rate of 10^{-6} with a 6 dB margin. For the Shuttle to ground link, the transmitter (Shuttle) terminal and receiver (ground) terminal aperture diameters and transmitter output power are specified as program inputs. The corresponding received data bandwidth S/N is calculated by the program. The link analysis program also calculates the weight and power requirement of the transmitter terminal.

Two ground receiver aperture diameters of particular interest are 16.5 cm and 35 cm. The 16.5 cm ground aperture requirement could be met by the existing experimental receiver opto-mechanical subsystem, which would otherwise be surplus to the 400 Mbps LDRL-10.6 Experiment. The experimental 16.5 cm aperture experimental receiver independently exceeds the minimum aperture requirements for the Shuttle to ground link, but would require an additional pointing mirror (GORF) to accommodate the ground terminal tracking field of view and angular rate requirements. The 35 cm aperture is the minimum transmitter aperture required for testing of the 400 Mbps Molniya orbit receiver terminal using a ground based Shuttle transmitter. This requirement is to be met by mating the transmitter back end to the Goddard Optical Research Facility optics, stepped down to 35 cm to reduce scintillation. Hence, a 35 cm effective aperture ground facility may be assumed to be available from this requirement. Shuttle to ground link power budgets (Design Control Tables) are given for both these alternative ground aperture options in Tables 4-8 and 4-9.

Inputs to the link analysis program are derived from two sources: 1) system requirements, and 2) technology status. System requirements inputs include the specified 400 Mbps data bit rate and a bit error rate of 10^{-6} with a 6 dB margin. System requirements also dictate the operational environment: communication range, point-ahead angle, doppler variation range, and required tracking rates and accuracies. Technology status defines the transmitter and receiver system losses and detector performance

TABLE 4-8. 500 KM ORBIT SHUTTLE TO GROUND LINK DESIGN CONTROL TABLE —
30° LOS ELEVATION ANGLE, 909 KM LOS RANGE, 16.5 CM RECEIVER APERTURE

Parameter	Nominal	Favorable Tolerance	Adverse Tolerance
Transmitter Parameters			
Modulated laser output power (1.00 W)	0.00	0.000	0.000
Beam splitter loss	-0.22	0.023	-0.023
Collimating lens loss	-0.09	0.009	-0.009
Diplexer loss	-0.41	0.043	-0.043
Beam preexpander loss	-0.44	0.090	-0.092
Image motion compensator loss	-0.22	0.022	-0.022
Relay mirrors loss	-0.22	0.045	-0.046
Beam expander loss	-0.44	0.090	-0.092
Pointing mirror loss	-0.11	0.022	-0.022
Obscuration loss (gamma = 0.362)	-2.85	0.000	0.000
Pointing loss	0.00	0.000	-0.079
Ideal aperture gain (0.180 m aperture)	94.54	0.000	0.000
Path Parameters			
Space loss (R = 909 km)	-240.65	0.000	0.000
Atmospheric attenuation loss	-8.00	0.000	0.000
Receiver Parameters			
Ideal aperture gain (0.165 m aperture)	93.79	0.000	0.000
Obscuration loss (gamma = 0.200)	-0.18	0.000	0.000
Image motion compensator loss	-0.46	0.048	-0.049
Local oscillator diplexer loss	-0.04	0.004	-0.004
Beacon diplexer loss	-0.13	0.013	-0.013
Optics reflectance losses	-0.44	0.086	-0.092
Heterodyne detection loss	-1.85	0.225	-0.237
Detector noise degradation	-0.48	0.084	-0.208
Planck's constant	331.78	0.000	0.000
Carrier frequency, dB (Hz)	-134.52	0.000	0.000
Detector quantum efficiency	-2.22	0.000	-0.792
Data bandwidth, dB (Hz) (352 MHz)	-85.47	0.000	0.000
Data bandwidth signal/noise	40.67	0.804	-1.823

4-32

TABLE 4-9. 500 KM ORBIT SHUTTLE TO GROUND LINK DESIGN CONTROL TABLE —
30° LOS ELEVATION ANGLE, 909 KM LOS RANGE, 35 CM RECEIVER APERTURE

Parameter	Nominal	Favorable Tolerance	Adverse Tolerance
Transmitter Parameters			
Modulated laser output power (1.00 W)	0.00	0.000	0.000
Beam splitter loss	-0.22	0.023	-0.023
Collimating lens loss	-0.09	0.009	-0.009
Diplexer loss	-0.41	0.043	-0.043
Beam preexpander loss	-0.44	0.090	-0.092
Image motion compensator loss	-0.22	0.022	-0.022
Relay mirrors loss	-0.22	0.045	-0.046
Beam expander loss	-0.44	0.090	-0.092
Pointing mirror loss	-0.11	0.022	-0.022
Obscuration loss (gamma = 0.362)	-2.85	0.000	0.000
Pointing loss	0.00	0.000	-0.079
Ideal aperture gain (0.180 m aperture)	94.54	0.000	0.000
Path Parameters			
Space loss (R = 909 km)	-240.65	0.000	0.000
Atmospheric attenuation loss	-8.00	0.000	0.000
Receiver Parameters			
Ideal aperture gain (0.350 m aperture)	100.32	0.000	0.000
Obscuration loss (gamma = 0.200)	-0.18	0.000	0.000
Image motion compensator loss	-0.46	0.048	-0.049
Local oscillator diplexer loss	-0.04	0.004	-0.004
Beacon diplexer loss	-0.13	0.013	-0.013
Optics reflectance losses	-0.44	0.086	0.002
Heterodyne detection loss	-1.85	0.225	-0.237
Detector noise degradation	-0.48	0.084	-0.208
Planck's constant	331.78	0.000	0.000
Carrier frequency, dB (Hz)	-134.52	0.000	0.000
Detector quantum efficiency	-2.22	0.000	-0.792
Data bandwidth, dB (Hz) (352 MHz)	-85.47	0.000	0.000
Data bandwidth signal/noise	47.20	0.804	-1.733

as well as system component weights (or power requirements) as a function of their performance (output power, aperture diameter, bandwidth, etc.).

4.3.2 LDRL-10.6 Signal Noise Calculations

The refined LDRL-10.6 link budget calculations are presented in the form of a Design Control Table. The intermediate frequency signal-to-noise ratio $(S/N)_{IF}$ for an optical heterodyne receiver is given by

$$(S/N)_{IF} = \frac{\left(\frac{G\eta q}{h\nu_c}\right)^2 R_L P_S P_{LO}}{qB_{IF}G^2\left[\frac{\eta q}{h\nu_c}\left(P_S + P_B + P_{LO}\right) + I_D\right]R_L + 2k\,TB_{IF}} \qquad (1)$$

where

B_{IF} = intermediate frequency bandwidth

G = detector gain

η = detector quantum efficiency

q = electronic charge

h = Planck's constant

ν_c = optical carrier frequency

R_L = detector load resistance

P_S = received optical signal power

P_B = received background power

I_D = detector dark current

k = Boltzmann's constant

T = postamplifier noise temperature

P_{LO} = local oscillator power

for the ideal case in which the local oscillator power dominates the other noise terms in the denominator, this expression reduces to

$$(S/N)_{IF_{ideal}} = \frac{P_s \eta}{h \nu_c B_{IF}} \tag{2}$$

A detector noise degradation factor defined by

$$\eta_N = \frac{(S/N)_{IF}}{(S/N)_{IF_{ideal}}} \tag{3}$$

accounts for the degradation from ideal performance due to all noise mechanisms. The $(S/N)_{IF}$ may then be written in the more compact form

$$(S/N)_{IF} = \frac{P_s \eta \, \eta_N}{h \nu_c B_{IF}} \tag{4}$$

which facilitates representation in dB form. The received signal power at the detector is given by*

$$P_s = P_T \, \eta_T \quad G_T \, \eta_S \quad G_R \, \eta_R$$

where

P_T = modulated laser output power

η_T = transmitter loss

G_T = transmitter aperture gain

η_S = space loss

G_R = receiver aperture gain

η_R = receiver loss

---

*Atmospheric losses included for a space to ground link.

Substituting this expression into Equation 4 gives

$$(S/N)_{IF} = \frac{P_T \, \eta_T \, G_T \, \eta_S \, G_R \, \eta_R \, \eta \, \eta_N}{h \nu_c B_{IF}}$$

or

$$(S/N)_o = \frac{P_T \, \eta_T \, G_T \, \eta_S \, G_R \, \eta_R \, \eta \, \eta_N}{h \nu_c B_o}$$

since $B_{IF} = 2 B_o$ and (for usably strong signals) $(S/N)_o = 2(S/N)_{IF}$.

The LDRL-10.6 Design Control Table (DCT) of Tables 4-8 and 4-9 expresses this Equation in logarithmic (dB) form. The losses are itemized in detail with respect to specific system elements. The DCT is a dB summation of power, gains, and losses that determine $(S/N)_{IF}$ for a specified link. Each DCT entry is defined and its evaluation discussed in the following paragraphs.

4.3.3 System Parameters

Transmitter Parameters

Modulated Laser Output Power. The modulated laser output power is the modulated sideband power into the transmitter optical system. Laser power may be specified as an input, determined by other specified inputs, or optimized for minimum system weight.

Beam Expander Loss. The beam expander loss is due to attenuation and reflection losses by the two element Zinc Selenide beam pre-expander optics. Attenuation for ZnSn is 0.01 percent per cm; reflectance is 0.999 per surface. There are six surfaces since one element is a doublet. The net beam expander loss is 0.986.

Diplexer Loss. The transmitter diplexer (beam splitter) reflects the incoming beacon signal to its receiver (during the acquisition phase) while transmitting the outgoing communication signal. The diplexer consists of a wire-grid polarizer and a quarter wave plate. The combination has a net loss of approximately 0.91.

Image Motion Compensator Loss. The transmitter IMC loss is due to reflectance of 0.975 at each of the two gold electroplated IMC mirror surfaces. The resultant IMC loss is $(0.975)^2 = 0.951$.

Optics Reflectance Loss. The optics reflectance is approximately 0.975 at each of the six gold electroplated reflecting elements in the transmitter optical system. These are follows:

1) Inner gimbal pointing mirror

2) Large folding mirror

3) Primary paraboloid

4) Secondary paraboloid

5) Small folding mirror

6) Relay mirror

The net loss due to these six elements is then $(0.975)^6 = 0.859$.

Obscuration Loss. The transmitter obscuration loss accounts for the reduced far field axial gain of a Gaussian illuminated and obscured circular aperture relative to a uniformly illuminated and unobscured one. The relative degradation is given by (Reference 1)

$$g_T = \frac{2}{\alpha^2} \left[e^{-\alpha^2} - e^{-\alpha^2 \gamma_T^2} \right]^2$$

where

γ_T is the transmitter optics diameter obscuration ratio. γ_T is a function of the aperture diameter, D_T

α is the laser beam truncation defined as the ratio of beam width (in the obscuration plane) to primary aperture diameter.

The obscuration loss is calculated by the Link Analysis Program using the γ_T (D_T) required for the 1° acquisition field of view and f/1.5 transmitter optics. The optimum value of α for a Gaussian laser beam intensity distribution is used, approximated by

$$\alpha = 1.12 - 1.30 \gamma_T^2 + 2.12 \gamma_T^4 .$$

Figure 4-22 depicts g_T, dB as a function of γ_T for $\alpha = \alpha_o$.

For the 0.18 meter aperture LDRL-10.6 system, $\gamma = 0.362$ and the obscuration loss is

$$g_T = 0.519 \text{ (or } -2.85 \text{ dB)}$$

Pointing Loss. Pointing loss results from the receiver being displaced from the maximum of the transmitter far field gain pattern due to pointing error. The nominal pointing loss is zero since it is intended that point-ahead angle be corrected entirely. However, even if point-ahead angle information were known with absolute accuracy, it is estimated that pointing error would be of the order of 5 μ rad. For the far field gain pattern corresponding to the aperture diameter obscuration $\gamma_T = 0.362$ (0.18 meter transmitter aperture), this represents a gain loss of 2.85 dB compared to the maximum (axial) gain.

Ideal Aperture Gain. The ideal aperture gain is the maximum axial far field gain (relative to an isotropic radiator) achievable with a uniformly illuminated, unobscured circular aperture

$$G_T = \left(\frac{\pi D_T}{\lambda} \right)^2$$

where λ is the wavelength and D_T is the transmitter aperture diameter.

Path Parameters

Space Loss. Space loss is given by

$$S = \left(\frac{\lambda}{4 \pi R} \right)^2$$

where λ is the wavelength and R is the communication range.

Receiver Parameters

Ideal Aperture Gain. The ideal gain for a uniformly illuminated, unobscured circular aperture of diameter D_R is

$$G_R = \left(\frac{\pi D_R}{\lambda} \right)^2$$

Obscuration Loss. Obscuration of the receiver aperture affects performance most directly by reducing the effective area of the receiver aperture.

In terms of the receiver diameter obscuration ratio , the receiver obscuration loss is the ratio of the obscured to unobscured aperture areas given by

$$g_R = (1 - \gamma^2) \cdot$$

Receiver obscuration loss, g_R, dB versus γ is plotted in Figure 4-23. Obscuration of the receiver aperture causes an additional loss by degrading the efficiency of the heterodyne detection process. This effect is included in the heterodyne detection loss. For the LDRL-10.6 receiver, $\gamma = 0.2$, and the obscuration loss is given by $g_R = 0.96$ (0.18 dB).

· Image Motion Compensator Loss. The receiver image motion compensator loss is due to a 0.975 reflectance at each of the two gold electroplated IMC mirrors and the nutation loss attendant to generating the IMC error signal. The receiver IMC net loss is approximately 0.90.

Local Oscillator Diplexer Loss. The local oscillator diplexer loss is primarily due to the imperfect reflection since the incoming beam is not transmitted by the diplexer. The local oscillator diplexer loss is a . approximately 0.99.

· Beacon Diplexer Loss. Beacon diplexer loss is due to both transmission and reflection of the incoming beam. The net beacon diplexer loss is approximately 0.97.

Optics Reflectance Losses. Optics reflectance loss is approximately 0.975 at each of the four gold electroplated reflecting elements in receiver optical system. These are as follows:

1) Pointing mirror

2) Primary paraboloid

3) Secondary paraboloid

4) Folding mirror

The loss of the four elements is then $(0.974)^4 = 0.904$.

Heterodyne Detection Loss. The heterodyne detection loss depends on the electric field distributions of the signal and local oscillator on the
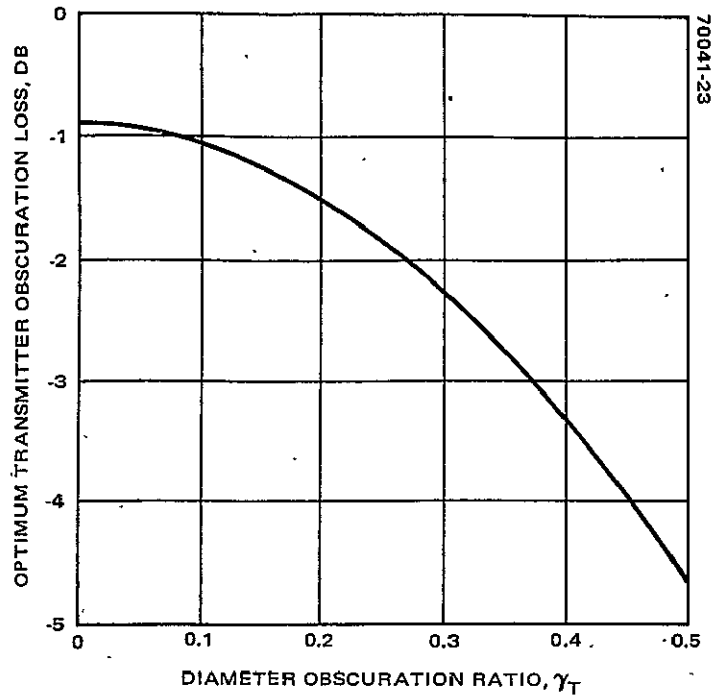
FIGURE 4-22. AXIAL GAIN OF OPTIMUM GAUSSIAN ANTENNA RELATIVE TO $(\pi D_T/\lambda)^2$ AS FUNCTION OF OBSCURATION RATIO γ_T
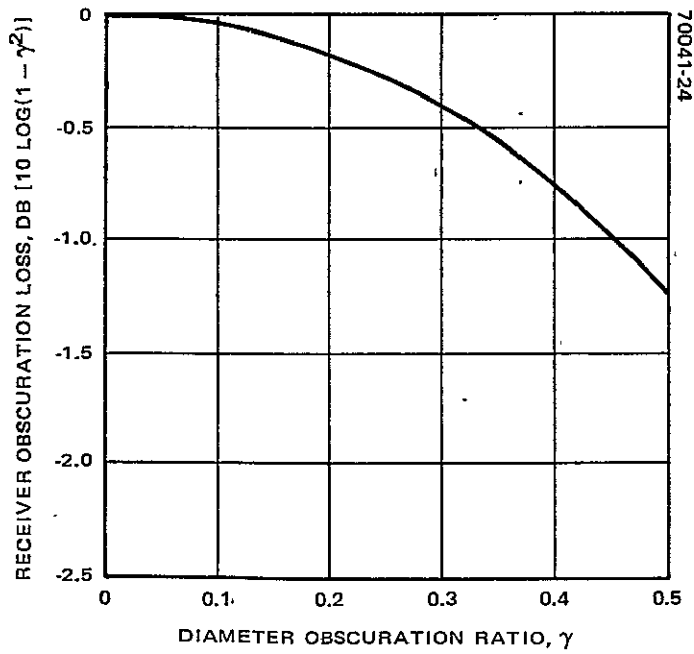
FIGURE 4-23. RECEIVER LOSS IN DECIBELS DUE TO CENTRAL OBSCURATION

detector. For the readily implemented case of a uniform local oscillator field distribution, the heterodyne detection loss is given by (Reference 2)

$$\eta_H = \left[4/(1 - \gamma^2)\right]\left\{\left[J_0(\gamma\sigma r) - J_0(\sigma r)\right]/\sigma r\right\}^2$$

where

γ = receiver optics diameter obscuration ratio

$\sigma = k R_A/2F_S$

$k = 2\pi/\lambda$

R_A = Airy disk size

F_S = system f number

$r = R_D/R_A$

R_D = detector radius

η_H is plotted in Figure 4-24 (Reference 2) as a function of R_D/R_A with γ as a parameter. It is evident from Figure 4-24 that η_H is a maximum for $R_D/R_A \approx 0.75$. This optimum detector size minimizes the (S/N) degradation due to local oscillator generated detector shot noise. For the LDRL-10.6 receiver, $\gamma = 0.2$ so that for $R_D/R_A = 0.75$, $\eta_H = 0.653$.

Detector Noise Degradation. As discussed previously, detector noise degradation η_N is an artifice to compactly account for all detector noise mechanisms

$$\eta_N = \frac{(S/N)_{IF}}{(S/N)_{IF_{ideal}}}$$

where $(S/N)_{IF_{ideal}}$ results from the dominant local oscillator noise case (all other noise sources negligible). η_N is calculated in the Link Analysis Program.
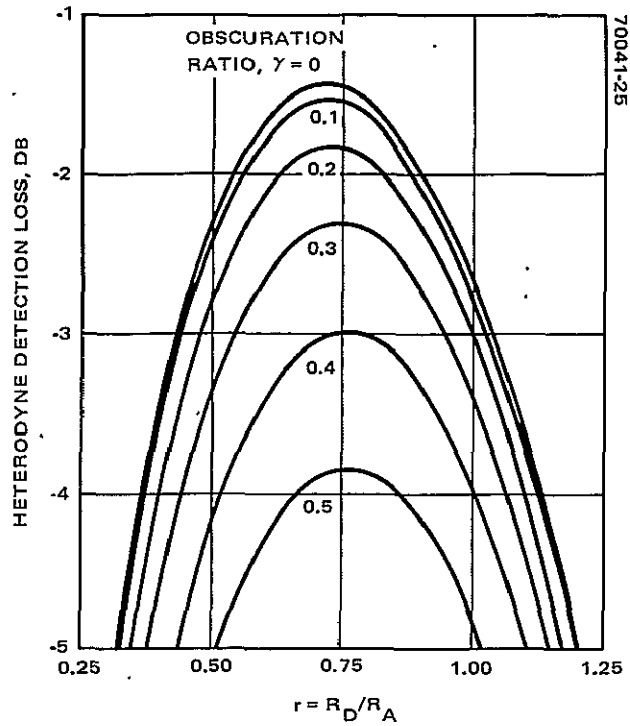
FIGURE 4-24. HETERODYNE DETECTION LOSS R_D/R_A WITH
OBSCURATION RATIO AS A PARAMETER
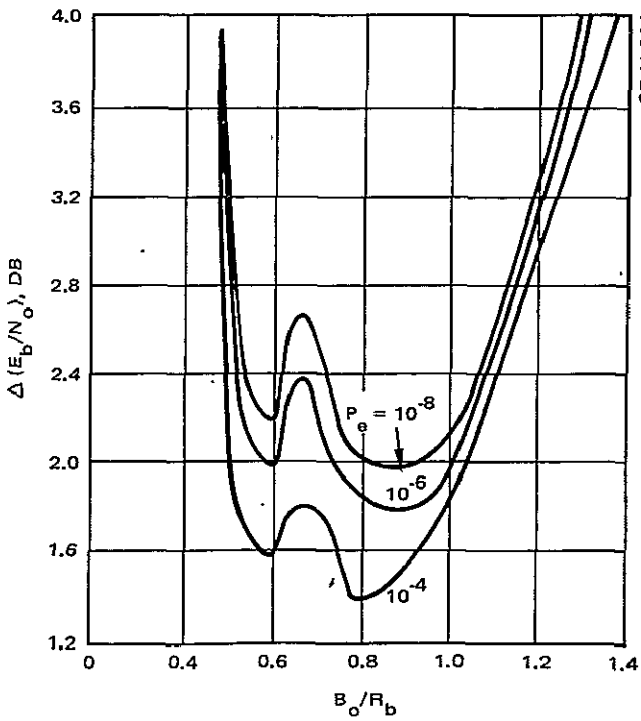
FIGURE 4-25. $\Delta (E_b/N_o)$ VERSUS B_o/R_b FOR
BAND LIMIT AND SAMPLE DETECTION
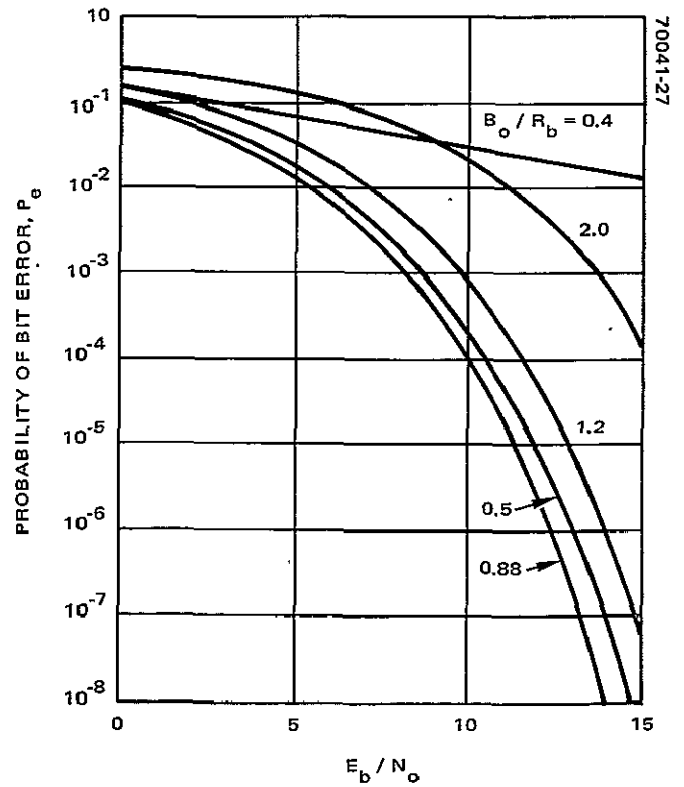
FIGURE 4-26. P_e VERSUS E_b/N_o FOR BAND LIMIT
AND SAMPLE DETECTION

Planck's Constant. Planck's constant relates photon energy to photon (carrier) frequency:

$$h \approx 6.625 \times 10^{-34} \, J \cdot sec$$

Carrier Frequency. The carrier frequency corresponding to the 10.6 micrometer wavelength is

$$\nu_c \approx 2.82823 \times 10^{13} \, Hz$$

Detector Quantum Efficiency. Quantum efficiency is the detector conversion efficiency between light and electrical energy. A quantum efficiency of 0.50 is readily realizable; 0.60 appears feasible.

IF Bandwidth. The system IF bandwidth (B_{IF}) requirement is a function of the link data rate (R_b). The signaling (low pass) bandwidth (B_o) corresponding to B_{IF} is $B_o = B_{IF}/2$. For a given detection method, the detector performance degradation from the ideal matched filter case due to thermal noise and intersymbol interference depends on the ratio B_o/R_b. The relationship between B_o/R_b and detector performance degradation has been examined for a number of detection methods (Reference 3). One readily implemented (hence, attractive) detection scheme for binary digital data uses the "band limit and sample" detector. For this situation, the detector performance degradation may be minimized by the optimal choice of B_o/R_b. The detector performance degradation may be characterized by the increase in P_e (for constant bit energy/spectral noise density, E_b/N_o) or, alternatively, by the increase in E_b/N_o required to maintain a constant P_e. Figure 4-25 depicts E_b/N_o (for constant P_e) as a function of B_o/R_b. Note that for the LDRL-10.6 requirement of $P_e = 10^{-6}$, the detector performance degradation is minimized for $B_o/R_b \approx 0.88$. The corresponding required IF bandwidth for the LDRL 400×10^6 bps data rate is then

$$B_{IF} = 2 \, B_o$$
$$= 2 \times 0.88 \times R_b$$
$$= 704 \times 10^6 \, Hz$$

Intermediate Frequency Bandwidth Signal-to-Noise Ratio. The required $(S/N)_{IF}$ to detect with specified P_e depends on the detection method used. For the chosen band limit and sample scheme, required $(S/N)_{IF}$ is determined by (B_o/R_b). Figure 4-26 (Reference 3) depicts P_e as a function

of E_b/N_o with B_o/R_b as a parameter. For $P_e = 10^{-6}$ and the corresponding optimum value of $B_o/R_b \approx 0.88$, the E_b/N_o required is approximately 17.159 (12.345 dB). The $(S/N)_{IF}$ is then determined,

$$(S/N)_{IF} = \left(\frac{E_b}{N_o}\right) / \left(\frac{B_{IF}}{R_b}\right)$$

= 9.749 or 9.89 dB

An additional 6 dB margin is included to accommodate design uncertainties. The resultant $(S/N)_{IF} = 15.89$ dB $((S/N)_o = 18.90$ dB) has been used as a basis for the LDRL system preliminary performance calculations.

4.3.4 Link Establishment Analysis

Introduction

The Shuttle to ground link consists of a one-way link between a Shuttle transmitter in a 500 km orbit and a ground receiver. The Shuttle transmitter will acquire and track a 10.6 μm beacon which is located at the ground receiver site and which continuously illuminates the Shuttle transmitter when the Shuttle is within view. The Shuttle transmitter configuration consists of a single detector and a single set of optics for both acquisition and tracking. The field of view of the Shuttle is a $\pm 0.5°$ cone, and the ground beacon must be acquired and continuously tracked within this field of view. It is assumed that the power of the ground beacon is great enough that signal/ noise ratio in a 6 μsec acquisition pulse is at least 30 dB, so that all acquisition pulses are detected and no false targets are acquired. Therefore, the problem of acquisition is one of first bringing the target into the $\pm 0.5°$ telescope field of view and then of moving the target across the detector at such a rate that tracking can be initiated.

The objective of this analysis is to derive the IMC (image motion compensation) requirements associated with this link and to define an acquisition concept that permits these requirements to be met within reasonable hardware restrictions. The problem is not a trivial one. It is known at the outset that the technique presently used for the receiver, which works fine for a small field of view acquiring a slow moving target, is not suitable for the case of a 1° FOV acquiring a fast moving target. To accommodate the larger FOV it is necessary to go from piezoelectric devices to electromagnetic (EM) devices. To keep the power consumption of the EM devices within reasonalbe bounds, the scan frequency must be kept below 200 Hz, which is not compatible with the higher target rates using the present acquisition concept.

To reconcile the conflicting requirements, a new acquisition concept is proposed. This new approach differs from the current approach is several ways. First, in order to reduce the apparent target motion, the gimbals are programmed to track out the known motion of the target. Second, in order to provide margin to the acquisition capability, a simple five-position gimbal scan is incorporated which is added to the programmed target motion. Third, in order to relax the IMC readout requirements, two IMC scan levels are used: a large scan covering the 1° field which requires no fine readout capability, and a miniscan covering all 0.1° field which requires a readout accuracy of a few arcseconds. Finally, the IMC position at the time the target is detected is stored as a reference for reacquisition on a second pass (the IMC is not required to stop on target as it presently is).

These changes in acquisition approach require considerably increased complexity in the servo electronics. However, the only practical alternative, given such a large FOV and high tracking rates, is to employ a separate acquisition detector (using direct detection). Such alternate techniques have not been investigated here because, under the study guidelines, only heterodyne detection and a 1° FOV are to be considered. In any case, given the current state of electronics miniaturization, the additional electronics complexity is not at all impractical; it is simply a matter of increased cost and reduced reliability due to the increased parts count. Since, for the shuttle application, reliability is not an overriding consideration, the approach described here appears the best available.

Tracking Requirements

The acquisition and track parameters are shown in Figure 4-27, where zenith angle (as viewed from the ground site), the tracking angle between the satellite and ground site, and the rate of change of this angle are plotted against time. The two angles are defined in the figure. It is assumed that, because of atmospheric effects, the high data rate communications link cannot be established until the zenith angle becomes less than 60°, which occurs approximately 4 minutes after the satellite is in view of the ground station. However, there is no reason to wait that long to attempt acquisition. If acquisition is initiated at a zenith angle of 80°, for example, 2 minutes are available to acquire before the 60° zenith is reached.

The tracking angle at 80° zenith is 65° and the rate is approximately 0.02 deg/sec, whereas at 60° zenith the tracking angle is 52° and the rate is increased to 0.24 deg/sec. The maximum tracking rate occurs at zero zenith angle and is 0.8 deg/sec. Therefore, it is important to achieve acquisition as soon as possible. It is assumed here that acquisition will occur at a zenith angle equal to or greater than 60°, so that acquisition must occur at rates up to 0.24 deg/sec, and tracking must be maintained at rates up to 0.8 deg/sec.
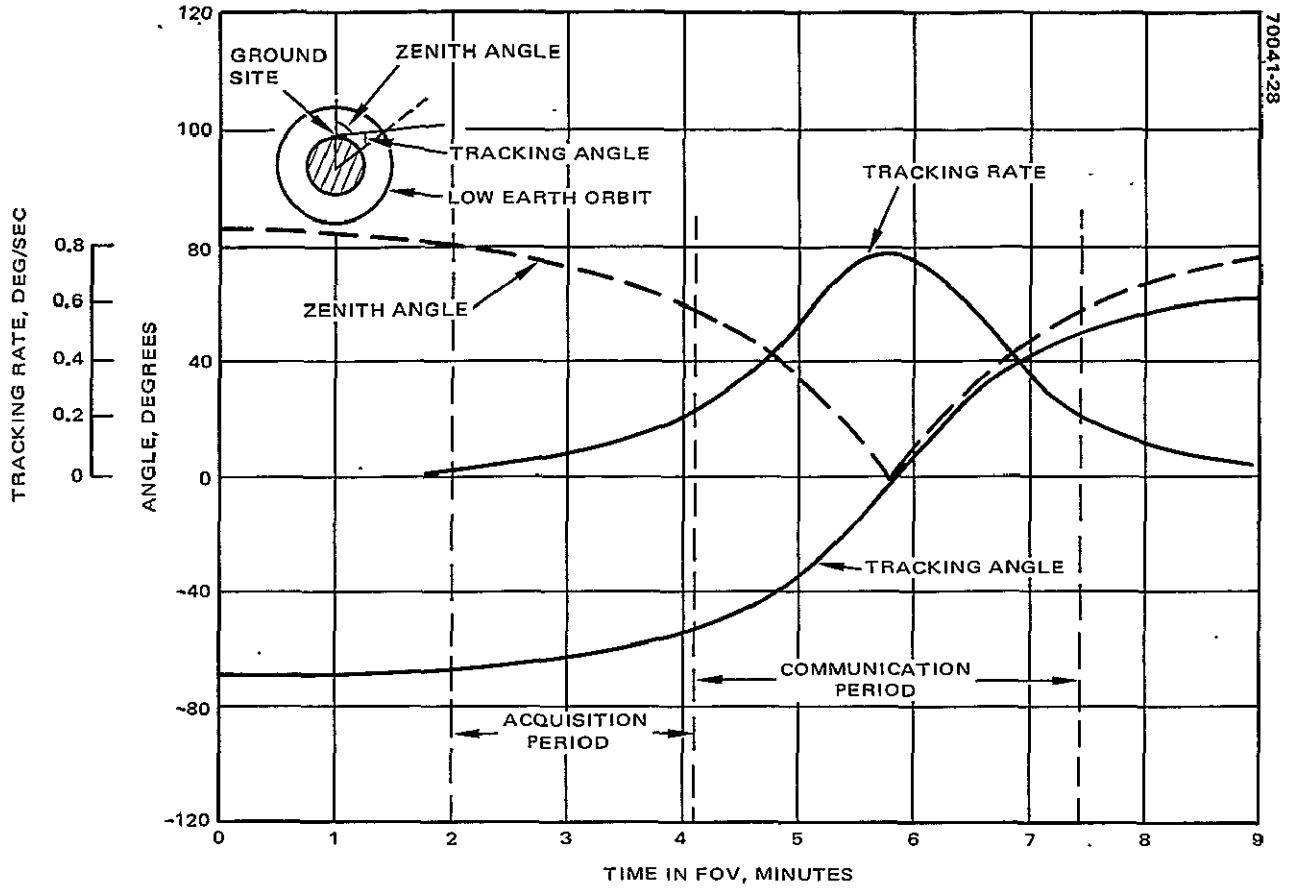
FIGURE 4-27. ACQUISITION PARAMETERS AS A FUNCTION OF SATELLITE
TIME IN FIELD OF VIEW

$$\theta_c \left[t \le t \le t_{i+i} \right] = \theta_i + R_i t$$

$$R_i = \frac{d\theta}{dt} \Bigg]_{t = t_i}$$
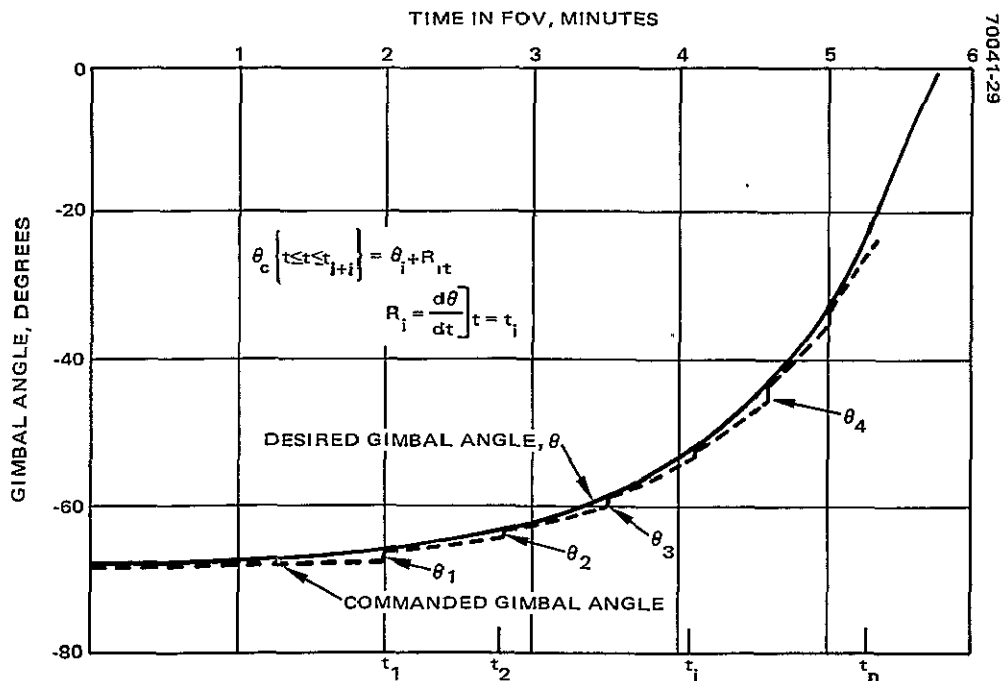
FIGURE 4-28. GIMBAL COMMAND SEQUENCE

Acquisition Concept

For the acquisition rates shown in Figure 4-27, there are basically two approaches available for beacon acquisition: a) use a line scan (fence) and let the natural target motion bring the target across the fence, or b) continuously direct the gimbals to the known position of the target so that the natural target motion is effectively cancelled. The concept proposed here is based primarily on the latter approach, but the requirements are formulated such that the former approach can also be used. That is, even though it is planned to effectively cancel the target motion through open-loop gimbal commands, the specified IMC dynamics will handle target rates up to 0.25 deg/sec, using a fence scan.

The proposed concept is as follows: The position of the ground beacon in shuttle coordinates is known to a certain accuracy at all times and can be pridicted ahead of time on the basis of ephemeris data. Therefore, just after the ground site comes into view of the Shuttle and RF communications have been established, the initial gimbal angles and rates are transmitted to the servo system. These initial values will be transmitted as five numbers:

$$t_1 = \text{time to execute command}$$

$$\theta_1 = \text{initial value of roll gimbal}$$

$$R\dot{\theta}_1 = \text{initial rate of roll gimbal}$$

$$\emptyset_1 = \text{initial value of pitch gimbal}$$

$$R\dot{\emptyset}_1 = \text{initial rate of pitch gimbal}$$

At the execution time t_1, the servo command electronics will generate and execute a command waveform of the appropriate shape (step plus ramp). After execution of the first command, five new numbers are transmitted corresponding to the new set of commands to be executed at time t_2, and so on, until acquisition takes place.

The command sequence is illustrated in Figure 4-28. As the gimbal angle (pitch angle is illustrated) gets smaller in absolute value (which means the zenith angle is getting smaller) the required time between updates also gets smaller because of the higher rates. The frequency of the updates at any point depends on the allowable error between the commanded gimbal position and the desired position. If the allowable error is 10 percent of the 1° field of view, the minimum time between updates is approximately 20 seconds for the first minute and reduces to 5 seconds by the end of the third minute.

The above sequence should ensure that the target will remain in the ±0.5° FOV long enough for the IMC to scan the detector across the target.
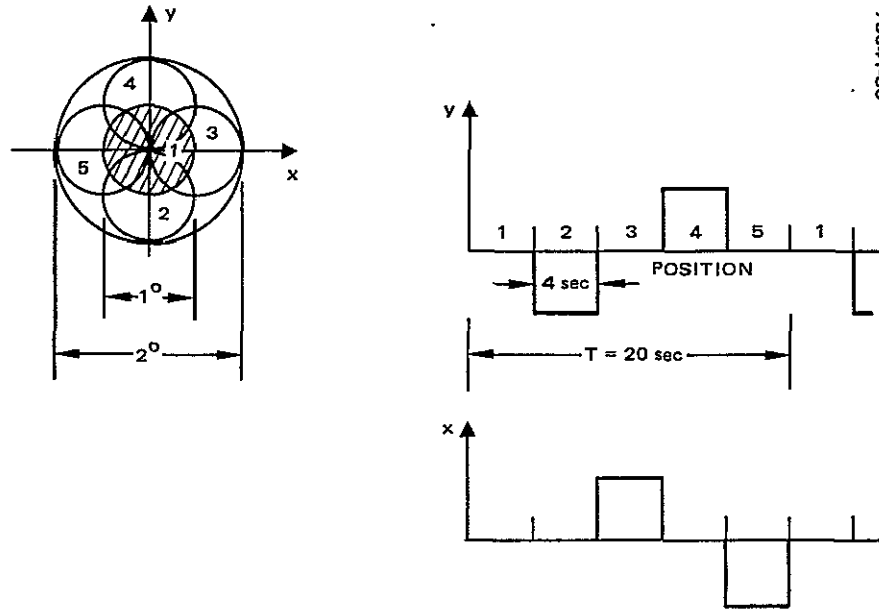
FIGURE 4-29. GIMBAL SCAN ROUTINE

A spiral scan is proposed which makes use of a single scan frequency and a sawtooth amplitude scan. The effective field of view of the optics is further extended through use of a gimbal scan. The proposed gimbal scan, which is illustrated in Figure 4-29, consists of five discrete positions of the gimbals. The gimbals will be stepped rapidly from one position to the next, but remains at each position long enough for an IMC scan frame to be completed. It is to be emphasized that the only purpose of the gimbal scan routine is to provide margin between the ±0.5° FOV and the pointing accuracy of the Shuttle, which is given as ±0.5° with a rate stability of either 0.01 deg/sec, depending on whether the RCS vernier jets are used.*

From the above discussion, the acquisition concept can be summarized as follows:

1) From Shuttle navigation data the position of the ground beacon is known to a certain accuracy at all times, and can be predicted far enough in advance to allow a command sequence to be generated on the ground.

2) The command sequence is transmitted to the transmitter servo system and executed at a rate that minimizes gimbal errors so that most of the target error is contributed by the Shuttle pointing error.

3) The Shuttle pointing error is nominally equal to the telescope FOV (±0.5°), so that the above procedures should bring the target within the telescope FOV.

_____

*Space Shuttle System Payload Accommodations: Level II Program Definition and Requirements, Vol. XIV, Revision C, pp 3-9.

4) To add margin to the above procedure a simple gimbal scan routine is proposed, which extends the effective telescope FOV by a factor of approximately two.

5) Within the telescope FOV two IMC spiral scans are employed: a large scan covering the entire telescope FOV, which initially brings the target across the detector, and a miniscan that "zeroes-in" on the target for capture.

6) A backup is provided in which the spiral scan would be replaced with a circular fence scan and the gimbal command sequence would be eliminated.

IMC Requirements

The IMC requirements are defined by the IMC scan frequency, IMC scan amplitude, the size of the IMC mirror and the resolution and accuracy of the IMC readout device. The scan frequency is somewhat independent of the other requirements and will be considered separately.

Scan Frequency. The scan frequency is determined by the target velocity and line resolution. The line resolution depends on the aperture size, which determines the angular subtense of the image. For the present system (receiver) a 6 inch aperture produces a 3 dB beam diameter of 0. 0.0046° (80 μ rad). Therefore, the 9 inch system will produce a diameter of approximately 0.003°, giving 167 diameters in 0.5° radial line.

The effective target velocity is composed of the actual target velocity minus the target velocity removed by the gimbal command sequence plus the body motion (unwanted) of the Shuttle plus the spiral rate. For the backup acquisition mode in which the circular fence is used, only the Shuttle rate and actual target motion are involved. The maximum target motion (at 60° zenith) is 0.24 deg/sec which, when added to the 0.01 deg/sec Shuttle rate, gives a total rate of 0.25 deg/sec. Therefore, for this case the target will cross the detector in 0.012 seconds. If a 50 percent line margin is used, the line period is 0.06 seconds, which gives a required scan frequency for this case of 167 Hz.

For the primary acquisition mode most of the target velocity is removed by the gimbal command sequence. The residual velocity, which depends on the command update frequency, is approximately 0.02 deg/sec for an update frequency selected to produce a residual error of 0.1°. Combining this with the 0.01 deg/sec Shuttle rate gives a total velocity of 0.03 deg/sec, plus that contributed by the spiral rate. The spiral rate is determined by the IMC scan period, which must be related also to the gimbal scan period. For the gimbal scan routine illustrated in Figure 4-29, the target should not be allowed to move more than approximately 0.6° during a gimbal scan period, which at 0.03 deg/sec requires a period equal to or less than 20 seconds. The IMC scan period should be no greater than one-fifth the gimbal scan period, that is, no less than 4 seconds.

On the other hand, a scan frequency of 167 Hz, with a 50 percent line overlap, will cover the 0.5° in 2 seconds, which produces an additional target velocity of 0.25 deg/sec. Therefore, it is proposed that the IMC scan period be increased to 4 seconds, thereby giving additional margin in case the Shuttle and/or gimbal residual rates are larger than estimated.

In summary, the IMC scan frequency is chosen to be 167 Hz, with an IMC scan period of 4 seconds; and the gimbal scan period is 20 seconds.

IMC Actuator. The size of the IMC mirror is determined by the ratio of the aperture to the magnification, whereas the mirror angle is determined by the product of the telescope FOV and magnification. Therefore,

$$d_M S_M = D(FOV)$$

$$d_M = \text{IMC mirror diameter}$$

$$A_M = \text{IMC mirror angle}$$

$$D = \text{telescope aperture}$$

$$FOV = \text{telescope FOV}$$

The required FOV is ±0.5°, and the aperture diameter D is between 7 inches and 12 inches. Thus, $d_M A_M$ is between 3.5 and 6 in-deg. For the PST IMC presently used, $d_M A_M = 0.25$ in-deg, which product is low by a factor of 14 to 24. Therefore, use of the PST devices is out of the question for the transmitter, since an order of magnitude improvement in these devices is not possible.

Since the PST device cannot be used, the next logical choice is an electromagnetic actuator driving the IMC mirror mounted on a flex pivot. These devices can be driven in the galvanometer mode or the servo mode. For the galvo mode the selected resonant frequency of the mirror/flex pivot combination is far enough above the driving frequency so that the mirror angle follows the torque input with little lag. In the servo mode the resonant frequency is chosen well below the drive frequency so that the flexures act as frictionless pivot bearings, and the mirror position is controlled through a servo loop. The latter operational mode is more complex but requires less power. The purpose of the following is to investigate the power and torque relationships in terms of the appropriate system design parameters.

The peak torque as a function of drive frequency is

$$T_{PK} = JA_M \omega^2 \left[\left(\frac{\omega_n}{\omega} \right)^2 - 1 + \frac{j2\xi\omega_n}{\omega} \right] \text{ft-lb}$$

and the peak power is

$$P_{PK} = \frac{T_{PK}\omega}{2} \text{ ft-lb/sec}$$

J = inertia

ξ = damping ratio

The power is plotted as a function of frequency in Figure 4-30. The numerical values used are based on the specific amplitude, damping ratio, and inertia given in the figure. A total power curve is given for a resonant frequency of 33 Hz and also for 500 Hz. These values are based on a required drive frequency of 167 Hz and represent, respectively, the case of servo operation and galvo operation. That is, for servo operation the resonant frequency is chosen a factor of five below the drive frequency, and for galvo operation the resonant frequency is chosen a factor of three above resonance. The third curve given is the power required simply to accelerate the inertia, which is proportional to frequency cubed. Both the other curves asymptotically approach the inertia curve for high frequencies. For servo case shown, for example, the total required power at the drive frequency is essentially the power required to accelerate the inertia on a set of frictionless bearings.

It is also obvious from the figure that use of the galvo approach requires approximately a factor of 15 more drive power than does the servo approach. This fact is true independent of the specific drive frequency and inertia used, as long as the proper resonant frequency-drive frequency separation is maintained. However, this fact in itself does not rule out use of the galvo approach. The numerical values used are based on a combined mirror-motor armature inertia of 10^{-4} lb-in-sec^2, most of which is due to the armature inertia and which is very sensitive to the particular magnetic design configuration. The selected value is also very conservative. Therefore, it might be possible to design a galvo type drive for which the power consumption would not be unrealistic.

General Parametric Relationships. The numerical values used in the above sections are generally based on specific values for the telescope aperture (9 inches), target velocity (0.25 deg/sec), telescope FOV (±0.5°), telescope magnification (9) and IMC mirror amplitude (±2.25°). The above parameters are not all independent, but it is possible, by combining equations, to develop part of the parameters as if they are independent and to write the power and torque requirements in terms of these. For example, the three parameters D (telescope aperture), d_M (IMC mirror diameter) and V_T (target velocity) can be treated independently. D is chosen on the basis of the required optical link power, independent of the other two parameters. Similarly, V_T is "chosen" by selection of the acquisition approach discussed above. Also, d_M can be varied by changing the telescope magnification. Obviously there are constraints on these parameters. If d_M is too small (much below an inch, for example) the optical design will be unduly complicated. However, these parameters can be varied over particular ranges, and it is instructive, therefore, in optimizing the overall system, to determine how the power, torque, and drive frequency depend on these three parameters.
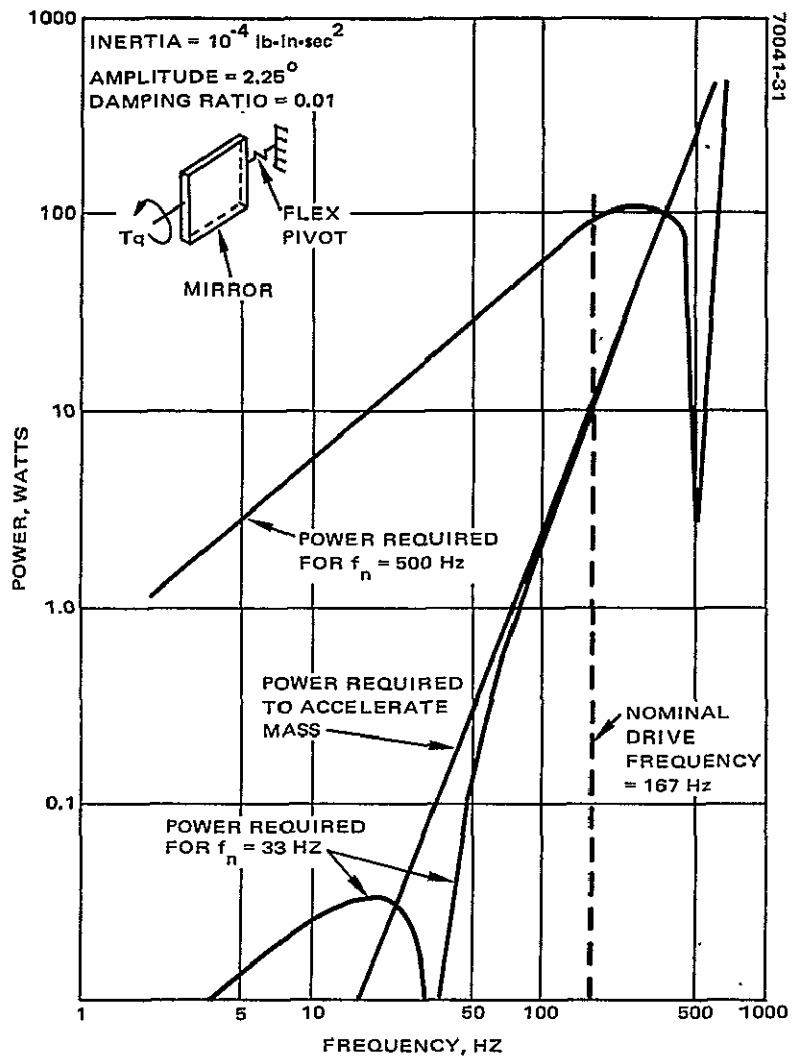
.FIGURE 4-30. MECHANICAL POWER VERSUS DRIVE
FREQUENCY FOR FLEX PIVOT MOUNTED INERTIA

First, the inertia of IMC mirror and rotor is written in terms of the mirror diameter:

$$J = K_1 d_M^5$$

The above equation assumes (a) that the mirror thickness is related directly to its diameter, and (b) that the total IMC drive inertia is directly proportional to the mirror inertia. Also, the mirror amplitude is related to the FOV, d_M, and aperture D as discussed above:

$$A_M = D(FOV)/2d_M$$

The maximum velocity is expressed as

$$\dot{\theta}_{MAX} = \omega A_M$$

which gives the required drive frequency in terms of V_T and D as

$$\omega = K_2 V_T D$$

D is in feet, V_T in deg/sec, and ω in rad/sec. For the resolution requirements discussed above,

$$K_2 = 5582$$

$$\dot{\theta}_{MAX} = (24.35) \frac{D^2 V_T}{d_M}$$

and the peak torque is

$$T_{PK} = K_3 \, d_M^4 \, D^3 V_T^2 \quad \text{ft-lb}$$

For the servo case, assuming $\omega_n = \omega/5$,

$$K_3 = 2.82 \times 10^5$$

FIGURE 4-31. SIMPLIFIED ACQUISITION/TRACK DIAGRAM FOR SHUTTLE TO GROUND LINK

The peak power is expressed as

$$P_{PK} = K_4 D^5 \dot{V}_T{}^3 d_M{}^3 \text{ watts}$$

where $K_4 = 4.67 \times 10^6$ for the above set of assumptions, plus the added assumption that the peak power is half the product of peak torque and peak velocity, since the latter two are approximately 90° out of phase.

The above equations show that the power required to drive the IMC mirror is very sharply dependent on the aperture size. Reducing the aperture from 9 inches to 7 inches will reduce the power requirement by a factor of 3.5. This is because both the scan frequency and scan amplitude decrease with decreasing aperture.

Servo System Block Diagram

A block diagram of the servo system is given in Figure 4-31. As discussed above, the position of the target relative to the detector is difference between the gimbal motion and the target motion summed with the IMC position. Initially the IMC position is scanned in a spiral scan over the entire telescope field of view (±0.5°). After the first acquisition pulse, the IMC scan field of view is reduced by a factor of ten to ±0.05° (miniscan) in response to acquisition discrete A3. At the same time, two other things happen. First, the gimbal scan is turned off and, second, an increment is added to the gimbal position in order to bring the target closer to the center of the IMC FOV. The required increment is obtained by sampling the IMC position at the instant of threshold detection. A third item, not illustrated in the diagram, may be required: change of the scale factor in the IMC loop to reduce its dynamic range by a factor of ten, thereby improving its resolution.

When the target is acquired in the miniscan mode, a second discrete A2 is generated. This causes the IMC position to be sampled at the instant the acquisition discrete is obtained, and the IMC loop subsequently to be commanded to the measured IMC position. The track scan (conical scan) is also enabled by the A2 discrete. Thus, acquisition of the target in the miniscan mode (fine acquisition) causes signal should be developed. The track error produces the fine track discrete A3, which closes the fine track loop. A few milliseconds later, after the fine track loop has settled, the delayed fine track (A3D) signal is produced, which closes the gimbal IMC loop. This completes the acquisition procedure.

4.3.5 References

1. B.J. Klein and J.J. Degan, "Optical Antenna Gain. 1: Transmitter Antennas," Applied Optics, September 1974.

2. B.J. Klein and J.J. Degan, "Optical Antenna Gain. 2: Receiving Antennas," Applied Optics, October 1974.

FIGURE 4-32. SHUTTLE LASER TRANSMITTER TERMINAL BLOCK DIAGRAM

4.4 SUBSYSTEM DESIGN

4.4.1 Shuttle Terminal

The Shuttle terminal has 18 cm diameter optics, a 400 Mbps transmitter subsystem, and a laser heterodyne beacon receiver. Cooling for the beacon receiver may be achieved with a radiation cooler for sky-viewing Shuttle sorties, or it may utilize a Joule-Thompson cryostat operating on bottled nitrogen gas. Figure 4-32 is a functional block diagram of the terminal.

This section discusses the design of the components and subsystems that comprise the complete Shuttle terminal. Particular emphasis is placed on the laser transmitter subsystem and the optomechanical subsystem unique to the Shuttle terminal, while mixer/cooler and local oscillator technology will be only briefly considered, as these are given in the description of the receiver terminal which is carried by the elliptical orbit (Molniya) satellite.

. Laser/Modulator

The laser transmitter subsystem is comprised of the laser discharge tube, the modulator, and the modulator driver. The transmitter is required to provide 1 watt of modulated sideband power. Design optimization was utilized to achieve a configuration that has the greatest overall efficiency. By using known characteristics of the laser tube, modulator and modulator driver, the optimum power split between the modulator driver and the laser can be determined. The transmitter subsystem design performance is given in Table 4-10.

The transmitter laser is similar in design to the local oscillator laser and uses a waveguide discharge structure and metal-ceramic construction. Beryllium oxide is used for the base material because of its high thermal conductivity and low optical waveguide loss. Heat from the discharge is conducted through the outer wall of the laser to the optomechanical structure heat sink. The laser design assumes that the basic heat sink temperature is regulated at 20° ± 15°C.

The transmitter laser voltage discharge is divided into four sections to reduce the high voltage requirements. The transmitter bore is 26 cm long (of which 24 cm is useful discharge length) and is square in cross section with 1.5 mm sides. When operated as a conventional laser with 10 percent output coupling mirror, the power output is 4.5 watts with 50 watt input or an operating efficiency of 9 percent.

The modulator rod is a 6 cm long crystal of cadmium telluride which also has a cross section 1.5 mm square. In the modulator design, the cadmium telluride rod is also used as a dielectric for the balanced parallel strip transmission line which couples the RF drive to the modulator rod. The line has an RF characteristic impedance of 100 ohms which are designed to match two unbalanced 50 ohm driver inputs. The equivalent circuit is shown in Figure 4-33. The transmission line design

TABLE 4-10. TRANSMITTER DESIGN PERFORMANCE

. Parameter	Design Performance
Output power	
Carrier plus sideband	0.95 W
Carrier	0.25 W
Sideband	0.70 W
Prime input power (transmitter subsystem)	145 W
Laser	
Laser bore material	BeO
Laser life	<5000 (goal) hr
Input power	55.5 W
Transition control	P20 or P14
Stabilization	±0.1 MHz
Discharge voltage	3.93 kV
Cooling	Conductive
Modulator	
Required driving voltage	120 V_{p-p}
Half-wave voltage	1325 $V\pi$
Modulator bandwidth	500 MHz
Modulator optical loss	<1.5%
Temperature control	0.05 °C
Modulator driver	
Modulator driver bit rate	400 Mbps
Input power, prime	90 W
Output voltage	120 V_{p-p}
Rise time	1 ns
Pulse droop	63/80 %/ns
Driver efficiency	>30%
Transmitter length (laser/modulator)	15 in.
Transmitter weight	3.3 lb

approach allows broad bandwidth termination of the modulator driver to a matched load. Such a matched termination impedance is highly desirable from the standpoint of modulator driver design. It should be emphasized that the transmission line loss of the modulator is only a few percent, and that most of the electrical power is dissipated in the termination, not in the modulator itself. This is due to the electrical resistivity and the dielectric loss tangent of the modulator crystal being such that negligible power is dissipated in the rod.

Figure 4-33 indicates the physical layout of the transmission line modulator before assembly. Central to this assembly is the CdTe crystal which has evaporated film (silver) electrodes on the top and bottom faces (the 110 faces). These thin film electrodes are 0.019 inch wide on rods

with thickness of 1.5 mm. This forms a 100 ohm parallel strip transmission line. The top electroded surface of the CdTe transmission line is contacted by a metalized strip on the under surface of the left BeO sleeve. Coaxial to microstrip transition sections are constructed at each of the four RF ports, thereby permitting a matched transition from a 50 ohm unbalanced RF system to a 100 ohm balanced line.

Improper coupling between the modulator rod and the acoustic load could lead to severe acoustical resonance effects. Therefore, acoustical loading of the modulator rod is provided by two alumina or beryllia ceramic rods, one on either side of the CdT rod as shown in Figure 4-34. The
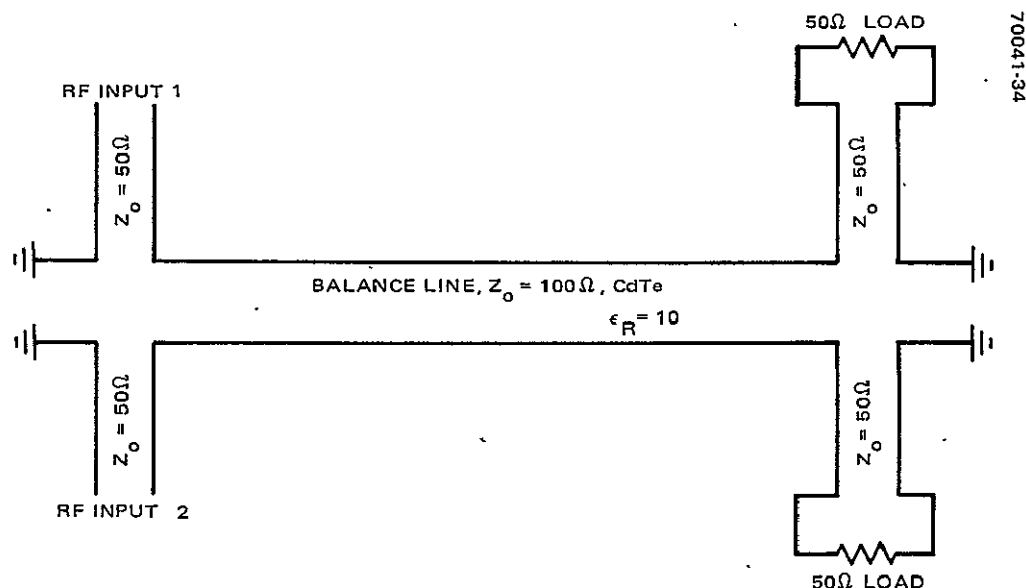
FIGURE 4-33. TRANSMISSION LINE LASER MODULATOR SCHEMATIC
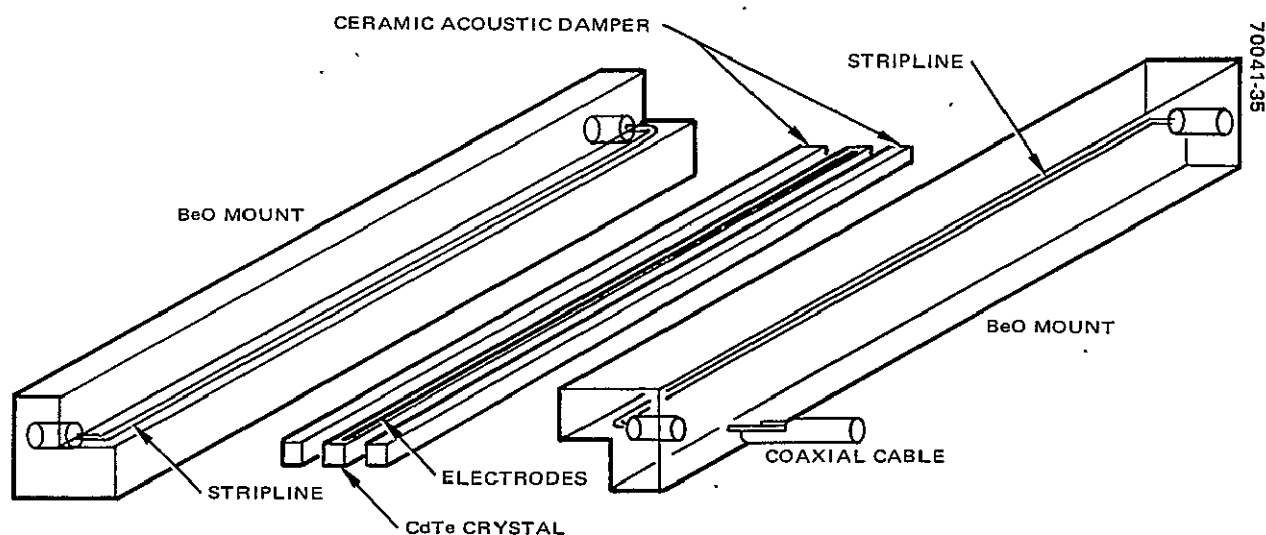
FIGURE 4-34. EXPLODED VIEW OF STRIPLINE TRANSMISSION LINE MODULATOR ASSEMBLY
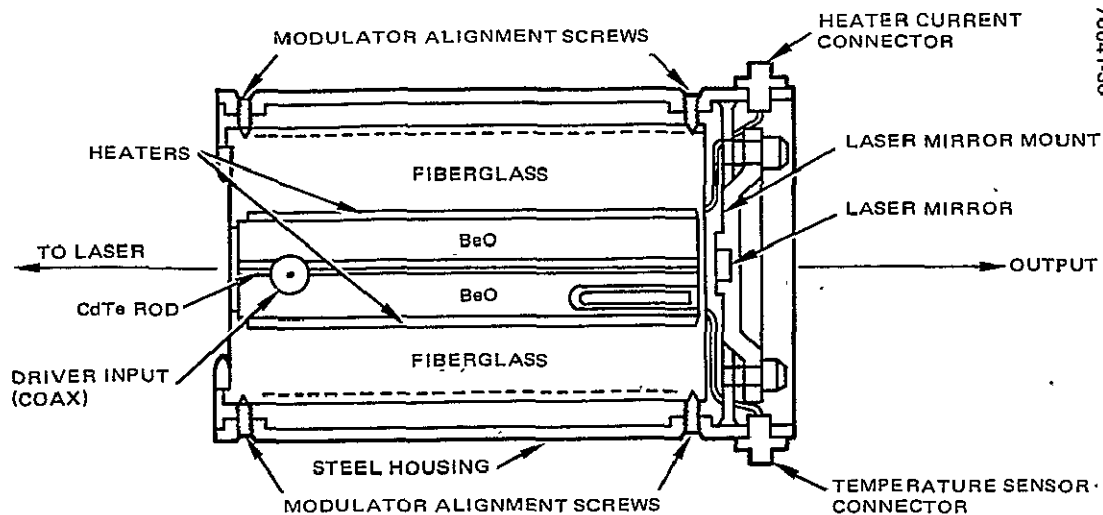
FIGURE 4-35. LASER MODULATOR MECHANICAL ASSEMBLY

acoustic impedance of the selected ceramic very nearly matches that of the CdTe rod. With a thin film bonding agent, only 4 percent of the acoustic energy is reflected at the interface; the remainder is dissipated in the ceramic sections.

The modulator housing temperature is regulated at approximately 50°C by a closed loop servo which has demonstrated ± 0.04°C stability. Temperature stabilization is required because of the dependence of the CdTe refractive index on temperature; 0.4λ phase shift occurs for each 1°C of temperature change.

The completed modulator assembly is shown in Figure 4-35. It is designed for mechanical mounting directly to the end of the transmitter laser tube. Mechanical corrections of the center position of the modulator rod as well as translation and rotation is accomplished by adjusting the supporting screws near the ends of the modulator housing. A section drawing of the complete transmitter laser is shown in Figure 4-36. The basic construction of the laser and the modulator provides high stability and ruggedness.

The laser discharge requires 55 watts of prime power with 90 watts required for the modulator driver. Under these conditions, a modulated sideband power of 0.7 watt is obtained. A residual, orthogonally polarized carrier power of 0.25 watt is also present in the output. The approximate weight of the laser and modulator is 3.3 pounds.

Modulator/Driver

The required 120 V_{p-p} modulator driver voltage is achieved through the technique shown in Figure 4-37. The details of the amplifier modules and hybrid interface are illustrated in Figure 4-38. Outputs from the current mode logic driver modules using selected RF bipolar transistors are combined using a custom designed network of hybrid couplers to produce

4-60

OUTPUT
BEAM

POLARIZER

SIGNAL
0.7W

CARRIER
0.25 W

ANODE

CATHODES

ANODE

CATHODES

ANODE

50 Ω
COAX
INPUT

REFLECTIVE
MIRROR

PZT
FIXTURE

GRATING

INDIUM
GASKET

BERYLLIUM OXIDE
LASER BORE

ALUMINUM
HEAT CONDUCTOR

KOVAR OUTER
CYLINDER

WINDOW

MODULATOR
ROD

MODULATOR
HOLDING
FIXTURE
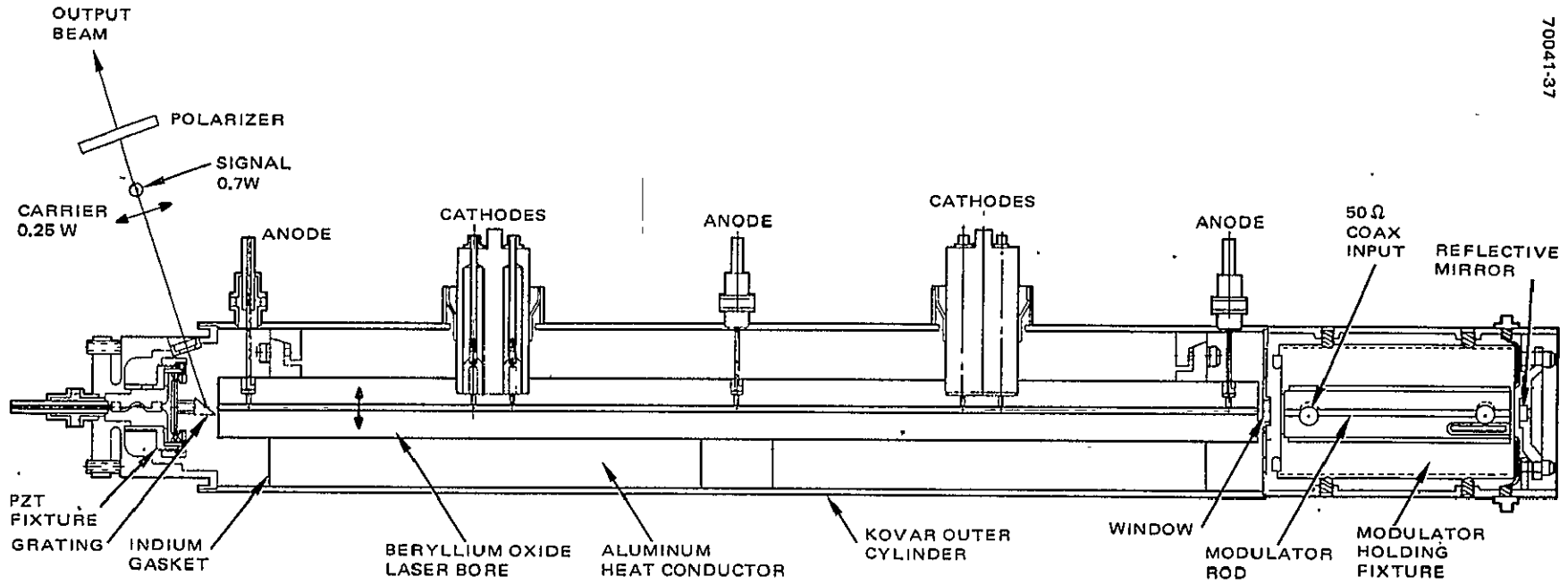
FIGURE 4-36. SECTION DRAWING OF LASER TRANSMITTER
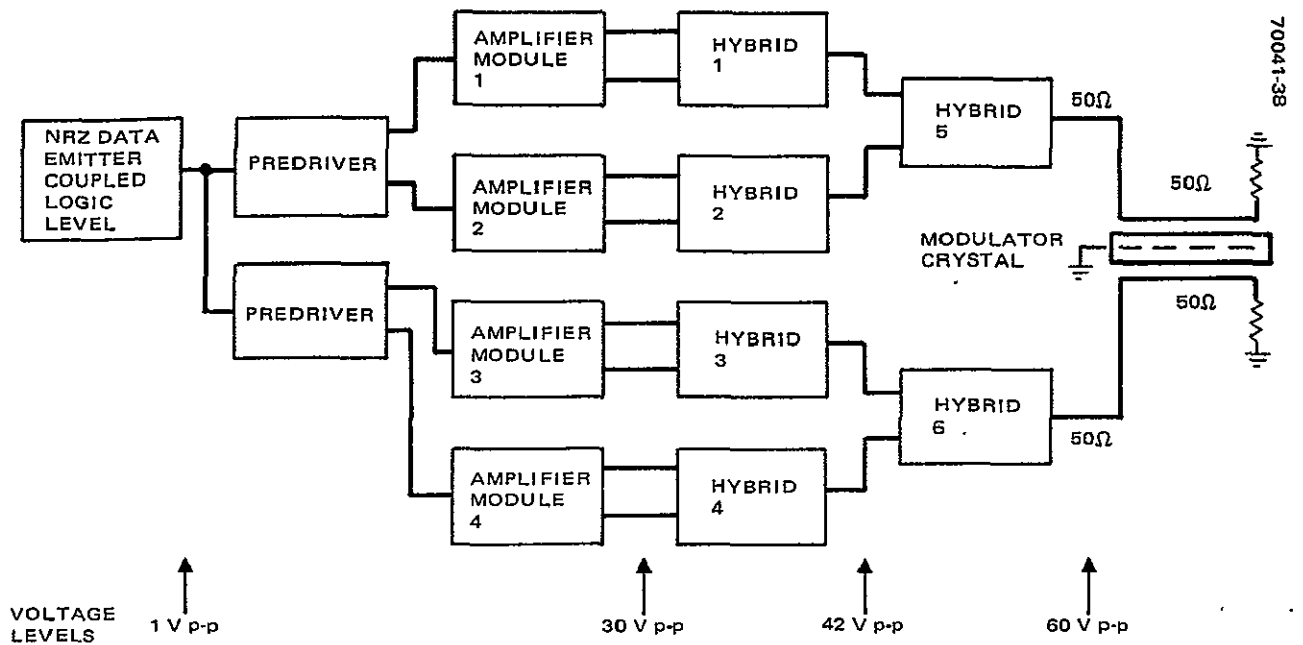
FIGURE 4-37. MODULATOR DRIVER BLOCK DIAGRAM
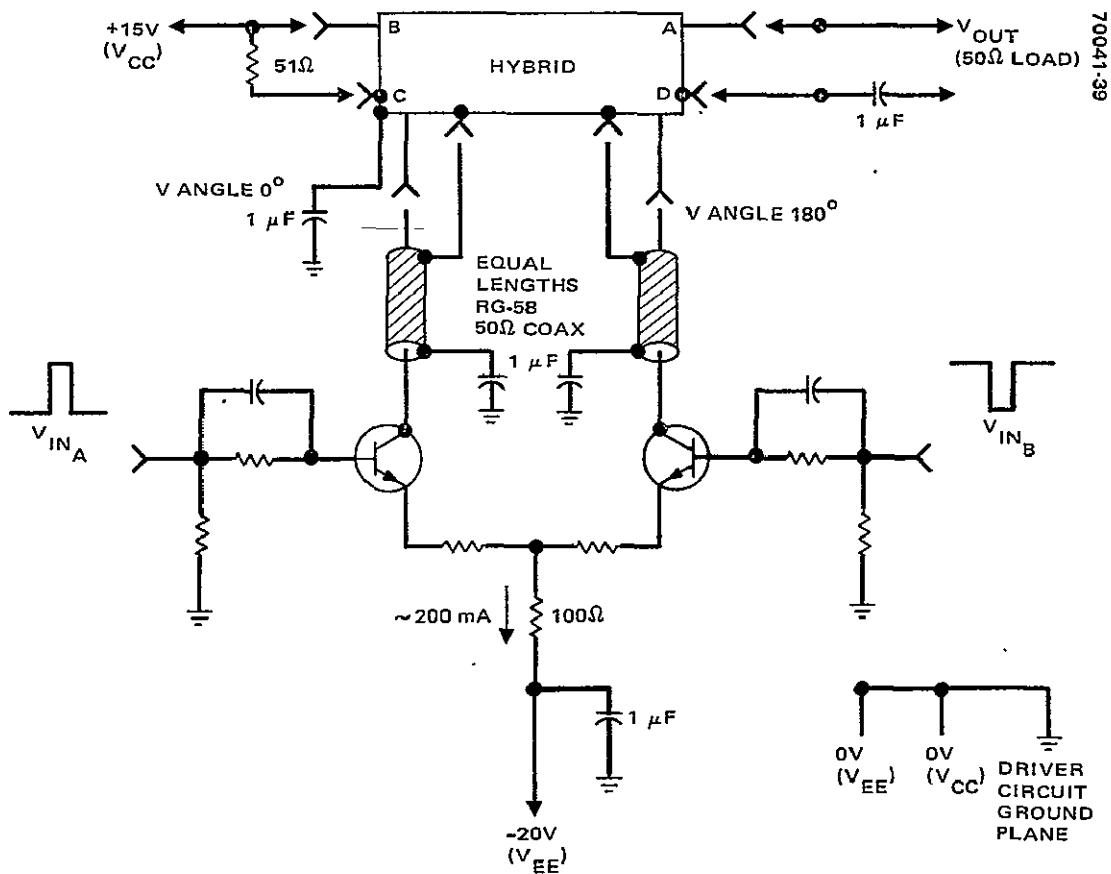
FIGURE 4-38. DRIVER AMPLIFIER MODULE AND HYBRID INTERFACE

42 V_{p-p} at the outputs of hybrids one through four. These outputs are again combined in hybrids five and six, each providing a 60 V_{p-p} output into a 50 ohm load. When these two 60 V_{p-p} signals are 180° out of phase, the full 120 V_{p-p} signal is seen by the modulator rod. When both driving signals are of the same amplitude, an imaginary ground plane exists through the center of the modulator rod and each input appears as a 50 ohm load to the driver.

The modulator driver was optimized for the modulation of NRZ-L type of data. The response of the individual driver modules to a 300 Mbps NRZ pseudorandom word is shown in Figure 4-39. The quality of this waveform is such that bit error rate measurements are very close to what may be expected from a theoretically perfect waveform. However, because of the poor low frequency response of the hybrids, the driver waveform to the modulator is distorted and must be corrected or compensated at the receiver. The technique for achieving the correction, known as quantized feedback, is described in the Bell Telephone Laboratories report.*

Mixer/Cooler and Beacon Receiver

The photovoltaic mixer and cooler required for the Shuttle terminal depends on whether a radiation cooler is feasible for the sortie or whether a Joule-Thompson cryostat must be used. For the details of the mixer/cooler design, refer to Section 4.4.2, Optical Mixer/Radiation Cooler. A Joule-Thompson cryostat operating from bottled nitrogen gas may be used on Shuttle
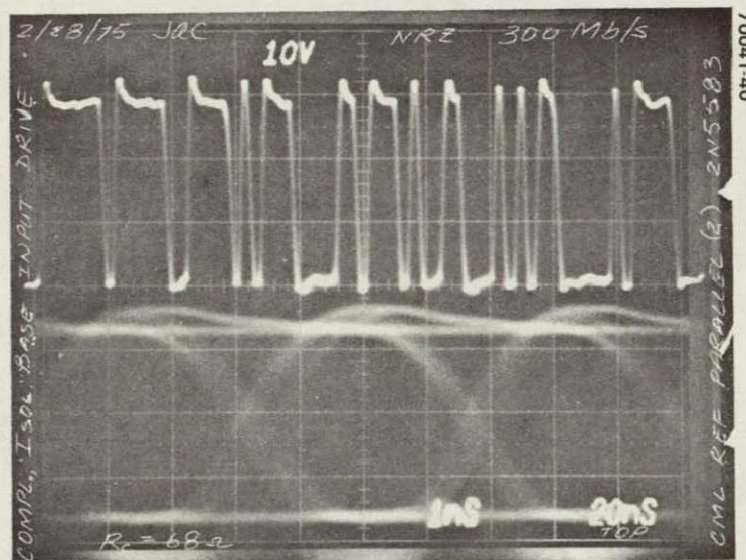
FIGURE 4-39. 300 Mbps NRZ DATA RESPONSE
(PHOTO 50151-27) MODULATOR DRIVER
MODULE

---

*Bell Telephone Laboratories, Transmission Systems for Communications, Western Electric Co., Inc., Winston-Salem, N.C., 1970, pp 654-658.

where the weight penalty of the bottled gas is not a consideration. Approximately 8 hours of operation can be obtained from 1 cubic foot of bottled nitrogen at a pressure of 200 atmospheres. An engineering model cryostat, together with the detector preamplifier and the detector housing lying alongside is shown in Figure 4-40. A flight model cryostat could be considerably smaller.

The beacon receiver required for the Shuttle will employ the same type of doppler tracking circuitry utilized in the synchronous terminal and is described in detail in Section 4.4.2, Doppler Tracking Receiver. However, the beacon signal need not carry information, and the phase lock demodulator required on the high altitude package is not required on the Shuttle package.

Local Oscillator Laser and Stark Frequency Controller

The local oscillator laser and frequency control technique is precisely the same as required for the high altitude or synchronous terminal package, and is described in detail in Section 4.4.2, Local Oscillator Laser and Stark Cell Frequency Stabilization.
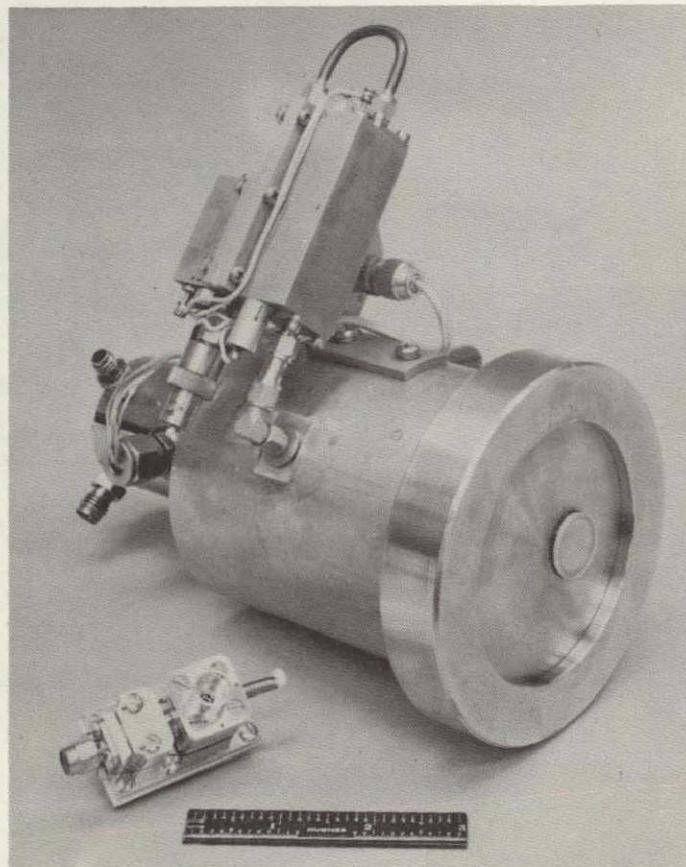
FIGURE 4-40. JOULE-THOMPSON CRYOSTAT USING
NITROGEN GAS FOR COOLING (PHOTO 74-31682)

Telemetry and Command

Dedicated LDRL-10.6 Experiment telemetry and command functions for the Shuttle terminal are obviated by the selected man-tended/quasi-automated mode of operation (discussed in Section 3). Control commands are input and system status is monitored directly via the payload specialist's console. In the interest of economy and simplicity, the Experiment results and history are simultaneously recorded in real time for subsequent post-flight analysis. The latter decision is predicated on the ready availability of adequate onboard Shuttle recording capacity.

Optomechanical and Servo System

General Arrangement. The optomechanical subsystem consists of the several subassemblies indicated in Figure 4-41. These are the motor/bearing packages (one per axis), the instrument cluster (one per axis), the secondary folding mirror package, the IMC/field stop package, and the folding mirrors for directing the beam to the base centerline, and the acquisition beam bypass. The optical components are all aligned as subassemblies and then the subassemblies are integrated into and aligned in the main package.

The materials used are:

1) Beryllium for all mirrors (marked P in the figure) and for the basic telescope box.

2) Stainless steel series 400, for the beryllium box base bulkhead, the motor/bearing subassemblies, the inner gimbal structure, mirror sub-assemblies, and alignment details. This stainless series is chosen for its thermal expansion coefficient which is compatible with beryllium.

3) Aluminum for the base compartment structure and for the instrument mounting bracket and gears. Aluminum is chosen for its light weight, heat sinking capability, and relative low cost.

System Block Diagram. The optomechanical system servo loop block diagram is shown in Figure 4-42. The system uses a multiloop concept in which a wideband, fine-track loop maintains the required track accuracy while a coarse loop maintains the fine loop actuator within its bounds. The actuator for the fine loop is the image motion compensator (IMC), which is located on the outer gimbal. Motion of the IMC affects the X-Z components of error as measured at the error sensor.

The error sensor uses the same beam dithering/synchronous demodulation technique that is used in the elliptical orbit terminal receiver. Error signals from the sensor are resolved into the proper components for application to the IMC actuator.

The coarse track loop for one axis consists of the IMC angle transducer, necessary frequency shaping (not shown), resolver, gimbal drive motor, and gimbal dynamics. The loop is completed through the laser beam and the laser detector.

7.750

±75°
INNER GIMBAL TRAVEL

INSTRUMENT
PACKAGE

OUTER GIMBAL
0 POSITION LOCK
(2)

MOUNTING
SURFACE

MAIN TELESCOPE BOX

BULKHEAD

BASE
COMPART-
MENT

1.455

12.130

8.100

1.500

7.750

9.250 DIA
B.C.

INNER GIMBAL
0 POSITION LOCK
(2)

10.960

8.37

FLAT RIBBON
CABLE

POINTING MIRROR
ROTATED 90°

DIMENSIONS IN INCHES
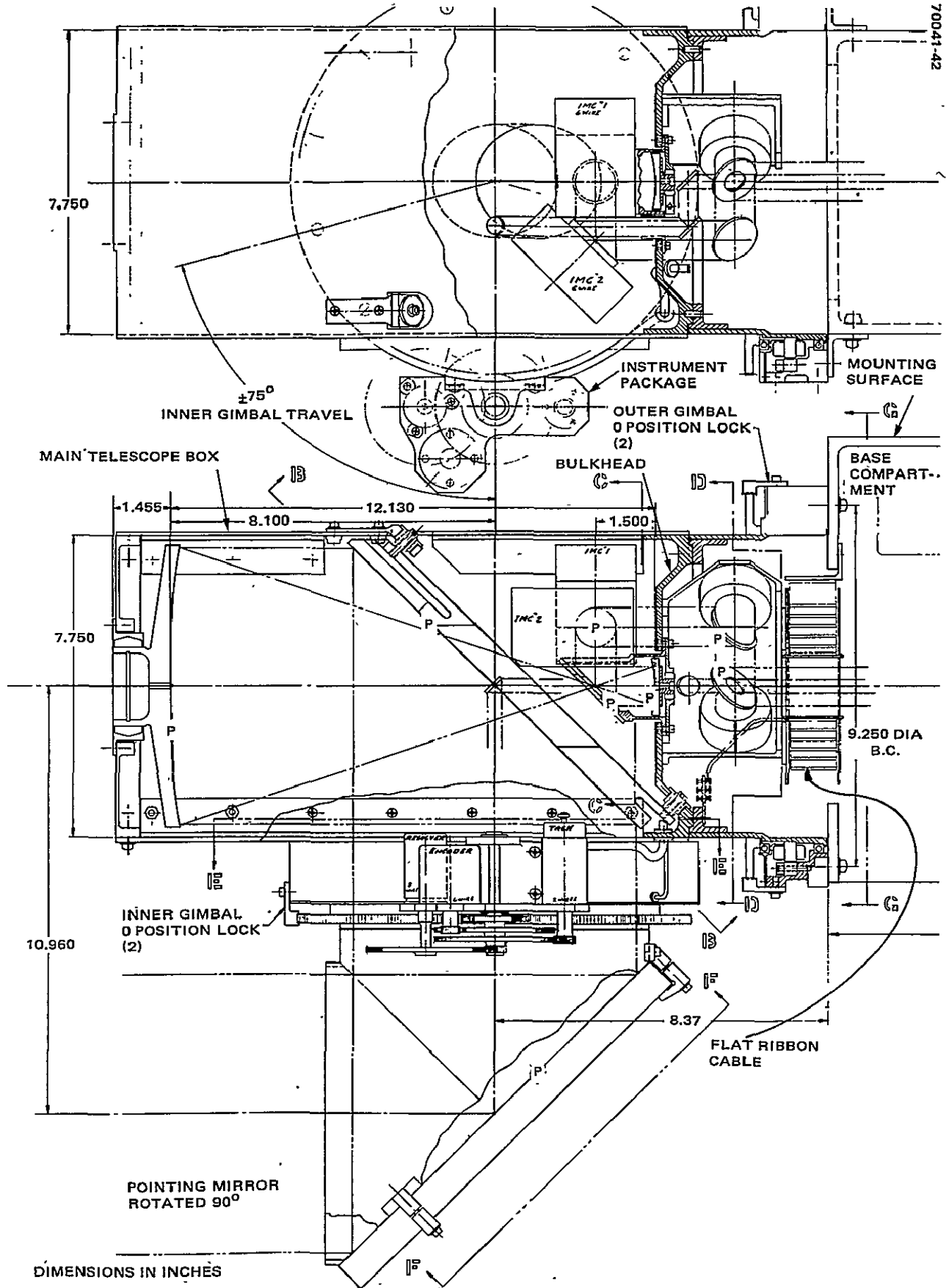
FIGURE 4-41. GENERAL ARRANGEMENT OF GIMBAL AND OPTICS
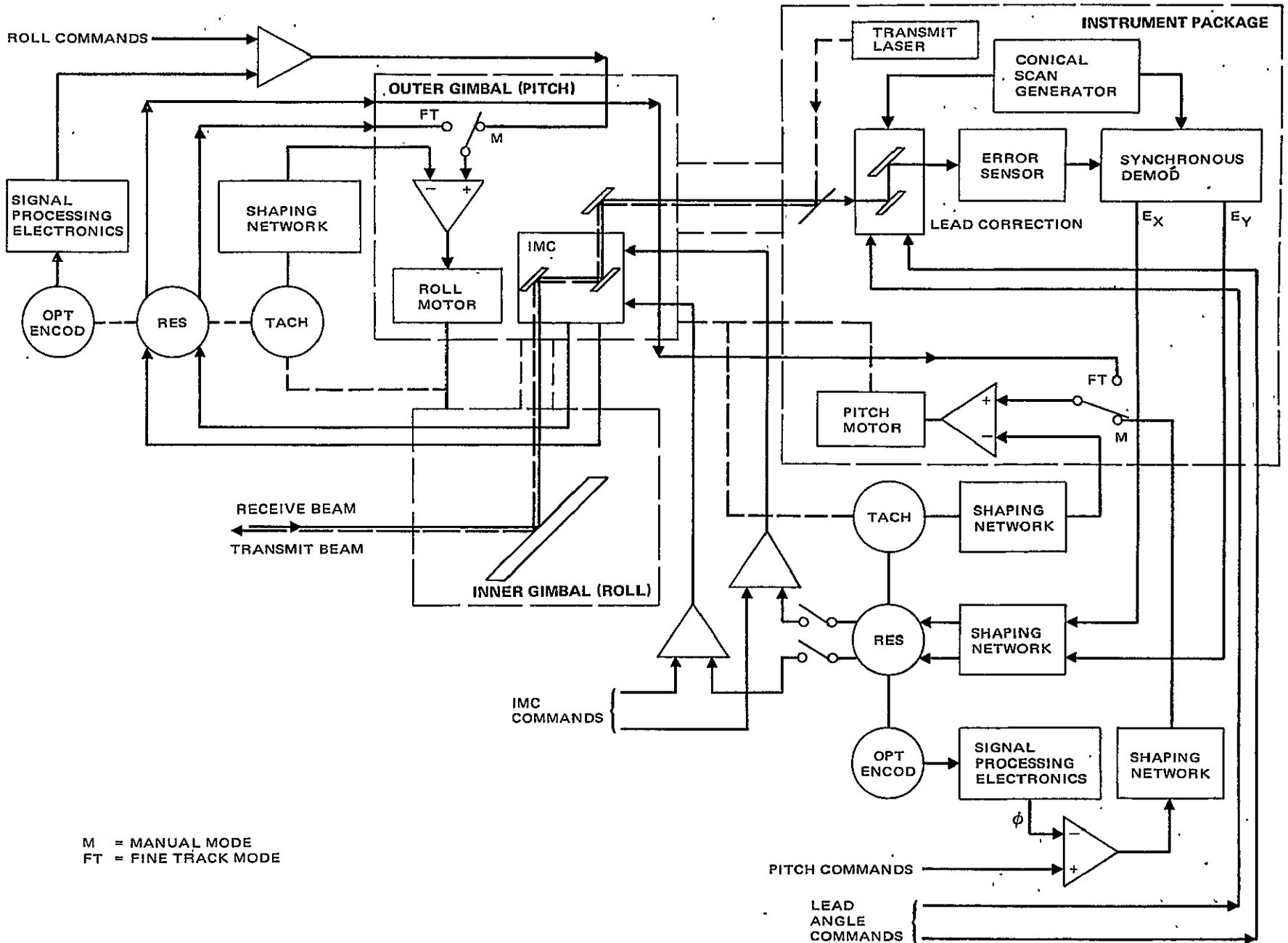
FIGURE 4-42. ACQUISITION AND TRACKING SYSTEM BLOCK DIAGRAM

TABLE 4-11. GIMBAL SERVO REQUIREMENTS

Operational Modes	Acquisition (search and pointing) Coarse track
Target Data	
Maximum target velocity	0.8 deg/sec
Acquisition target velocity	0.25 deg/sec
Maximum target acceleration	0.007 deg/sec^2
Time in field of view	10 min
Allowable acquisition time	2 min
Base Motion	
Short term	0.01 deg/sec
Long term	0.1 deg/hr
Gimbal Motion	
Roll angle	±68°
Roll rate	0.2 deg/sec
Pitch angle	±68°
Pitch rate	0.8 deg/sec
Gimbal Control Requirements	
Bandwidth	10 Hz
Coarse track accuracy	±0.1^o
Pointing accuracy	±0.02^o

TABLE 4-12. FINE TRACKING AND POINT-AHEAD REQUIREMENT SUMMARY

Fine Track Requirements	
Bandwidth	50 Hz
Total track error (10 μrad)*	
Noise error	5 μrad
Dynamic error	5 μrad
Signal-to-noise ratio	20 dB
Dynamic range*	±0.1^o
Lead Angle Corrector	
Angular deflection	0.124^o
Pickoff linearity	1%
Aperture size	5 mm

*Referred to object space.

TABLE 4-13. OPTICAL DESIGN CONSTRAINTS/SPECIFICATIONS

- Field of view: ±0.5^o
- Maximum IMC dimensions: 2.54 cm x 3.592 cm
- Maximum quarter-wave plate and wire-grid polarizer dimensions: ≈20 mm
- Minimize optical component cost
- Coaxial acquisition beam along outer gimbal axis
- Maximize energy transfer through system

Both the IMC actuator and gimbal control loops are subject to external control in the manual mode (M) as indicated in Figure 4-42. The gimbal control will be used during acquisition to point the gimbals to the expected target position and at the same time the IMC will execute a command search pattern.

Finally, for lead angle correction (point-ahead) a special actuator is provided. The required angle will be continuously commanded during flight from an onboard program which is addressable from the ground through a command link.

Gimbal Servo Requirements. The assumed Shuttle gimbal servo requirements are given in Table 4-11. These requirements are dictated by the Shuttle to ground link. This link was selected as a servo baseline because the tracking dynamics are generally more stringent than for the Shuttle to Molniya orbit satellite link. The maximum acquisition target velocity is based on the assumption that acquisition will take place before the ground terminal zenith angle reaches 60°. The field of view is 80° each side of zenith. The angular acquisition sector is the sector from 80° to 60° zenith in a 500 km orbit. This sector is traversed by the Shuttle in approximately 2 minutes.

The base motion required is the expected Shuttle base motion. The maximum gimbal angles and rates are for a 500 km orbit and for a ground station on the equator. These represent worst case conditions.

The servo bandwidth is based on the required pointing rates during the acquisition mode.

Fine Tracking and Point-Ahead Requirements. The requirements for the fine track loop and point-ahead angle corrector are given in Table 4-12. The fine track bandwidth is chosen large enough to minimize interaction with the gimbal control loop and also to stabilize the image to ± 5 μrad against residual target motion not removed by the gimbal loop. The signal-to-noise ratio requirement is based on maintaining ± 5 μrad angular noise with a 10 μrad conical scan amplitude modulation of a 58 μrad beamwidth.

The same device used for nutating (conically scanning) the received beam to develop an error signal is used to impart the required point-ahead angle. The amplitude of the required angular deflection is based on the magnification at that point (45 μrad) and upon the required beam deflection in object space (48 μrad). The specified linearity is sufficient to essentially eliminate that source of error from the point-ahead angle correction.

Shuttle Terminal Optical Design (Table 4-13). The final configuration that was chosen for the main telescope and preexpander optics is similar to that used for the optomechanical receiver subsystem. The tradeoff study* that reviewed the possible optical designs with respect to their applicability

---

*Optomechanical Subsystem of a 10 Micrometer Wavelength Receiver Terminal. Interim Test Report, September 1974, NASA Contract NAS 5-21859.

LIMIT RAY DATA

SURFACE	LIMIT RAY
IMC MIRROR ELEM 7	1.796*
STOP	1.270
IMC MIRROR ELEM 6	1.796*
SMALL FOLDING MIRROR ELEM 5	2.152*
SECONDARY MIRROR ELEM 4	1.652
PRIMARY MIRROR ELEM 3	8.999
LARGE FOLDING MIRROR ELEM 2	12.861*
POINTING MIRROR	13.451*

*MEASURED ALONG MIRROR SURFACE

OPTICAL CHARACTERISTICS

MAGNIFICATION	7.0866
F - NUMBER PRIMARY	1.5
F - NUMBER SECONDARY	1.15
FIELD OF VIEW	± 1/2°
DIAMETER OBSCURATION RATIO	0.417
OUTPUT BEAM DIAMETER	18 cm (7.0866 in.)

4-70
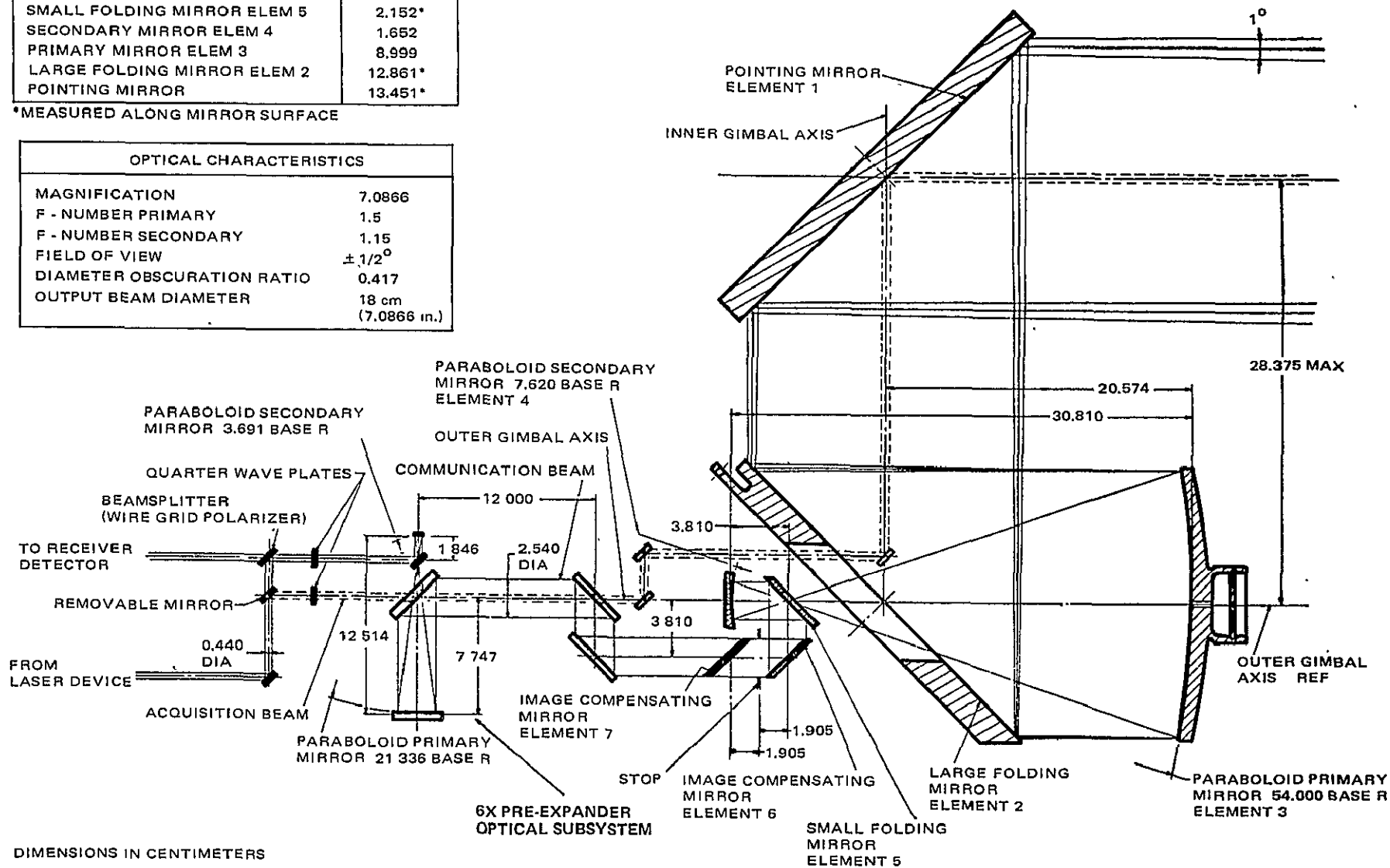
DIMENSIONS IN CENTIMETERS

FIGURE 4-43. SHUTTLE TERMINAL OPTICAL LAYOUT

to the receiver subsystem is also valid for the transmitter subsystem. The Gregorian configuration has been studied in detail, and this design type offers the best design solution for a laser transmitter. Although this design effort was primarily oriented toward the system design for a transmitter, the transmitter and the beacon receiver will share common optics in order to reduce the overall size and weight requirements. The following considerations were instrumental in arriving at the final optical design. Figure 4-43 is the optical layout for the Shuttle terminal.

Central obscuration minimization. The output from the telescope is reflected out of a Gregorian system using a folding mirror located with its center close to the focus of the primary mirror. The folding mirror has a cutout in the center to permit light from the secondary mirror to reach the primary. This design approach minimizes the central obscuration of the output beam in order to maximize the optical system far field gain.

Alignment tolerance minimization. Because of the confocal arrangement of the two positive power mirrors, the sensitivity due to the misalignments and decentrations is not as critical in other design configurations.

Field of view (±0.5°). The central obscuration of the Gregorian telescope is essentially determined by the inside apertures in the folding mirrors. The size of these apertures in turn depends on the telescope acquisition field of view and the focal length of the primary mirror. The inside apertures must be sufficiently large so as not to obscure any part of the imaged FOV of the incoming beacon beam during acquisition. For a given field of view (1° total) and primary mirror diameter, the central obscuration can be minimized only if the focal length of the primary is minimized. This implies that the f-number of the primary must be small to minimize the power loss resulting from a central obscuration. Based on practical experience, the f-number of the primary should not fall much below f/1.5 or else the misalignment tolerances will become extremely small and thus very difficult to maintain.

Maximum IMC dimensions. In order to achieve the necessary mirror response bandwidths with a minimum of power, it is desired that the optical element of the IMC that performs this task have as low an inertia as possible. The preferred location for this function is at, or very close to, the position where the diameter of the optical aperture is the smallest. Thus the IMCs indirectly determined the system magnification to this point.

Maximum quarter-wave plate and wide grid polarizer dimensions. The sizes of available components set these sizes and contributed to the requirement of a two-stage expansion of the laser beam.

Minimum optical component cost. The size of the beam expander output aperture determines the maximum achievable antenna gain for both the beacon receiver and the transmitter. However, practical considerations dictate only as large an aperture as necessary. Based on the result of a tradeoff study and fabrication cost estimates, it was concluded that an 18 cm output aperture would provide a good compromise between the overall performance and cost.
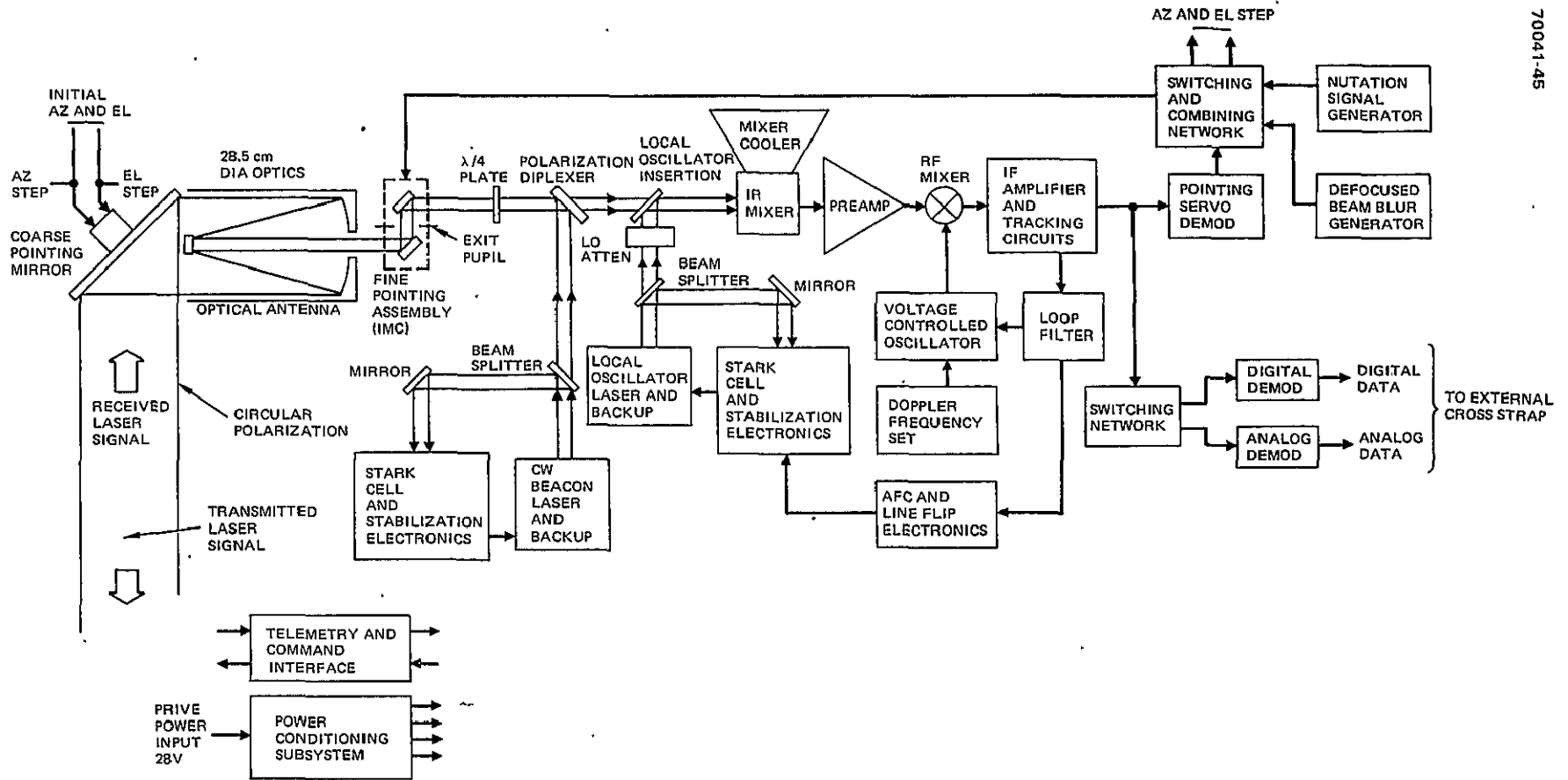
FIGURE 4-44. RECEIVER (MOLNIYA ORBIT) TERMINAL BLOCK DIAGRAM

Coaxial acquisition beam along outer gimbal axis. The acquisition beam must be along the outer gimbal axis since the main beam expander rotates around this axis with respect to the fixed base structure.

Maximum far field aperture gain. The gaussian beam profile of a CO_2 laser has its highest energy concentration in the center of the beam. This central portion of the beam is lost in the presence of a central obscuration. However, once the field of view is set and the diameter of the primary is selected, the obscuration ratio is automatically determined. There are several methods for reconstituting the gaussian beam profile in order to minimize the output losses resulting from the central obscuration. The following is a brief description of the method used for the laser transmitter. Basically, this method requires the gaussian beam from the CO_2 laser to be suitably expanded so as to overfill the aperture stop of the telescope. By broadening the beam profile, the high energy center will spread; consequently a given obscuration will block a smaller fraction of the laser energy. The increase in output power is achieved by truncating the lower energy portion of the gaussian beam profile and passing more of the high power regions.

4.4.2 Elliptical Orbit Satellite Terminal

The deployed elliptical orbit receiver terminal consists of a 28.5 cm aperture optomechanical subsystem, the receiver front-end (detector and wideband preamplifier), the receiver back-end (IF stage, doppler tracking, and data demodulation electronics), and the detector radiation cooler. The 28.5 cm optomechanical subsystem is based on developmental experience with the existing 16.5 cm experimental prototype built by Hughes. The back and front ends were built by Airborne Instruments Laboratory; the cooler was developed by A. D. Little Company. These components are to be integrated by Hughes into a complete receiver package meeting the LDR L-10.6 requirement of a 400 Mbps data rate with a bit error probability of 10^{-6}. The receiver acquires and tracks the transmitter within the 20° by 20° receiver gimbal FOV with a peak tracking error such that the required communication performance is maintained. The maximum permissible target rate during acquisition is assumed to be 0.03 deg/sec. Figure 4-44 is a block diagram of the Molniya orbit receiver terminal.

Laser/Beacon and Power Conditioning

The laser beacon is a 4 watt CO_2 laser. No modulation is imposed on this laser allowing a laser efficiency of 9 percent.

Optical Mixer/Radiation Cooler

Photovoltaic(PV) diodes, which operate near liquid nitrogen temperatures, exhibit frequency responses beyond 1 GHz, and require relatively small amounts of dc bias and incident laser local oscillator power, have been found to be ideally suited for $10\mu m$ hetrodyne receiver applications. Under laser illumination, hole electron pairs are generated within the reverse-biased photodiode depletion layer and collected at the contacts.

A high performance PV HgCdTe photodiode is the most suitable photomixer for 10.6 μm satellite communication receiver applications. Selected photomixers which exhibited a quantum efficiency of $\eta > 50$ percent, a low incident laser local oscillator power requirement (~1 mW), and a 3 dB cutoff frequency of $f_c \approx 800$ MHz (for $V_B = -800$ mV and $R_l = 50$ ohms) permit efficient operation at IF frequencies up to 1500 MHz and result in a receiver NEP between 1×10^{-19} W/Hz and 1.45×10^{-19} W/Hz for photomixer temperatures between $T_m - 77°$ and $130°$K. The hermetically sealed RF detector housing (Figure 4-45) is compatible with a satellite environment, provides RFI immunity and exhibits an IF response beyond 1500 MHz. It has been developed in cooperation with the photomixer manufacturer (SAT, Paris, France). The PV HgCdTe photomixer/housing was interfaced with a wideband 5 to 1500 MHz preamplifier and tested in a dual CO_2 laser test setup. Heterodyne receiver measurements were carried out at a variety of photomixer temperatures, applied dc bias voltages, incident laser LO power levels, and IF frequency offsets. These data appear in AIL Final Report for Contract NAS 5-23119, August 1974.

The only proven spaceborne cryogenic cooling system appropriate for long duration missions involving $100°$K temperatures and relatively modest thermal loads is the radiative cooler. A previously developed radiative cooler was modified to meet the special requirements of the receiver engineering model. The special requirements included more extensive RFI control, the use of an infrared mixer considerably heavier than the infrared
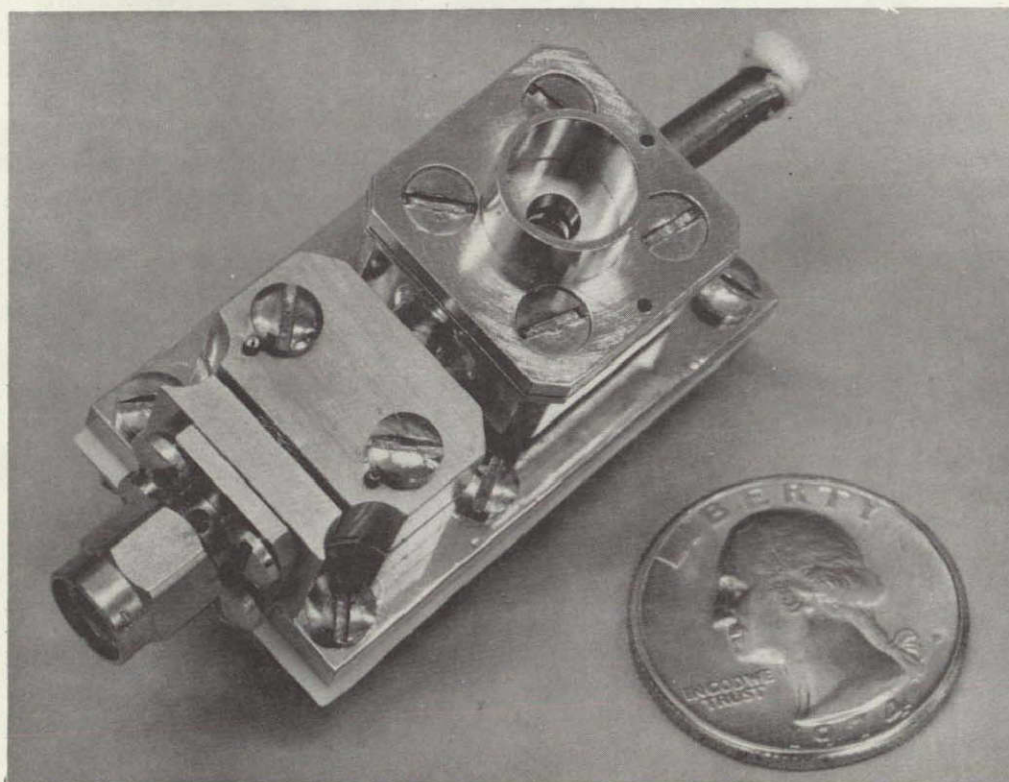
FIGURE 4-45. WIDEBAND HgCdTe DETECTOR IN SEALED HOUSING

detector in the original design, and the use of a coaxial cable to carry the broadband signal from the cold stage of the cooler. Figure 4-46 is a photograph of the radiative cooler.

The principle of operation of the cooler is that the infrared mixer is attached to a central cold patch that is thermally insulated and shaded from thermal radiation from the sun, earth, or other parts of the spacecraft. By keeping the cold patch pointed at dark space and limiting other inputs, the necessary 100° to 120° K temperature can be obtained. The coaxial cable represents a critical thermal path between the infrared mixer on the cold patch and the remainder of the electronics (at nominally 20° ± 10° C). To limit the thermal load imposed by the cable, it was fabricated from 0.034 inch (0.086 cm) diameter stainless steel cable, which was gold-plated to give it low emissivity. The cooler weighs 3.49 pounds (1.59 kg) and has a
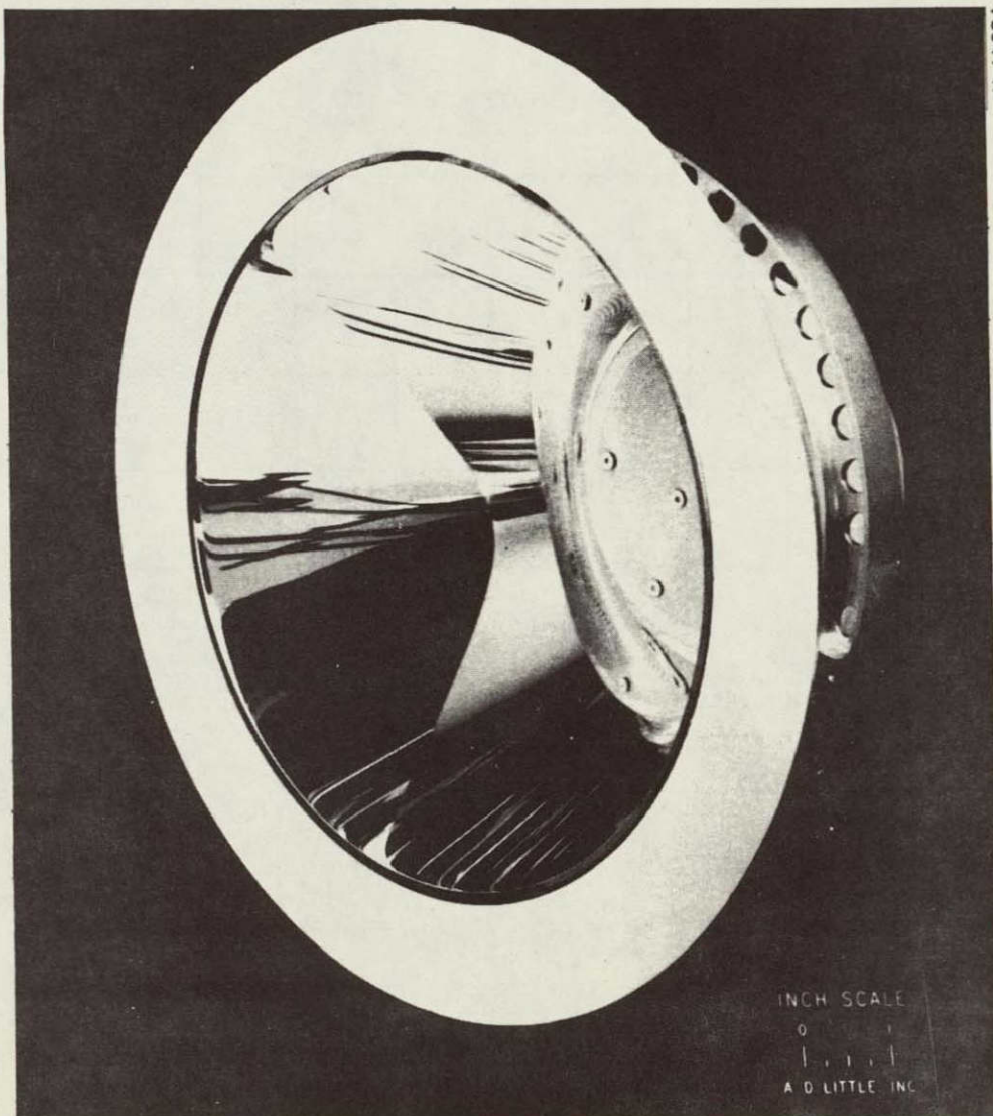
FIGURE 4-46. A.D. LITTLE RADIATIVE COOLER (PHOTO 60518-57)

CATHODES

ANODE

ANODE

OUTPUT

REFLECTIVE
MIRROR

PZT

GRATING

INDIUM
GASKET

HEAT

KOVAR CYLINDER

ALUMINUM HEAT SINK

BERYLLIUM OXIDE LASER BORE
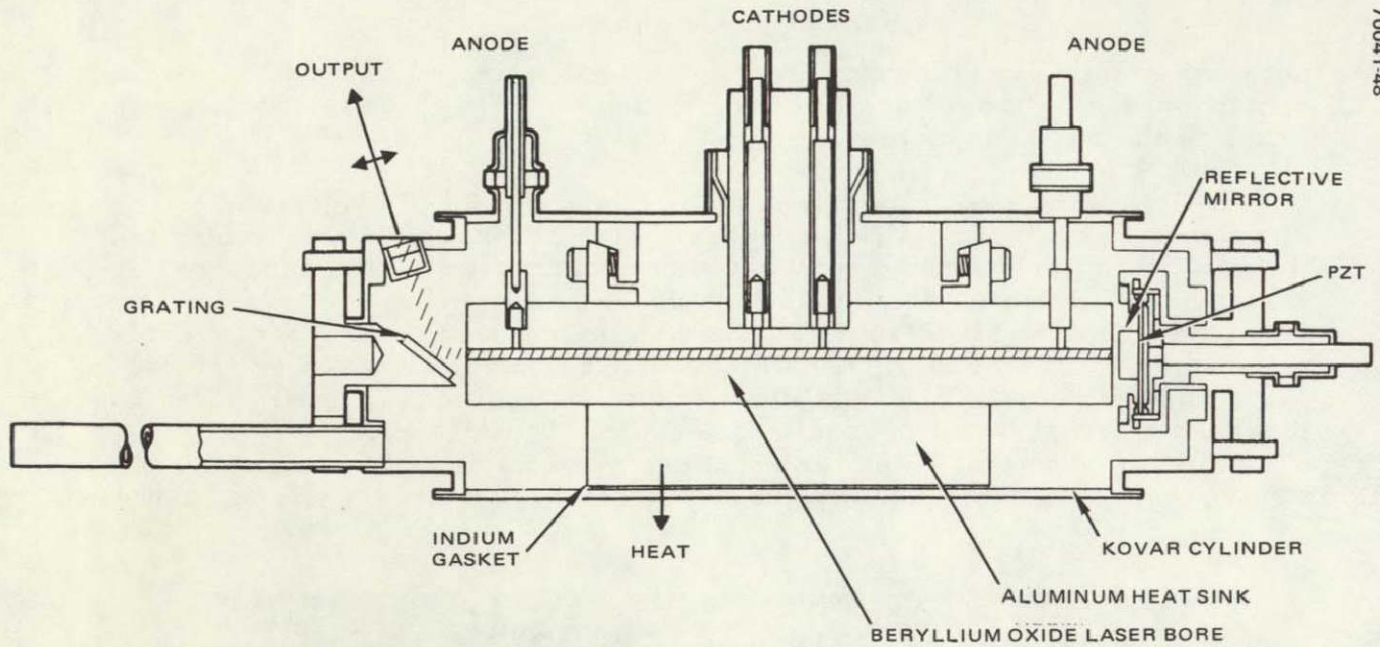
FIGURE 4-47. SECTION LAYOUT OF LOCAL OSCILLATOR LASER

1dB TUNING = ±200 MHz

POWER, MILLIWATTS
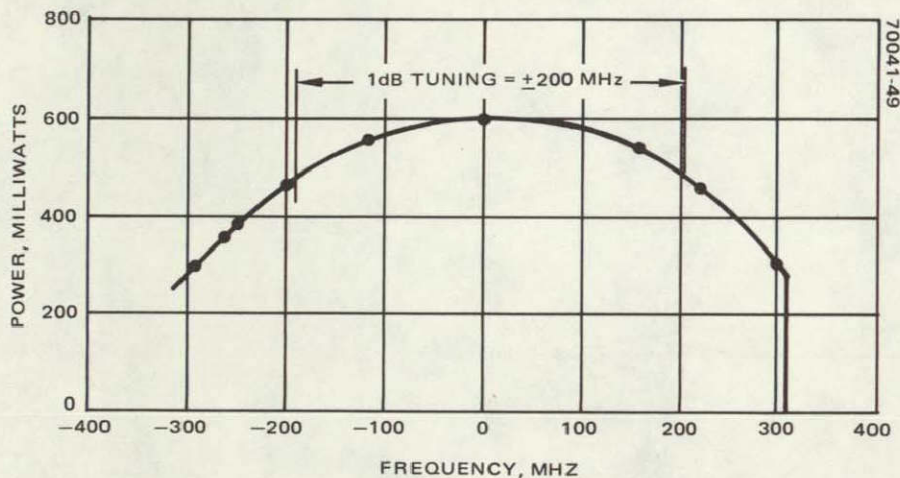
FREQUENCY, MHZ

FIGURE 4-48. CO_2 LASER LOCAL OSCILLATOR OUTPUT POWER VERSUS
MEASURED FREQUENCY RELATIVE TO LINE CENTER

nominal 120° clear field-of-view to dark space. The cooler was given
extensive thermal and vibration tests to verify performance and it success-
fully met all requirements. During the thermal tests, electrical power was
supplied to the inner stage to simulate the effect of laser local oscillator and
mixer bias power. With no power supplied the cooler reached an equilibrium
temperature of 101.17° K and with 40 mW supplied it reached 111.91° K.

Local Oscillator Laser and Stark Cell Frequency Stabilization

The tunability of conventional CO_2 lasers is limited by the gain line-
width of the doppler-broadened molecular transition to about ±60 MHz. The
tunability of high pressure waveguide lasers, however, is improved by about
an order of magnitude due to collision broadening of the molecular linewidth.

A tunable range of ±400 MHz is required for the 400 Mbps optical heterodyne receiver and the waveguide laser was selected to provide this function.

The laser is constrained to oscillate on one transition at a time through the use of a blazed grating serving multiple functions as a laser mirror, a polarizer, and as a coupling device. As a mirror, the grating is 97 percent reflective. As a polarizer, the grating is 80 percent efficient. As a coupling device, the grating couples out of the cavity about 0.5 percent or less of the laser circulating power. By adjusting the angle of the grating, the laser can be made to oscillate on any of 16 separate transitions in the 00°1 - 10°0 branch. These range in wavelength from 10.467 to 10.788 μm. Further, through the use of isotopes of carbon and oxygen, the same branch can be shifted to the 11.1, 11.7, or 9.4 μm bands, yielding a total of 64 separate usable wavelengths.

The preliminary model local oscillator laser used in the receiver integration was developed on Contract NAS5-21859. The tuning specification was ± 200 MHz from line center and the unit was to be compatible with the dimensional constraints of the receiver. The final configuration, shown in Figure 4-47, has a tuning range in excess of ± 300 MHz of line center (see Figure 4-48), a power output at line center of 540 mW, and operates with a total input power of 19.4 watts. Although this laser has been used throughout the receiver integration and testing, a later version was developed under Contract NAS5-20623. It is the intention to replace the original developmental laser with one of the productized versions prior to environmental or other mechanical tests. Figure 4-49 is a photo of the preliminary model used in the receiver integration. Figure 4-50 is a photo of the productized version. Relative performance data of the two devices are given in Table 4-14.

TABLE 4-14. CHARACTERISTICS AND PERFORMANCE OF
PRODUCTIZED WAVEGUIDE LOCAL OSCILLATOR LASERS

Parameter	Productized Model	Preliminary Model
Power output, mW	65 on P(20)	540 on P(20)
Discharge input power, W	10	19
Tuning range (1 dB), MHz	>±300	>±300
PZT mechanical range, μm	>20	>20
PZT voltage, V	±140	±140
Discharge length, cm	6.48	10
Bore size, mm	1.25	1.5
Overall length, cm	17.8	14
Gas pressure, Torr	150	150
Discharge current, mA	2	2
Weight, kg	0.63	1.2
Diameter of cylinder, cm	4.5	6.0
Transmitions avilable by grating adjustment	P(8) through P(38), 00°1 - 10°0 branch	
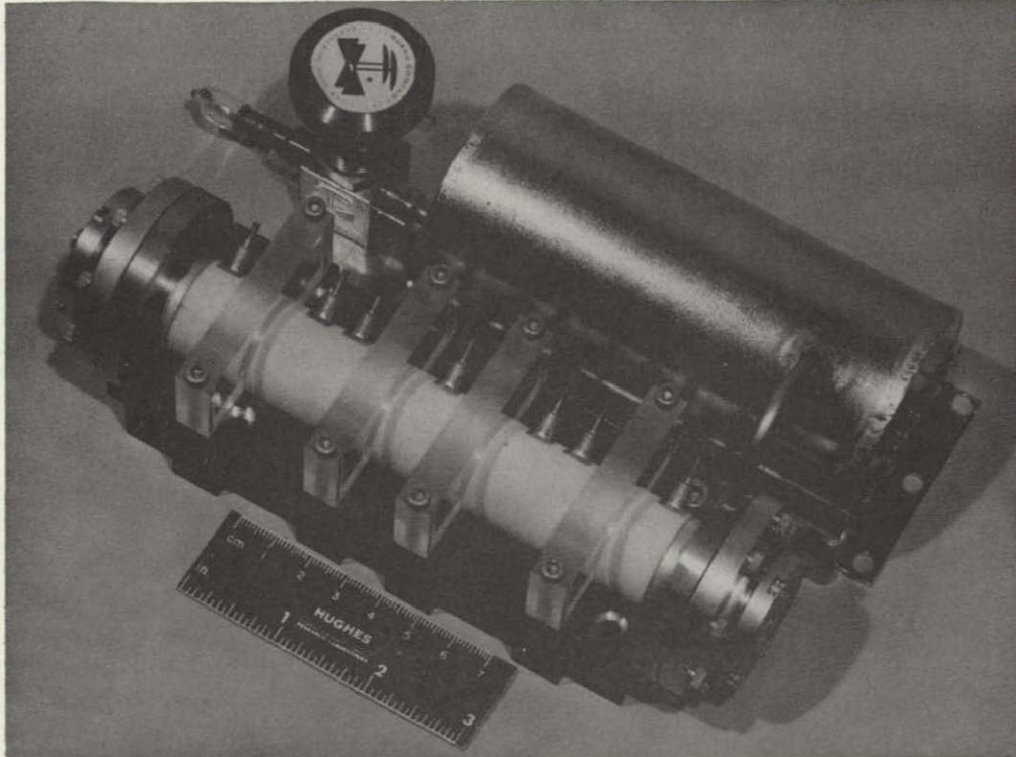
FIGURE 4-49. PRELIMINARY MODEL OF CO_2 LASER LOCAL OSCILLATOR
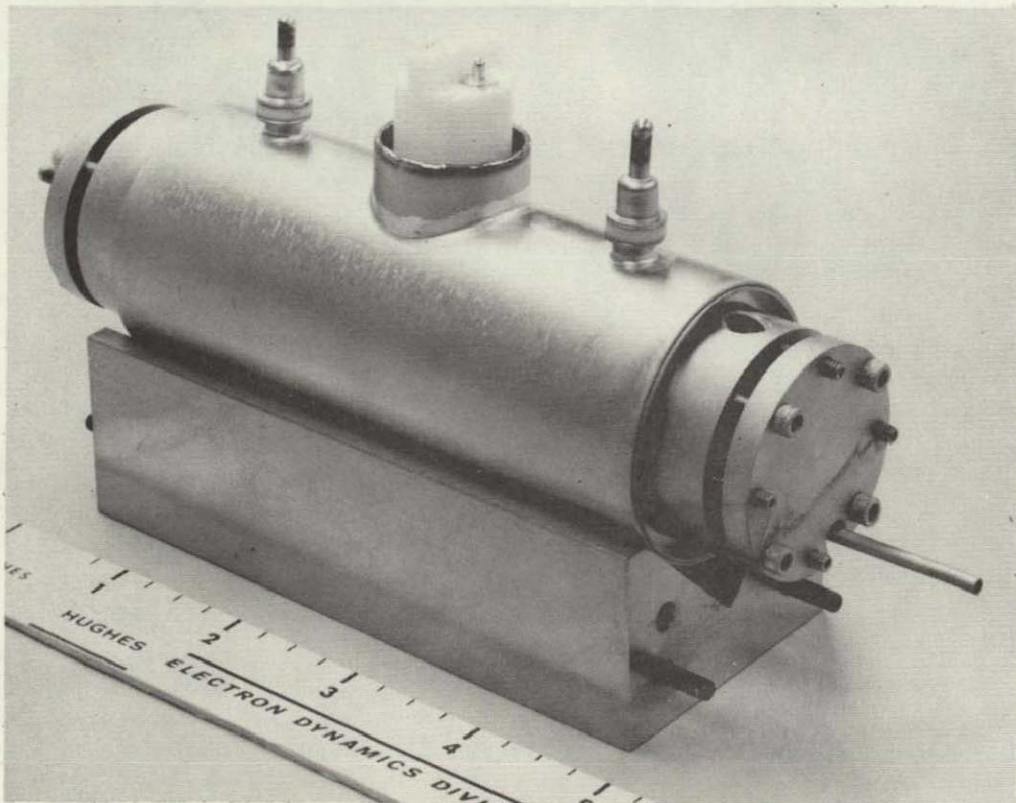
FIGURE 4-50. FINAL VERSION OF CO_2 LASER LOCAL OSCILLATOR

When the desired transition is selected by the mirror grating, the local oscillator may be tuned over a frequency range of ±300 MHz or more by positioning the reflective mirror. This is accomplished by mounting the mirror on a circular piezoelectric bender. Prior to the development of the Stark cell frequency controller, the laser was stabilized on line center of the gain profile and then either open-loop offset from line center or square-wave dithered for closed loop control. These approaches were not satisfactory for use in the receiver engineering model and the use of a Stark absorption cell to stabilize and control the frequency of a CO_2 laser was developed. Stabilization is achieved by directing some of the laser energy through the Stark cell and locking the laser frequency to the Stark absorption line. A dc electric field applied to the cell causes the frequency of the absorption line and, therefore, the laser frequency to be tuned. In this way, the dither modulation used to develop a frequency discriminant is applied to the Stark cell rather than the laser and the laser frequency varies only with tracking errors rather than by the sum of the dither plus the tracking errors. Long term and short term laser frequency stability of 100 kHz has been achieved. Because no dither signal appears in the laser frequency, this stabilization technique is optimum for the transmitter as well as the LO laser.

The Stark cell contains a mixture of ND_3-NH_3 which combine to form NH_2D, as well as other mixed isotopic forms of ammonia. At a total pressure of 1 Torr, the absorption coefficient is 0.01 cm^{-1} when the Stark cell is tuned to the P(20) line center (at an electric field of 3570 volts/cm). At higher pressures, the 80 MHz wide doppler broadened absorption line becomes pressure broadened and the dc breakdown voltage of the cell is reduced. If an arc develops, dissociation of the gas occurs, reducing the signal level. A convenient set of parameters which works satisfactorily for this application is:

Laser transition	P(20), 10.59μm P(14), 10.53μm
Cell length	10 cm
Field gap	1.28 mm
Pressure	1 Torr
ND_3:NH_3 ratio	1:1
Resonant voltage (calculated)	456 volts on P(20), 570 volts on P(14)
Absorption coefficient (calculated)	10 percent

A 10 percent absorption coefficient is more than adequate to provide an excellent signal-to-noise ratio for locking of the laser to the Stark cell, while the 10 cm cell length is a reasonable size for the laser package. The resonant voltages are convenient values in a range where a number of precision power supplies are available.

ELECTRODES
DEPOSITED ON
SURFACE OF
CERAMIC BORE

STARK CELL
VOLTAGE

TEFLON
SLEEVE

99.5 ALUMINA
END WASHERS

PUMP OUT

END CAP

BEAM TO
DETECTOR

INCOMING
LASER BEAM

99.5 ALUMINA BORE
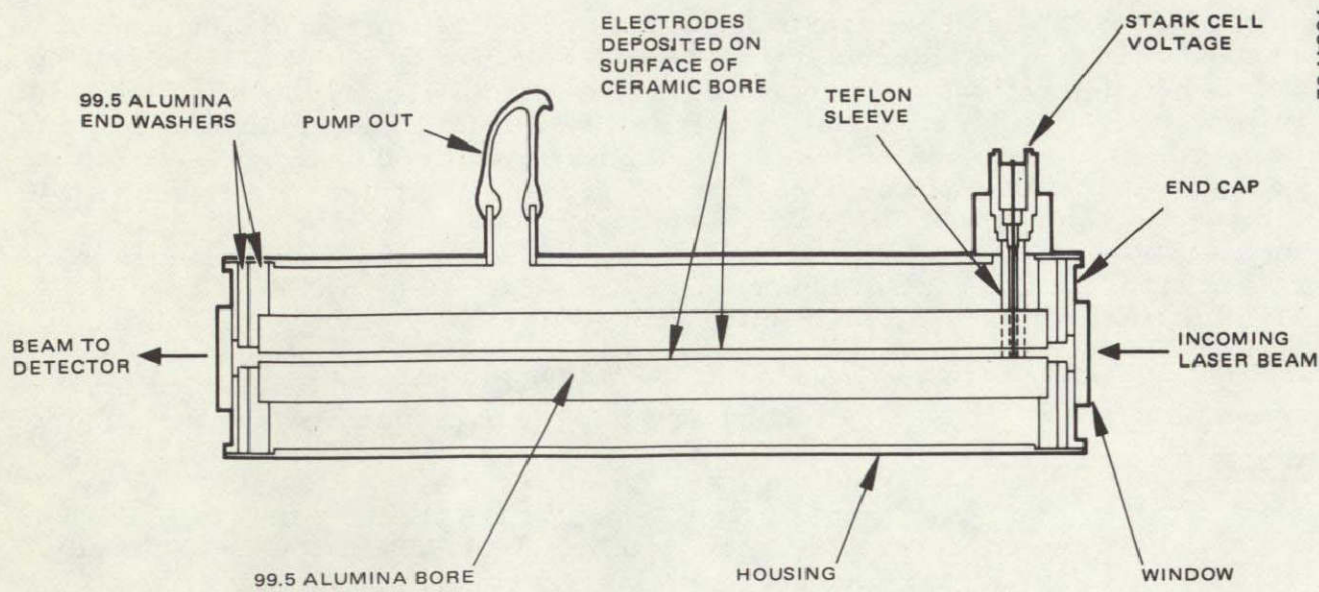
HOUSING

WINDOW
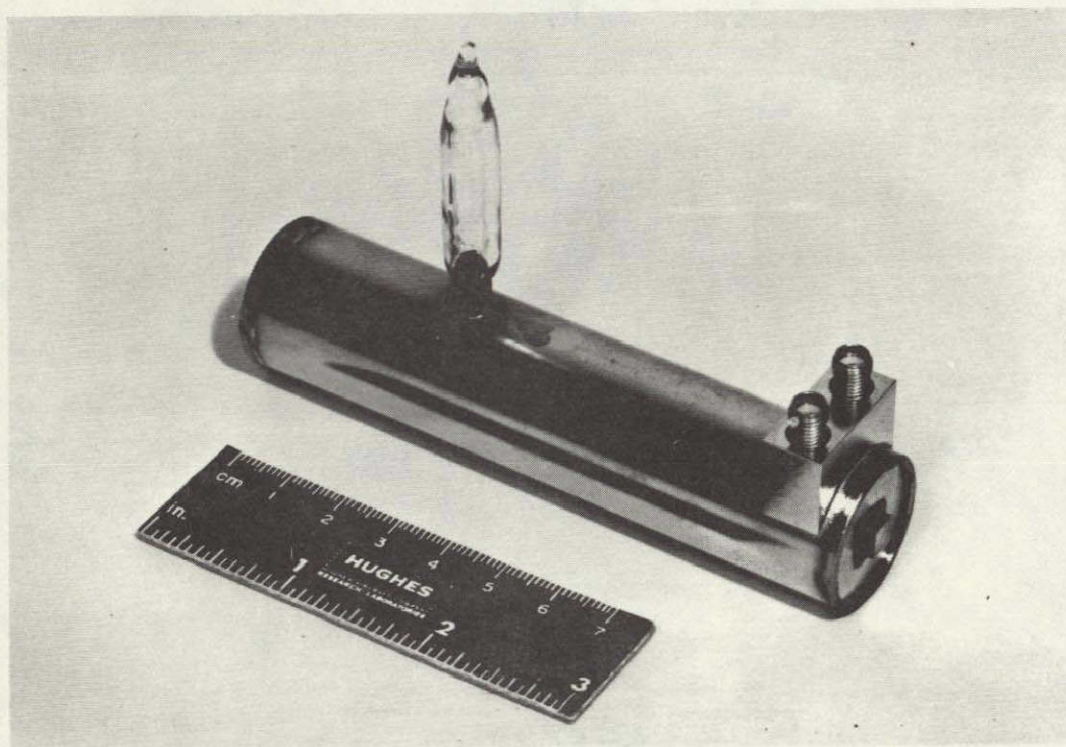
a) SECTION DRAWING

b) PHOTO 60518-63

FIGURE 4-51. STARK CELL

The Stark cell consists of five main components: bore structure, end washers, end cap window assemblies, housing, and electrical feedthroughs. A section drawing and a photograph of the Stark cell are shown in Figure 4-51.

Doppler Tracking Receiver

Since CO_2 laser communications use a heterodyne receiver, the doppler shift of the received signal appears at the intermediate frequency. Since the carrier frequency of a CO_2 laser is very high, 28 THz $(28 \times 10^{12}$ Hz), and the relative satellite velocities are also high (7.8 km/sec for a 185 km orbit) a large doppler shift results. The doppler frequency can be as great as 736 MHz for a link between a synchronous satellite and a 185 km altitude satellite. For 556 and 1850 km orbits, the maximum doppler shifts are 715 and 658 MHz respectively. The doppler shift varies during the orbit of the low earth satellite and varies with the inclination angle the plane of the satellite orbit makes with the line of sight. Figure 4-52 shows a typical set of variations.

Because of restrictions in the tunability of currently available laser local oscillators, which prohibit complete doppler tracking with the laser local oscillator, a double-conversion receiver is employed as shown in Figure 4-53. In this receiver, the doppler frequency is tracked in the first loop by the waveguide laser local oscillator to maintain a first IF greater than 400 MHz. Phase lock is maintained in the second loop by the voltage controlled oscillator (VCO). The operation can be visualized by means of the chart shown in Figure 4-54. In Figure 4-54a, the received signal is at the peak positive doppler +700 MHz, and the laser local oscillator is set at +300 MHz, both with respect to the center frequency of the molecular transition. As the doppler decreases, the automatic frequency control loop maintains the first IF at 400 MHz. When zero doppler is approached (Figure 4-54d), the laser local oscillator is approaching -400 MHz and data foldover is imminent. At that point, the laser local oscillator is switched to +400 MHz (Figure 4-54e) and AFC tracking continues as the doppler frequency takes on negative values with respect to the center frequency.

In phase lock receivers, a squaring loop has the advantages of high utilization of the signal energy and simplicity of implementation. A squaring loop configuration is shown on Figure 4-55. The square law device converts the binary modulated sidebands to carrier energy at twice the input carrier frequency. This $2f_{IF}$ component is then filtered and compared in phase with a $2f_{IF}$ component derived from a stable oscillator at frequency f_{IF}. Any phase difference between the two IF components produces an error voltage that tends to minimize their phase difference by adjusting the frequency of the VCO so that its output frequency is just $f_{IF} + f_s$, the exact frequency required to convert the signal frequency f_s to the IF frequency, f_{IF}. Thus the two coherent references are available to track the doppler frequency and to demodulate the incoming communication signal.

The parameters of a tracking loop determine its noise bandwidth, its ability to track signals over a range of doppler shift and doppler rates, and the time required for the loop to acquire the signal. The loop bandwidth required to minimize the effects of oscillator noise within the system is an
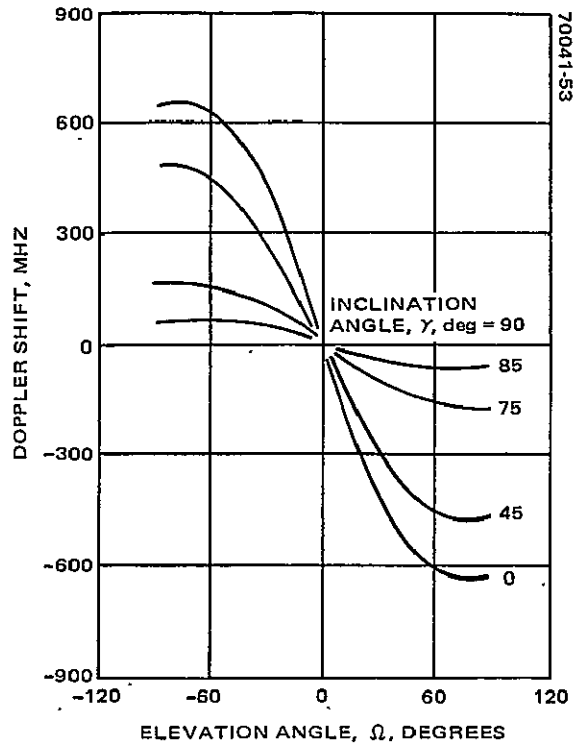
FIGURE 4-52. TYPICAL DOPPLER SHIFTS
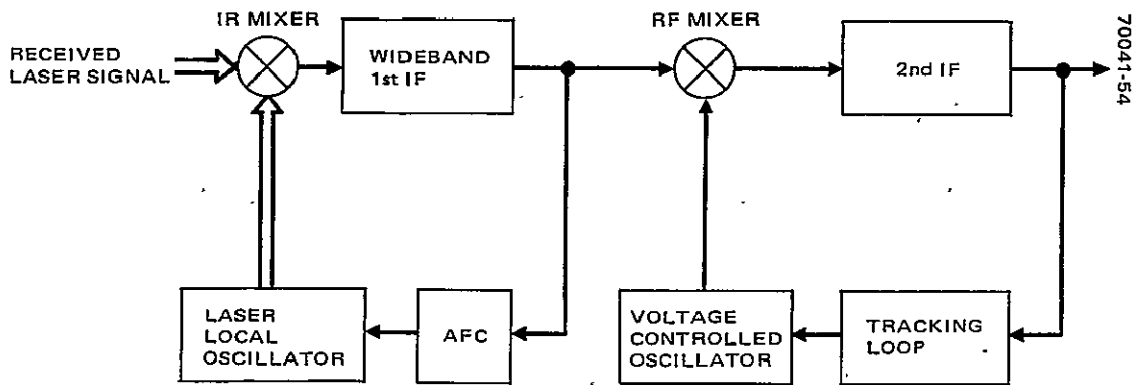
FIGURE 4-53. DOUBLE CONVERSION CO_2 LASER HETERODYNE RECEIVER
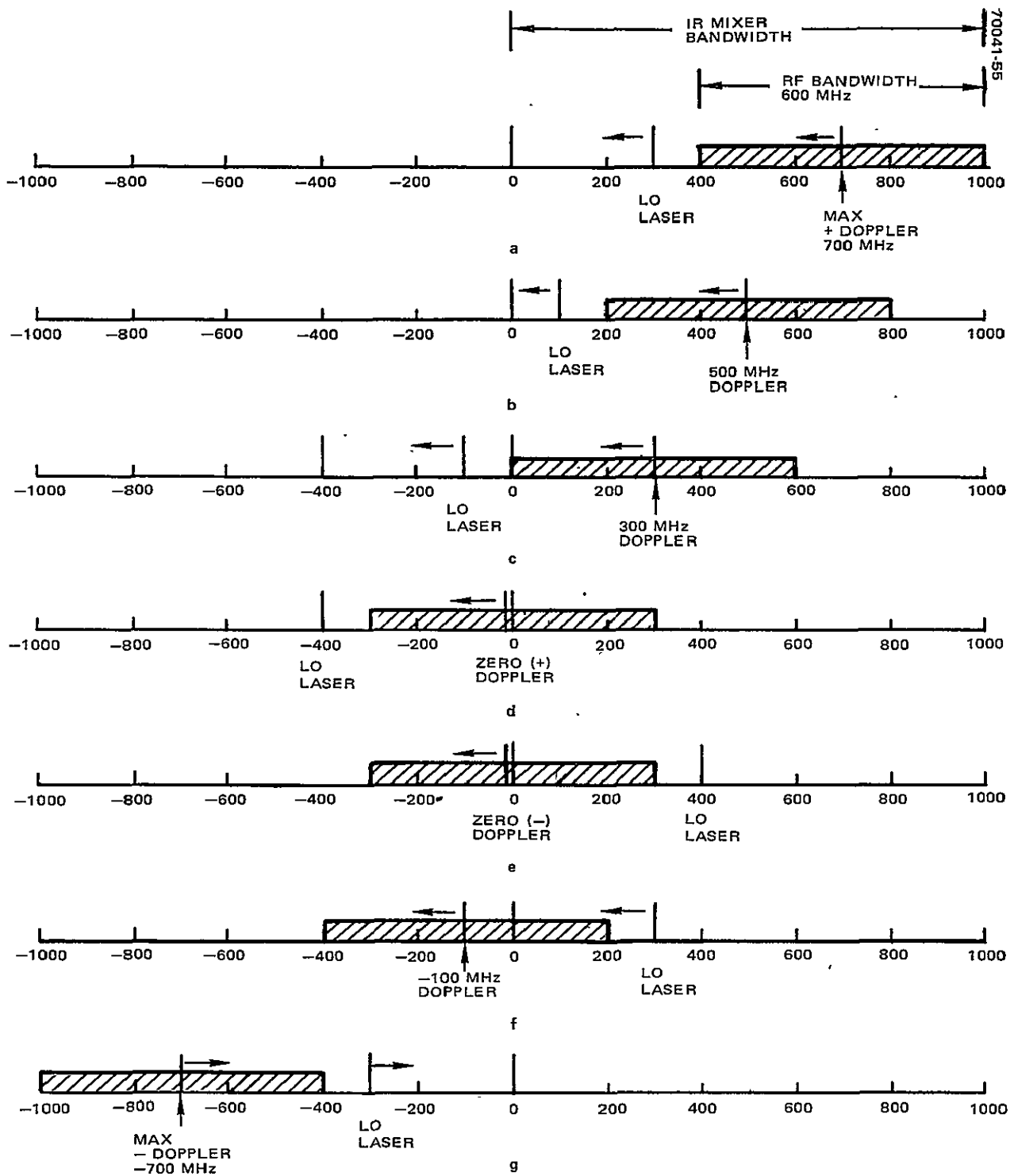
FIGURE 4-54. DOUBLE CONVERSION RECEIVER FREQUENCY TRACKING
DOPPLER FREQUENCY SHIFTS

4-83
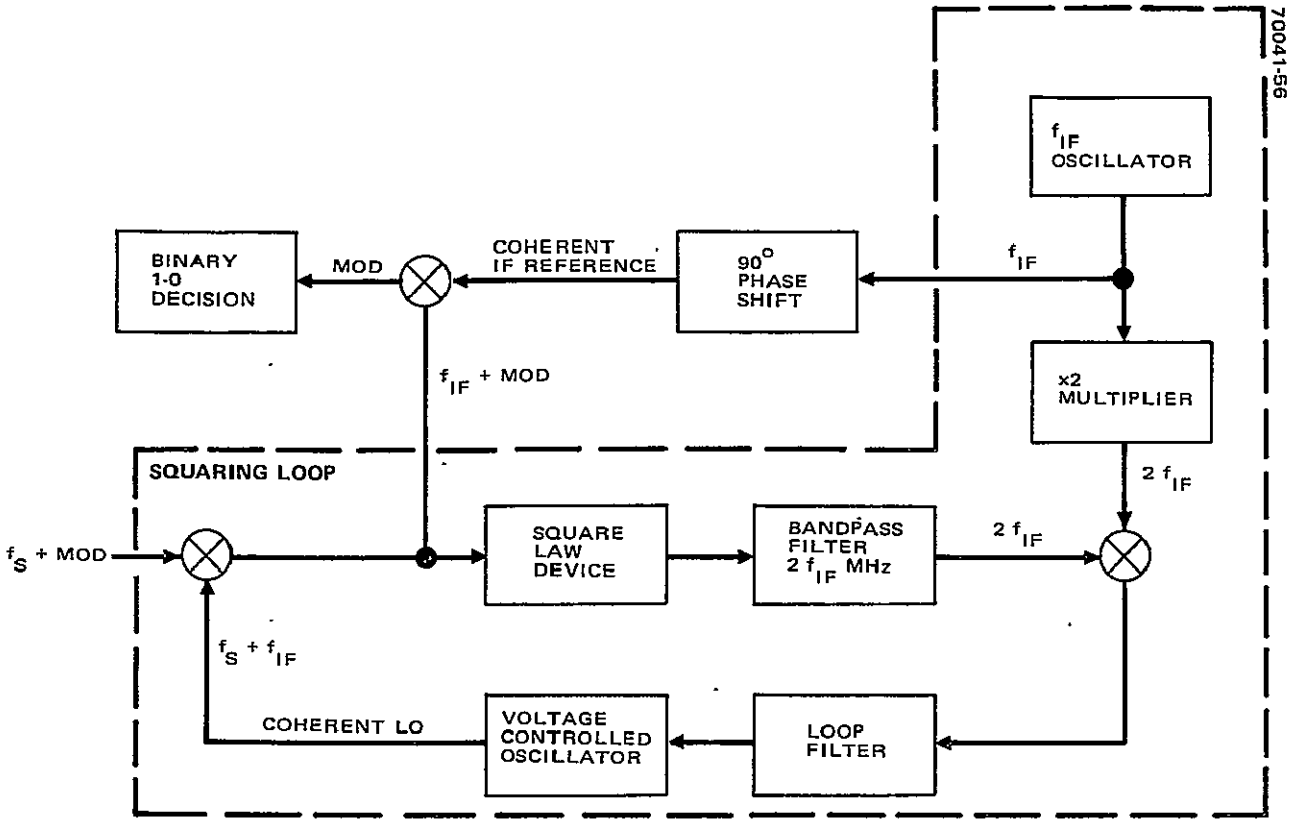
FIGURE 4-55. PHASE-LOCKED LOOP SQUARING LOOP
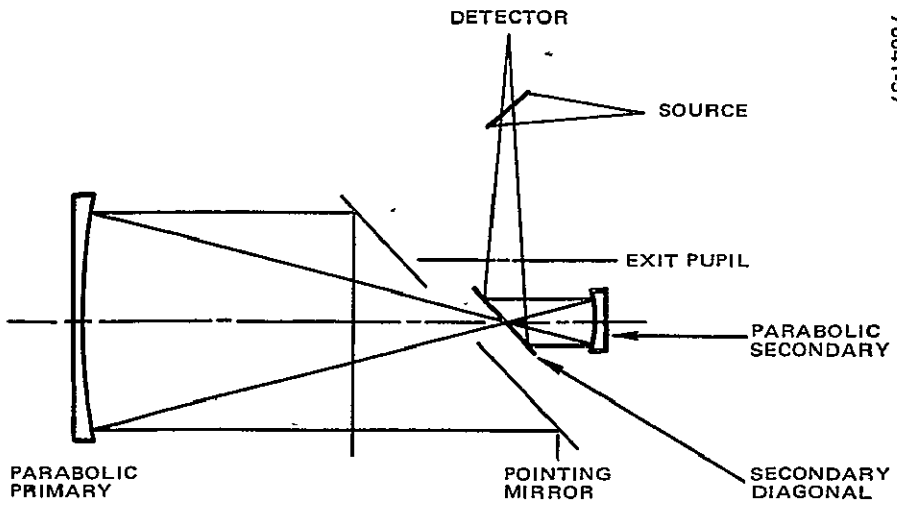
FIGURE 4-56. FOLDED GREGORIAN OPTICAL SYSTEM

4-84

additional consideration in the tracking loop design. Such factors have been considered and derived a tracking loop design that exhibits a noise bandwidth of 500 kHz and has the ability to track signals with doppler rates well in excess of 20 MHz per second. This loop acquires a signal in less than 0.12 second by searching frequencies 85 MHz on either side of a preset RF frequency.

The signal from the RF preamplifier of the infrared heterodyne receiver is passed through a linear phase bandpass filter with a 3 dB bandwidth of 400 MHz. It is then split into two paths, one path goes to the data demodulator and the other serves to provide the tracking loop signal (see Figure 4-55). The second path is applied to a frequency doubler where the sideband energy is converted to carrier power at 3 GHz. This carrier is then compared in phase with a 3 GHz reference derived from a crystal controlled reference source. The quadrature loop phase detector provides loop lock indication. The error voltage from the loop phase detector is conditioned by the loop filter and amplifier so that the VCO tracks the modulated signal frequency. The 1500 MHz reference is also applied to the data demodulator so that, when the loop is locked, the two inputs to the data demodulator have the proper phase to demodulate the signal.

Telemetry and Command

The pulsed and magnitude commands are provided for the flight hardware. Telemetry signals are either analog or on-off signals. A partial telemetry and command function list is given in Table 4-15.

Receiver Optical Mechanical System and Acquisition/Tracking Servo System

Optomechanical System. The optical system needed for space optical communications must be compact and tolerant of the mechanical and thermal environments of launch and in-orbit operation. These are conflicting requirements since the more compact the optical system is the tighter are its mechanical tolerances. The depth of focus of an f/2 optical system at a wavelength of 10 μm is only 0.0025 cm. Further, all-reflective systems are preferable since alignment and testing can be done with visible light and the temperature dependence of refractive elements can be avoided. Two very compact all-reflective optical systems have been thoroughly evaluated for the 10 μm: the Cassegrain and the folded Gregorian. The folded Gregorian was chosen as more suitable for several important reasons: 1) the confocal arrangement of the primary and secondary mirrors leads to zero spherical aberration on-axis and negligible coma and astigmatism off-axis; 2) the configuration can withstand relatively large misalignments without deterioration of the heterodyne signal; 3) thermal compensation of system focus can be achieved provided the mirror and structure are made of the same material. Figure 4-56 shows the basic folded Gregorian optical system layout. The optical mechanical system uses an 18.5 cm (7.3 inch) diameter primary mirror which gives a 92 dB antenna gain at 10 μm. It should be pointed out that the focal nature of the design is determined by the requirement that the

SURF	ELEM	DWG	RAD	MATERIAL	THK	OUTER LIMIT RAY	INNER LIMIT RAY
1	SUN SHIELD		∞	AIR	10.478	11.086	1.218
2	I		∞	AIR	36.873		
3	II		-83.000 MARK R **	AIR	-50.292	8.988	1.245
4	III		14.100 MARK R **	AIR	9.271	2.144	.186
5	IV		∞	AIR	4.053		
6	V		∞	AIR	1.270		
7	STOP		∞	AIR	1.270	.957	.144
8	VI		* ∞	AIR	3.175		
9	VII		∞	AIR	5.398		
10	VIII		∞	Ge	.200		
11			∞	AIR	5.478		
12			∞				.300

OPTICAL CHARACTERISTICS	
EQUIVALENT FOCAL LENGTH	132.080 CM
F-NUMBER OF SYSTEM	8.0
F-NUMBER OF PRIMARY	2.22
F-NUMBER OF SECONDARY	1.94
FIELD OF VIEW	±0.13°
INPUT ACQUISITION FIELD	20° X 20°
ACTUAL DETECTOR SIZE	.207 MM

* PARABOLOIDAL, C.C. = -1.0

** ELLIPSOIDAL, C.C. = -.28264

ALL DIMENSIONS ARE IN CENTIMETERS

.707
.278
.393
1.154
1.208
ELLIPSE
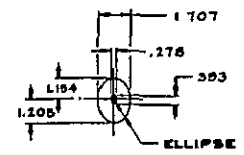
COMBINING MIRROR BEAM PATTERN

1.492 1.408
2.123
ELLIPSE
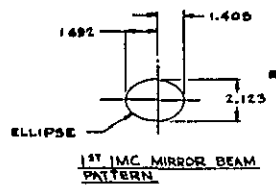
1ST IMC MIRROR BEAM PATTERN

1.845
1.236
1.350
ELLIPSE

2ND IMC MIRROR BEAM PATTERN

.242 .225
BACK SURFACE .156
2.846 .289
1.822 .275
2.148 .278
ELLIPSE
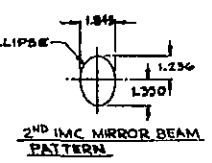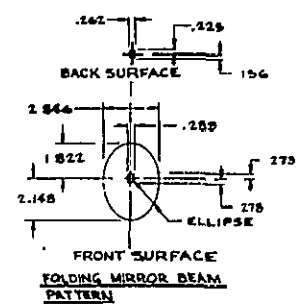
FRONT SURFACE

FOLDING MIRROR BEAM PATTERN

GₐAₛ LASER BEACON SOURCE

BEACON CONDENSER SYSTEM

14.219 APPROX

BEAM COMBINING MIRROR

5.398

BEACON FIELD LENS

ELEM VIII SURF 10 — SURF 11

ELEM I SURF 2

PRIMARY MIRROR (PARABOLOIDAL)

18.142

2.490

LOCAL OSCILLATOR AND CONDITIONER

5.479

.278 DIA

ELEM VII SURF 9

45°

.200

.116 DECENTER

BEACON BEAMSPLITTER

POINTING MIRROR RANGE OF SCAN = ±5°

ELEM II SURF 3

1ST IMAGE MOTION COMPENSATOR MIRROR

3.175

1.270

SURF 12

DETECTOR .0207 DIA

2ND IMAGE MOTION COMPENSATOR MIRROR

ELEM VI SURF 8

APERTURE STOP SURF 7

28.208

ELEM III SURF 4

2.540

ELEM V SURF 6

45°

.372 DIA INNER LIMITING RAY HEIGHT

4.053

3.822

SECONDARY MIRROR (ELLIPSOIDAL)

FOLDING MIRROR

ELEM IV SURF 5

10.478

SURF 1

SUN SHIELD

36.873

9.291

50.292

FIGURE 4-57. 10.6 MICROMETER LASER HETERODYNE 16.5 CENTIMETER
APERTURE RECEIVER OPTICAL LAYOUT

TABLE 4-15. TELEMETRY AND COMMAND REQUIREMENTS

ANALOG TELEMETRY	ANALOG COMMANDS
Pointing mirror position, pitch	Pointing mirror position, pitch
Pointing mirror position, roll	Pointing mirror position, roll
IMC position, pitch	Local oscillator frequency set
IMC position, roll	Spare (2)
Laser local oscillator current (2)	**DIGITAL COMMANDS**
Stark cell voltage	Beacon on
Receiver control signal, pitch	Beacon off
Receiver control signal, roll	Receiver on
Laser local oscillator temperature	Receiver off
Structure temperature (3)	Acquisition mode on
Power supply currents (3)	Acquisition mode off
Power supply voltages (6)	Spare (3)
Beacon power	Release radiation cooler caging mechanism
Receiver signal strength	
Spares (3)	
DIGITAL TELEMETRY	
Angle acquisition mode	
Angle track mode (2)	
Stark cell load lock	

focused spot, or Airy disk, match the detector sensitive area in the optical heterodyne receiver. In the receiver engineering model, that has been built, the sensitive area of the infrared mixer is 200 μm in diameter.

A schematic optical layout and the optical characteristics of the experimental 16.5 cm Gregorian receiver system are presented in Figure 4-57 and Table 4-16, respectively. The ellipsoidal secondary mirror is located so that its first focus coincides with the focus of the paraboloidal primary, and the final image is located at the second focus of the secondary. The f-number of the system is f/8.0. The input acquisition field is 20° x 20°. This is achieved with the pointing mirror covering a range of scan of ±5°, about the nominal 45° tilt relative to the optical axis, and a range of roll of ±10°. The pointing accuracy of this gimbal-mounted mirror is ±0.13°, and this defines the field coverage of the receiver system.

The axial input signal beam, after reflecting off the pointing and primary mirrors, is brought to a focus at the center of the folding mirror (see Figure 4-57). The signal beam is then reflected off the secondary mirror and directed toward the image motion compensators via the folding mirror. Nominally, the IMC pair is tilted at 45° relative to the optical axis, and the axial input beam, after reflecting off the IMCs, is focused onto the on-axis
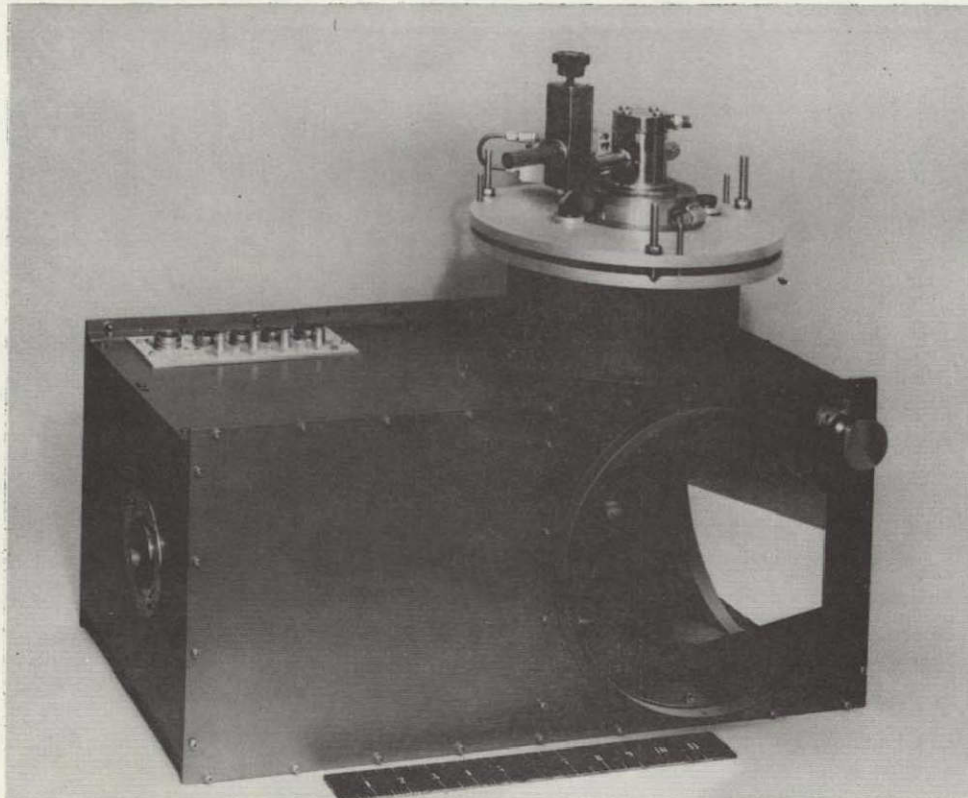
a) COVER IN PLACE (PHOTO 4R 42473)
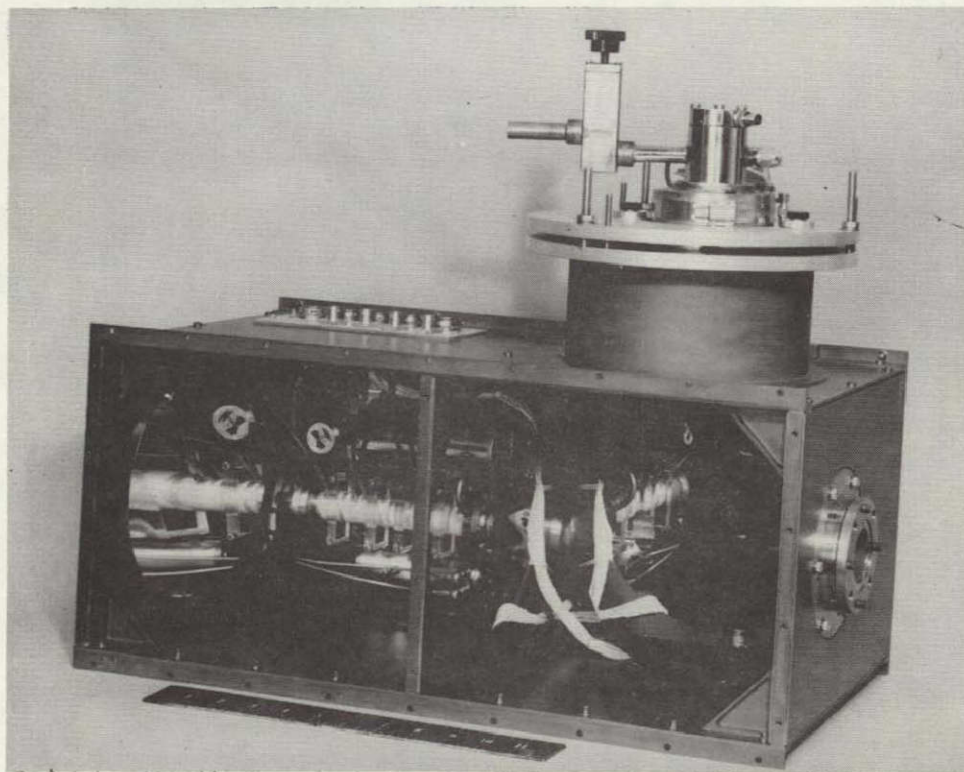
b) FRONT COVER REMOVED (PHOTO 4R 42470)

FIGURE 4-58. RECEIVER ENGINEERING MODEL

TABLE 4-16. OPTICAL CHARACTERISTICS OF GREGORIAN
HETERODYNE RECEIVER

Design configuration	Gregorian system with paraboloidal primary and ellipsoidal secondary
Diameter of primary	18.50 cm
Diameter of secondary	4.80 cm
Diameter of input beam	16.50 cm
Diameter of exit pupil	1.92 cm
f number of system	8.00
f number of primary	2.22
f number of secondary	1.94
Focal length of primary	41.00 cm
Focal distances of secondary	9.291 cm
	30.135 cm
Magnification	4.41
Separation: primary/secondary	50.292 cm
Spectral region	10.60 μm
Field coverage	$\pm 0.13^\circ$
Input acquisition field	$\pm 10^\circ$
Image diameter	0.60 cm
Distance from center of exit	
Pupil to: a) First IMC	-1.27 cm
b) Second IMC	1.27 cm

detector.* For off-axis inputs, the IMCs are suitably tilted so that the signal beam is once again focused on the same on-axis detector.

The details of this optical design are contained in Contract NAS 5-21859 Final Report, March 1975. The theoretical antenna gain is compared with the net antenna gain achieved in Table 4-17.

Figure 4-58a shows the receiver engineering model with the front cover in place and Figure 4-58b shows it with the cover removed. The cylinder on top is the supporting structure for the radiation cooler. A cryostat is mounted on the cylinder support ring and can be used to vary the temperature of the infrared mixer.

The mechanical configuration that can best meet the severe requirements of stability is a shell structure where the optical elements are supported on the walls and bulkheads of the shell. The elements should be both

---

*The optimum detector size is 0.72 times the Airy disk size to achieve a mixing efficiency of 72 percent.

Antenna gain (16.5 cm clear aperture unobscured)	93.78
Antenna losses:	
Absorption loss (1% per surface)	-0.28
Surface figure loss (2 fringes at 6328 Å at 2 surfaces)	-0.16
Distortion loss (thermal-mechanical)	
Without focal compensation	-0.06
With focal compensation	-0.00
Mixing efficiency (power in Airy disk divided by power in aperture, assuming 0.15 central obscuration)	-1.67
Off-axis loss (beam tilt)	-0.01
Total antenna losses	-2.18
Net antenna gain	91.60

mechanically and thermally hard mounted to the shell structure. Under this guideline, a casting would provide an ideal structure for the frame. However, castings and subsequent machining are quite expensive and bonded and riveted plates with web-type connecting brackets provide a similar mechanical structure which is acceptable and far less costly.

An important characteristic of the 10.6 μm laser heterodyne system concept is that solar background has very little effect on the heterodyne system. This is in marked contrast to optical systems using direct detection. The basic reason for this characteristic is the narrow bandwidth provided by the IF amplifier in the heterodyne receiver as compared to the wideband optical (or RF) filter in direct detection receivers. Advantage can be taken of this feature only if the system thermal design is capable of accommodating the sun's thermal energy entering the aperture of the optical system. Optical filtering at the input aperture using an appropriately coated germanium window to reject the solar spectrum is an unsatisfactory solution since the germanium window would have to be inordinately large and heavy. A satisfactory approach with an open aperture is through the use of an isothermal, all-beryllium optomechanical structure including beryllium optics. The exposed optical components can be coated with high reflectivity coatings in the solar spectrum that reject about 96 percent of the total solar energy. The solar heat load on both the optics and the walls of the structure is conducted away rapidly due to the very high termal conductivity of beryllium. This isothermal characteristic tends to keep all elements of the optics and structure at very near the same temperature. The optical performance evaluation during the worst case conditions shows a signal loss of only 1.5 percent, a value considered negligible.

A structural analysis of the receiver engineering model was also performed. Analytical results were obtained from static 1 g loading and dynamic sinusoidal sweep loading of the structure. The former case showed no signal loss through the optical chain. In the latter case, the lowest mechanical resonance is on the order of 617 Hz, which is well above that of high spectral energy vibration inputs. Also, the worst case loads produced maximum stresses only one-tenth of the material stress limit. The vibration profile assumed in the analysis was that required for the ATS-6 satellite, which is representative of modern geosynchronous communication satellites.

The optical-mechanical subsystem has rectangular dimensions of nominally 25.4 x 25.4 x 54.6 cm (10 x 10 x 21.5 in.), not including the support cylinder for the radiative cooler or the cooler itself, and the subsystem alone weighs 11.3 kg (24.8 pounds).

Acquisition and Tracking Servo System. Spatial tracking is accomplished in a 10 μm laser heterodyne receiver by conical scanning the input signal, sensing the angular error and positioning the optical system through a servo system. The movable optical elements are divided into coarse pointing and fine pointing devices. The coarse pointing element is the large gimbaled mirror and the fine pointing elements are the small IMCs (image motion compensators) located at the exit pupil of the optical system. The fine tracking is accomplished with the IMCs which permit the coarse pointing element to be moved in steps with stepping motors. Therefore, the amount of electrical power needed to drive the gimbal is minimized since commands occur in the form of pulses.

The overall characteristics of the coarse pointing mirror and gimbal assembly are given in Table 4-18 and a photograph with the assembly removed from the structure is given in Figure 4-59. Coarse pointing of the flat pointing mirror is obtained by a two-gimbal assembly. The flat mirror is

TABLE 4-18. COARSE POINTING MIRROR/
GIMBAL CHARACTERISTICS

Major axis	28.3 cm
Minor axis	18.1 cm
Rotation range	$\pm 5^\circ$ tilt (elevation)*
	$\pm 10^\circ$ roll (azimuth)
Gear ratio	15 000:1 tilt
	7 500:1 roll
Step size	0.001° tilt
	0.002° roll
Maximum slew rate	0.05 deg/sec tilt
	0.10 deg/sec roll

*Tilt range needs to be only half that of the roll range due to optical angle doubling inherent in the tilt axis.
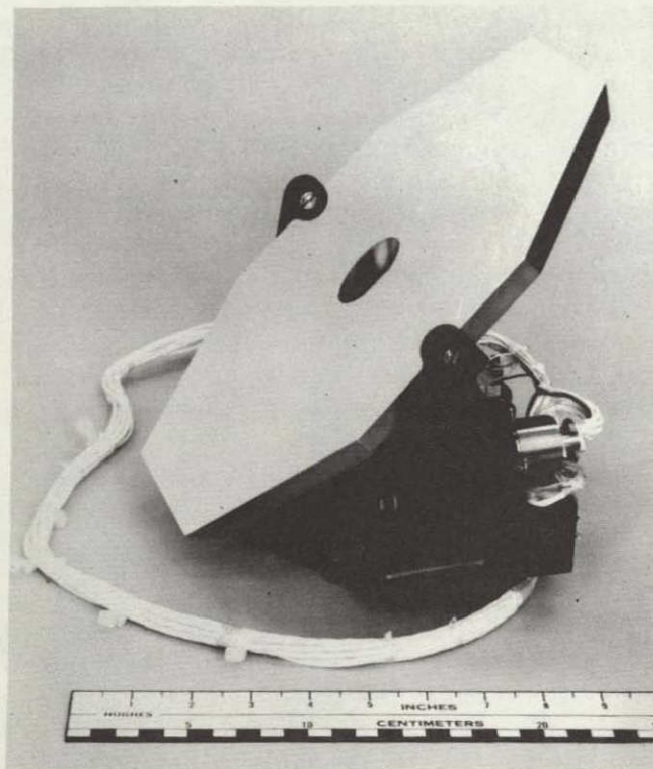
FIGURE 4-59. COARSE POINTING MIRROR AND
GIMBAL ASSEMBLY

mounted in a yoke on a rotatable pedestal. Rotation of the pedestal provides
azimuth (or roll) sweep, while elevation sweep results from declination or
tilt about the mirror's pivot axis in the yoke. Positioning is independent in
each axis and is performed by a space qualified stepper motor drive. The
positioning drive for each axis consists of a spur gear reduction from the
motor shaft to a final single-thread worm gear engaged in a matching worm
wheel. These gears are lubricated with a dry film suitable for space use
which will not migrate to optical surfaces or boil off in vacuum.

Fine pointing and conical scanning are accomplished with the IMCs.
The IMCs developed for the high orbit system are driven with piezoelectric
bimorph strips and will deflect the beam at the exit pupil by 1° with the
application of 500 volts. The resonant frequency is 900 Hz. The far field
coverage of the system is 0.2° due to the magnification factor between the
far field and the exit pupil. The IMC assembly, shown in Figure 4-60,
utilizes a modified version of the GTE-Sylvania PBM-8GIMC, which has been
space qualified on a previous program.

The IMCs for the low orbit configuration are required to produce a
beam scan angle of 5° at the exit pupil in order to achieve the 1° far field
acquisition. The piezoelectric bimorphs cannot provide this amount of scan
angle and a dc torquer must be used. The development of the dc torquer IMC
is straightforward, but has not yet been accomplished.
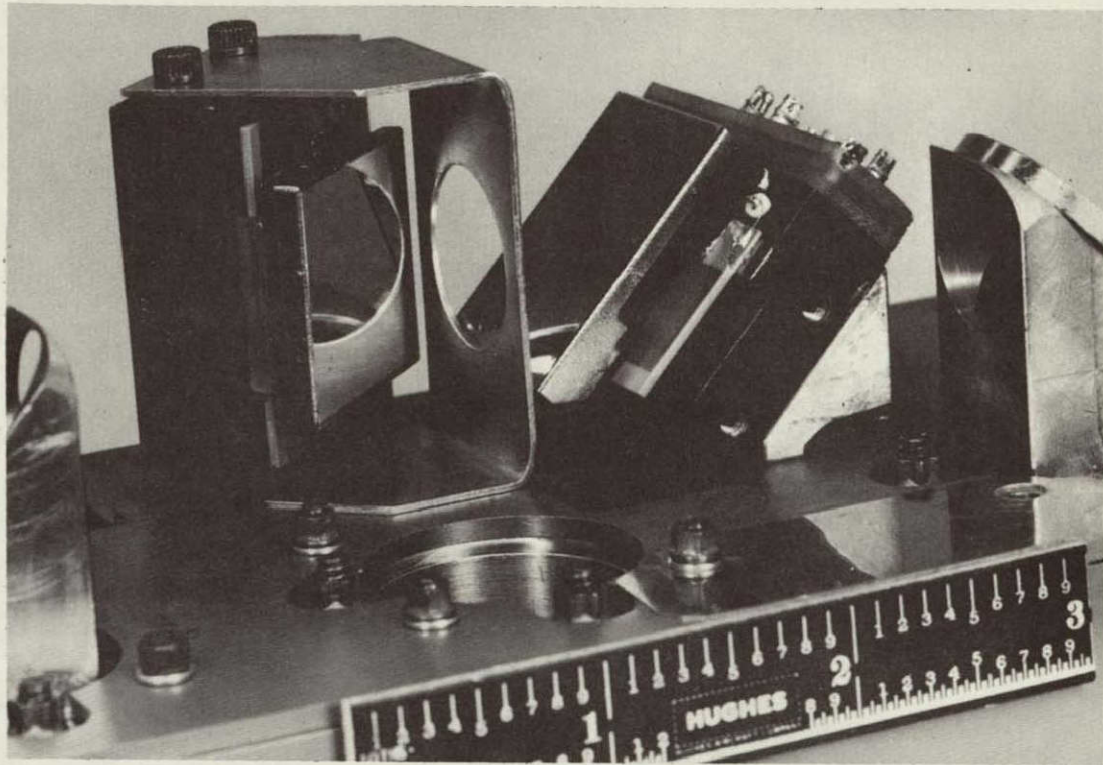
FIGURE 4-60. IMAGE MOTION COMPENSATOR OPTICAL ASSEMBLY

The servo system consists of three basic units: the acquisition scan generator, fine tracking loop, and tracking step command. Figure 4-61, a simplified servo system block diagram for the roll axis, includes these basic units. Since acquisition and tracking are accomplished through sensing the communication received signal strength, the receiver's automatic gain control (AGC) is a convenient signal source from which to derive the acquisition and tracking data.

Whenever there is no signal (no AGC voltage) the acquisition/track threshold circuit turns off the fine tracking loop, turns off the tracking step command, and turns on the raster scan generator. The IMCs are then driven through an x-y scan pattern as shown in Figure 4-62. When the target is encountered, the acquisition/track threshold circuit stops the search scan generator and turns on the fine tracking loop. If the target lies near the center of the IMCs field of coverage, the fine tracking continues in the normal manner. However, if the target lies near the edge of the field of coverage, a tracking step command is generated which instructs the gimbal stepper motor to move in such a way as to bring the target to the center of the IMC field.

One of the parameters strongly influencing the design of both the acquisition and tracking subsystems is the target maximum angular rate. This rate is the sum of the actual target motion and the angular motion produced by the optical-mechanical base. The angular motion of the base is strongly dependent on the attitude control system of the satellite (e.g., firing

4-93

FIGURE 4-61. SIMPLIFIED SERVO SYSTEM BLOCK DIAGRAM FOR ROLL AXIS ONLY

STEPS PER LINE = 128
LINES PER FRAME = 128
DWELL TIME PER STEP = 0.4×10^{-3} sec
TIME TO COMPLETE LINE = 0.0512 sec
TIME TO COMPLETE FRAME = 6.5 sec

TARGET CAPTURE PROBABILITY
TARGET VELOCITY   0.1 deg/sec = 30%
                  0.03 deg/sec = 100%

FIGURE 4-62. RASTER SCAN PATTERN

a reaction jet during an acquisition scan might produce a 0.1 deg/sec rate, which would make the acquisition process more difficult. If such firing is prohibited during acquisition, the maximum rate probably would be less than 0.01 deg/sec. The present system can accommodate rates of 0.03 deg/sec which is ten times the specification for the ATS-6 satellite.

Beacon Transmitter

The high altitude receiver terminal utilizes all-reflective optics and thus can accommodate a beacon transmitter of any wavelength from the visible to the far infrared region. The beacon transmitter may be diplexed through the use of a dichroic mirror or a wire grid polarizer. Figure 4-63 is an optical layout of the diplexing technique for a 10.6 μm beacon. The key diplexing elements are the $\lambda/4$ plate and wire grid polarizer.

It is also possible to utilize a gallium arsenide array laser as a beacon source in the system. In this case, a dichroic mirror would be used in place of the wire grid polarizer and a special optical train would be used to condition the output of the gallium arsenide array. Figure 4-64 illustrates an optical ray design of the beacon array operating in the f:8 Gregorian optical system. This produces an overall beamwidth in the far field of 0.25°, the same field coverage of the acquisition search system for the 10 μm receiver.
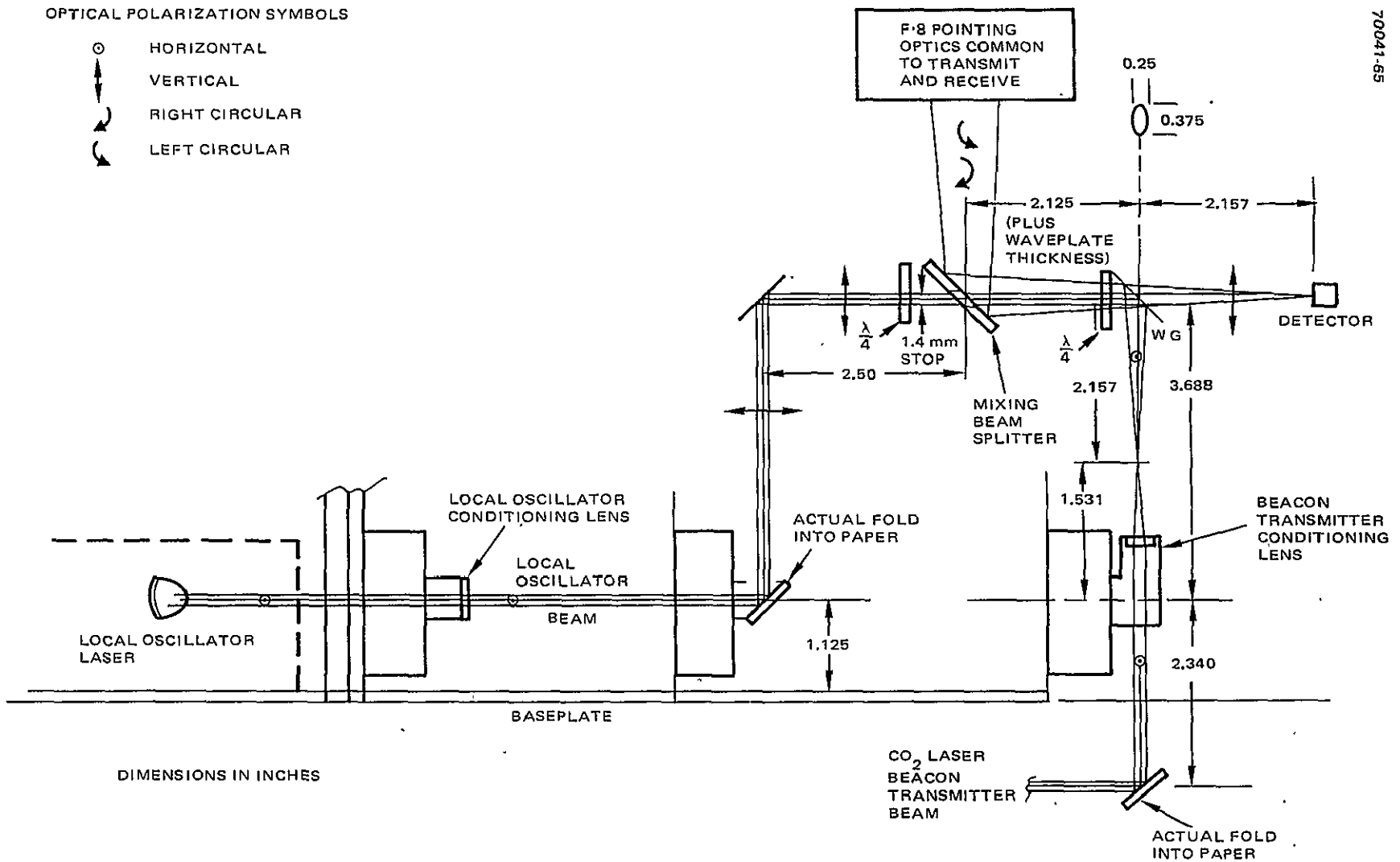
FIGURE 4-63. TRANSCEIVER OPTICAL TRAIN LAYOUT SHOWING BEACON PATH
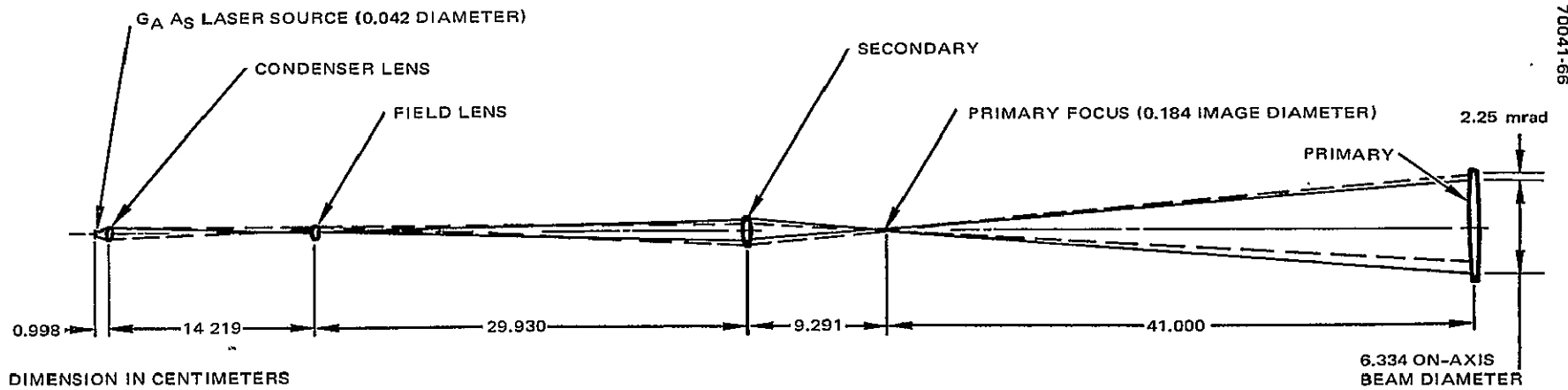
FIGURE 4-64. FIRST ORDER LAYOUT OF GALLIUM ARSENIDE BEACON SYSTEM

$G_A A_S$ LASER SOURCE (0.042 DIAMETER)

CONDENSER LENS

FIELD LENS

SECONDARY

PRIMARY FOCUS (0.184 IMAGE DIAMETER)

PRIMARY

2.25 mrad

0.998

14 219

29.930

9.291

41.000

DIMENSION IN CENTIMETERS

6.334 ON-AXIS
BEAM DIAMETER

5. TECHNOLOGY STATUS AND DEVELOPMENT REQUIREMENTS

In any space hardware development program it is essential that fully functional engineering model hardware be available to demonstrate feasibility, performance, reliability, and to minimize risk. Further, technical problems solved during a modest preliminary engineering model development are much less costly than solving the same problems later in a flight program. The technology status of the various components and subsystems required for the high altitude receiver (Molniya) terminal are presently in a completed, engineering model stage of development. The singular development area recommended for continued work is laser starting reliability and laser life.

The status of components and subsystems for the low altitude (Shuttle) terminal are not in the completed engineering model stage. Although many of the components and subsystems are in an advanced state of development, further work is required on these components as well as system integration of the Shuttle terminal.

The following description of development requirements is based on the status of technology at the date of this report. The efforts described are broadly aimed at supporting the completion of the Shuttle terminal integration, but also are intended to support the fundamental reliability and performance of the entire laser link.

5.1 TRANSMITTER TECHNOLOGY

Further transmitter technology development is recommended to improve the performance of high data rate CO_2 laser transmitters. The task includes improvement of technologies related to laser efficiency, starting reliability, modulator frequency response, and modulator driver performance. The overall goal is to define the laser transmitter configuration which satisfies the needs for space experiments and which shows the greatest promise of meeting future data relay mission requirements.

Previous programs have developed a highly efficient waveguide laser and a wideband intracavity coupling modulator for high data rate CO_2 laser experiments. Individually, the component performance goals have been met or exceeded. The waveguide transmitter laser produces 5 watts of

power at 10 percent efficiency. The modulator exceeds 1 GHz of bandwidth, and the modulator driver meets the voltage and waveform requirements for high quality 300 Mbps digital modulation.

The integrated transmitter subsystem performance is strongly dependent, however, upon modulator rod loss. Transmitter frequency response is dependent on component interface factors. For example, power output of the transmitter is dependent on modulator rod loss, a loss which is in the laser cavity, and transmitter frequency response is dependent upon the polarization quality of the mirror grating in the laser cavity. Further, the conventional high voltage regulated power supplies used in previous programs do not produce reliable waveguide CO_2 lasers starting.

The solution to the interface problems of the transmitter subsystem appear straightforward and can be achieved with modest effort. Baseline equipment for the effort is the lasers, modulators, driver amplifiers, and power supplies developed on previous programs. The techniques necessary to improve the performance of the integrated transmitter subsystem have been demonstrated at the laboratory level. The objective of the proposed work is to modify, upgrade, and refine the transmitter subsystem to meet the performance requirements for the mission.

5.1.1 Modulator Material Improvement

Modulator rods have been fabricated which are 6 cm long and which have a loss at 10 μm of the order of 0.002 cm^{-1}. Analysis and experiment have shown this value to be only marginally acceptable for high performance intracavity coupling modulators. Loss factors of 0.001 cm^{-1} are desired.

The proposed effort is designed to improve the quality of cadmium telluride used in intracavity coupling modulators. The task includes material production selection, loss measurement, coating evaluation, and determination of specifications. The goal is to achieve modulator rods having loss factors of 0.001 cm^{-1} or less and coatings which are physically capable of handling power densities of 10 kW cm^{-2} and which have a total coating loss of less than 0.25 percent per surface.

5.1.2 Modulator-Laser Interface Improvement

Present frequency response performance shows the effects of imperfect grating polarization. An improved polarizer is required. Modification of laser configuration to accommodate this requirement is necessary.

The modulator-laser configuration will be modified to achieve a transmitter bandwidth of 400 MHz or greater flat within ±1 dB.

5.1.3 Modulator Driver Improvement

Performance of the modulator driver is presently limited by lack of uniformity in the intermediate-stage driver transistors. A selection procedure is required which can provide uniform beta values, thereby improving the rise time and voltage output of the modulator driver. When optimized, the driver is now capable of handling data rates in excess of 300 Mbps.

This task is to develop a procedure to select high beta HP-35821E transistors for the intermediate stage in the driver amplifier modules. The selection procedure will serve as a specification for the manufacturer who will assign a new nomenclature for the selected units. Marginal or nonuniform units in the existing modulator driver modules will be replaced with new units.

5.1.4 Transmitter Laser Starting Improvement

Reliable starting of the transmitter laser occurs only if the ionization transients are isolated from each of the four sections. Presently, a single regulated high voltage power supply is used with separate ballast resistors for each section. Transients occurring when one discharge section ignites are coupled through the power supply to the other arms; this prevents the other sections from starting. Repeated starting attempts are required to reach the condition where all four discharge sections are operating. Separate high voltage power supplies are required for each of the four discharge sections to achieve reliable starting.

This task is to facilitate starting of the transmitter laser. An existing commercial high voltage power supply will be modified to provide separate high impedance sections for each of the four discharge sections.

5.1.5 Transmitter Subsystem Integration and Test

This task is to integrate, test, demonstrate, and evaluate the transmitter subsystem in a communication system. Documentation shall be prepared to confirm the performance of the subsystem.

5.2 400 MBPS BIT ERROR RATE MEASUREMENTS

This effort is the measurement of bit error rates (BER) of a 400 Mbps CO_2 laser heterodyne communication system which simulates a space-to-space data relay link.

Hughes' development of a 300 Mbps 10.6 μm receiver terminal engineering model for NASA is completed. The development of a complementary transmitter is in a state of semicompletion. The 10.6 μm

TEST
NUMBER

1 NRZ-L GENERATOR → ATTENUATOR → NOISE SOURCE → NRZ-L RECEIVER

2 NRZ-L GENERATOR → MODULATOR DRIVER → ATTENUATOR → NOISE SOURCE → NRZ-L RECEIVER

3 NRZ-L GENERATOR → MODULATOR DRIVER → ATTENUATOR → NOISE SOURCE → DC RESTORATION → NRZ-L RECEIVER

4 NRZ-L GENERATOR → MODULATOR DRIVER → LASER TRANSMITTER → ATTENUATOR → HETERODYNE RECEIVER → NRZ-L RECEIVER

5 NRZ-L GENERATOR → MODULATOR DRIVER → LASER TRANSMITTER → ATTENUATOR → HETERODYNE RECEIVER → DC RESTORATION → NRZ-L RECEIVER

FIGURE 5-1. PROGRESSIVE TEST CONFIGURATIONS FOR 400 MBPS BER TESTS

transmitter subsystem (laser/modulator/modulator driver) is sufficient to conduct critical BER tests using the receiver terminal.

· The two data formats which have been considered are NRZ-L and Miller. To faithfully transmit the NRZ data format, a frequency response to very low frequencies is required. However, the modulator driver amplification passband is limited by the hybrids to a lower limit of 10 MHz. This distorts the NRZ waveform. The waveform distortion results in an increase in the signal-to-noise ratio (SNR) required to achieve a given BER.

· An alternative to NRZ coding is Miller encoding. This shifts the data spectrum away from zero frequency and permits the use of a passband driver amplifier. However, the Miller code also requires a greater SNR to achieve a given BER performance.

Another alternative to the NRZ-L format is to use the conventional NRZ-L data format together with bit dc restoration at the receiver to compensate for the bit distortion in the driver amplifier. This technique has the promise of achieving a given BER with an SNR very close to the theoretical values.

· The objective of the proposed work is to use the NASA 10.6 μm receiver engineering model, the NASA 10.6 μm transmitter subsystem, and the NASA BER test equipment to conduct 400 Mbps data transmission tests. These tests will measure and evaluate the effects of critical performance parameters.

5.2.1 Modification of Receiver to Accommodate 400 Mbps

This task is for the modification of the AIL and NASA receiver terminals from the present 300 Mbps design to accommodate 400 Mbps. Mainly, the Bessel filter which limits the IF bandwidth must be increased from the present 400 MHz to 550 MHz.

5.2.2 Measurements

BER will be measured for several test configurations. In each configuration the BER will be measured as a function of the video SNR and, where appropriate, the IF SNR. Other parameters which will be varied in the measurements are sync phasing, transmitter bit rise and fall times, and bit rate.

The measurement configurations are shown in Figure 5-1. The progressive incorporation of subsystem components will allow the effects of each to be isolated.

5.3 CO_2 LASER LIFE STUDIES

This effort is to study and develop controls of the catalytic reaction in sealed-off CO_2 waveguide lasers. This is needed to assure long laser life.

The transmitter and local oscillator CO_2 waveguide lasers developed by Hughes for NASA are well suited for this test program. Past CO_2 laser development effort has resulted in significant cathode performance improvement (sputtering and adsorption of gases); oxidation has been reduced to negligible values; and the amount of CO_2 and CO in cathode discharge test cells has shown long term stability. These developments provide the potential for extremely long laser life, but the laser lifetime also depends on the catalysis of the CO - CO_2 reaction in the laser discharge. At present, the catalysis is provided by a residual amount of hydrogen in the laser envelope after the oxygen scrubbing process prior to filling the laser. Poor control of the residual hydrogen results in inconsistent laser efficiency and lifetime performance.

The objective of the proposed work is to quantify the effects of hydrogen on laser efficiency and to investigate methods of stabilizing the amount of hydrogen and stabilizing CO - CO_2 reaction in the sealed-off CO_2 waveguide laser. The two types of NASA lasers will be used to conduct these investigations. Spectraphotometry will be used to quantify the partial pressures of CO, CO_2, and hydrogen in the form of water vapor.

5.3.1 Parametric Measurements

Parametric measurements will be made to determine laser efficiency as a function of hydrogen partial pressure. These will be conducted for a number of CO - CO_2 fill combinations determined from previous parametric measurements.

5.3.2 Hydrogen Source Investigation

Hydrogen emitters and absorbers will be investigated for potential use in the lasers to act as stabilizers of hydrogen partial pressure.

5.3.3 Processing and Sealing Procedure

The processing and sealing procedure for long life CO_2 waveguide lasers will be developed.

5.3.4 Life Tests

Life tests will be initiated on the six local oscillator lasers. Data to be monitored during life tests include tube voltage, current, optical

power output, gas spectra, partial pressures of CO_2, CO,. hydrogen (water vapor), and tube operating temperature.

5.3.5 Reliability Plan

A reliability plan will be developed for the purpose of gathering mean time between failures (MTBF) and failure rate data on lasers and for using these data to predict the reliability of these lasers used in systems.

5.4 COMPLETION OF LDRL-10.6 ENGINEERING MODEL

This effort is to complete the development of the LDRL-10.6 transmitter terminal which was begun under this contract (NAS5-20018). To date, the optomechanical subsystem has been designed and an engineering model partially built.

Previous tasks on this contract included the definition of a Shuttle to ground and Shuttle to Molniya orbit satellite. A hardware task included the design and construction of an optomechanical subsystem to accommodate the requirements for any of these potential experiments.

Development of the hardware has progressed to the point of completing the assembly of the optomechanical portion of the engineering model. However, there are many elements which require further development. These include the servo design and construction and the communication system electronics.

The objective of this task is to complete the development of the LDRL-10.6 transmitter suitable for full scale acquisition, tracking, and 400 Mbps communication tests in the laboratory.

5.4.1 IMC Development

An IMC having a 5° angular coverage will be developed to provide fine pointing and acquisition scan.

5.4.2 Optomechanical Front-End Integration

The LDRL-10.6 optomechanical subsystem consists of the motors and transducers for angular pointing and tracking and the optics for expanding the transmitter beam. The tasks required for completion of this subsystem are integration of the new IMCs, optical alignment, and optical testing. Optical testing will include measurement of beamwidth, antenna pattern, optical transmission loss and field of view.

5.4.3 Optomechanical Back-End Development

The optomechanical back-end development includes the optical train to diplex the beacon receiver and transmitter beams, point-ahead compensation, transmitter beacon bypass optics, beacon receiver, and a GFE 10.6 μm transmitter subsystem. This task includes the optical train design, construction, and integration of all components.

5.4.4 Servo Subsystem Development

The servo subsystem development task includes: 1) design and development of an IMC inner control loop, interfacing with existing motors, tachometers, resolvers, and encoders, 2) design and development of circuitry for extracting pointing error signals from the beacon receiver, and 3) design and development of main servo loop to process the error signals, to perform the necessary coordinate transformations, and to dri the main positioning motors and IMCs.

5.4.5 Command and Monitor Subsystem

This task is for the design and construction of the circuitry for sequencing the LDRL-10.6 system. It will provide initial pointing commands, search commands, and acquisition signals. Search to track transfer will be controlled. Provisions will be included to control the point-ahead function and the transmitter beacon bypass optics. The subsystem will be installed in a console with metering and test points for monitoring all functions of the LDRL-10.6 performance.

5.4.6 Integration and Testing

The integration and testing will include checkout of all subsystems and their integration into the complete transmitter unit. System tests include command pointing, acquisition, tracking, and communication tests. Testing will be conducted in the laboratory using television equipment for qualitative evaluation and BER tests for quantitative evaluation. Tests will be conducted between the LDRL-10.6 transmitter terminal and the GFE 10.6 μm receiver terminal.

6. EXPERIMENT PLAN

6.1 INTRODUCTION

The Shuttle to ground link experiment plan falls into five categories: acquisition, equipment performance evaluation, communication channel experiment, propagation experiment, and the communication demonstration experiment. For each experimental run, a test plan will be followed to obtain a full set of data for each set of test conditions.

Characterization of the communication channel requires measurements of all aspects of the operational sequence of the laser relay link. These can be summarized to include signal statistics as a function of data from orbital parameters, from solar background, and from ambient spacecraft mechanical and thermal patterns. Other factors to be measured which influence signal statistics are transmitter power and frequency stability, radiation cooler temperature, tracking error signal, and doppler shift.

Signal statistics may be obtained by analyzing the carrier-to-noise (C/N) ratio and error count on a statistical basis.

Atmospheric propagation measurements are used to study the effects of thermal turbulence and attenuation in the atmosphere. In this case, signal statistics are used to measure amplitude variance and covariance and phase structure function. These data are correlated with macro and micro meteorological data and starlight scintillation data in an effort to verify the mathematical model of atmospheric disturbances. They will also be correlated with visual observations of cloud data to determine accurately the penetration of the 10.6 µm beam through various types of clouds.

Table 6-1 lists some of the most important experiments from each category. The individual experiments are listed roughly in the order or sequence in which they will actually be performed. The amount of time needed to conduct a given experiment will depend, to some extent, upon familiarity with the equipment. Initially, perhaps 4 to 8 hours will be required for learning the techniques of operating the equipment and conducting the experiments. Eventually, however, the amount of time required to perform the measurements will be reduced so that the required number of experiments can be performed during the lifetime of the equipment. Therefore, Table 6-1

TABLE 6-1. TIME REQUIRED FOR CONDUCTING EXPERIMENT SETS

	Time Required Per Set
<u>Acquisition Experiments</u>	
Measurements to be made	40 minutes
Initial pointing	
Acquisition time (1 minute)	
Acquisition S/N	
False alarm rate	
Average acquisition time	
Initial point error	
Warmup requirements (30 minutes)	Time Per Experiment Set
<u>Equipment Performance Evaluation Experiments</u>	
Measurements to be made	10 minutes
Laser local oscillator power	
Laser transmitter power	
Laser frequency stability	
Power supply voltages	
Tracking S/N	
Beam profile	
Transmitter antenna patterns	
Receiver antenna patterns	
Boresight check	
Collimation check	
Antenna reciprocity	
Doppler tracking	Time Required Experiment Set
<u>Communication Channel Experiments</u>	
Measurements to be made	120 minutes
Received signal power	
Spacecraft receiver minimum detection power	
C/N	
Error count	
Intermodulation distortion	
Harmonic distortion	
Phase linearity	
Pulse response	
Signal statistics	
Bit error rates	Time Per Experiment Set
<u>Atmospheric Propagation Experiments</u>	
Primary and Reduced Data	60 minutes
C/N	
Error count	
Aperture separation	
Microthermal	
Thermal structure function	
Log amplitude variance	
Log amplitude covariance	
Phase structure function	
Coherence area at 10.6 μm	
Meteorological variables	Time Required Experiment Set
<u>Communication Demonstration Experiment</u>	
400 Mbps Shuttle to ground downlink	60 minutes
<u>Continuous Telemetry Data of Relevant Parameters</u>	
Orbital data	
Solar background	
Spacecraft thermal and mechanical stresses	
Radiation cooler temperature	
Spacecraft acoustic noise and vibration	
Tracking error and mirror nutation	

also lists the approximate amount of time that will be required to conduct the experiment after thorough familiarity is established. Assuming the experiment set is conducted 3 days per week, with approximately 5 hours per experiment set, a total of 15 hours of operation is planned per week. In addition, one 3-hour communication demonstration per week will bring the total operating time to 18 hours per week. In 1 month the laser experiment will thus have operated for approximately 78 hours.

6.2 EXPERIMENT PLAN

6.2.1 Acquisition Plan

The 500 km Shuttle orbit of the Shuttle to ground link was dictated by acquisition considerations. Lower orbits result in acquisition LOS angular rates exceeding the capabilities of the Shuttle transmitter.

Figure 6-1 shows zenith angle (viewed from the ground site), tracking angle (between the satellite and ground site), and tracking angle rate plotted against time in ground station FOV. It is assumed that because of atmospheric effects the 400 Mbps communications link cannot be established until the zenith angle becomes less than 60°, which occurs approximately 4 minutes after the Shuttle crosses the ground station's horizon. Acquisition is initiated at a zenith angle of 80° by the ground station illuminating the Shuttle, so that 2 additional minutes are available to acquire before the communication period begins.

The tracking angle at 80° zenith angle is 65°, and the rate is approximately 0.02 deg/sec, whereas at 60° zenith angle the tracking angle is 52°, and the rate is increased to 0.24 deg/sec. The maximum tracking rate occurs at zero zenith angle and is 0.8 deg/sec. Therefore, it is important to achieve acquisition as soon as possible. It is here assumed that acquisition will occur at a zenith angle equal to or greater than 60°, so that acquisition must occur at rates up to 0.24 deg/sec, and tracking must be maintained at rates up to 0.8 deg/sec.

The link establishment procedure can be summarized as follows:

1) From shuttle navigation data the position of the ground beacon is known to a certain accuracy at all times and can be predicted far enough in advance to allow a command sequence to be generated.

2) The command sequence is transmitted to the transmitter servo system and executed at a rate that minimizes gimbal errors so that most of the target error is contributed by the Shuttle pointing error.

3) The Shuttle pointing error is nominally equal to the telescope FOV (±0.5°), so that the above procedures should bring the ground beacon within the telescope FOV.
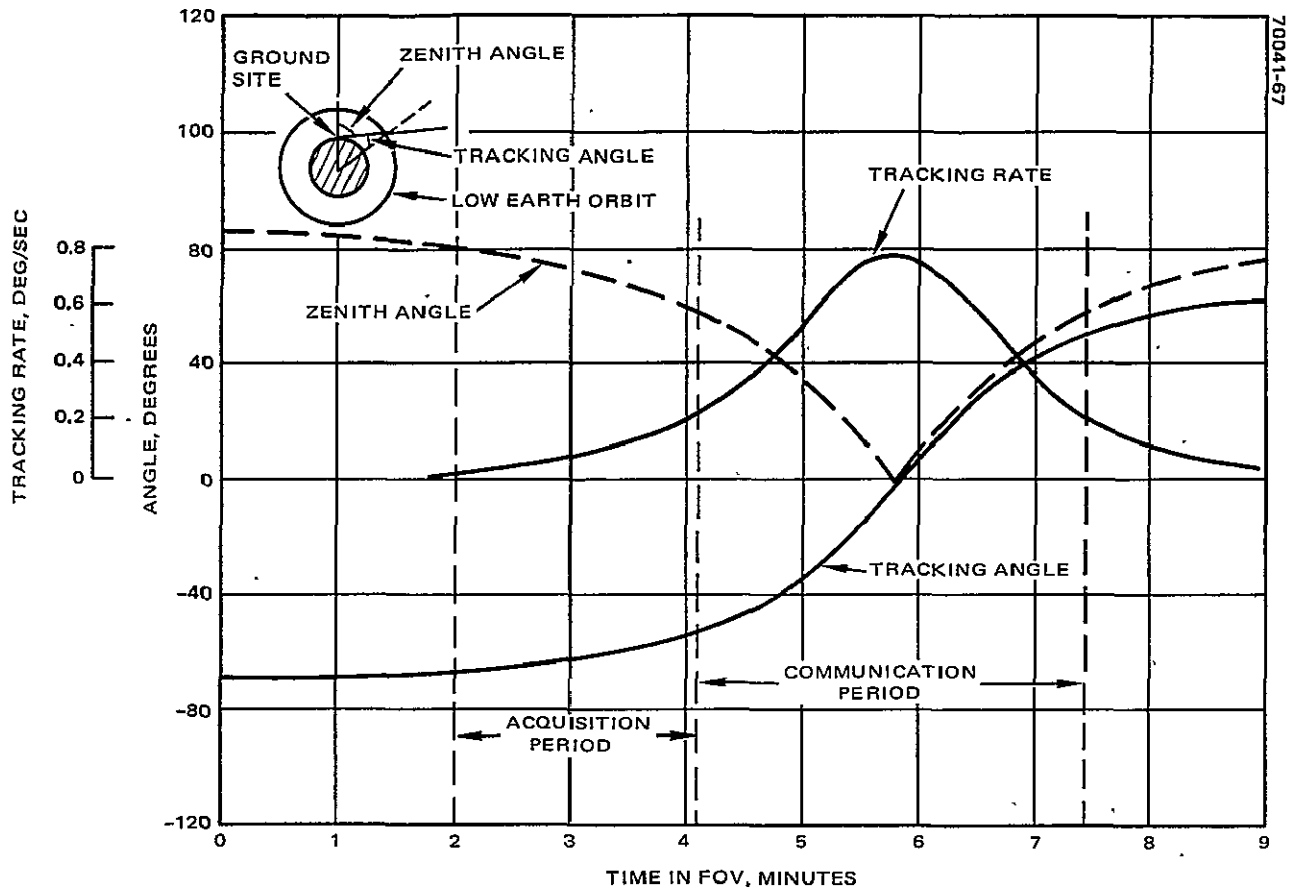
FIGURE 6-1. ACQUISITION PARAMETERS AS FUNCTION OF SATELLITE
TIME IN FIELD OF VIEW

by these spacecraft environmental factors. Experimental measurements of C/N and error count will be continuous during these experiments. Other measurements will include receiver signal power, intermodulation distortion, harmonic distortion, phase linearity, pulse response, carrier spectral broadening, and intersymbol interference.

Signal Strength

The measurement of received signal strength can be obtained directly from the AGC of the ground receiver IF amplifier. Fluctuations will occur in the signal strength due to mechanical or acoustic noise in the spacecraft or any sporadic transient in the system. It is the purpose of these measurements to obtain correlation of the fluctuations with the influential parameter. Signal power fluctuation measurements are needed for two purposes. The first is to establish the validity of optical communication link reciprocity theories which have been generated but never tested. The second reason is that signal fluctuations are anticipated to be sufficiently pronounced to play a key role in establishing optimum modulation methods, acquisition schemes, and tracking.

The signal carrier strength at the spacecraft receiver is measured at the AGC output and is continuously telemetered.

Error Count

Error count is obtained by transmitting a stored word through the 400 Mbps channel. After detection at the receiver end, the word is compared with a reference word and any bit errors are then counted.

Harmonic Distortion

Harmonic distortion is measured using a sine wave signal that is set at specified frequencies across the video passband. After transmission through the channel, the sine wave is then compared with a standard signal.

Communications Channel Response

Other important communication parameters such as amplitude response, phase characteristics, and pulse response will be measured before launch and compared with measurements during each measurement period after launch.

Receiver Sensitivity

Normally, receiver sensitivity measurements are made by attenuation of the input signal. We are limited in this respect because signal attenuation will also interfere with spatial and frequency tracking. In view of this, we attenuate the power in the sideband by decreasing the modulation index of a tone modulated transmitted signal. Prior to installation, a careful measurement is made of the modulator voltage required for tone modulation to achieve a particular modulation index. From this, one establishes a known

4) To add margin to the above procedure, a simple gimbal scan routine is proposed, which extends the effective telescope FOV by a factor of approximately two.

5) Within the telescope FOV, two IMC sprial scans are employed: a large scan covering the entire telescope FOV, which initially brings the ground beacon across the detector, and a miniscan that "zeroes in" on the target for capture..

6) A backup is provided in which the spiral scan would be replaced with a circular fence scan and the gimbal command sequence would be eliminated. Figure 6-2 illustrates the foregoing procedure.

Figure 6-2 illustrates the foregoing procedure.

6.2.2 Equipment Performance Evaluation

Beam Profile Measurement

The beam profile experiment will be conducted after acquisition and after the preliminary measurements. The tracking S/N is measured and recorded. While locked to the beacon, the optical axis of the transmitter and receiver is rotated. The nutation amplitude is then slowly increased. The tracking S/N will decrease slowly at first, and then will drop off rapidly as the nutation amplitude exceeds the half beamwidth.

Correlation of this data with the S/N at the opposite terminal will give a measure of the transmitter antenna pattern profile. Correlation of the nutation amplitude with the S/N at the same terminal will yield the receiver antenna pattern of that terminal. These patterns are represented isometrically in Figure 6-2. This important experiment provides data to evaluate the tracking performance of the system.

Boresight

An immediate indication of misalignment is given by comparing the antenna pattern of the receiver with that of the transmitter. Adjustments can be made accordingly.

Point-ahead Angle Measurements

In operation the transmitter beam pattern will be located off-center by the actual point-ahead angle. The actual value of the point-ahead angle can be determined from the IMC inputs. This measurement can then be compared with the theoretical value determined from orbital/tracking data.

6.2.3 Communication Channel Experiments

Communication channel experiments are planned to determine the influence of the spacecraft environment on the communication channel. The results will be a characterization of the Shuttle to ground link as influenced

fraction of power in the Shuttle transmitter sideband. The modulation index is gradually decreased permitting a measurement of sideband S/N, which is related directly to receiver system sensitivity. The threshold level of sideband detection will be observed as a function of the modulation index, Shuttle transmitter power, and atmospheric loss and will allow calculations of receiver system noise temperature.

6.2.4 Communication Demonstration Experiments

The communication demonstration experiment is designed to directly verify the performance of the Shuttle to ground 10.6 μm link while transmitting 400 Mbps digital data. Ground receiver signal parameters of interest (as discussed in 6.2.3) will be monitored.

NORMAL TRACKING
NUTATION $\theta_\eta \sim 0.1 \theta_b$

$\theta_n \sim \theta_b$

$\theta_n > \theta_b$

BEAM AXIS

RECONSTRUCTED ANTENNA PATTERN
(USING C/N FROM NEAR TERMINAL)

POINT
AHEAD
ANGLE

θ_{PA}

RECONSTRUCTED ANTENNA PATTERN
(USING C/N FROM OPPOSITE
TERMINAL)
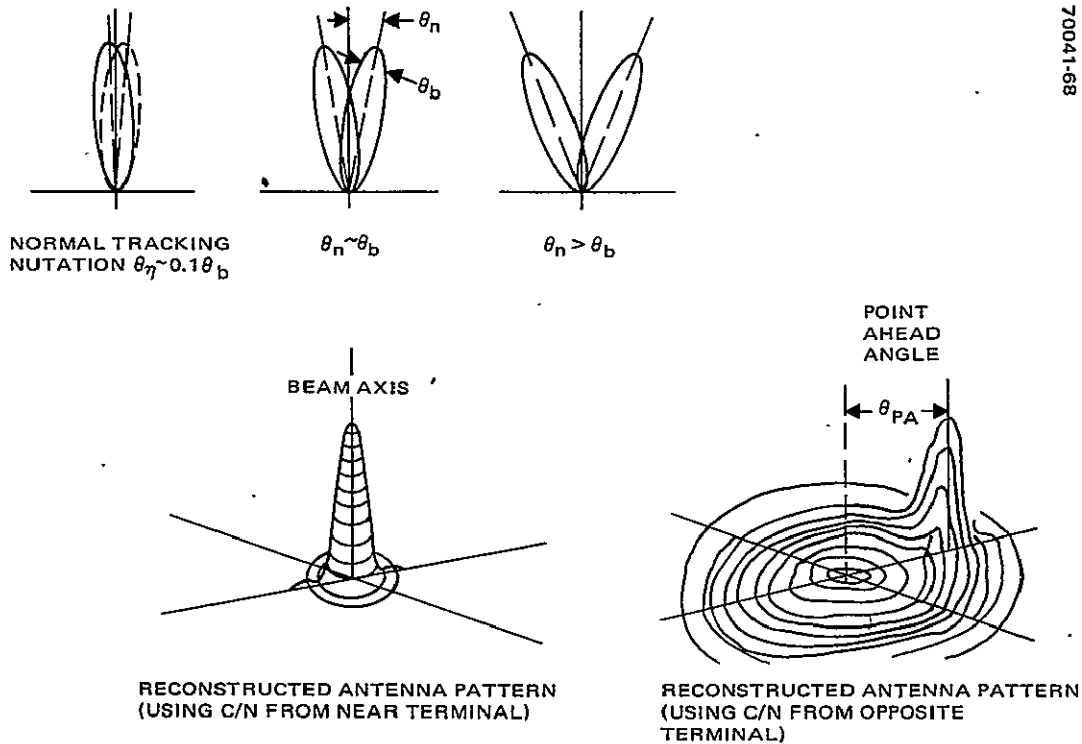
FIGURE 6-2. BEAM PROFILE MEASUREMENT EXPERIMENT

7. TEST AND EVALUATION

7.1 INTRODUCTION

Experimental measurements are required to verify the performance of the laser communication terminals. The measurements task is defined in this section, which includes the planning, coordination, integration, and testing of the Space Shuttle terminal and the ground terminal in sufficient detail to achieve performance verification. The task includes: 1) the collection and assembly of subsystems and components, 2) collection and assembly of special test equipment, 3) integration of the communication terminal, and 4) testing of the communication terminal.

This section is given in two basic parts: testing which is primarily applicable to the ground terminal, and tests which are primarily applicable to the Space Shuttle.*

7.2 GROUND TERMINAL

A simplified block diagram of the laser receiver terminal is shown in Figure 7-1. The diagram illustrates the functional relationships among the components and subsystems and the special test equipment.

A brief description of the principal components and subsystems which comprise the receiver terminal in the measurements configuration are given below:

7.2.1 Optomechanical Subsystem

The optomechanical subsystem is an all-beryllium structure consisting of structure, optics coarse pointing gimbal, and fine pointing subassembly. The subsystem was designed to have a 20° x 20° range, compact size, and light weight. Further, the structure is an isothermal design capable of accommodating direct sunlight without distorting the optics or the structural frame.

_____

*The ground terminal described in this testing is the same terminal used in the Molniya orbit. It will be optically coupled in a yet-to-be-defined manner to a ground optical terminal such as GORF.

RF SIMULATOR

DATA IN

10 MICROMETER TEST SIGNAL

BLACK BODY SOURCE

RECEIVER OPTO-MECHANICAL SUBSYSTEM

LASER LOCAL OSCILLATOR

STARK CELL FREQUENCY CONTROLLER

RADIATION COOLER OR CRYOSTAT

GIMBAL CONTROL

IMC CONTROL

MIXER

SERVO SYSTEM

0 1 TO 1 2 GHz AMPLIFIER

WIDEBAND DATA IF 1500 MHz

VOLTAGE CONTROLLED OSCILLATOR

PHASE LOCKED LOOP

PHASE DEMODULATOR

DATA OUT

1500 MHz CRYSTAL OSCILLATOR

AMPLITUDE MODULATION DETECTOR

AGC AMPLIFIER AND FILTER

CONSOLES

DIGITAL TRANSMITTER EQUIPMENT		SERVO		RECEIVER FRONT END		POWER SUPPLIES				RF DISPLAY	DIGITAL RECEIVER EQUIPMENT			RECEIVER BACK END	
BIT ERROR RATE GENERATOR	TELEVISION ENCODER	POINT	SEARCH AND TRACK	DETECTOR BIAS CONTROL	LOCAL OSCILLATOR CONTROL	SERVO SYSTEM	RECEIVER ELECTRONICS	LASER HIGH VOLTAGE	LOCAL OSCILLATOR LASER STABILIZATION ELECTRONICS	SPECTRUM ANALYZER	DEMULTI-PLEXER	BIT ERROR RATE RECEIVER	TELEVISION DISPLAY	PHASE LOCK CONTROL	AUTO/ MANUAL

FIGURE 7-1. EXAMPLE OF INTEGRATED RECEIVER BLOCK DIAGRAM

7.2.2 Servo System

The servo electronics provide acquisition, and tracking of the receiver subsystem. The design accommodates the use of a single detector for both the communication and the acquisition and tracking functions. The servo system also accommodates the coarse-pointing gimbal driven by stepper motors and a fine pointing assembly which is driven with analog signals.

7.2.3 Receiver Front End

The receiver front-end consists of a Joule-Thompson cryostat for detector cooling, a wideband HgCdTe detector assembly, and a wideband preamplifier.

7.2.4 Receiver Back-End

The receiver back-end consists of the RF section of the receiver electronics. The receiver is tunable from 200 to 900 MHz. It has a 1.5 GHz IF and a phase-lock detection system. The output of the receiver back-end is digital (ECL) level.

7.2.5 Local Oscillator Laser

The local oscillator laser is an integral part of the receiver subsystem, providing about 1 mW of power at the mixer detector. The local oscillator laser used in this integration task is a breadboard model unit.

7.2.6 Stark Cell Frequency Controller

The frequency control of the local oscillator laser is provided by a Stark cell control system. Part of the laser local oscillator power is passed through the cell to a pyroelectric detector. The cell consists of a small amount of deuterated ammonia gas between two parallel electrodes. The laser frequency is locked to the absorption line of the Stark cell, and tunability can be achieved by varying the dc voltage on the Stark cell.

7.2.7 Special Test Equipment

The special test equipment accumulated for these tests will include:

1) RF Simulator — This unit provides a test signal which can be used to test the receiver back-end electronics. The unit produces the same double-sideband suppressed carrier signal which is expected of the laser transmitter.

2) High Data Rate 10 μm Transmitter — The transmitter source used on these tests may be bench hardware.

3) Blackbody Source — The blackbody source is used to measure receiver NEP. It consists of a calibrated blackbody, a chopper, and a lock-in amplifier.

7-3

4) Collimator — A bench collimator with a diameter greater than 12 inches will be used in the tests for collimating the test optical signals and simulating space link conditions.

5) Rotary Table — A precision rotary table will be used to measure the tracking dynamics of the optomechanical/servo subsystem.

6) Covered Cart — The receiver subsystem will be mounted on a wheeled cart and covered with a lucite shroud to protect the unit from dust and humidity.

7) 300 Mbps Instrumentation — This equipment includes encoders, decoders, BER word generator, and a BER receiver.

8) Console — A console will be built to accommodate all the test equipment and instrumentation necessary to complete the measurements task.

7.3 GROUND RECEIVER MEASUREMENTS

The receiver measurements fall into the general categories of optomechanical subsystem, communication subsystem, and receiver NEP measurements. The following gives a more specific description in the order in which the results are presented.

7.3.1 Receiver NEP Measurements

The receiver NEP shall be measured using a blackbody source, a light chopper, and the receiver in a Dicke radiometer mode of operation. This measurement takes into account the performance of the complete receiver system, including optics, local oscillator, obscurations, losses, and the thermal noise in the receiver front end.

Heterodyne Receiver Sensitivity

Heterodyne receiver input power sensitivity, P_n, can be written in terms of its basic noise equivalent power per unit bandwidth (NEP) as

$$P_n = NEP \cdot B = \frac{h\nu B}{\eta'} \tag{1}$$

where h is Planck's constant, ν is the optical frequency, and B is the noise bandwidth of the receiver. η' is a term representing all receiver losses. Defined independently, η' can be written as

$$\eta' = \eta L_m L_o L_t \tag{2}$$

where η is the quantum efficiency of the photovoltaic device, L_m is the geometrical mixing efficiency (0.72 for the ideal case), L_o is the optical loss of the receiver (typically 0.5), and L_t is the thermal noise degradation due to insufficient local oscillator power (typically 0.5). The overall quality of the heterodyne receiver can be assessed by measuring $NEP \cdot B$. One very accurate method of making this measurement is through the radiometric measurement of a blackbody source. The following discussion illustrates the method and the results of this type of measurement.

Infrared Heterodyne Dicke Radiometer[1]

The conventional signal-to-noise ratio $(SNR)_{IF}$ of an optical heterodyne receiver is usually expressed as

$$(SNR)_{IF} = \frac{P_s}{NEP \cdot B} = \eta' \frac{P_s}{h\nu B} \tag{3}$$

where P_s is the signal power within the receiver IF passband B. In the Dicke radiometer, the output video signal-to-noise ratio $(SNR)_v$ is

$$(SNR)_v = \frac{1}{8\beta}(SNR)_{IF}^2 \cdot (B\tau) \tag{4}$$

where β is the IF passband shape factor, and τ is the integration time of the radiometer. In this expression it is assumed that the chopper has a 50 percent duty cycle and that $(SNR)_{IF} << 1$.

Heterodyne Signal Power From Thermal Source[2]

The spectral radiant emittance written in terms of frequency of a thermal source at temperature T_s is given from Planck's law by

$$W_\nu = \frac{2\pi}{\lambda^2} \cdot \frac{h\nu}{\exp(h\nu/kT_s) - 1} \left(\frac{watts}{area \cdot Hz \cdot hemisphere} \right) \tag{5}$$

To determine the power being directed into the receiver three factors must be applied to Equation 5: 1) the area of the blackbody that is radiating energy, 2) the bandwidth that is receiving the radiated energy, and 3) the

---

[1]Appendix B.

[2]B. J. Peyton, A. J. DiNardo, S. C. Cohen, J. H. McElroy, R. J. Coates, "Infrared Heterodyne Radiometer," JQE, QE-11, No. 8, Aug 1975.
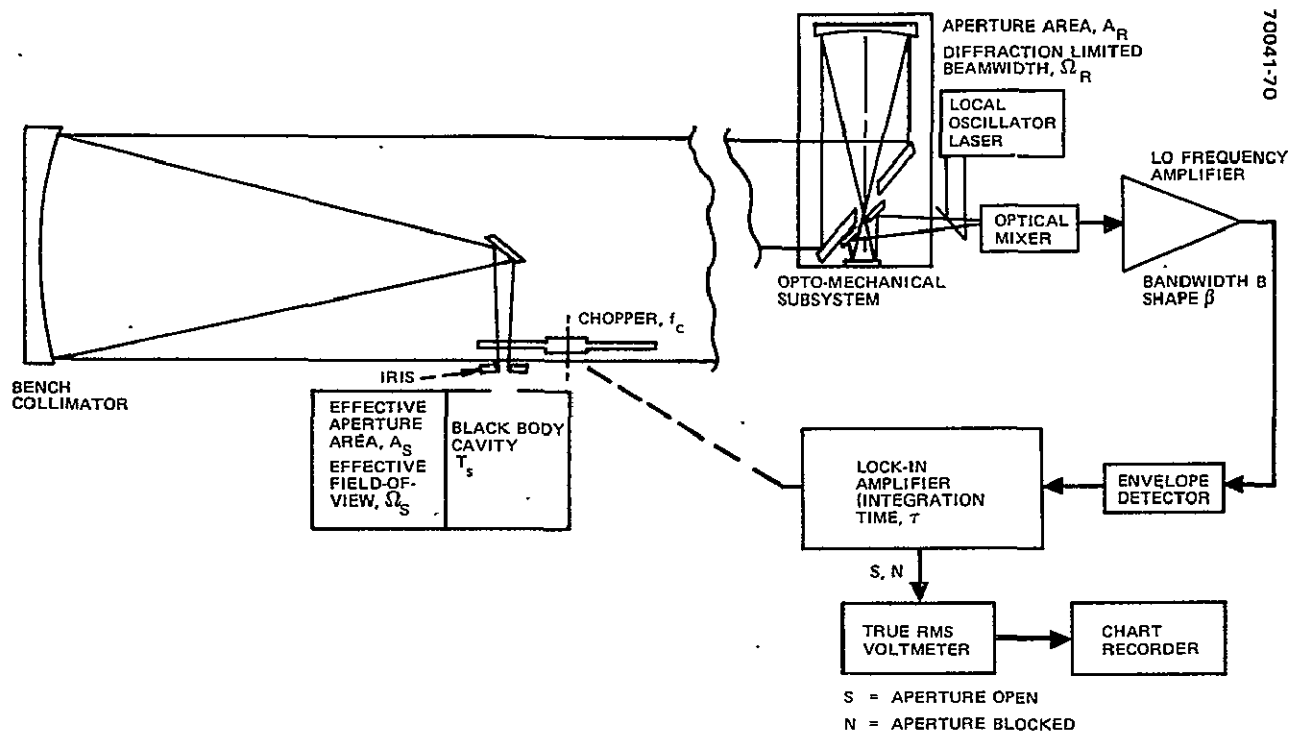
FIGURE 7-2. RECEIVER NEP MEASUREMENT BLOCK DIAGRAM

solid angle that is being intercepted by the receiver. Also two modifying tors must be applied to the spectral radiant emittance: 1) $1/\pi$ which recognizes the Lambertian radiation pattern from the surface and 2) 0.5 which accounts for the partial reception of the energy due to the linear polarization of the receiver. The three primary factors will be considered and then applied to Equation 5. Before this is done, however, it is helpful to review the laboratory test setup given in Figure 7-2 to appreciate the factors in determining the area, bandwidth, and field of view.

The energy from blackbody source of Figure 7-2 is collimated in the 20 inch collimator. This places the optical receiver in the far field of the blackbody source. This fact relates two important properties of the blackbody source, its effective radiating area, and the effective FOV of that radiating area. The relationship is as follows. The field of view is the diffraction limited solid angle resulting from the effective radiating area. This is true since only the in-phase portion of the energy being emitted by the source area, A_s, will be radiated in the desired direction in the far field. For a circular aperture this relationship is given by

$$\Omega'_s = \frac{\pi}{4}\left(\frac{\lambda}{D_s}1.03\right)^2 = \left(\frac{\pi}{4}1.03\right)^2\frac{\lambda^2}{A_s}.$$

where Ω_s is measured at the half-power points. However, the half-power points of the FOV, Ω'_s, does not account for all the energy transmitted. Siegman[3] has shown that the more exact relationship is:

$$\Omega_s = \frac{\lambda^2}{A_s} \tag{6}$$

Note that Ω_s can also be related to the diameter of the receiver aperture by a very large range, R, in the following way:

$$\Omega_s = \left(\frac{D_R}{R}\right)^2\frac{\pi}{4} = \frac{A_R}{R^2} \tag{7}$$

---

[3]A. E. Siegman, "Antenna Properties of Optical Heterodyne Receivers," Proc. IEEE, Vol. 54, pp 1350-1356, October 1966.

The FOV of the receiving aperture, Ω_R, can similarly be related to the source area, A_s, and the large range value, R, by

$$\Omega_R = \left(\frac{D_s}{R}\right)^2 \frac{\pi}{4} = \frac{A_s}{R^2} \tag{8}$$

In fact, this equation defines D_s. It remains to set the actual experiment such that this D_s is the true limiting value rather than some other experimental setting. The proper relationship was confirmed by the use of the iris shown in Figure 7-2. It could be set so as to reduce the energy reaching the receiver and it could be set such that the energy reaching the receiver was set by the relationship of Equation 8; that is, that the receiver FOV sets and defines D_s.

Now the receiver optics are diffraction-limited; therefore, the receiver solid angle FOV, Ω_R, may also be related to its area, A_R, by

$$\Omega_R = \frac{\lambda^2}{A_R} \tag{9}$$

Blackbody Radiating Area and FOV. From the above discussion the following relationships may be derived. Rearranging Equations 6 and 9 yields:

$$\Omega_s A_s = \lambda^2 \tag{10}$$

$$\Omega_R A_R = \lambda^2 \tag{11}$$

From Equations 7 and 8 (or Equations 6 and 11)

$$\Omega_s A_s = A_R \Omega_R \tag{12}$$

This is the convenient result being sought, replacing the somewhat uncertain values of Ω_s and A_s with known values of A_R and Ω_R through the relationship of the collimation and the boundary check provided by the iris.

From Equation 5, the power density into the receiver may now be given as:

$$W(f) = \left[\frac{A_R \Omega_R}{2\pi}\right]\left[\frac{2\pi}{\lambda^2} \cdot \frac{h\nu}{\exp(h\nu/kT - 1)}\right] \text{ W/Hz} \tag{13}$$

But from Equation 9 and Reference 3

$$A_R \Omega_R = \lambda^2 \tag{14}$$

therefore,

$$W(f) = \left[\frac{h\nu}{\exp(h\nu/kT - 1)}\right] \text{ W/Hz} \tag{15}$$

Receiver Bandwidth and Received Power. The receiver bandwidth, B, is set by the receiver IF amplifier. Since there is no predetection filtering, both the desired and image energies fall into this band. Therefore, a factor of 2B is used to determine received power from the power spectral density.

$$P_s = \left[\frac{2Bh\bar{\nu}}{\exp(h\nu/kT - 1)}\right] \text{ watts} \tag{16}$$

Measurement of Receiver NEP

Given the sensitivity of the optical heterodyne receiver in the radiometric mode and the signal power from a thermal source, it is possible to write an expression of receiver NEP as a function of measured $(SNR)_{IF}$, blackbody source temperature, and radiometric integration time. From the expression of $(SNR)_V$

$$(SNR)_V = \frac{1}{8\beta}(SNR)_{IF}^2 \cdot (B\tau) \tag{17}$$

$(SNR)_{IF}$ is substituted by using

$$(SNR)_{IF} = \frac{P_s}{NEP \cdot B} = \frac{2h\nu}{NEP \left\{ \exp(h\nu/kT_s) - 1 \right\}} \cdot \tag{18}$$

or from Equation 17

$$(SNR)_v = \frac{1}{8\beta} \frac{(2h\nu)^2}{(NEP)^2 \left\{ \exp(h\nu/kT_s) - 1 \right\}^2} \cdot (B\tau) \tag{19}$$

Solving for NEP,

$$NEP = \frac{h\nu}{\sqrt{2\beta}} \frac{1}{\left\{ \exp(h\nu/kT_s) - 1 \right\}} \left(\frac{B\tau}{(SNR)_v} \right)^{1/2} \tag{20}$$

The IF passband shape factor, β, is 1/2 for a single tuned circuit, $\sqrt{2}/2$ for a gaussian shaped circuit, and 1 for a rectangular passband.[4]   The five-pole Bessel filter used in the receiver subsystem is closest to a gaussian shape, and the above expression becomes

$$NEP = \frac{h\nu}{\sqrt[4]{2}} \frac{1}{\left\{ \exp(h\nu/kT_s) - 1 \right\}} \left(\frac{B\tau}{(SNR)_v} \right)^{1/2} \tag{21}$$

Figure 7-2 is a block diagram of the NEP measurement setup. The blackbody cavity source is placed near the focus of the bench collimator. An iris is placed precisely at the focus of the collimator. The source is regulated at a temperature T_s, and the chopper is located such that the output radiation is modulated at the chopping frequency, f_c. At the receiver, the output of the IF amplifier is filtered by its characteristic bandwidth B and shape factor β. The output of the amplifier is detected and drives the lock-in amplifier. The synchronously detected output or the ac output, can be monitored for signal-to-noise measurements. A true rms voltmeter is used to measure the ac output of the amplifier.

---

[4]Appendix B.

In the actual measurement, the following values were used:

		Trial 1	Trial 2	Trial 3
B = 100 MHz	τ =	0.036	0.071	0.143
β = $\sqrt{2}/2$	$(SNR)_v^{1/2}$ =	20	27.5	42.0
f_c = 89 Hz	NEP =	79 hν	82 hν	75 hν
T_s = 1000 °K				

From Equation 21

$$NEP = (1.46 \pm 0.06) \times 10^{-18} \text{ W-Hz}^{-1}$$

The factor of 79 times the quantum limit, hν, is in accordance with what is expected from the measuring conditions. Recalling that NEP = hν/η', and that η' = $\eta L_m L_o L_t$, the following typical values for each loss term are assigned:

$$\eta = 0.3$$

$$L_m = 0.5$$

$$L_o = 0.5$$

$$L_t = 0.2 \quad \text{(for a measured LO induced current of 0.2 mA)}$$

and calculated value of NEP is hν/η' = 67 hν.

7.3.2 Bit Error Rate Tests

All quantitative bit error rate (BER) measurements through the system shall be conducted at a data rate of 400 Mbps with NRZ coding, the specified data rate of the LDRL-10.6 program.

The modulator driver used for these tests shall be the ECL driver which was developed under the Transmitter Program, NAS5-20623. The low frequency rolloff characteristics of this driver make it necessary to use the short NRZ word for bit error rate tests.

Measurement Method

The method of measuring signal-to-noise (S/N) is illustrated in Figure 7-3. The signal plus noise power (S+N) and the noise power (N) is
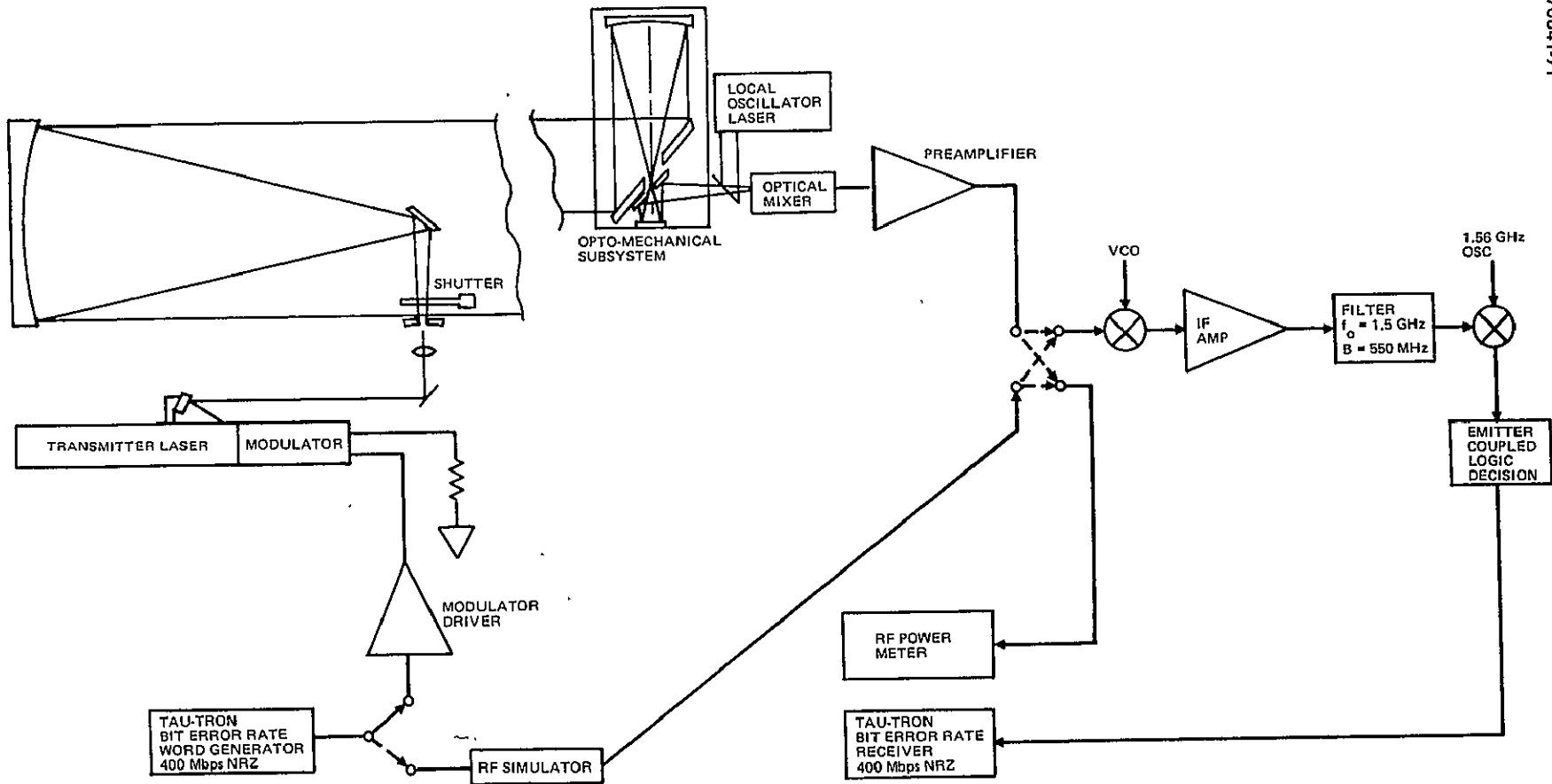
FIGURE 7-3. 400 MBPS BIT ERROR RATE MEASUREMENT TEST ARRANGEMENT FOR CO_2 LASER COMMUNICATIONS

measured with an RF power meter at the output of the preamplifier. The beam is completely blocked for the measurement of noise power. Thus, the measured ratio is:

$$\left(\frac{S + N}{N}\right)_P$$

and

$$\left(\frac{S}{N}\right)_{IF} = \left[\left(\frac{S + N}{N}\right)_P - 1\right] \frac{B_p}{B_{IF}}$$

where B_p is the noise bandwidth at the output of the preamplifier and B_{IF} is the bandwidth of the Bessel filter in the IF. For each measurement of $(S/N)_{IF}$ a corresponding measurement of BER shall be made and the points plotted. The resultant data are plotted to produce a BER curve.

Tests to be Performed

Bit error rate tests shall be made using various test configurations for the purpose of isolating the limiting components. Figure 7-4 illustrates five such configurations. Setups 1, 2, and 4 can be achieved using the short word from the data generator. Setups 3 and 5 may use a long word, provided the system is implemented with dc restoration.

7.3.3 Acquisition and Tracking Tests

Acquisition and tracking tests shall be conducted in the laboratory, first using direct detection for evaluating the servo system and later using heterodyne detection for evaluating the communication channel under dynamic tracking conditions. These tests shall be conducted with the receiver subsystem mounted on a precision rotary table. Optical performance shall be conducted as well as acquisition dynamics, error transfer characteristics, tracking tests with fine pointing only, and tracking tests with fine and coarse control.

Test Setup

A sketch of a typical test setup is shown in Figure 7-5. The opto-mechanical assembly is mounted to the top of a precision rotary table which is free to rotate within constraints about the vertical axis. The rotation angle about the vertical is continuously displayed to a resolution of 0.0001°. A signal proportional to the rate about the vertical axis is also available for recording. The other axis is adjustable by hand, but no readout is available.

70041-72

TEST
NUMBER

1

| NRZ-L GENERATOR | → | ATTENUATOR | → | NOISE SOURCE | → | NRZ-L RECEIVER |

2

| NRZ-L GENERATOR | → | MODULATOR DRIVER | → | ATTENUATOR | → | NOISE SOURCE | → | NRZ-L RECEIVER |

3

| NRZ-L GENERATOR | → | MODULATOR DRIVER | → | ATTENUATOR | → | NOISE SOURCE | → | DC RESTORATION | → | NRZ-L RECEIVER |

4

| NRZ-L GENERATOR | → | MODULATOR DRIVER | → | LASER TRANSMITTER | → | ATTENUATOR | → | HETERODYNE RECEIVER | → | NRZ-L RECEIVER |

5

| NRZ-L GENERATOR | → | MODULATOR DRIVER | → | LASER TRANSMITTER | → | ATTENUATOR | → | HETERODYNE RECEIVER | → | DC RESTORATION | → | NRZ-L RECEIVER |

FIGURE 7-4. PROGRESSIVE TEST CONFIGURATIONS BER TESTS
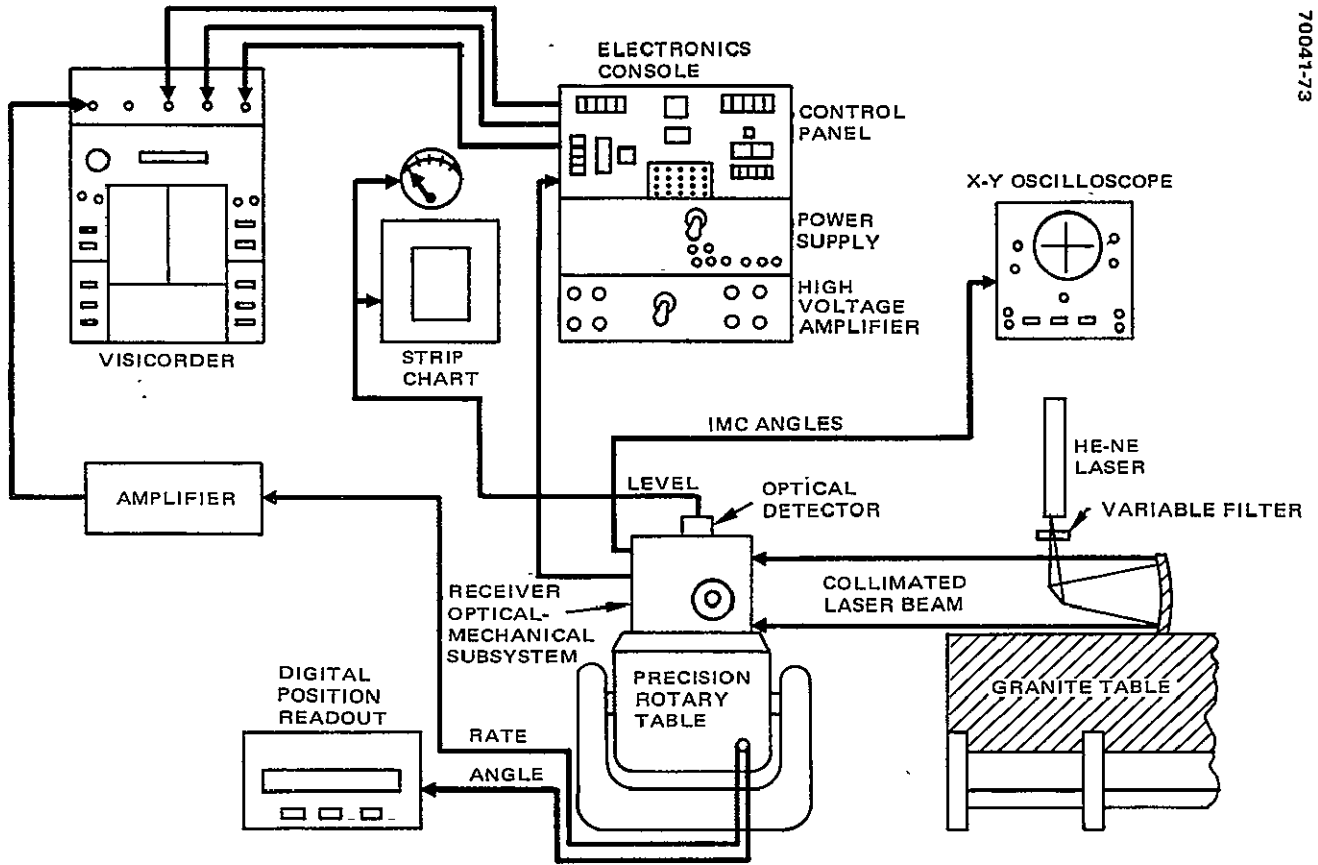
FIGURE 7-5. ANGULAR ACQUISITION AND TRACKING SETUP

During testing, the coherent 10.6 µm optical detector is replaced by a direct detection photosensor operating at 0.6328 µm. The photosensor is placed behind a pinhole located in the focal plane where the coherent sensor normally is placed. The pinhole produces a transfer curve similar to that produced by the coherent system.

Tracking Loop Measurements

1) Noise Equivalent Error — This test is a measure of the noise equivalent angle (NEA) of the tracking loop, when the input beam is not power limited. This quantity is determined by measuring the rms voltage at the output of the detector and relating this voltage through the proper scale factor to input beam jitter. For this test, the rotary table will be fixed.

2) Tracking Error With Target Motion — This procedure is the same as above except the table is moved by hand back and forth within the 0.2° by 0.2° IMC field of view at rates up to 0.03 deg/sec.

3) Tracking Error Caused by Stepper Disturbance — This procedure is the same as above except that the table is rotated to cause the stepper to be energized. The output of the detector is recorded. For this test the peak error is of interest.

4) Tracking Loop Bandwidth — This bandwidth is determined by injecting a constant amplitude sinusoid into the outer loop at the integrator output and measuring the relative amplitude and phase of the signal after transversing the loop and returning to the integrator output. As the frequency is increased the relative amplitude will decrease. The frequency at which the relative ratio = 0.707 is the bandwidth.

5) Acquisition Field of View — This is determined by moving the rotary table each side of zero with the gimbal loop disabled and determining when the PZT amplifier used to drive the IMC saturates.

6) Acquisition Dynamics — For this test the gimbal loop is disabled. The beam is placed in a known position just outside the 0.2° by 0.2° IMC field of view. With the tracking loop enabled, the rotary table is swept slowly through the IMC field of view. This is repeated for increasing rates up to 0.03 deg/sec.

7) IMC Bandwidth — Procedure is the same as for the tracking loop bandwidth except the generator signal is injected at the unused input to the IMC amplifier, and the output is recorded at the other input.

Gimbal Loop Measurements

1) <u>Gimbal Range</u> — The maximum gimbal range for each axis is determined by rotating the table slowly in each direction and noting when the electrical stops are actuated.

2) <u>Gimbal Step Rate</u> — The gimbal step rate is determined by measuring the time required to traverse a selected gimbal range, measured by the table readout.

3) <u>Gimbal Tracking</u> — The rotary table is moved by hand within the 20° by 20° field of view, while angle position, IMC drive voltage, and table rate are monitored.

4) <u>Gimbal Angle Readout Accuracy</u> — The point-to-point repeatability of the gimbal readout will be determined as follows: The tracking systems are disabled (manual mode). The rotary table is rotated to bring the beam within the detector field of view to give a peak detector response. The table is then rotated to a selected angle, and the gimbal is stepped manually until the response is again at a peak. The table angle and gimbal angle readouts are then recorded. This procedure is repeated for several points throughout the gimbal range.

5) <u>Gimbal/IMC Alignment</u> — This is determined as follows. First the gimbals are "zeroed" using the optical slip reference. Next the tilt gimbal will be manually rotated to 0.05°, while the system is tracking. The gimbal angle and IMC position (Burr-Brown output) for both axes will be recorded. If the X-axis IMC has an output other than zero, the roll gimbal is adjusted in steps, and the above test is repeated until the X-axis IMC shows a minimum dc offset. The required roll axis adjustment is recorded.

6) <u>Gimbal Axes Orthogonality</u> — With the roll axis adjusted as in item 5 above, the gimbals ±0.05° are stepped (in turn) and the IMC outputs for both axes are recorded.

7) <u>Gimbal Axis Cross-Coupling Dynamics</u> — With the system tracking, each gimbal is stepped in turn for short bursts and the filtered error signal for each axis is recorded.

7.3.4 Optical Measurements

Optical measurements shall be made to determine the quality of the optical system and of the individual elements. The 10 µm tests are conducted on the system to verify 10 µm element gain and loss. Visible light tests made with a HeNe laser are used initially to identify distorted elements in the system.
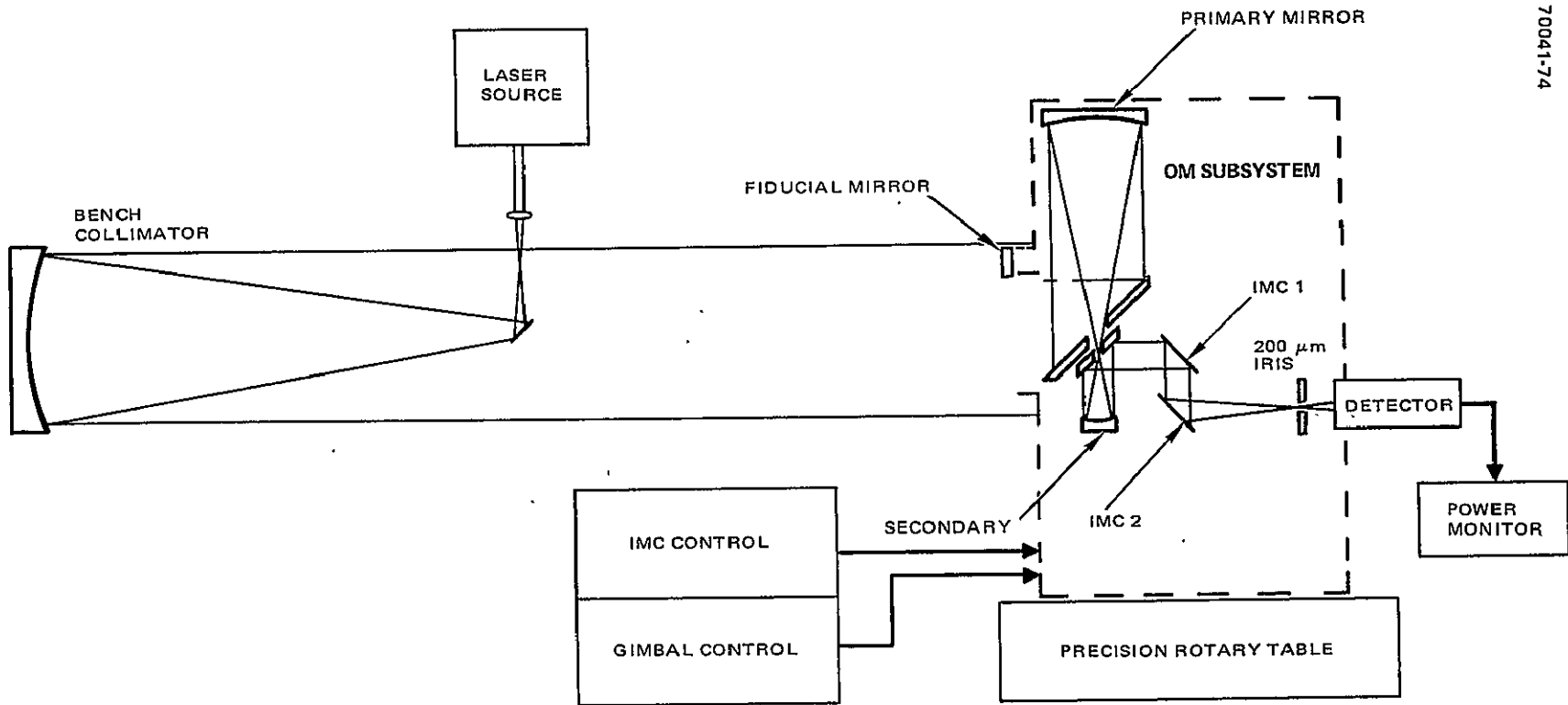
FIGURE 7-6. ELECTRO—OPTICAL TEST CONFIGURATION FOR RECEIVER (MOLNIYA ORBIT SATELLITE PACKAGE)

10 μm Tests

The test equipment necessary to perform the 10 μm optical tests are a 10 μm source, a collimator, a precision rotary table, and a power monitor. The test configuration is illustrated in Figure 7-6.

Gain Versus Field of View. This test uses a 10.6 μm laser signal monitored with a power meter at the 200 μm detector iris. The precision mount is rotated by 0.10°, and the correction is made with the IMCs to bring the signal back through the 200 μm iris. The power is again monitored and compared with the previous reading. These measurements are limited to ±0.10° by the built-in mechanical limit of the IMCs.

Fiducial Mirror Boresight. The purpose of the fiducial mirror is to provide an optical reference axis for the receiver subsystem. This test consists of initial boresight alignment of the fiducial mirror with the optomechanical subsystem in the centered or gimbal-lock position, scanning the gimbal through ±1.0° in each axis, and returning the gimbal to the center position. A comparison is then made between the fiducial mirror and the optomechanical subsystem axis. Tests show that the boresighting axis is maintained to less than 0.01°.

Loss Through System. The 10.6 μm loss through the optical system is measured by two independent methods. The first is accomplished by measuring the flux density of the collimated beam and computing the power entering the aperture and then comparing this power with that measured at the 200 μm iris. The second method is sending a 1 cm diameter collimated laser beam through the system and measuring the total power at the detector plane. The second method measures the optical surface loss of all the optical surfaces while the first method also takes into account the diffraction loss. The loss per surface is typically measured to be less than 2 percent, and the loss through the entire system is measured to be typically between 0.5 dB and 1.1 dB.

Ne-Ne Laser Tests

Measurements using a HeNe laser at 6328 A° provide an additional measure of the optical performance by observing a wavelength some 17 times shorter than the 10 μm wavelength for which the optical system was designed. Two techniques are especially useful. The first, observing the far field diffraction pattern of the entire system, is illustrated in Figure 7-7. The second, a double pass interferometer setup, is illustrated in Figure 7-8.

Far Field Diffraction Pattern

A portion of the HeNe collimated beam is focused by the receiver to plane of the detector. Projection optics are used to magnify the image and
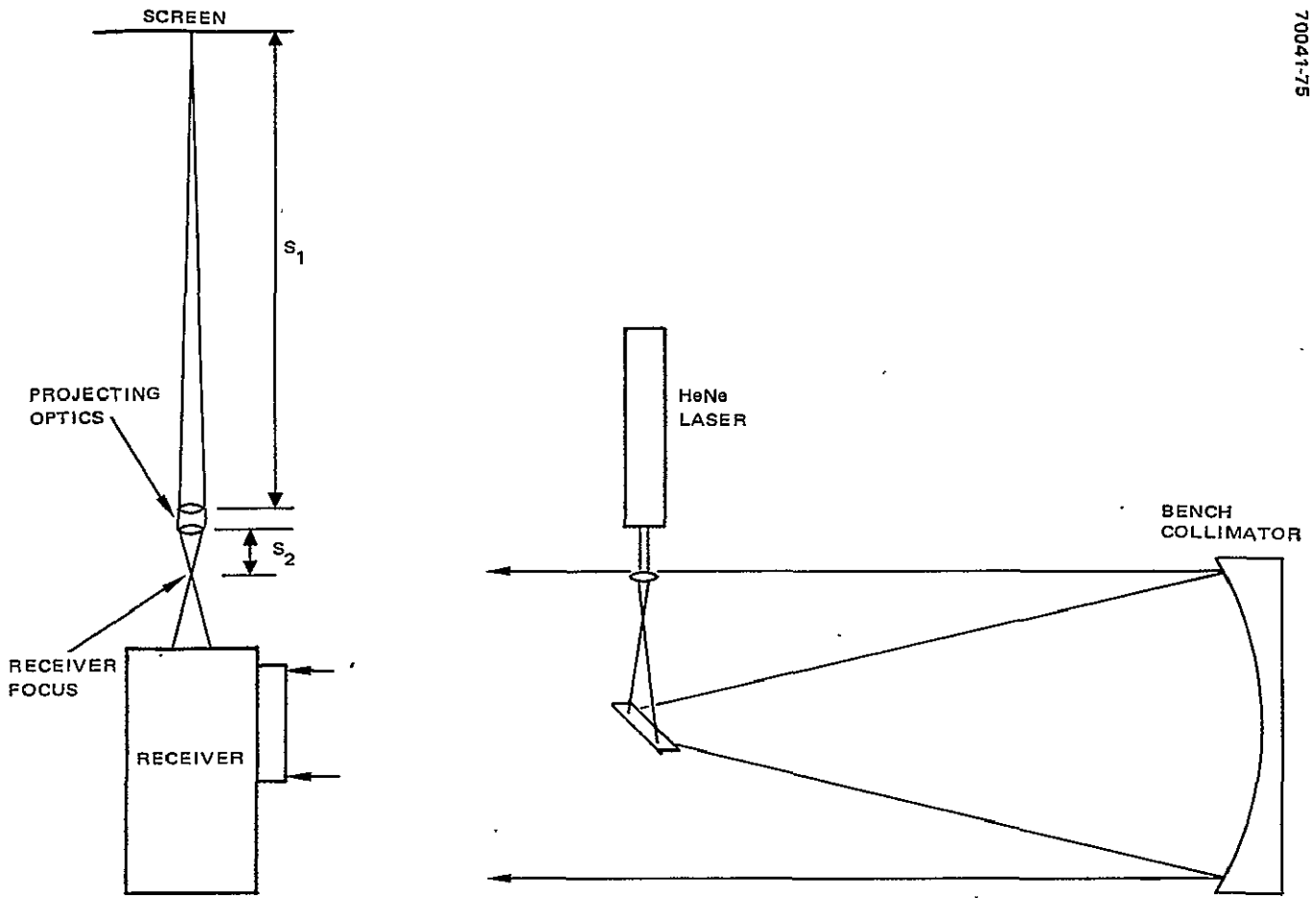
FIGURE 7-7. TEST ARRANGEMENT FOR FAR FIELD DIFFRACTION PATTERN OPTICS EVALUATION
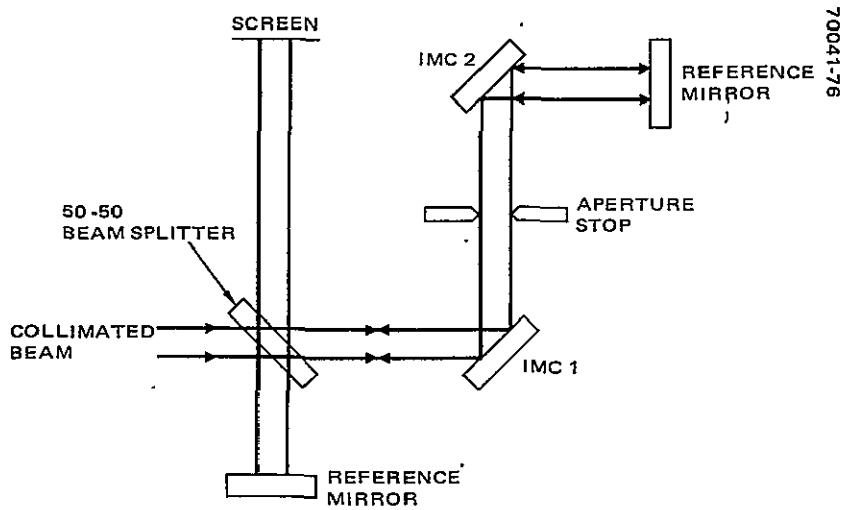
FIGURE 7-8. DOUBLE PASS INTERFEROMETER TEST SETUP

display it on a screen; the magnification of the projection optics is S_1/S_2 where S_1 and S_2 are the distances from the two focal planes to the principal planes of the projection optics. In practice, a 1 inch f/1 projection lens used at high magnifications (>50) so the magnification is approximately equal to S_1.

Double-Pass Interferometer

The double-pass interferometer produces a fringe pattern of the individual element. Acceptable fringe counts for an individual element are about 3, although fringes of spherical symmetry can be accepted up to 10 fringes.

7.4 TRANSMITTER (SHUTTLE) TERMINAL COMPONENTS AND SUBSYSTEMS

A simplified block diagram of an integrated transmitter terminal is shown in Figure 7-9. The diagram illustrates the functional relationships of the components and subsystems and the special test equipment. The following is a brief description of the principal components and subsystems which comprise the Shuttle transmitter terminal in the measurements configuration.

7.4.1 Optomechanical Subsystem

The optomechanical subsystem consists of an all-beryllium mechanical structure, optics, coarse pointing gimbal, and fine pointing assembly. The subsystem is designed to have a hemispherical range of coverage, compact size, and light weight. Further, the structure is an isothermal design capable of accommodating direct sunlight without distorting the optics or the structural frame.

7.4.2 Servo System

The servo electronics contains the acquisition and tracking circuits. The servo design accommodates a single detector for acquisition and tracking, using conical scanning. The servo system drives the coarse-pointing inner and outer gimbals and the fine pointing assembly. Because of the large field of view, the servo system must have the capability of resolving true target coordinates in order to apply the proper signals to coarse and fine pointing assemblies.

7.4.3 Transmitter Laser/Modulator

This subsystem consists of the transmitter laser and coupling modulator mounted integrally in the optomechanical back-end. Its function is to provide a wideband modulated optical signal power to the optical train for transmission.
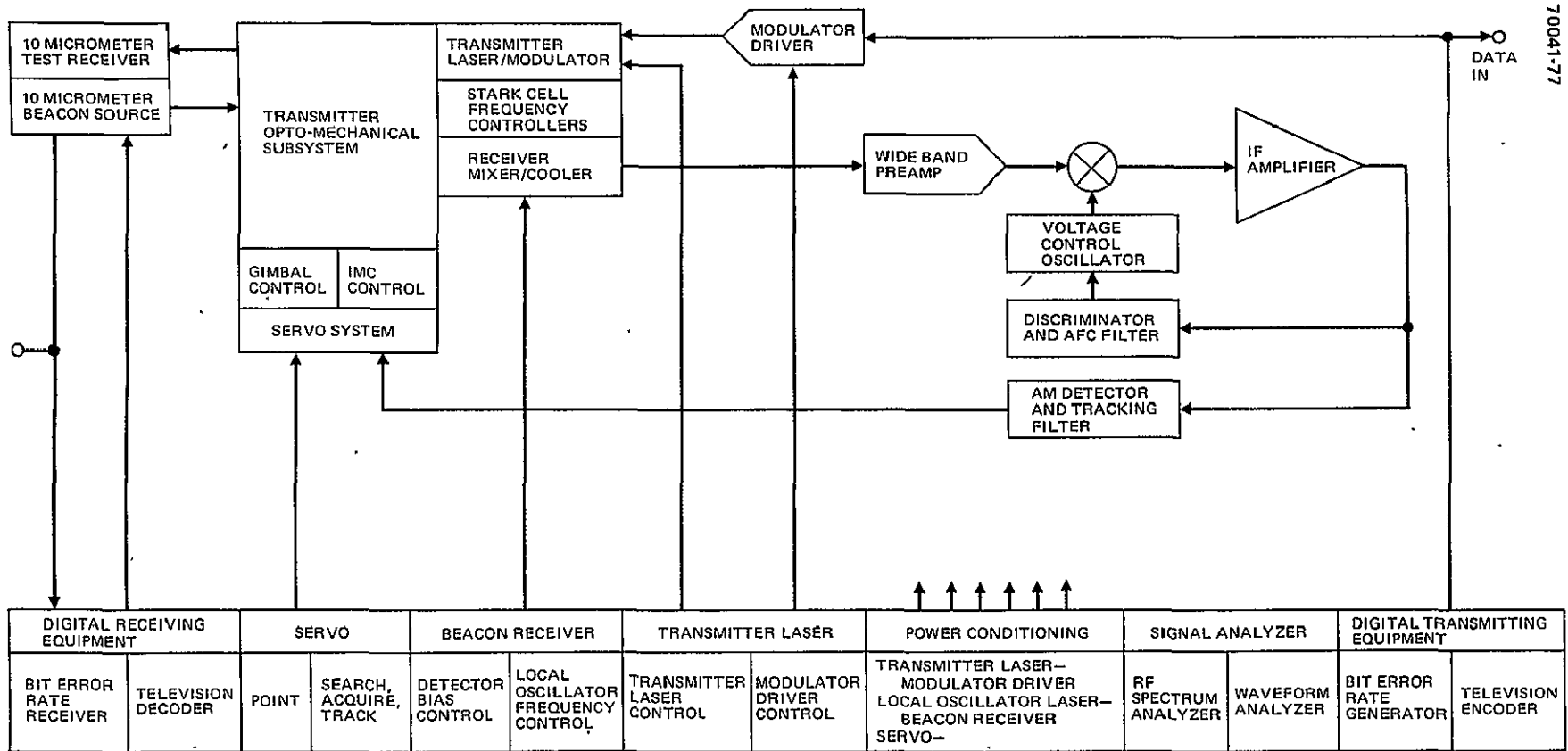
FIGURE 7-9. INTEGRATED TRANSMITTER BLOCK DIAGRAM

70041-77

7.4.4 Modulator Driver

The modulator driver is part of the laser transmitter subsystem. Its function is to amplify the level of the digital data signal from ECL level to 120 V_{p-p} for the laser modulator. Ideally, the modulator driver would be located next to the laser transmitter. The modulator driver will require a suitable spacecraft heat sink, since approximately half the transmitter subsystem power is dissipated in this driver.

7.4.5 Beacon Receiver Front End

The beacon receiver front-end consists of the mixer, cooler, and wideband preamplifier.

7.4.6 Beacon Receiver Back-End

The beacon receiver back-end consists of an electronically tunable tracking receiver capable of frequency tracking the beacon signal over a range of 200 to 900 MHz. Tracking error is provided by a discriminator tuned to the IF frequency. An AM detector and tracking filter is used to provide a suitable discriminate for the servo system.

7.4.7 Local Oscillator Laser

The local oscillator laser is integrally mounted in the optical opto-mechanical back-end and provides 1 mW of local oscillator power at the mixer detector.

7.4.8 Stark Cell Frequency Controllers

Both the transmitter laser and the local oscillator laser use Stark cells for frequency control. The local oscillator for the beacon signal will utilize the P-14 line of stabilization. The transmitter laser will utilize the P-20 line of stabilization.

7.4.9 Special Test Equipment

Special test equipment required for transmitter terminal test and evaluation will include:

1) 10 μm Beacon Laser

2) 10 μm Receiver Subsystem — This unit must have the capability of receiving 400 Mbps data from the transmitter. It must perform equivalently to the high altitude Molniya terminal receiver.

3) Digital Test Equipment — This equipment consists of a 400 Mbps NRZ word generator and a matched receiver for measuring BER.

4) Signal Analyzer — The signal analyzer must be capable of analyzing the RF spectrum of the modulator driver or that from the test receiver. A capability of observing the signal waveform must also be provided.

5) Console — A console shall be used to house all control and test equipment used for the transmitter test and evaluation.

6) Covered Cart — The transmitter optomechanical assembly shall be mounted on a movable cart with a suitable cover for protection from dust and moisture.

7) Collimator — A bench collimator shall be used for providing a collimated beacon and for collecting and measuring the output of the transmitter subsystem.

8) Rotary Table — A precision rotary table will be required for acquisition and tracking dynamical testing.

7.5 TRANSMITTER TERMINAL MEASUREMENTS

7.5.1 Transmitter Laser Tests

In a birefringent crystal aligned for amplitude modulation, the fraction C_m of the incident optical power rotated in polarization by 90° during a single pass is

$$C_m = \sin^2 (\Gamma/2)$$

In the equation, Γ is the phase shift experienced in a single pass through the modulator. In terms of the half-wave voltage V_π,

$$\Gamma = \pi \frac{V}{V_\pi} \quad \text{where} \quad V_\pi = 53,000 \cdot \frac{d}{\ell} \text{ for CdTe}$$

Here ℓ is the modulator length and d is the modulator height (width). Typically phase shifts of approximately 0.1 radian are encountered. Therefore, one writes $C_m \simeq \Gamma^2/4$. To determine the modulation properties of the crystal, let $\Gamma = \Gamma_m \sin \omega_m t$. The time average power is $C_m = (\Gamma_m^2/4) \sin^2 \omega_m t = \Gamma_m^2/8$. Now for an intracavity modulator, light experiences two passes through the rod, resulting in a phase shift twice the single pass value. Consequently, $C_m \simeq \Gamma_m^2/2$ for this arrangement.

For the intracavity modulator, the average output power is

$$P_1 \simeq \eta_g P_c \frac{\Gamma_m^2}{2} = \eta_g P_c \pi^2 \left(\frac{V_{rms}}{V_\pi}\right)^2$$

where η_g is the efficiency of the grating in coupling out the modulated light.

The prime power P_M required to drive the crystal is given by

$$P_M = \frac{V_m^2}{2R\,\eta_{md}} \, ,$$

where V_m is the peak voltage across the crystal, R is the impedance seen by the modulator driver, and η_{md} is the electrical efficiency of the modulator driver. Combining these equations yields

$$P_1 = \frac{\pi^2 \eta_g \eta_{md} R P_c P_M}{(V_\pi)^2}$$

In the measurement of transmitter laser performance, the most important parameter is the modulated sideband power out, P_1. Its measurement is straightforward. However, the factors which contribute to the power output should also be determined. From the above equation, these are circulating power (and associated laser prime power), modulator driver power, waveform, and associated modulator driver prime power.

Laser Circulating Power

Laser circulating power shall be measured by measuring the power transmitted through a high reflectivity mirror with known (calibrated) transmission characteristics. Typically, the high reflectivity mirror may be 99 percent reflective and 1 percent transmissive. The target circulating power for this design is the order of 50 watts, which will provide a sample of 0.5 watt through the reflective mirror (see Figure 8-10).

Modulated Output Power Versus Modulator Driving Voltage

This measurement is a test of the relation

$$P_1 = \eta_g P_c \left(\frac{V}{V_\pi}\right)^2 \pi^2$$

where V is the rms modulating voltage, P_c is the circulating power, η_g is the coupling coefficient, and V_π is the half-wave retardation voltage of the modulator. The measurement of circulating power and the modulated output power P_1 should be consistent. If they are not, then the performance of the modulator is not as it should be.

Modulator Bandwidth

Measurement of modulator bandwidth should be performed only after the modulator is integrated with the laser, since the bandwidth performance is critically dependent on the grating (or polarizer) coupling coefficient. The input to the modulator driver amplifier is a variable frequency source, preferably a sweep generator which sweeps from 1 MHz to 500 MHz. The sweep rate should be slow, corresponding to the response of the optical power meter. The modulated output power should be plotted against driving frequency for a fixed rms driving voltage (see Figure 7-10).

Output Beam Radiation Pattern

The radiation pattern of the output beam should be measured and recorded. A suitable method of observing the pattern is using a UV fluorescent target. However, a suitable method for recording this pattern has not yet been developed.

Modulator Temperature Stabilization

The modulator temperature is regulated using a proportional controller. The temperature is sensed using a thermocouple which is embedded in the beryllium oxide modulator structure, very close to the modulator rod. Measurement of the modulator temperature control characteristics and temperature stability can be achieved by recording the millivolt output of the thermocouple on a chart recorder as a function of time.

Laser Stabilization

Stark cell frequency stabilization of the transmitter laser produces a discriminant which is a precise linear function of the laser frequency. The discriminant has a time constant depending on the dither frequency of the Stark cell, and can be as short as 1 ms. Thus, the instantaneous laser frequency can be monitored to measure its relative stability. In addition to the laser frequency history, the discriminant time constant and the overall loop gain and time constant should be recorded.

The laser frequency stabilization is a strong function of the ambient acoustical and vibrational environment. It is thus advisable to record the ambient acoustical noise levels, and to isolate the transmitter and local oscillator lasers as much as possible to avoid extraneous vibrational coupling.

7.5.2 Modulator Driver Tests

Modulator Driver Output Voltage

The rms output voltage of the modulator driver shall be measured while operating into its characteristic load impedance. The signal source for these tests shall be a pseudorandom word generator operating at bit rates of 50, 100, 200, and 400 Mbps. The rms output voltage is expected to drop to approximately 0.7 as the data rate is increased from 50 to 400 Mbps. This effect is due to the change of basic waveform from a near rectangular waveform to a near sinusoidal waveform.

Modulator Driver Output Waveform

The waveform of the modulator driver shall be photographed for digital data rates of 50, 100, 200, and 400 Mbps at full output voltage. Eye patterns shall also be taken. The voltage and time scales shall be accurately calibrated.

Input Power and Driver Efficiency

The input voltages and currents shall be monitored and recorded for each of the tests above. The efficiency of the modulator driver shall be computed for each data rate from

$$\text{Driver Efficiency, } \% = \frac{(V_{rms})^2}{Z_o} \cdot \frac{1}{(\text{Total input power})} \cdot 100.$$

7.5.3 Acquisition and Tracking Tests

Acquisition and tracking tests shall be conducted in the laboratory, first using direct detection to evaluate the servo system and then using heterodyne detection to evaluate the beacon channel and the servo system. These tests shall be conducted with the optomechanical subsystem mounted on a precision rotary table. Optical performance as well as acquisition dynamics, error transfer characteristics, and tracking tests shall be conducted.

Test Setup

A typical acquisition and tracking test setup is shown in Figure 7-11. The optomechanical assembly is mounted to the top of a precision rotary table which is free to rotate within constraints about the vertical axis. The rotation angle about the vertical axis is displayed to an accuracy of 0.0001° (1.75 μrad). A signal proportional to the rate of rotation is also available for recording. The other axis is adjustable by hand, but no readout is necessary.
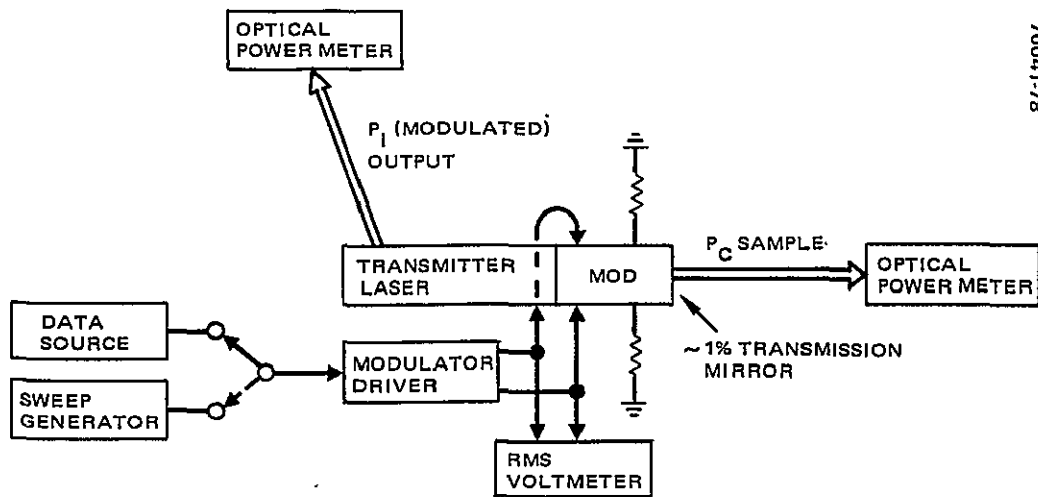
FIGURE 7-10. TEST SETUP FOR MEASURING CIRCULATING POWER, MODULATED POWER OUTPUT, AND TRANSMITTER BANDWIDTH
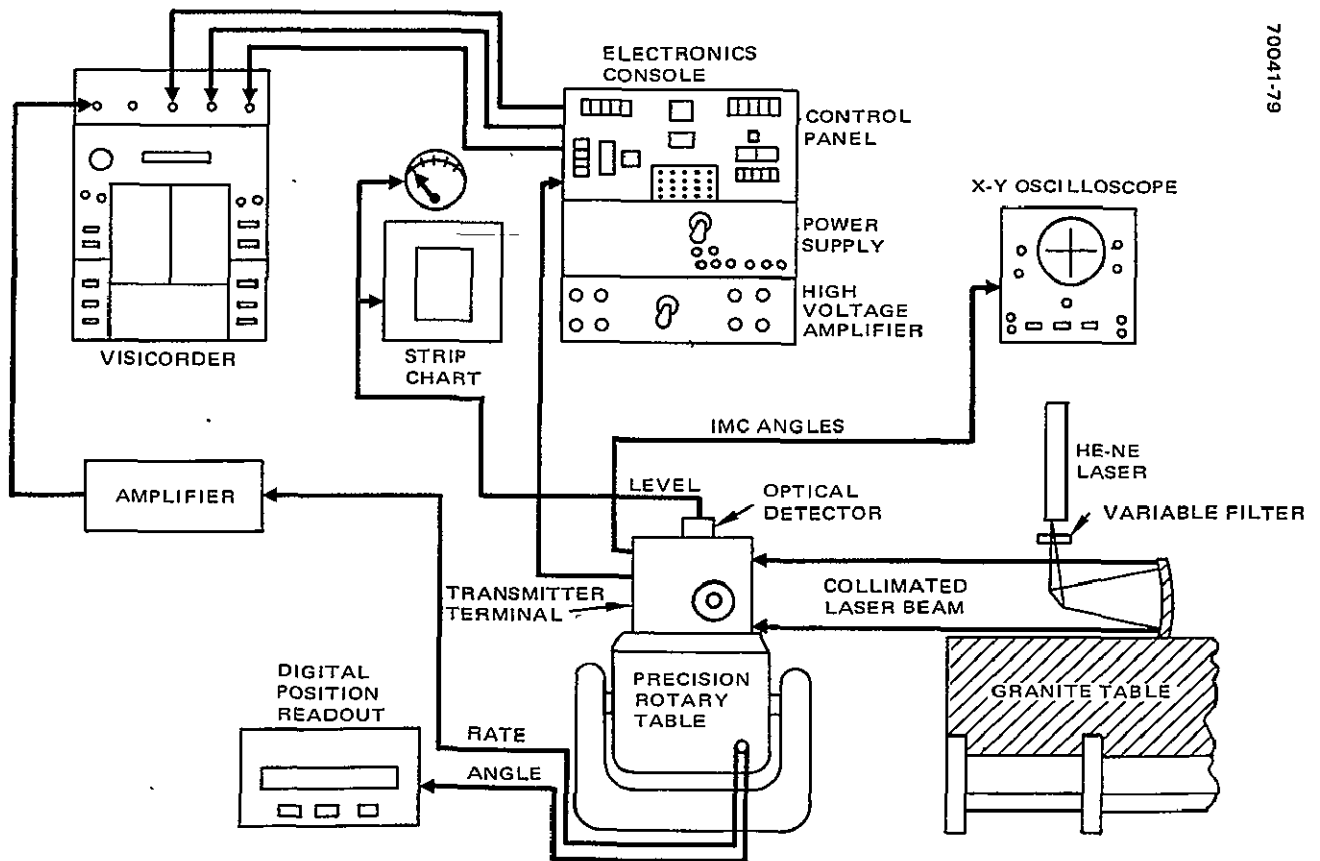
FIGURE 7-11. TRANSMITTER (SHUTTLE) TERMINAL SERVO TEST SETUP

For preliminary tests, the coherent 10 μm detector may be replaced with a silicon photodiode sensitive to 6328 Å light. The photosensor must be placed behind a pinhole in the focal surface, the pinhole matching the 10 μm diffraction limit. Under these conditions, the transfer characteristic of the visible light beam is similar to that obtained with a coherent 10 μm beam and receiver.

Tracking Loop Measurements

The following subsections delineate the parameters to be measured in the servo tests and briefly describe how the measurements are made.

1) Noise Equivalent Error — This test is a measure of the noise equivalent angle (NEA) of the tracking loop, when the input beam is not power limited. This quantity is determined by measuring the rms voltage at the output of the detector and relating this voltage through the proper scale factor to input beam jitter. For this test, the rotary table will be fixed.

2) Tracking Error With Target Motion — This procedure is the same as above except the table is moved by hand back and forth within the 1.0° by 1.0° IMC field of view at rates up to 0.8 deg/sec.

3) Tracking Error Caused by Gimbal Noise — This procedure is the same as above except that the table is rotated to cause the coarse gimbal to be energized. The output of the detector is recorded. For this test the peak error is of interest.

4) Tracking Loop Bandwidth — This bandwidth is determined by injecting a constant amplitude sinusoid into the outer loop at the integrator output and measuring the relative amplitude and phase of the signal after transversing the loop and returning to the integrator output. As the frequency is increased the relative amplitude will decrease. The frequency at which the relative ratio = 0.707 defines the bandwidth of the loop.

5) Acquisition Field of View — Determined by moving the rotary table about zero with the gimbal loop disabled and determining when the IMC driver saturates.

6) Acquisition Dynamics — For this test the gimbal loop is disabled. The beam is placed in a known position just outside the IMC field of view. With the tracking loop enabled, the rotary is swept slowly through the IMC field of view. This is repeated for increasing rates up to 0.8 deg/sec.

7) IMC Bandwidth — Procedure is the same as for the tracking loop bandwidth except the generator signal is injected at the unused input to the IMC amplifier and the output is recorded at the other input.

Gimbal Loop

1) Gimbal Range — The maximum gimbal range for each axis is determined by rotating the table slowly in each direction and noting when the electrical stops are actuated.

2) Gimbal Step Rate — The gimbal rate is determined by measuring the time required to traverse a selected gimbal range, which is measured by the table readout.

3) Gimbal Tracking — The table is driven at a steady rate for each axis over the field of view, while angle position, IMC drive voltage, and table rate are monitored.

4) Gimbal Angle Readout Accuracy — The point-to-point repeatability of the gimbal readout will be determined as follows: The tracking systems are disabled (manual mode). The rotary table is rotated to bring the beam within the detector field of view to give a peak detector response. The table is then rotated to a selected angle, and the gimbal is driven in steps until the response is again at a peak. The table angle and gimbal angle readouts are then recorded. This procedure is repeated for several points throughout the gimbal range.

5) Gimbal/IMC Axes Orthogonality — Determined as follows: First the gimbals are "zeroed". Next, one gimbal will be manually rotated 1° while the system is tracking. The gimbal angle and IMC position for both axes will be recorded. If the orthogonal axis IMC has an output other than zero, nonorthogonality of axes is indicated and realignment of the IMCs is required.

6) Gimbal Axis Cross-Coupling Dynamics — With the system tracking, each gimbal is driven for short bursts and the filtered error signal for each axis is recorded.

7.5.4 Optical Measurements

The optomechanical subsystem for the transmitter terminal is an afocal system. Measurements shall be made to determine the quality of the optical system and of the individual elements. The 10 μm tests are conducted on the system for the purpose of verifying beacon antenna pattern and transmitter illumination efficiency. Helium neon (6328 Å) laser tests may be used to confirm system optical quality. However, these are mainly useful for analyzing the figure of the individual optical elements. Collimation of the system may be determined with an autocollimator.

10 μm Tests

The test equipment necessary to perform the 10 μm beacon optical tests are a 10 μm beacon source, a bench collimator, a precision rotary table, and a power meter. To perform the 10 μm transmitter throughput, a

7-30

transmitter subsystem with the specified beam pattern must be used. This unit may be a complete transmitter subsystem or a CW laser which has the correct radiation pattern. The test configuration is illustrated in Figure 7-12.

Gain Versus Field of View. This test uses the 10 μm source in the bench collimator and the power meter in the optomechanical structure under test. The conditioning optics in the system focus the 10 μm energy through a pinhole which will match the diffraction limit of the system. When the energy is maximized through the pinhole, 84 percent will be transmitted for a perfect system. The precision mount is driven through alignment and the power transmitted is measured. This measurement is made for the IMCs on-axis and at their maximum deflection to verify that the antenna gain is uniform over the entire IMC or fine pointing field of view.

10 μm Loss Through System — Receive Mode. The optical flux density is measured at the aperture of the system, and the amount of power entering the aperture is computed. The amount reaching the detector is measured. This is a measure of optical loss (including obscuration) through the entire optical system in the receive mode with uniform illumination.

10 μm Loss Through System — Transmit Mode. The test transmitter with a known optical power illuminates the system through the proper conditioning optics. The power reaching the power monitor of the bench collimator is measured and the net throughput is determined.

Helium-Neon Laser Tests. Measurements using a helium neon laser at 6328 Å provide an additional measure of the optical performance by observing a wavelength some 17 times shorter than the 10 μm wavelength for which the optical system was designed. Two techniques are especially useful, the first is by observing the far field diffraction pattern of the entire system. The second is with a double pass interferometer to obtain an actual fringe pattern of the individual optical elements.
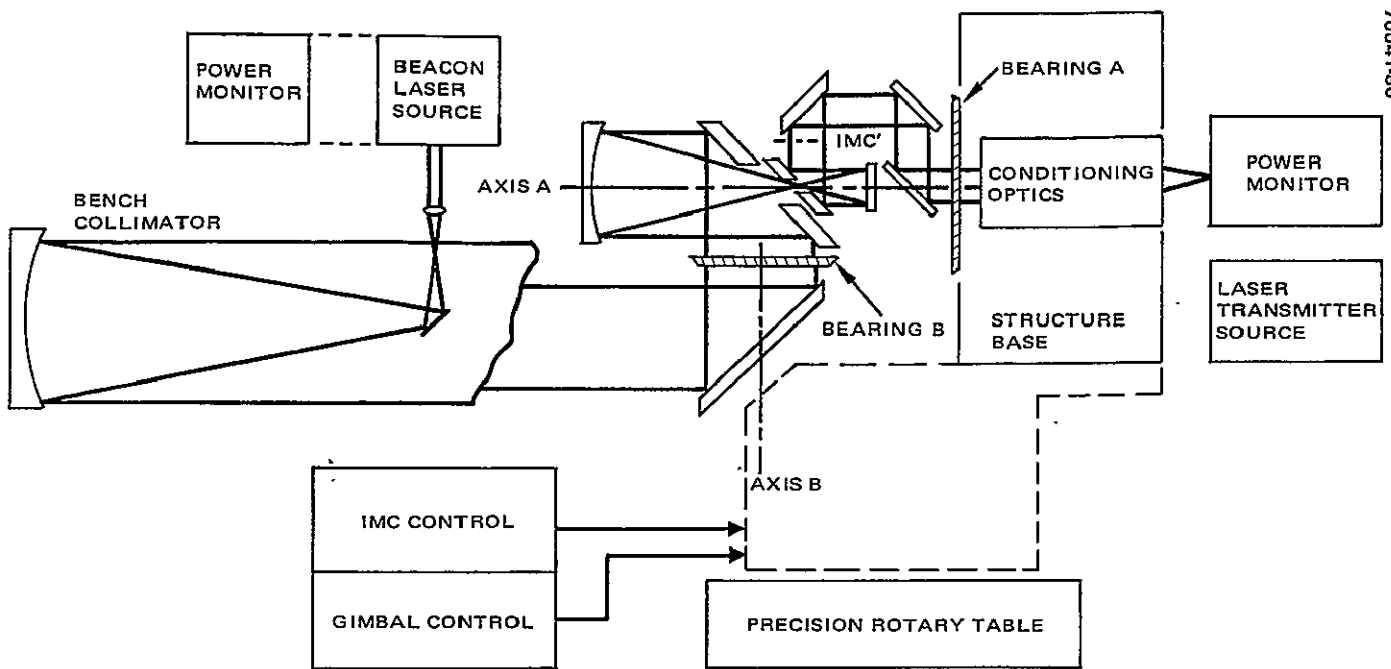
FIGURE 7-12. ELECTRO-OPTICAL TEST CONFIGURATION FOR
TRANSMITTER (SHUTTLE) PACKAGE

8. WORK BREAKDOWN STRUCTURE

The Work Breakdown Structure (WBS) covers all aspects of the development of the experimental hardware and the performance of the experiment. It is divided into the categories of program management, documentation, system engineering, design and development, fabrication, assembly and test, ground support, and reliability and quality assurance. The WBS reflects the effort required for a thermal structural model, an engineering model, a prototype, a flight model, and flight spares. In ground support the effort required at the spacecraft contractor's site, ground station, and the effort required for data acquisition and reduction is included. Within each element of the WBS, man-hour and skill level requirements are listed (See Section 9.)

For the Shuttle-to-ground experiment, the Shuttle terminal is assumed to have full flight quality hardware just as required for a normal 1 'to 2 year satellite experiment. The elliptical orbit satellite is also required to have full flight quality hardware.

The full WBS is illustrated in Figure 8-1. The level 1 designator is for the terminal. Level 2 defines the work categories, while levels 3 and 4 break down the effort into subcategories and subsystems. Level 5, the component level, is not given here.

LEVEL 1

TERMINAL
DESIGNATION
S-SHUTTLE, M-MOLNIYA

LEVEL 2

| A MANAGEMENT | B DOCUMENTATION | C SYSTEMS ENGINEERING | D DESIGN DEVELOPMENT | E FABRICATION/ ASSEMBLY AND TEST | F QUALIFICATION- ACCEPTANCE TESTS | G GROUND SUPPORT | J QUALITY ASSURANCE |

LEVEL 3

A (MANAGEMENT)
- A PROGRAM OFFICE
- B SUPPORTING LABORATORIES

D (DESIGN DEVELOPMENT)
- A DEVELOPMENT
- B DESIGN

E (FABRICATION/ASSEMBLY AND TEST)
- A ENGINEERING MODEL
- B THERMAL/ STRUCTURAL MODEL
- C PROTOTYPE MODEL
- D FLIGHT MODEL
- E SPARES

F (QUALIFICATION-ACCEPTANCE TESTS)
- A ENGINEERING MODEL
- B THERMAL/ STRUCTURAL MODEL
- C PROTOTYPE MODEL
- D FLIGHT MODEL
- E SPARES

G (GROUND SUPPORT)
- A DESIGN
- B FABRICATION/ ASSEMBLY/TEST
- C CALIBRATE
- D REFURBISH

J (QUALITY ASSURANCE)
- A PERFORMANCE ASSURANCE
- B INSPECTION

LEVEL 4 SUBSYSTEMS

E
- A TRANSMITTER
- B RECEIVER
- C OPTO- MECHANICAL
- D DETECTOR- COOLER
- E SYSTEM- INTEGRATION AND TEST
- F T&C INTERFACE

F
- A TRANSMITTER
- B RECEIVER
- C OPTO- MECHANICAL
- D DETECTOR- COOLER
- E SYSTEM INTEGRATION AND TEST
- F T&C INTERFACE

G
- A TRANSMITTER
- B RECEIVER
- C OPTO-MECHANICAL
- D BENCH TEST EQUIPMENT
- E GROUND TEST EQUIPMENT
- F LAUNCH SUPPORT EQUIPMENT
- G DATA REDUCTION AND ANALYSIS

LEVEL 5 COMPONENTS

FIGURE 8-1. WORK BREAKDOWN STRUCTURE

9. MAN-HOUR ESTIMATES

9.1 FLIGHT QUALITY HARDWARE PROGRAM

Table 9-1 gives the man-hour estimates for the development of a Shuttle terminal and ground support for a Shuttle Sortie to ground laser communication experiment. The listing conforms with the WBS defined in Section 8 of this document. The equipment and services included in this estimate are:

Terminal Description

- 400 Mbps transmitter subsystem, 1 W, 10 μm

- Beacon receiver subsystem, heterodyne, 10 μm

- 180° FOV optomechanical subsystem, 18 cm aperture

Design/Development

- Laser life tests and transmitter subsystem development

- Modulator material development

- Detector development

- J-T cryostat integration

- Servo system design

Models

- Engineering model

- Thermal structural model

- Prototype model

- Flight model

- Spares (for flight hardware)

TABLE 9-1. MAN-HOUR ESTIMATES FOR SHUTTLE SORTIE CO_2 LASER TRANSMITTING TERMINAL, FLIGHT QUALITY HARDWARE PROGRAM

	SMTS	MTS	TE	GE	Shop	Total
Grand Total	68,737	100,326	124,787	41,528	30,763	366,141
Management	12,168		28,392			40,560
Program office	6,084		14,196			20,280
Supporting laboratories	6,084		14,196			20,280
Documentation			20,280			20,280
Program office			14,040			14,040
Supporting laboratories			6,240			6,240
Systems Engineering	10,140	8,112	2,028			20,280
Design and Development	17,129	30,000	30,000	8,517		85,646
Development	6,116	10,718	10,718	3,026		30,578
Transmitter	2,652	4,649	4,649	1,310		13,260
Receiver	1,030	1,810	1,810	499		5,149
Optomechanical						0
Detector cooler	312	546	546	156		1,560
System integration and test	1,810	3,167	3,167	905		9,049
T&C interface	312	546	546	156		1,560
Design	11,013	19,282	19,282	5,491		55,068
Transmitter	1,435	2,512	2,512	718		7,177
Receiver	1,248	2,184	2,184	624		6,240
Optomechanical	5,772	10,109	10,109	2,870		28,860
Detector cooler						0
System integration and test	2,246	3,931	3,931	1,123		11,231
T&C interface	312	546	546	156		1,560
Fabrication, Assembly, and Test	14,135	42,401	28,267	28,267	28,267	141,337
Engineering model	4,695	14,086	9,392	9,392	9,392	46,957
Transmitter	686	2,059	1,373	1,373	1,373	6,864
Receiver	749	2,246	1,498	1,498	1,498	7,489
Optomechanical	2,028	6,084	4,056	4,056	4,056	20,280
Detector cooler	125	374	250	250	250	1,249
System integration and test	1,076	3,229	2,153	2,153	2,153	10,764
T&C interface	31	94	62	62	62	311
Thermal/structural	328	983	655	655	655	3,276
Transmitter	78	234	156	156	156	780
Receiver	78	234	156	156	156	780
Optomechanical	156	468	312	312	312	1,560
Detector cooler	16	47	31	31	31	156
System integration and test						0
T&C interface						0

9-2

Table 9-1 (continued)

	SMTS	MTS	TE	GE	Shop	Total
Prototype	3,167	9,500	6,334	6,334	6,334	31,669
Transmitter	390	1,170	780	780	780	3,900
Receiver	530	1,591	1,061	1,061	1,061	5,304
Optomechanical	1,248	3,744	2,496	2,496	2,496	12,480
Detector cooler	94	281	187	187	187	936
System integration and test	827	2,480	1,654	1,654	1,654	8,269
T&C interface	78	234	156	156	156	780
Flight	3,058	9,174	6,114	6,114	6,114	30,574
Transmitter	406	1,217	811	811	811	4,056
Receiver	499	1,498	998	998	998	4,991
Optomechanical	1,170	3,510	2,340	2,340	2,340	11,700
Detector cooler	94	281	187	187	187	936
System integration and test	811	2,434	1,622	1,622	1,622	8,111
.T&C interface	78	234	156	156	156	780
Spares	2,887	8,658	5,772	5,772	5,772	28,861
Transmitter	359	1,076	718	718	718	3,589
Receiver	484	1,451	967	967	967	4,836
Optomechanical	1,170	3,510	2,340	2,340	.2,340	11,700
Detector cooler	94	281	187	187	187	936
System integration and test	702	2,106	1,404	1,404	1,404	7,020
T&C interface	78	234	156	156	156	780
Qualification Acceptance Test	11,232	11,232	5,616			28;080
Engineering model	2,808	2,808	1,404			7,020
Thermal/structural ____						0
Prototype	2,808	2,808	1,404			7,020
Flight	2,808	2,808	1,404			7,020
Spares	2,808	2,808	1,404			7,020
Ground Support	3,933	7,770	7,770	3,933	2,496	25,902
Design	1,513	3,042	3,042	1,561	984	10,142
Transmitter	62	140	140	78	47	467
Receiver	62	140	.140	78	47	467
Optomechanical	62	140	140	78	47	467
Bench test equipment	515	1,030	1,030	515	343	3,433
Ground test equipment	406	796	796	406	250	2,654
Launch support equipment	406	796	796	406	250	2,654
Data reduction and analysis						· 0
Fabrication/assembly/test	1,951	3,838	3,838	1,951	1,216	12,794
Transmitter	593	1,170	1,170	593	374	3,900
Receiver	562	1,123	1,123	562	. 374	3,744
Optomechanical	94	187	187	94	62	624

Table 9-1 (continued)

	SMTS	MTS	TE	GE	Shop	Total
Bench test equipment	172	328	328	172	94	1,094
Ground test equipment	265	515	515	265	156	1,716
Launch support equipment	265	515	515	265	156	1,716
Data reduction and analysis						0
Calibrate	469	890	890	421	296	2,966
Transmitter	47	94	94	47	31	313
Receiver	47	94	94	47	31	313
Optomechanical	47	94	94	47	31	313
Bench test equipment	78	140	140	62	47	467
Ground test equipment	125	234	234	109	78	780
Launch support equipment	125	234	234	109	78	780
Data reduction and analysis						0
Refurbish						0
Transmitter						
Receiver						
Optomechanical						
Bench test equipment						
Ground test equipment						
Launch support equipment						
Data reduction and analysis						
Quality Assurance		811	2,434	811		4,056
Performance assurance						
Inspection						

- Transmitter 10 μm beacon subsystem for ground station

- Receiver subsystem for ground station

- Ground support equipment

The equipment on the Shuttle consists of an optomechanical package of the same size and general design as that developed under NAS5-20018, LDRL-10.6 program. The transmitter subsystem is a high data rate 10 μm system. A 10 μm heterodyne beacon receiver subsystem is included, the detector being cooled with J-T cryostat, since a radiation cooler cannot be used for earth-viewing experiments.

Ground support equipment includes a 10 μm beacon transmitter subsystem and a 10 μm heterodyne receiver capable of receiving high data rate digital data. It also includes special test equipment for ground station and launch support.

9.2 FLYABLE ENGINEERING MODEL PROGRAM

Because of the relatively short duration of the Shuttle flights (7 days), the vehicle can serve as a space environment test bed for experimental equipment. Equipment of engineering model quality can be flight tested without great risk; if an equipment failure occurs, it can be repaired and flown on the next Shuttle flight. For these reasons, it is of interest to tabulate the elements of the WBS which apply to such a simplified program. An important disclaimer must be made, however: successful demonstration of engineering model hardware on Shuttle does not make it space qualified. Without traceability and configuration management, such a test has limited value.

Table 9-2 gives the man-hour estimates for the development of a Shuttle terminal and ground support for a Shuttle to ground laser communication experiment. The listing conforms with the WBS defined in Section 8 of this document. The equipment and services included in the estimate are:

Terminal Description

- 300 Mbps transmitter subsystem, 0.3 W, 10 μm

- Silicon quad tracker for beacon receiver

- 180° FOV optomechanical subsystem, 18 cm aperture

Models

- Flyable engineering model — no prototype model

- Minimal documentation and quality control — no laser life test program

9-5

- Quad beacon tracker on shuttle hardware (Argon ground beacon)

- Configuration management (drawings) under REA (responsible engineering authority) control

- Ground support: argon laser beacon, refurbished receiver subsystem ground support equipment

The equipment on the Shuttle consists of the optomechanical package developed under NAS 5-20018, modified for unit qualification tests. The transmitter subsystem is an upgraded transmitter laser subsystem from NAS5-20623. Ground support equipment includes an argon laser beacon, the receiver subsystem from NAS5-21859, and the special test equipment for ground station and launch support.

TABLE 9-2. MAN-HOUR ESTIMATES FOR SHUTTLE SORTIE CO_2 LASER TRANSMITTING
TERMINAL, FLYABLE ENGINEERING MODEL PROGRAM

	SMTS	MTS	TE	GE	Shop	Total
Grand Total	19,891	31,107	42,263	·13,978	8,518	115,757
Management	3,370		· 7,862	·		11,232
Program office	1,685		3,931			5,616
Supporting laboratories	1,685		3,931			5,616
Documentation			5,616			5,616
Program office			3,744			3,744
Supporting laboratories			1,872			1,872
Systems Engineering	2,808	2,246	562			· 5,616
Design and Development	4,836	8,471	8,471	2,402		24,180
Development	2,652	4,649	4,649	1,310	·	13,260 ،
Transmitter	2,028	3,557	3,557	998 ·		10,140
Receiver						0
·Optomechanical						0
Detector cooler	. 312	546	546	156	·	1,560
System integration and test	312	546	546	156		1,560
T&C interface			·		·	0
Design	2,184	3,822	3,822	1,092		10,920
Transmitter						0
Receiver		·				0
Optomechanical	1,404	2,465	2,465	686		7,020
Detector cooler	624	· 1,092	1,092	312		3,120
System integration and test						0
T&C interface _____	156	265	· 265	94		780
Fabrication, Assembly, and Test	3,572	10,717	7,145	7,145	7,145	35,724
Engineering model ·	3,572	10,717	7,145	7,145	7,145	35,724
Transmitter	780	2,340	1,560	1,560	1,560	7,800
Receiver	749	2,246	1,498	1,498	1,498	7,489
Optomechanical	· 780	2,340	1,560	1,560	1,560	7,800 ·
Detector cooler	156	468	312	312	312	1,560
System integration and test	1,076	3,229	2,153	2,153	2,153	10,764
T&C interface	31	94	62	62	62	311
Thermal/structural						0
Transmitter						
Receiver						
Optomechanical	،					·
Detector cooler						
System integration and test				·		
T&C interface						

9-7

Table 9-2 (continued)

	SMTS	MTS	TE	GE ·	Shop	Total
Prototype						0
Transmitter						
. Receiver						
Optomechanical						
Detector cooler						
System integration and test						
T&C interface						
Flight						0
Transmitter						
Receiver						
Optomechanical						
Detector cooler						
System integration and test						
·T&C interface						
Spares						0
Transmitter						
Receiver						
Optomechanical						
Detector cooler						
System integration and test						
T&C interface						
Qualification Acceptance Test	3,120	3,120	1,560			7,800
Engineering model	3,120	3,120	1,560			7,800
Thermal/structural						0
Prototype						0
Flight						0
Spares						0
Ground Support	2,185	4,307	4,307	2,185	1,373	14,357
Design	1,374	2,716	2,716	1,374	874	9,054
Transmitter						0
Receiver	47	94	· 94	47	31	313
Optomechanical						0
Bench test equipment	515	1,030	1,030	515	343	3,433
Ground test equipment	406	796	796	406	250	2,654
Launch support equipment	406	796	796	406	250	. 2,654
Data reduction and analysis						0
Fabrication/assembly/test	811	1,591	1,591	811	499	5,303
Transmitter						0
Receiver	94	187	187	94	62	624
Optomechanical						0

Table 9-2 (continued)

	SMTS	MTS	TE	GE	Shop	Total	(3 of 3)
Bench test equipment	187	374	374	187	125	1,247	
Ground test equipment	265	515	515	265	156	1,716	
Launch support equipment	265	515	. 515	265	156	1,716	
Data reduction and analysis						0	
Calibrate						0	
Transmitter							
Receiver							
Optomechanical							
Bench test equipment							
Ground test equipment							
Launch support equipment							
Data reduction and analysis							
Refurbish						0	
.Transmitter							
Receiver							
Optomechanical							
Bench test equipment							
Ground test equipment							
Launch support equipment							
Data reduction and analysis							
Quality Assurance		2,246	6,740	2,246		11,232	
Performance assurance		1,123	3,370	1,123		5,616	
Inspection		1,123	3,370	1,123		5,616	

APPENDIX A. TRANSMITTER OPTICAL ALIGNMENT PROCEDURE

A.1 INTRODUCTION

The optical configuration of the LDRL transmitter system consists of two afocal Gregorian telescopes with a large (0.362) central obscuration. The relatively high speed (f/1.5) of the primary makes accurate alignment crucial.

There are four aspheric surfaces comprising the two telescopes, each surface having a specific optical axis and a focal point on that axis. For proper alignment, all four axes must be collinear with the system axis and each pair of focal points for the two beam expanders must coincide. The system axis follows a complex path as it is folded through the mechanical structure by nine flat-folding mirrors. The reference mechanical axis is the rotational axis of the outer gimbal bearing located between the two Gregorian telescopes. All optical elements must eventually be aligned to this reference axis.

A.2 SPECIAL TEST-FIXTURES

Several test fixtures must be available for system alignment and test. These fixtures are described throughout this procedure. For convenience, all of the required devices are listed here:

1) Rigid mount to hold the transmitter optical structure to a standard optical table

2) Means for rigidly caging the inner and outer gimbal bearings

3) Means for reading the position of the gimbal resolvers

4) Two test mirrors and means for mounting these to the rotating portion of the inner and outer gimbals

5) Alignment fixture for IMC subassembly alignment

6) Two autocollimating telescopes with fully adjustable mounts

OUTER GIMBAL

IMC 2   IMC 1   FOLD 4

PRE-EXPANDER
ASSEMBLY

FOLD 3

PRIMARY

SEC   FOLD 5

LOCATION OF
TEST FLAT 2
(TS 2)

INNER.
GIMBAL

FOLD 2

LOCATION OF
TEST FLAT 1
(TS 1)

FOLD 1
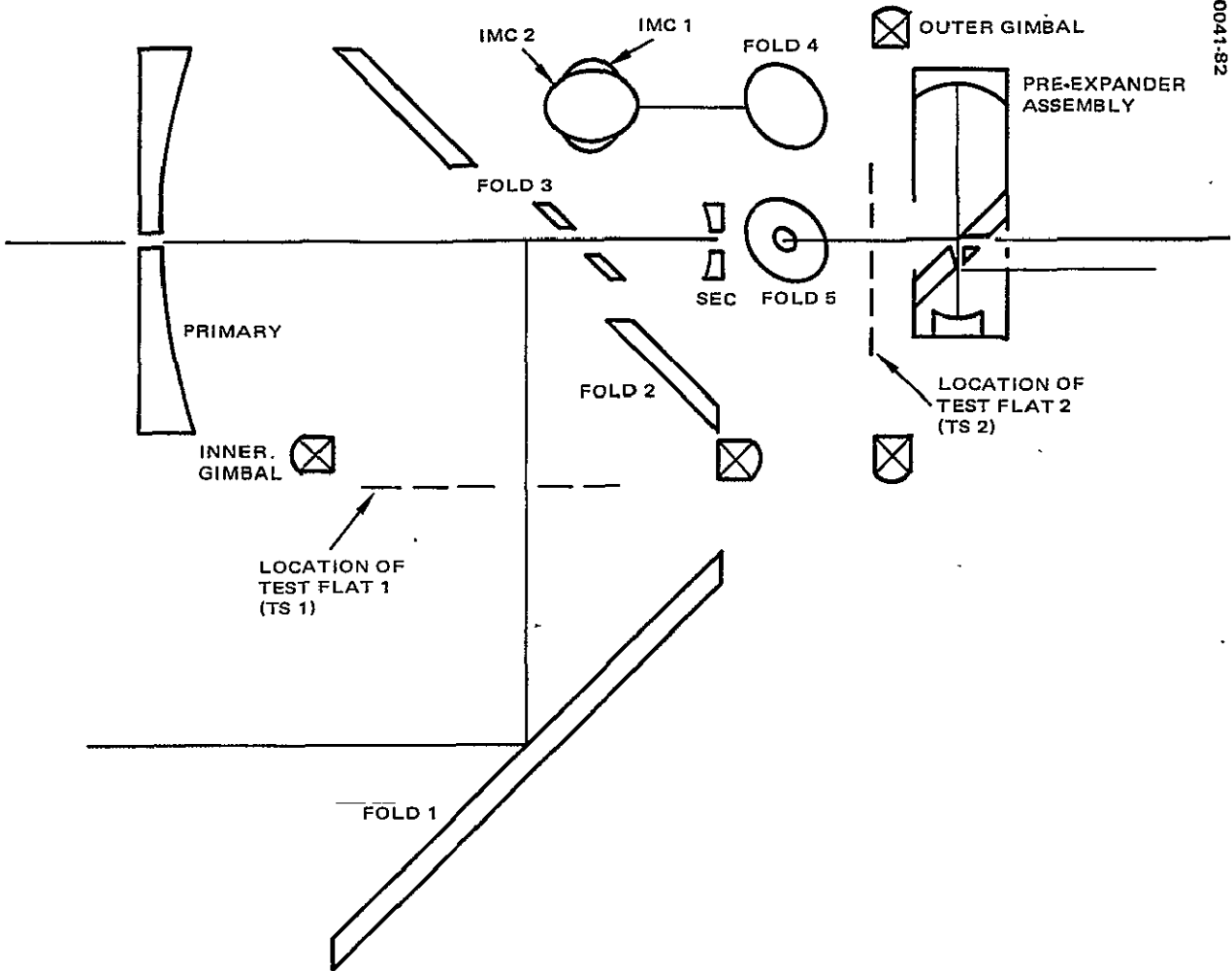
FIGURE A-1. LDRL-146 OPTICAL CONFIGURATION WITH MIRROR LABELS

7) Two steerable flat mirrors, of at least 7 inch diameter

8) A HeNe alignment laser

9) A collimated visible source of at least 8 inch diameter

10) Reticle for location of the center of the small folding diagonal mirror (fold 3)

11) Alignment fixtures for the primary and secondary mirrors

A.3 ALIGNMENT PROCEDURE

The system will be aligned using a step-by-step procedure. It is assumed that the preexpander will be received as an aligned subassembly. Under this assumption, the large 7x beam expander will require alignment, followed by relative alignment between the two expanders.

The first task in the alignment procedure is alignment of the 7x beam expander telescope consisting of the primary, secondary, and one folding mirror. The IMC subassembly alignment is next, followed by the alignment of the two folding mirrors following the IMCs. Next, the two large output flat-folding mirrors will be aligned. Alignment will be completed with the installation of the preexpander telescope. Figure A-1 is a diagram of the optical system with all mirrors labeled. These labels will be used throughout this procedure.

Two test mirrors are shown in Figure A-1, TS1 and TS2. These mirrors must mount to the rotating portion of the inner and outer gimbals and be adjustable in_angle. They should be flat. TS1 must be about 6 inches in diameter while TS2 may be as small as 1 inch diameter.

A.4 7x BEAM EXPANDER ALIGNMENT

Figure A-2 is a schematic representation of the 7x optical beam expander, along with the optical alignment devices to be used in this procedure. Two autocollimating telescopes (AC1 and AC2) and two steerable flat mirrors (flat 1 and flat 2) are required. AC1 is used in two positions, A and B. The principal mirrors of the expander have been labeled. An alignment crosshair or reticle is required to locate the center of the opening in fold 3. Alignment will be much easier if this centering device consists of an etched crosshair pattern on a transparent substrate.

Several alignment fixtures must be available. The most important fixture will be the mount for the telescope housing. This mount must support the telescope on an optical table in a manner that will allow installation and removal of the major optical components and subassemblies without
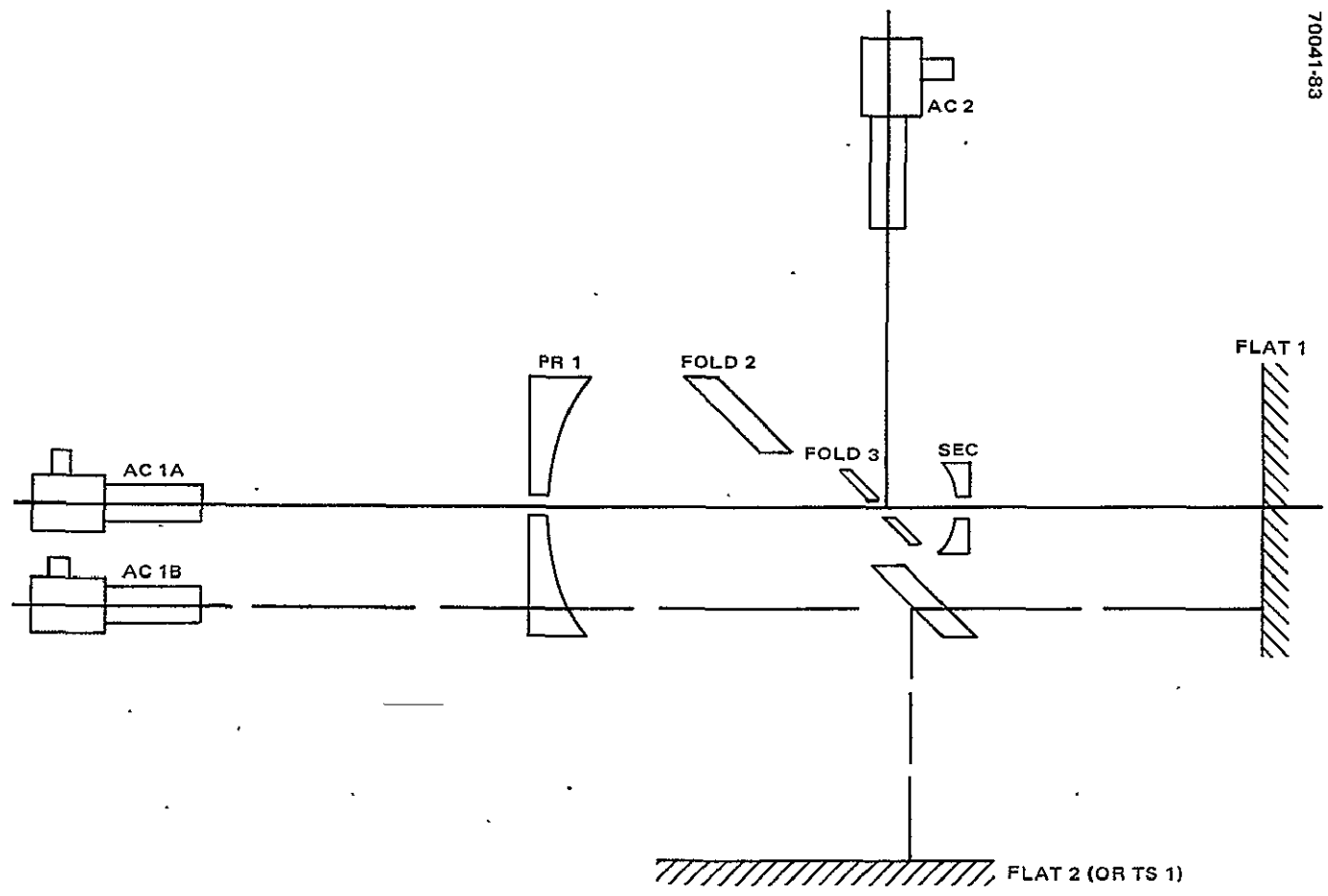
FIGURE A-2. TEST CONFIGURATION FOR LDRL-10.6 7X BEAM EXPANDER ALIGNMENT

disturbing the position of the box. It must mount the box as if the view in Figure A-1 were a top view so that the principal axis of the telescope is parallel to the surface of the table. It is not necessary that the mount be adjustable, only that it be rigid. If gimbals are installed, they must be locked.

Mounts must also be available for the two autocollimators. These mounts must be securely fastened to the table, and must be adjustable in four dimensions, two angular rotations, and two linear translations.

The three elements to be aligned are the primary, secondary, and fold 3. Fold 3 has no adjustments. The center of fold 3 thus locates a point on the reference axis. The secondary has three degrees of freedom, two angular adjustments, and a focus translation. The center of this mirror establishes a second point on the reference axis and establishes the reference axis. The primary mirror has five degrees of freedom, and is adjusted to coincide with the established reference axis and focal point.

The alignment procedure is as follows (referring to Figure A-2):

1) Mount the mechanical structure so it is rigid. Install fold 3 and the reticle to locate the center of fold 3. Temporarily install the secondary.

2) Mount AC2. Align AC2 so that the reticle in fold 3 and the center reference hole of the secondary are on the axis of AC2. This establishes the reference axis.

3) Mount AC1 in position A. Adjust AC1 to align its axis with the reticle in fold 3 and the center hole of the secondary.

4) Remove the secondary. Align flat 1 so that AC2 autocollimates. Check AC1 for autocollimation. Both AC1 and AC2 should autocollimate with flat 1 and coincide with the reticle in fold 3. Repeat steps 2 through 4 until this condition exists.

5) Install the secondary and its alignment fixture. Focus AC1 on the reticle in fold 3. Illuminate the target graticule in AC2. Adjust the secondary until the target from AC2 is in focus and aligned with the reticle in fold 2, as viewed through AC1. Focus may be checked by a lack of parallax between the target and the reticle.

6) Lock the secondary and remove the alignment fixture.

7) Move AC1 to position B. Adjust AC1 for autocollimation with flat 1.

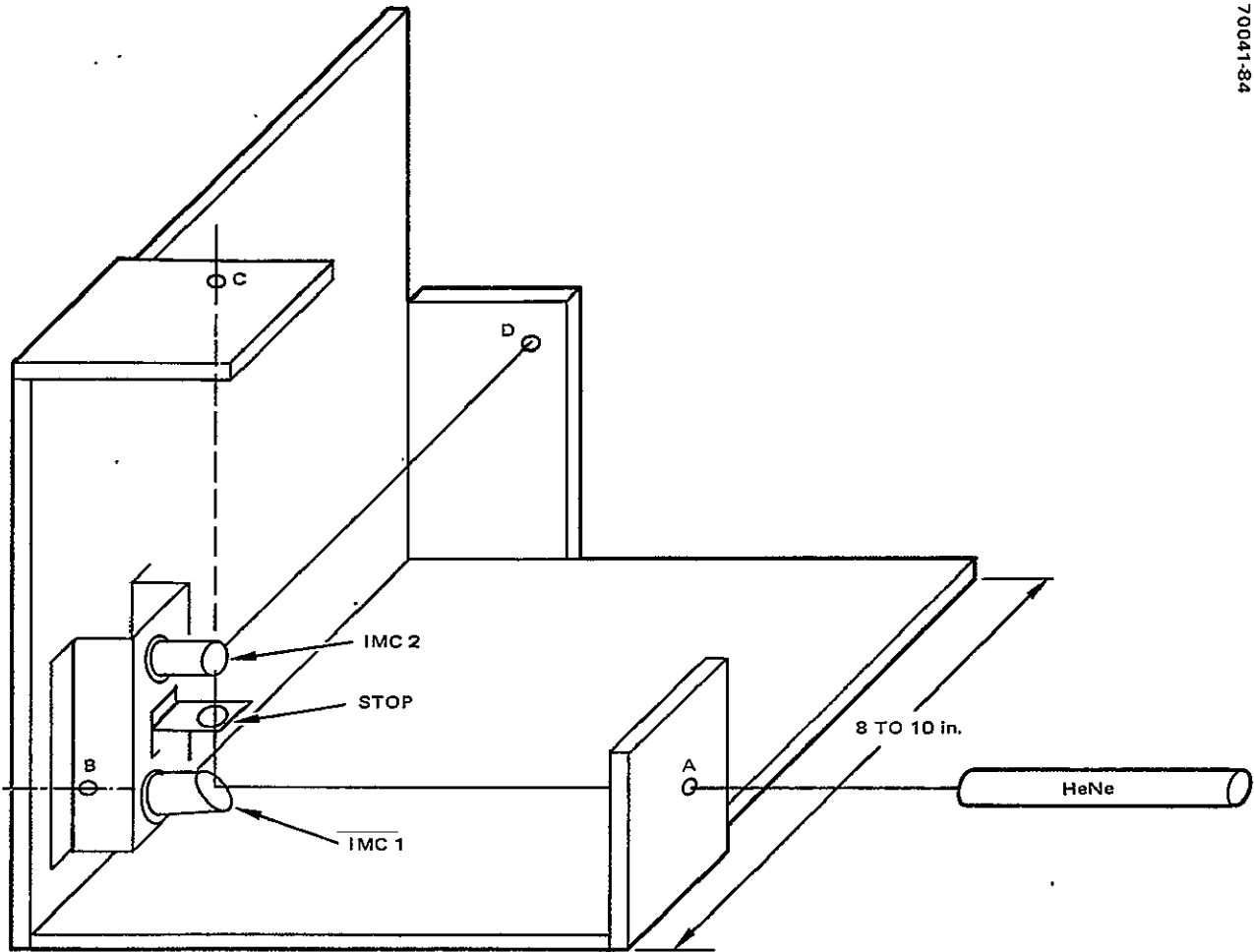8) Install fold 2 in the box. Align flat 2 so that AC1 is autocollimated.

FIGURE A-3. IMC SUBASSEMBLY OPTICAL ALIGNMENT

9) Install the primary mirror. Remove the reticle from fold 3. Translate the primary until the center reference hole is aligned with AC2.

10) Focus AC2 to infinity. Adjust the primary until AC2 is auto-collimating through the beam expander to flat 2 and is in focus. Alignment of the 7x beam expander is now complete.

A. 5 PRELIMINARY ALIGNMENT OF IMC SUBASSEMBLY

The IMC assembly has not been fully designed. This procedure suggests the steps necessary for alignment. These adjustments or equivalent adjustments should be considered during final design.

Figure A-3 depicts a suggested alignment fixture. The IMC assembly must be adjustable as a unit to compensate for tolerance buildup in the 7x beam expander. The IMC subassembly should mount to the test fixture in its nominal or centered position.

The test fixture is built up of 1/4 or 3/8 inch aluminum plates. Small holes (1/8 inch) are located as shown along the nominal optical axes of the IMC subassembly. The alignment procedure is as follows:

1) Mount the test fixture to a suitable table.

2) Align a HeNe laser through holes A and B that establish the input axis.

3) Mount the IMC subassembly with IMC 1 in place.

4) Adjust IMC 1 so that the beam from the HeNe hits the center of the mirror and exits through hole C.

5) Install the stop and adjust to center it on the HeNe beam.

6) Install IMC 2 so that the HeNe beam hits the center of the IMC mirror and exits through hole D.

A. 6 ALIGNMENT OF IMC ASSEMBLY

Refer to Figure A-2. It is now necessary to illuminate the primary mirror with a collimated source. This may be accomplished by the following procedure.

1) Establish the conditions shown in Figure A-2.

2) Position an adjustable flat mirror to reflect a collimated HeNe source onto fold 2. Adjust the angle of the flat to place

a point HeNe image on the crosshair of AC2 (use eye protection if necessary).

3) Check to see that the entire primary of the system is illuminated. If not, move the flat mirror and repeat the alignment in step 2.

4) Examine the beam emerging from fold 3. A symmetrical toroid representing the primary mirror and the hold in fold 3 should emerge with no other shadows. If this is not the case, alignment to this point is not correct and must be repeated.

5) Install the IMC subassembly and again examine the emerging image. Adjust the IMC assembly until the shadow cast by the stop is symmetrical with the outline of the primary mirror. These two circles should be very nearly identical in diameter.

A. 7. ALIGNMENT OF FOLDING MIRRORS BEHIND IMC ASSEMBLY

Fold 4 and fold 5 following the IMCs are used to align the optic axis to the center of the outer gimbal bearing axis. Two additional aignment fixtures are required. These are the adjustable flat mirrors, TS1 and TS2, described earlier and shown in Figure A-1. Use the following procedure:

1) Assuming the system is set up as in step 5 of the previous alignment, the 1 inch diameter HeNe laser beam is still exiting the system. Set up an autocollimator to accept this beam, and adjust the autocollimator until the focused HeNe laser beam coincides with the crosshair.

2) Turn off the HeNe laser. Mount alignment mirror TS1. Adjust for autocollimation through the system.

3) Move the autocollimator so that it coincides approximately with the optic axis of the telescope. Align it to view the hole in the back of the secondary mirror.

4) Install flat alignment mirror TS2. Adjust the mirror and/or the autocollimator for autocollimation. Uncage and rotate the outer gimbal through its travel range and note the motion of the target relative to the reticle. Adjust the mirror to a new position, and readjust the autocollimator for autocollimation. Repeat the rotation check. Iterate until the target remains stationary during rotation.

5) Focus the autocollimator on the mirror surface. Rotate the bearing. Note the center of rotation relative to the crosshair. (A mark placed on the mirror may make this observation easier.) Translate the autocollimator until the crosshair coincides with the center of rotation.

6)   Repeat steps 4 and 5 until no motion is apparent in either step.

7)   Remove the alignment mirror TS2 from the bearing center. Install fold 4 and fold 5. Install the reticle in fold 3. Adjust fold 4 and fold 5 until the autocollimator crosshair is aligned to the reticle in fold 3 and the center of the primary and secondary mirrors.

8)   Focus the autocollimator to infinity. The target reflected from TS1 should be visible. Rotate the outer gimbal and note any motion of the target.

9)   Adjust the fold 4 and fold 5 to obtain the best compromise between the alignment in step 7 and minimum motion in step 8. Record the angular excursion of any motion in step 8.

A. 8 ALIGNMENT OF FOLD 2

The system should be set up as in step 9 of the above procedure, with the following steps:

1)   Cage the outer gimbal in a convenient position where the inner gimbal is free to rotate.

2)   Check to be sure the autocollimator is still aligned to TS1.

3)   Uncage and rotate the inner gimbal through its full range. Note any target motion.

4)   Adjust fold 2 to a new position. Readjust TS1 for autocollimation.

5)   Repeat steps 3 and 4 until there is no relative motion in step 3.


A. 9. ALIGNMENT OF FOLD 1

Continue from step 5 of the above procedure:

1)   Remove TS1.

2)   Rotate the outer gimbal until the line of sight emerging from fold 2 is nearly parallel to the table.

3)   Set up a large flat mirror to intercept this line of sight. This mirror should be elevated above the table so that only the lower portion is used (see Figure A-4a).

4)   Adjust the flat for autocollimation.

5)   Using the resolver readout, rotate the outer gimbal 90° to the position shown in Figure A-4b.

6)   Install fold 1 on the inner gimbal. Rotate the inner gimbal to view the large flat, as shown in Figure A-4b.

7)   Adjust the inner gimbal position and shim fold 1 until auto-collimation is achieved.
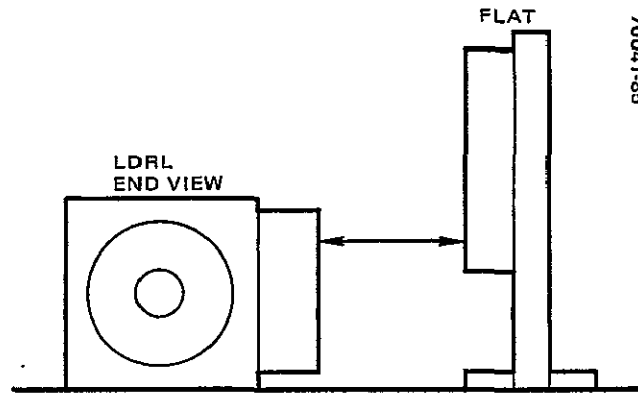
a) INITIAL SETUP
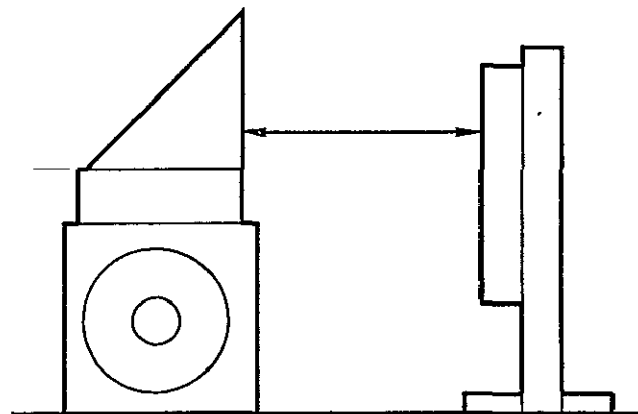
b) AFTER 90° ROTATION

FIGURE A-4. MIRROR ALIGNEMNT

APPENDIX B. HETERODYNE RADIOMETER
PERFORMANCE ANALYSIS

B.1 INTRODUCTION

This appendix provides a performance analysis of the heterodyne radiometer in a convenient form for making preliminary estimates of system sensitivity. To simplify the derivations, it will be assumed that the signal in an IF filter is unmodulated and centered in the filter band. The bandpass characteristic of the IF filter is assumed to be rectangular. While the analysis can be carried through for more general signals and more general IF bandpass characteristics, the derivations are notationally somewhat more awkward, and the results require considerable care for proper interpretation. The analysis under the simplifying assumptions stated above displays the essential features of the heterodyne radiometer and yields results substantially equivalent to those for the more general case; in fact, the important features of the device are more readily comprehended when freed from the analytical complications of the more general case. The analysis is extended to remove the simplifying assumptions in the latter part of the discussion.

B.2 TOTAL POWER HETERODYNE RADIOMETER

Consider first an idealized heterodyne radiometer in which the receiver gain is not subject to drift or fluctuations. In this case, chopper stabilization is not required, and all the received power can be employed efficiently. One begins by obtaining an expression for the output signal-to-noise ratio of such a total power radiometer. Let the signal have the form

$$S(t) = A \cos 2\pi f_o t \tag{1}$$

and let the noise be represented as

$$N(t) = X(t) \cos 2\pi f_o t + Y(t) \sin 2\pi f_o t \tag{2}$$

Here f_o is the center frequency of the IF filter and X(t) and Y(t) are independent stationary gaussian processes with zero means and low pass power spectra. The bandwidths of the X(t) and Y(t) processes are half the bandwidth of the IF bandpass noise, N(t), and their spectral densities are twice that of N(t).

$\overline{F(t)}$ represents the time average of F(t). It is well known that

$$\overline{X^2(t)} = \overline{Y^2(t)} = \sigma_N^2 \tag{3}$$

where σ_N^2 is the average power of the noise, N(t),

$$\overline{N^2(t)} = \sigma_N^2 \tag{4}$$

Also write

$$\psi_F(\tau) = \overline{F(t) F(T + \tau)} \tag{5}$$

for the correlation function of F(t). If G(f) is the spectral density of N(t) and the frequency f is measured with respect to the center frequency, f_o, the spectral density of the low pass function X(t) (and similarly for Y(t)) is simply 2G(f) where now f is measured from $f = 0$. Note that, as here defined, G(f) for negative values of f merely refers to the spectral density of N(t) for frequencies less than the IF center frequency, f_o. Also needed is the spectrum corresponding to the correlation function $\psi_X{}^2(\tau)$. This will be a low pass spectrum with spectral density given by

$$G_2(f) = 2 \int_{-\infty}^{\infty} G(f + \nu) G(\nu) d\nu \tag{6}$$

For the calculations to follow, the values of $\overline{X^2(t) X^2(t + \tau)}$ and similarly for Y(t) are needed. To evaluate this expression, which is merely $\psi_X{}^2(\tau)$, the time average is evaluated as an ensemble average,

$$\psi_X 2(\tau) = \overline{X^2(t) X^2(t + \tau)} = E\{X^2(t) X^2(t + \tau)\} \tag{7}$$

B-2

where $E\{\ \}$ is the expectation operator. Let X_1, X_2, X_3, X_4 be variables with a multivariate gaussian distribution. Then

$$E\{X_1 X_2 X_3 X_4\} = E\{X_1 X_2\}\ E\{X_3 X_4\} + E\{X_1 X_3\}\ E\{X_2 X_4\}$$

$$+ E\{X_1 X_4\}\ E\{X_2 X_3\}$$

(8)

By using Equation 8,.

$$E\{X^2(t)\ X^2(t + \tau)\} = E\{X^2(t)\}\ E\{X^2(t + \tau)\} + 2\left[E\{X(t)\ X(t + \tau)\}\right]^2 \quad (9)$$

Since $E\{X^2(t)\} = E\{X^2(t + \tau)\} = \sigma_N^2$, Equation 8 becomes

$$E\{X^2(t)\ X^2(t + \tau)\} = \sigma_N^4 + 2\psi_X^2(\tau) \tag{10}$$

Insertion of the results of Equation 10 into Equation 7 yields

$$\psi_X^2(\tau) = \sigma_N^4 + 2\psi_X^2(\tau) \tag{11}$$

This completes the summary of the analytical machinery required for the derivations to follow. While the results are all well known, citing them in the context of the problem at hand will facilitate following the derivations. Actually, much of the derivation for the case of the total power radiometer is also to be found, in another context, in a number of literature sources. However, it is desirable to give the derivation for the total power radiometer in full rather than merely citing the literature since an understanding of this derivation simplifies following the corresponding derivation for the Dicke (chopped) radiometer.

The total intermediate frequency signal, $I(t)$, is (from Equations 1 and 2)

$$I(t) = S(t) + N(t) = \{X(t) + A\}\cos 2\pi f_o t + Y(t)\sin 2\pi f_o t \tag{12}$$

To simplify the derivation and obtain explicit expressions for the signal and noise outputs of a receiver, it will be convenient to suppose that square-law detection is employed. It can be shown that the threshold performance of the heterodyne radiometer is substantially unaffected by the choice of the detector law; this is the case because, at low input signal-to-noise ratios, all envelope detectors act in substantially the same manner independent of the precise detector law. Since the square-law detector permits an explicit analysis valid for all IF signal-to-noise ratios, its use for this analysis will facilitate interpretation of the results to be obtained.

The output of the square-law detector, $D(t)$, will be proportional to the square of the envelope of the IF signal. Since the concern here is only with signal-to-noise ratios, proportionality factors may be neglected and, by use of Equation 12, the detector output may be taken to be given by

$$D(t) = \left\{ X(t) + A \right\}^2 + Y^2(t) \tag{13}$$

The right-hand side of Equation 13 can be written in the more useful form

$$D(t) = X^2(t) + Y^2(t) + 2AX(t) + A^2 \tag{14}$$

The $X^2(t) + Y^2(t)$ term is due to noise, $N(t)$, beating with itself in the detector; accordingly, it is called the noise-cross-noise term. The term $2AX(t)$ results from the noise beating with the signal; consequently, it is referred to as the signal-cross-noise term. The term A^2 results from the signal beating with itself in the detector.

The right-hand side of Equation 14 is now examined to determine what changes one may expect to observe in the detector output in the presence of a signal. When only noise is present, the dc output of the detector will be

$$\overline{D_N(t)} = \overline{X^2(t)} + \overline{Y^2(t)} = 2\sigma_N^2 \tag{15}$$

When signal is present, the dc component of the detector output becomes

$$\overline{D_{N+S}(t)} = \overline{X^2(t)} + \overline{Y^2(t)} + \overline{2AX(t)} + A^2 \tag{16}$$

B-4

Since X(t) has a zero mean, the right side of Equation 16 reduces to

$$\overline{D_{N+S}(t)} = 2\sigma_N{}^2 + A^2 = \overline{D_N(t)} + A^2 \tag{17}$$

Detection of the presence of the signal, S(t), is recognized by the increase in the dc output of the detector. However, this increase is partially obscured by the fluctuations caused by the noise terms in the detector output. The fluctuating terms may be recognized more readily by writing Equation 14 in the form

$$D(t) = \left[\{X^2(t) - \sigma_N{}^2\} + \{Y^2(t) - \sigma_N{}^2\} + 2AX(t)\right] + 2\sigma_N{}^2 + A^2 \tag{18}$$

In Equation 18, the term in square brackets is the fluctuating noise. Note that the signal-cross-noise term contributes to the output fluctuation. The detector output must be heavily filtered to remove the major portion of the fluctuating noise power, and hence to enhance the output signal-to-noise ratio.

To proceed further, the spectrum of the fluctuating noise in the detector output must be determined. It is readily seen that the three terms within the square brackets are uncorrelated, so that their spectral densities are additive. The spectral densities may readily be determined from the corresponding correlation functions. For brevity, write

$$X_1(t) = X^2(t) - \sigma_N{}^2$$
$$\tag{19}$$
$$Y_1(t) = Y^2(t) - \sigma_N{}^2$$

Then

$$\psi_{X_1}(\tau) = \overline{X_1(t)X_1(t+\tau)} = \overline{X^2(t)X^2(t+\tau)} - \sigma_N{}^2\overline{X^2(t)}$$
$$\tag{20}$$
$$- \sigma_N{}^2\overline{X^2(t+\tau)} + \sigma_N{}^4 = \psi_{X^2}(\tau) - \sigma_N{}^4$$

Reference to Equation 11 shows that Equation 20 may be written as

$$\psi_{X_1}(\tau) = 2\psi_X^2(\tau) \tag{21}$$

with similar results for Y_1. Since $X(t)$ and $Y(t)$ have identical distributions the correlation function corresponding to the fluctuating portion of the noise-cross-noise components in the detector output, $\psi_{NxN}(\tau)$, may be written as

$$\psi_{NxN}(\tau) = \psi_{X_1}(\tau) + \psi_{Y_1}(\tau) = 4\psi_X^2(\tau) \tag{22}$$

The correlation function of the signal-cross-noise fluctuations, $\psi_{SxN}(\tau)$, is seen at once from Equation 18 to be given by

$$\psi_{SxN}(\tau) = 4A^2\psi_X(\tau) \tag{23}$$

From Equations 22 and 23, the correlation function of the fluctuating noise at the detector output, $\psi_N(\tau)$, may be written as

$$\psi_N(\tau) = 4\left\{\psi_X^2(\tau) + A^2\psi_X(\tau)\right\} \tag{24}$$

From Equations 6 and 24 and the observation that the spectral density of $X(t)$ is $2G(f)$, it may be seen at once that the spectrum of the fluctuating noise output of the detector has a density, $G_D(f)$, given by.

$$G_D(f) = 8\left\{\int_{-\infty}^{\infty} G(f + \nu)G(\nu)\,d\nu + A^2 G(f)\right\} \tag{25}$$

On noting that the IF signal power, P_S, is given by

$$P_S = \frac{1}{2}A^2 \tag{26}$$

it is seen that the right-hand side of Equation 25 can be rewritten as

$$G_D(f) = 8 \left\{ \int_{-\infty}^{\infty} G(f + \nu) G(\nu) d\nu + 2P_S G(f) \right\} \qquad (27)$$

The noise output of the radiometer is the result of passing the detector output through a low pass filter. The bandwidth of this filter will be very narrow relative to the width of the IF noise spectrum, and hence of the video noise spectrum given by Equation 27. Accordingly, the noise power output of the radiometer may be calculated merely by multiplying the noise bandwidth of the video output filter, B_V, by the fluctuating noise spectral density at $f = 0$; that is, with adequate accuracy, the approximation may be made

$$G_D(f) \approx G_D(o) \qquad (28)$$

and the output mean square noise power of the radiometer, σ_{VN}^2 (VN for video noise), calculated as

$$\sigma_{VN}^2 = B_V G_D(o) \qquad (29)$$

From Equations 29 and 27, then

$$\sigma_{VN}^2 = 8 \left\{ \int_{-\infty}^{\infty} G^2(\nu) d\nu + 2P_S G(o) \right\} B_V \qquad (30)$$

Thus far only the symmetry of the IF bandpass characteristic about the filter center frequency has been used. At this point, it will be convenient to render the result expressed by Equation 30 somewhat more specific by making explicit use of the assumption that the IF filter has a perfect rectangular bandpass of bandwidth B_{IF}; note that in this case B_{IF} is both the noise bandwidth of the IF filter and the bandwidth as measured by, say, the 3 dB points. In the more general case of an arbitrary bandpass characteristic, B_{IF} must be understood to refer to the IF noise bandwidth. Let ξ_o be the spectral density of the IF noise, $N(t)$. Then, for the rectangular filter case and with the convention that f is measured from the IF center frequency, $G(f)$ is given by

$$G(f) = \begin{cases} \xi_o & \text{for } -\frac{1}{2} B_{IF} \leq f \leq \frac{1}{2} B_{IF} \\ \\ 0 & \text{for } |f| > \frac{1}{2} B_{IF} \end{cases} \qquad (31)$$

Hence, one has $G(o) = \xi_o$ and

$$\int_{-\infty}^{\infty} G^2(\nu) \, d\nu = \xi_o^2 B_{IF} \qquad (32)$$

from which Equation 30 may be rewritten in the form

$$\sigma_{VN}^2 = 8 \left\{ \xi_o^2 B_{IF} + 2P_S \xi_o \right\} B_V$$

$$= 8 \left\{ \left(\xi_o B_{IF} \right)^2 + 2P_S \left(\xi_o B_{IF} \right) \right\} \frac{B_V}{B_{IF}} \qquad (33)$$

But $\xi_o B_{IF}$ is just the total IF noise power, σ_N^2; thus Equation 33 becomes

$$\sigma_{VN}^2 = 8 \sigma_N^2 \left\{ \sigma_N^2 + 2P_S \right\} \frac{B_V}{B_{IF}} \qquad (34)$$

Now the radiometer output signal-to-noise ratio can be calculated. The signal component of the detector output is A^2 and this, according to Equation 26, is just $2P_S$. It follows that the power of the signal component at the detector output, P_{VS}, is given by

$$P_{VS} = 4P_S^2 \qquad (35)$$

From Equations 34 and 35 the output signal-to-noise ratio, $(S/N)_V$, may be expressed in terms of the IF signal-to-noise ratio. Then

$$\left(\frac{S}{N}\right)_V = \frac{P_{VS}}{\sigma_{VN}^2} = \frac{P_S^2}{2\sigma_N^2\left\{\sigma_N^2 + 2P_S\right\}} \cdot \frac{B_{IF}}{B_V}$$

(36)

$$= \frac{\left(\dfrac{P_S}{\sigma_N^2}\right)^2}{2\left\{1 + 2\left(\dfrac{P_S}{\sigma_N^2}\right)\right\}} \cdot \frac{B_{IF}}{B_V}$$

Since P_S/σ_N^2 is just the IF signal-to-noise ratio, Equation 36 can be rewritten in the more useful form

$$\left(\frac{S}{N}\right)_V = \frac{\left(\dfrac{S}{N}\right)_{IF}^2}{2\left\{1 + 2\left(\dfrac{S}{N}\right)_{IF}\right\}} \cdot \frac{B_{IF}}{B_V}$$

(37)

This is the desired result for the total power radiometer, which will serve as a standard of comparison.

B.3 DICKE RADIOMETER

In practice, gain fluctuations and drifts limit the applicability of the total power heterodyne radiometer. This is a familiar problem in radio astronomy where a signal chopping technique is frequently employed to reduce the receiver gain stability requirement to an achievable value. The resulting receiver, known as a Dicke radiometer, in effect automatically references the signal component of the detector output to the receiver noise power. The same technique is applicable in the present instance, although the signal source for this case differs in some essential respects from the broadband noise which, in the radio astronomy case, occupies the entire IF bandwidth of the receiver independent of the choice of this bandwidth.

The Dicke radiometer operates as follows for the case at hand. The received optical signal is periodically chopped at the input to the optical

detector. The result of this chopping action is to produce a modulation of the IF detector output at the chopping frequency. The IF detector output is ac coupled to remove the large component of the detector output due to the dc component produced by receiver noise-cross-noise products. This ac coupling may be accomplished by a high pass filter, a transformer, or a bandpass amplifier tuned to the fundamental of the chopping frequency. The output of the circuit which removes the dc component of the IF detector output is then synchronously detected with respect to a reference signal synchronized with the chopper, and the synchronously detected signal is passed through a low pass filter to provide the desired radiometer output signal.

The optical chopper is basically a signal modulator. It can be shown that the optimum signal modulator is simple on-off chopping with a 50 percent duty factor, and this form of signal modulation will be assumed in the analysis that follows. It can also be shown that the radiometer sensitivity is maximized when all the harmonics of the modulation frequency at the IF detector output are passed to the synchronous detector and when synchronous detection is performed with respect to a square wave reference signal. Use of the tuned amplifier preceding the synchronous detector produces a degradation of about 0.9 dB in output signal-to-noise ratio relative to the case in which all harmonics of the chopper frequency at the IF detector output are passed to the synchronous detector (frequently called a synchronous rectifier by radio astronomers). Since the object is to maximize output signal-to-noise ratio and since transformer coupling provides a simple way of suppressing the dc component of the IF detector output while passing the harmonics of the chopping frequency, it will be supposed that dc suppression is effected without deletion of the chopping frequency harmonics in the analysis to follow.

Actually, suppression of the dc component of the IF detector output prior to synchronous detection is not necessary in principle since this dc component will be suppressed by the synchronous detection process. However, for the threshold signal case, the signal component at the detector output is so small relative to the dc level produced by noise that the balance requirements on the synchronous detector become prohibitive unless some form of dc suppression is employed.

In analyzing the performance of the chopped (Dicke) radiometer, let $C(t)$ be the chopper modulation which may be considered to be a periodic function equal to unity for the first half of the chopping cycle and equal to zero on the latter half. With this notation, the IF signal, $\tilde{I}(t)$, can be represented in the form

$$\tilde{I}(t) = C(t)S(t) + N(t) = \left\{ X(t) + C(t)A \right\} \cos 2\pi f_o t$$

$$+ Y(t) \sin 2\pi f_o t$$

(38)

Here use $\tilde{I}(t)$ rather than $I(t)$ as in Equation 12 to distinguish the chopped case from the case of the total power radiometer. (This tilde convention will be used in the sequel when it is important to emphasize the distinction.) Equation 14 for the output of the IF square-law envelope detector now becomes

$$\tilde{D}(t) = X^2(t) + Y^2(t) + 2AC(t)X(t) + C^2(t)A^2 \qquad (39)$$

The dc component of the detector output is, according to Equation 39, given by

$$\overline{\tilde{D}(t)} = \overline{X^2(t)} + \overline{Y^2(t)} + \overline{C^2(t)}A^2 \qquad (40)$$

$$= 2\sigma_N^2 + \frac{1}{2}A^2$$

From Equations 40 and 41 it can be seen that, after suppression of the dc component of the detector output, the input to the synchronous detector, $F(t)$, is given by

$$F(t) = \left\{ X^2(t) - \sigma_N^2 \right\} + \left\{ Y^2(t) - \sigma_N^2(t) \right\} + 2AC(t)\dot{X}(t)$$

$$+ \left\{ C(t) - \frac{1}{2} \right\}A^2 \qquad (41)$$

where use has been made of the fact that $C^2(t) = C(t)$. With the notation of Equation 19, Equation 41 can be rewritten as

$$F(t) = X_1(t) + Y_1(t) + 2AC(t)X(t) + \left\{ C(t) - \frac{1}{2} \right\}A^2 \qquad (42)$$

Now consider the effect of the synchronous demodulator synchronized with the chopping frequency. When a square wave reference is employed, the operation of the synchronous demodulator, up to an inessential proportionality factor, can be viewed as multiplication of the dc-suppressed detector output by $R(t)$, where

$$R(t) = \begin{cases} 1 & \text{for } C(t) = 1 \\ -1 & \text{for } C(t) = 0 \end{cases} \tag{43}$$

$C(t)$ can be expressed in terms of $R(t)$ as

$$C(t) = \frac{1 + R(t)}{2} \tag{44}$$

Use of the expression for $C(t)$ in terms of $R(t)$, as given by Equation 44, permits Equation 42 to be rewritten as

$$F(t) = X_1(t) + Y_1(t) + A\{1 + R(t)\}X(t) + \frac{1}{2}R(t)A^2 \tag{45}$$

On multiplication of $F(t)$ by $R(t)$ and use of the fact that $R^2(t) = 1$, it is found from Equation 45 that the synchronous detector output, $H(t)$, has the form

$$H(t) \doteq \left[R(t)X_1(t) + R(t)Y_1(t) + A\{1 + R(t)\}X(t) \right] + \frac{1}{2}A^2 \tag{46}$$

Equation 46 is the analog, for the Dicke radiometer, of Equation 18 for the total power radiometer. The resemblance can be made even closer by introducing the functions $\tilde{X}_1(t)$, $\tilde{Y}_1(t)$, and $\tilde{X}(t)$ defined by

$$\tilde{X}_1(t) = R(t)X_1(t)$$

$$\tilde{Y}_1(t) = R(t)Y_1(t) \tag{47}$$

$$\tilde{X}(t) = \{1 + R(t)\}X(t)$$

in terms of which the output of the synchronous detector (Equation 46) becomes

$$H(t) = \left[\tilde{X}_1(t) + \tilde{Y}_1(t) + A\tilde{X}(t) \right] + \frac{1}{2}A^2 \tag{48}$$

The terms within the square brackets are the noise terms. Each has zero mean. $\tilde{X}_1(t)$ and $\tilde{Y}_1(t)$ are the noise-cross-noise terms and $A\tilde{X}(t)$ is the signal-cross-noise term, all as modified by the switching action of the synchronous detector. To obtain the output noise spectrum, the correlation function of the output noise is calculated. Examination of the definitions of $\tilde{X}_1(t)$, $\tilde{Y}_1(t)$, and $\tilde{X}(t)$ and the properties of the underlying noise functions $X(t)$ and $Y(t)$ shows that the three terms in the square brackets in Equation 48 are uncorrelated; hence, the correlation function of the noise component of the synchronous detector output is merely the sum of the correlation functions of the three components taken separately. Moreover, $R(t)$ is uncorrelated with $X_1(t)$, $Y_1(t)$, and $X(t)$.

By use of the preceding relations, the correlation functions of $\tilde{X}_1(t)$ become

$$\psi_{\tilde{X}_1}(t) = \overline{R(t)\,X_1(t)\,R(t+\tau)\,X_1(t+\tau)} = \overline{R(t)\,R(t+\tau)} \cdot$$

$$= \overline{X_1(t)\,X_1(t+\tau)} \tag{49}$$

$$= \psi_R(\tau)\psi_{X_1}(\tau)$$

In the same way, it is found

$$\psi_{\tilde{Y}_1}(\tau) = \psi_R(\tau)\psi_{Y_1}(\tau) = \psi_R(\tau)\psi_{X_1}(\tau) \tag{50}$$

Finally, for the correlation function of $\tilde{X}(t)$,

$$\psi_{\tilde{X}}(\tau) = \overline{\{1 + R(t)\}X(t)\{1 + R(t+\tau)\}X(t+\tau)}$$

$$= \overline{\{1 + R(t)\}\{1 + R(t+\tau)\}} \cdot \overline{X(t)\,X(t+\tau)} \tag{51}$$

$$= \{1 + \psi_R(\tau)\}\,\psi_X(\tau)$$

B-13

In principle, determination of the spectra of $\tilde{X}_1(t)$, $\tilde{Y}_1(t)$, and $\tilde{X}(t)$ requires taking the Fourier transforms of the products of the correlation functions which appear in Equations 49, 50, and 51. While these calculations can be carried out explicitly, there is another means, in this case, for determining the power spectral densities which provides more physical insight into the operation of the chopped radiometer. The spectral widths of $X_1(t)$, $X_2(t)$, and $X(t)$ are very large relative to that of $R(t)$; more explicitly, the spectral widths of the X's are of the order of $B_{IF}/2$ or greater, while all the significant power in $R(t)$ is confined to a total spectral range equal to a few times the chopping frequency. The correlation times of $X_1(t)$, $X_2(t)$, and $X(t)$ are thus of the order of B_{IF}^{-1}, and the correlation functions $\psi_{X_1}(\tau)$, $\psi_{Y_1}(\tau)$, and $\psi_X(\tau)$ will, for all practical purposes, vanish for all τ greater than a few times B_{IF}^{-1}. By contrast, $\psi_R(\tau)$ will be, for all practical purposes, effectively constant and equal to $\psi_R(o)$ for all values of τ in the region where $\psi_{X_1}(\tau)$, $\psi_{Y_1}(\tau)$, and $\psi_X(\tau)$ are significantly different from zero. This follows either from the fact that the sensible spectrum of $R(t)$ is confined to the first few harmonics of the chopping frequency or from examination of the explicit expression for $\psi_R(\tau)$, which is readily seen to be given by

$$\psi_R(\tau) = 1 - 4 \frac{|\tau|}{T} \qquad \text{for } |\tau| \leq T/2 \qquad (52)$$

where T is the chopping period. $\psi_R(\tau)$ is periodic with period T, and hence determined for all τ by its values on $|\tau| \leq T/2$; it is unnecessary to use this fact in the following argument.

Since $\psi_{X_1}(\tau)$, $\psi_{Y_1}(\tau)$, $\psi_X(\tau)$ are, for all practical purposes, zero outside of the region where $\psi_R(\tau)$ is effectively constant, one has, from Equations 49, 50, 51, to an adequate approximation

$$\psi_{\tilde{X}_1}(\tau) = \psi_{\tilde{Y}_1}(\tau) = \psi_R(o)\psi_{X_1}(\tau) \qquad (53)$$

and

$$\psi_{\tilde{X}}(\tau) = \left\{ 1 + \psi_R(o) \right\} \psi_X(\tau) \qquad (54)$$

As $\psi_R(o) = 1$, Equations 53 and 54 now become

$$\psi_{\tilde{X}_1}(\tau) = \psi_{\tilde{Y}_1}(\tau) = \psi_{X_1}(\tau) \qquad (55)$$

and

$$\psi_{\tilde{X}}(\tau) = 2\psi_{\tilde{X}}(\tau) \qquad (56)$$

The correlation functions on the right side of Equations 55 and 56 are identical to those encountered in the analysis of the total power radiometer. Reference to Equation 48 and the results obtained previously now shows that the correlation function, $\tilde{\psi}_N(\tau)$, of the fluctuating noise at the output of the synchronous detector is given by

$$\tilde{\psi}_N(\tau) = 4\psi_X^2(\tau) + 2A^2\psi_X(\tau) \qquad (57)$$

From Equation 6 and the fact that the spectral density of $X(t)$ is $2G(f)$, it is seen at once that the spectral density of the noise at the synchronous detector output, $G_H(f)$, is

$$G_H(f) = 4\left\{ 2 \int_{-\infty}^{\infty} G(f + \nu) G(\nu) d\nu + A^2 G(f) \right\}$$

$$(58)$$

$$= 8\left\{ \int_{-\infty}^{\infty} G(f + \nu) G(\nu) d\nu + P_S G(f) \right\}$$

where, in the extreme right-hand side of Equation 58, use has been made of Equation 26. On using the approximation $G_H(f) \approx G_H(o)$, which is valid for the range of frequencies passed by the output filter of bandwidth B_V, and Equation 32, the output noise power, $\tilde{\sigma}_{VN}^2$, becomes

$$\tilde{\sigma}_{VN}^2 = 8\left\{ \xi_o^2 B_{IF} + P_S \xi_o \right\} B_V \qquad (59)$$

In the same manner that Equation 33 was transformed to Equation 34, the result expressed by Equation 59 can be rewritten in the form

$$\tilde{\sigma}_{VN}^2 = 8\sigma_N^2 \left\{ \sigma_N^2 + P_S \right\} \frac{B_V}{B_{IF}} \tag{60}$$

From Equation 48, the dc component of the synchronous detector output due to the signal is $A^2/2 = P_S$; thus the output signal power is P_S^2. From this observation and Equation 60, the output signal-to-noise ratio of the Dicke radiometer, $(S/N)_V$, becomes

$$\left(\frac{\tilde{S}}{N}\right)_V = \frac{P_S^2}{8\sigma_N^2 \left\{ \sigma_N^2 + P_S \right\}} \cdot \frac{B_{IF}}{B_V} \tag{61}$$

$$= \frac{\left(\dfrac{P_S}{\sigma_N^2}\right)^2}{8\left\{ 1 + \left(\dfrac{P_S}{\sigma_N^2}\right) \right\}} \cdot \frac{B_{IF}}{B_V}$$

Equation 61 can be written in the more useful form

$$\left(\frac{\tilde{S}}{N}\right)_V = \frac{\left(\dfrac{S}{N}\right)_{IF}^2}{8\left\{ 1 + \left(\dfrac{S}{N}\right)_{IF} \right\}} \cdot \frac{B_{IF}}{B_V} \tag{62}$$

It is instructive to compare the performance of the Dicke radiometer with that of the total power radiometer. To this end, Equation 62 may be rewritten in the form

$$\left(\frac{\tilde{S}}{N}\right)_V = \frac{\left[\dfrac{1}{2}\left(\dfrac{S}{N}\right)_{IF}\right]^2}{2\left\{ 1 + 2\left[\dfrac{1}{2}\left(\dfrac{S}{N}\right)_{IF}\right] \right\}} \cdot \frac{B_{IF}}{B_V} \tag{63}$$

Observe now that

$$\frac{1}{2}\left(\frac{S}{N}\right)_{IF}$$

is just the average signal-to-noise ratio in the IF filter when account is taken of the chopping action. With this interpretation, the right-hand side of Equation 63, and hence also Equation 62, is equivalent to that of Equation 37 for the total power radiometer. From this observation, it is clear that the price of the chopper stabilization of the receiver is a 3 dB loss of sensitivity, and that this sensitivity loss results from the fact that the chopper (with the optimum choice of the chopper modulation function) suppresses precisely half of the received signal power.

B.4 EXTENSION TO ARBITRARY SIGNALS AND IF BANDPASS CHARACTERISTICS

It is apparent from consideration of typical values for the ratio B_{IF}/B_V that the threshold signal case always occurs for the applications of present interest when $(S/N)_{IF} \ll 1$. Under these circumstances, Equations 37 and 62 reduce to

$$\left(\frac{S}{N}\right)_V \approx \frac{1}{2}\left(\frac{S}{N}\right)_{IF}^2 \frac{B_{IF}}{B_V} \quad , \quad \left(\frac{S}{N}\right)_{IF} \ll 1 \tag{64}$$

for the total power radiometer and

$$\left(\frac{\tilde{S}}{N}\right)_V \approx \frac{1}{8}\left(\frac{S}{N}\right)_{IF}^2 \frac{B_{IF}}{B_V} \quad , \quad \left(\frac{S}{N}\right)_{IF} \ll 1 \tag{65}$$

for the Dicke radiometer. It is a remarkable fact that, for $(S/N)_{IF} \ll 1$, these equations remain valid, with proper interpretation, for much more general signal characteristics than those for which the foregoing derivations have been given; namely, a sinusoidal signal centered in the IF passband. The purpose of the following discussion is to show that this is indeed the case.

Take the signal in the IF filter (more properly, at the input to the IF detector) to have the form

$$S(t) = A(t) \cos\{2\pi f_o t - \alpha(t)\} \tag{66}$$

This is a general representation which encompasses any combination of amplitude and frequency modulation. It also includes the case where the signal center frequency is offset from the IF center frequency; such an offset corresponds merely to inclusion of a linear term in the phase function $\alpha(t)$. Now write $S(t)$ in the form

$$S(t) = A(t) \cos \alpha(t) \cos 2\pi f_o t + A(t) \sin \alpha(t) \sin 2\pi f_o t \qquad (67.)$$

By use of Equations 2 and 67, it follows that, for the total power radiometer,

$$S(t) + N(t) = \left\{ X(t) + A(t) \cos \alpha(t) \right\} \cos 2\pi f_o t$$

$$\qquad (68)$$

$$+ \left\{ Y(t) + A(t) \sin \alpha(t) \right\} \sin 2\pi f_o t$$

From Equation 68, it is found that the output of the square law detector has the form

$$D(t) = \left\{ X(t) + A(t) \cos \alpha(t) \right\}^2 + \left\{ Y(t) + A(t) \sin \alpha(t) \right\}^2$$

$$\qquad (69)$$

$$= X^2(t) + Y^2(t) + 2X(t)A(t) \cos \alpha(t) + 2Y(t)A(t) \sin \alpha(t)$$

$$+ A^2(t) \left\{ \cos^2 \alpha(t) + \sin^2 \alpha(t) \right\}$$

Equation 69 may be further rewritten in the form

$$D(t) = \left\{ \left[X^2(t) - \sigma_N^2 \right] + \left[Y^2(t) - \sigma_N^2 \right] + 2X(t)A(t) \cos \alpha(t) \right.$$

$$\qquad (70)$$

$$\left. + 2Y(t)A(t) \sin \alpha(t) + \left[A^2(t) - \overline{A^2(t)} \right] \right\} + 2\sigma_N^2 + \overline{A^2(t)}$$

The right-hand side of Equation 70 should be compared with that of Equation 18. It is clear that the term

$$\left[X^2(t) - \sigma_N^2\right] + \left[Y^2(t) - \sigma_N^2\right] = X_1(t) + Y_1(t)$$

results from the noise-cross-noise products formed in the detector. The term

$$2X(t)A(t)\cos \alpha(t) + 2Y(t)A(t)\sin \alpha(t)$$

is the signal-cross-noise term, while the term

$$A^2(t) - \overline{A^2(t)}$$

is the fluctuating portion of the detector output caused by the signal beating with itself. When $(S/N)_{IF} \ll 1$, the contributions of the signal-cross-noise and the signal-cross-signal terms to the spectral density of the fluctuations in the detector output in the region of $f = 0$ will be very small relative to the contribution from the noise-cross-noise terms. Accordingly, to a good approximation, one need only consider the contributions from the noise-cross-noise terms in calculating the output noise from the radiometer. With this approximation, one will have, by the same arguments used previously,

$$\sigma_{NV}^2 \approx 8\sigma_N^4 \frac{B_V}{B_{IF}} \tag{71}$$

The dc portion of the signal output is, from Equation 70, $\overline{A^2(t)}$. Reference to Equation 66 shows that

$$P_S = \overline{S^2(t)} = \frac{1}{2}\overline{A^2(t)} \tag{72}$$

so that

$$\overline{A^2(t)} = 2P_S \qquad (73)$$

where P_S is the signal power in the IF filter. Equations 72 and 73 correspond to Equation 26 for the case of the simple sinusoidal signal. From Equations 71 and 73, the radiometer output signal-to-noise ratio becomes

$$\left(\frac{S}{N}\right)_V \approx \frac{\left(2P_S\right)^2}{8\sigma_N^4 \dfrac{B_V}{B_{IF}}} = \frac{1}{2}\left(\frac{P_S}{\sigma_N^2}\right)^2 \frac{B_{IF}}{B_V} \qquad (74)$$

Equation 74 can now be expressed as

$$\left(\frac{S}{N}\right)_V \approx \frac{1}{2}\left(\frac{S}{N}\right)_{IF}^2 \frac{B_{IF}}{B_V}$$

which is identical to the assertion of Equation 64.

The argument proceeds in the same manner for the Dicke radiometer, beginning with the analog to Equation 39 obtained by using the more general signal given by Equation 67. Neglect of all fluctuating components, except those produced by the noise beating with itself and by the action of the chopper, leads by means of the same approximations used previously for the correlation functions to the result

$$\left(\frac{\tilde{S}}{N}\right)_V \approx \frac{1}{8}\left(\frac{S}{N}\right)_{IF}^2 \frac{B_{IF}}{B_V}$$

which is the assertion of Equation 65.

The preceding arguments for the case of an arbitrary signal at the input to the IF detector clearly show that, as regards the detection of threshold signals, the operation of both the total power and the Dicke radiometers depends only on the signal power at the input to the detector and not on the details of the signal structure. This is not the case at higher IF signal-to-noise ratios where the signal-cross-noise and the fluctuating portion of the signal-cross-signal terms at the detector output become significant.

To account for the approximation of Equation 32, write for the general case,

$$\int_{-\infty}^{\infty} G^2(\nu)\,d\nu = \beta\left(\xi_o^2 B_{IF}\right) \tag{78}$$

where B_{IF} is the IF filter noise bandwidth. The IF shape factor, β, will be of the order of unity, but its precise value will depend on the details of the IF filter. In any case, $\beta \leq 1$, and the strict inequality will hold for any physically realizable filter. Straightforward calculations yield the following values for β for illustrative filter characteristics

$$\beta = \begin{cases} \dfrac{1}{2} & \text{single-tuned filter} \\[2ex] \dfrac{\sqrt{2}}{2} & \text{gaussian filter} \\[2ex] 1 & \text{rectangular bandpass filter} \end{cases} \tag{79}$$

If the IF filter consists of several synchronously tuned stages, the value of β for a gaussian filter will provide a very good approximation.

For reference-purposes, Equations 37, 62, 64, and 65 are given below with the correction factor β defined by Equation 78 included.

$$\left(\frac{S}{N}\right)_V = \frac{\left(\frac{S}{N}\right)_{IF}^2}{2\left[\beta + 2\left(\frac{S}{N}\right)_{IF}\right]} \cdot \frac{B_{IF}}{B_V} \tag{80}$$

$$\left(\frac{\tilde{S}}{N}\right)_V = \frac{\left(\frac{S}{N}\right)_{IF}^2}{8\left[\beta + \left(\frac{S}{N}\right)_{IF}\right]} \cdot \frac{B_{IF}}{B_V} \tag{81}$$

B-22

It is of some interest to observe that the only essential use made of the assumed rectangular IF bandpass characteristic in the preceding analysis was in Equation 32 in which

$$\int_{-\infty}^{\infty} G^2(\nu)d\nu$$

was evaluated in terms of the noise spectral density at band center and the noise bandwidth of the IF filter. The corresponding equation,

$$\int_{-\infty}^{\infty} G(\nu)d\nu = \xi_o B_{IF} \tag{75}$$

is equivalent to the definition of the IF noise bandwidth, and hence is valid for an arbitrary (unimodal and, by hypothesis, symmetric about band center) IF filter. For anything other than an idealized rectangular bandpass characteristic, use of Equation 32 overstates the spectral density of the noise-cross-noise products at f = 0. To see this, it is observed that, in the general case,

$$\int_{-\infty}^{\infty} G^2(\nu)d\nu \le \xi_o \int_{-\infty}^{\infty} G(\nu)d\nu = \xi_o^2 B_{IF} \tag{76}$$

and it is noted that the condition for equality to hold in Equation 76 is that

$$G^2(\nu) = \xi_o G(\nu) \tag{77}$$

Equation 77 requires that $G(\nu)$ have the value 0 or ξ_o, and this condition is equivalent to the assumed rectangular IF filter characteristic. A careful examination of the approximation made by Equation 32 in the general case shows that this approximation will be worst for bandpass characteristics which fall off slowly beyond the essential filter bandwidth.

$$\left(\frac{S}{N}\right)_V \approx \frac{1}{2\beta} \left(\frac{S}{N}\right)_{IF}^2 \frac{B_{IF}}{B_V} \quad , \quad \left(\frac{S}{N}\right)_{IF} \ll 1 \tag{82}$$

$$\left(\frac{\tilde{S}}{N}\right)_V \approx \frac{1}{8\beta} \left(\frac{S}{N}\right)_{IF}^2 \frac{B_{IF}}{B_V} \quad , \quad \left(\frac{S}{N}\right)_{IF} \ll 1 \tag{83}$$

Performance estimates obtained using $\beta = 1$ will be somewhat conservative. For the single tuned IF filter, this conservatism corresponds to a change of 1.5 dB in the IF signal-to-noise ratio required for a given video output signal-to-noise ratio, while the corresponding change in required IF signal-to-noise ratio will be only 0.75 dB for the gaussian IF filter. Since the gaussian IF filter will be a reasonable approximation for most cases of interest, the error incurred by neglecting the correction factor β will be small enough to be ignored for most purposes.

Finally, the tacit assumption has been made in the preceding analysis of the Dicke radiometer that the IF noise is independent of whether the chopper is in the on or off position. While this is not precisely true, it is such a good approximation for an infrared heterodyne radiometer that the error incurred in estimating the radiometer performance using the results here derived will be completely inconsequential.

APPENDIX C. EVALUATION OF SNR DEGRADATION IN A LASER HETERODYNE RECEIVER WITH OBSCURATION

We are interested in the explicit evaluation of the SNR degradation due to atmospheric turbulence in a 10.6 μm CO_2 laser communication link from a low altitude Space Shuttle to earth. From earth's receiving station, the Shuttle's zenith angle (θ) of interest for acquisition and communication ranges from -80° to +80°. Two earth station optical receivers are considered. The GSFC station outside of Washington, D.C. has a receiving mirror with a diameter of 48 inches (D = 1.2192 m) and a circular obscuration of 9.6 inches diameter (d = 0.24384 m). The portable station's mirror has a diameter of 30 inches (D = 0.762 m) and a circular obscuration of 6 inches diameter (d = 0.1524 m).

In order to obtain the SNR degradation, we consider the technique developed by Fried [1] r_o. In [1], r_o was developed for a nonobscured optical receiving system. Here we will develop this technique for the use of an arbitrarily circular obscured receiving system. Furthermore, we will obtain explicit SNR degradation from 0° to ±80° zenith angle for the obscuration ratio a = d/D = 0.20 for both systems.

From [1], let $\Psi(D/r_o)$ be defined by

$$\Psi(D/r_o) = \frac{S/N \mid \text{Diameter = D with atmosphere}}{S/N \mid \text{Diameter = } r_o \text{ with no atmosphere}},\tag{1}$$

then it is shown that

$$\Psi(D/r_o) = \frac{32}{\pi r_o^2 D^2} \int_0^D r \, dr \, K(r) \exp(-0.5D(r)),\tag{2}$$

where D(r) is the wave structure function. In [1], it is assumed there is no log-amplitude variation across the mirror. Thus, there is only phase

variation and $D(r) = 6.88 \ (r/r_0)^{5/3}$ where the dependency of r_0 on θ is given by

$$r_0 = \left[\frac{6.88}{2.91 \ (2\pi/\lambda)^2 \ \sec\theta \int_0^\infty C_N^2(h)dh} \right]^{3/5} \qquad (3)$$

By using $C_N^2(h) = 1.4 \times 10^{-14} \ h^{-1/3} \ \exp \ (-h/1000)$ from [2] and [3], $\int_0^\infty C_N^2(h)dh = 5.55 \times 10^{-12} \ M^{1/3}$, and r_0 can be readily evaluated. In (2), $K(r)$ is shown in [1] as the area of overlap of two circles of diameter D separated by distance r. This follows from the fact that in [1] the receiving aperture is a circle of diameter D.

In the present case, we want to find the new $K(r)$ for the area of overlap of two circles with outer diameters D and circular obscured inner diameters d separated by distance r. It turns out that the evaluation of $K(r)$, while geometrically simple to describe, has a somewhat involved algebraic form. Upon some tedious analysis using elementary trigonometry, we can show for $a = d/D \le 1/3$, $K(n)$, where $u = r/D$, is given by

$$K(u) = \begin{cases} K_0(u), & 1/2(1+a) \le u \le 1 \\ K_0(u) - K_2(u), & 1/2(1-a) \le u \le 1/2(1+a) \\ K_0(u) - \pi a^2, & a \le u \le 1/2(1-a) \\ K_0(u) - \pi a^2 + K_3(u), & o \le u \le a \end{cases} \qquad (4)$$

with

$$K_0(u) = \frac{D^2}{2} \cos^{-1} u - u(1-u^2)^{1/2}] \qquad (5)$$

$$K_2(u) = 2 \ (\tfrac{d}{2})^2 \ (\theta_2 - \cos\theta_2 \sin\theta_2) + (\tfrac{D}{2})^2 \ (\theta_1 - \cos\theta_1 \sin\theta_1) \qquad (6)$$

$$\theta_1 = 2 \cos^{-1} \left\{ [u + 1/2(1+a)) \ (u + 1/2(1-a))/2u]^{1/2} \right\} \qquad (7)$$

$$\theta_2 = 2\cos^{-1}\left[u + 1/2(1+a)\ (u + 1/2(a-1))/2ua\right]^{1/2} \qquad (8)$$

$$K_3(u) = \frac{D^2}{2}\left[a^2\cos^{-1}(u/a) = u(a^2-u^2)^{1/2}\right] \qquad (9)$$

For an obscuration ratio a $\geq 1/3$, the form of K(u) is given in Appendix A, although we will have no use of it here. In the present case, upon substituting (4) to (9) into (2), we can obtain $\Psi(D/R_o)$. Details on the computer program for the evaluation of $\Psi(U)$ are given by PHA U and are discussed in Appendix B.

Now since

$$S/N\Big|_{\substack{\text{Diameter} = D \\ \text{with no atmosphere}}} = (D/r_o)^2 \ S/N\Big|_{\substack{\text{Diameter} = r_o \\ \text{with no atmosphere}}} \qquad (10)$$

then

$$\frac{S/N\Big|_{\substack{\text{Diameter} = D \\ \text{with atmosphere}}}}{S/N\Big|_{\substack{\text{Diameter} = D \\ \text{with no atmosphere}}}} = (r_o/D)^2 \ \Psi(D/r_o) \qquad (11)$$

Thus, L, the gain in dB (in actuality since this is a negative number, it is a loss in dB) from the atmospheric effect for an optical heterodyne receiver of diameter D is

$$L = \text{gain in dB} = 10\log_{10}(r_o/D)^2\ \Psi(D/r_o) \qquad (12)$$

Now by using $\lambda = 10.6 \times 10^{-6}$ m for CO^2 laser, r_o in meters as a function of θ are evaluated by using (3) and are presented here.

θ	0°	±10°	±20°	±30°	±40°	±50°	±60°	±70°	±80°
r_o(m)	1.1225	1.112	1.081	1.030	0.9566	0.86106	0.74058	0.5897	0.3926

By using these values of r_o and direct evaluation of $\Psi(\cdot)$ in Appendix B, the gain in dB for the 30 inch diameter and 48 inch diameter mirror receivers are given below.

30 Inch Diameter Mirror (D = 0.762 m; a = 0.20)

θ	0°	±10°	±20°	±30°	±40°	±50°	±60°	±70°	±80°
$\Psi(D/r_o)$	0.2603	0.2634	0.2730	0.2898	0.3162	0.3549	0.4109	0.4929	0.6199
L = Gain in dB	-2.48	-2.51	-2.60	-2.76	-3.02	-3.44	-4.11	-5.30	-7.84

48 Inch Diameter Mirror (D = 1.2192 m; a = 0.20)

θ	0°	±10°	±20°	±30°	±40°	±50°	±60°	±70°	±80°
$\Psi(D/r_o)$	0.4308	0.4343	0.4446	0.4620	0.4881	0.5238	0.5719	0.6372	0.7330
L = Gain in dB	-4.37	-4.42	-4.57	-4.82	-5.22	-5.83	-6.68	-8.27	-11.19

From these two tables, we note that for a given diameter receiver, L decreases monotonically as $|\theta|$ deviates away from 0°. This result follows from the fact that as $|\theta|$ deviates away from 0°, the path of propagation through the atmosphere increases. Furthermore, for a given zenith angle θ, L decreases with increasing receiver diameter. This result follows from the fact that there is greater phase variation across the larger receiver aperture as compared to that of the smaller receiver aperture. In conclusion, we see that the degradation in SNR due to turbulence for a heterodyne receiver with obscuration is not negligible, particularly at large absolute value of the zenith angle.

References

[1] D. L. Fried, "Optical Detection of an Atmospherically Distorted Signal Wave Front," Proc. IEEE, Vol. 55, Jan 1967, pp 57-67.

[2] J. L. Bufton, "Correlation of Microthermal Turbulence Data with Meteorological Soundings in the Troposphere," J. Atmos. Sci., Vol. 30, Jan 1973, p. 83.

[3] NASA Laser Data Relay Link Experiment for the DOD/NASA Cooperative Space Laser Communication Test Flight, Vol. II, Appendices to the Technical Proposal, Appendix C, May 1974.

ATTACHMENT 1

For obscuration ratio $a = \frac{d}{D} \geq 1/3$, detailed analysis shows that $K(u)$ in (4) must be replaced by

$$
K(u) = \begin{cases}
K_o(u), & 1/2(1+a) \leq u \leq 1 \\[2ex]
K_o(u) - K_2(u), & a \leq u \leq 1/2(1+a) \\[2ex]
K_o(u) - K_2(u) + K_3(u), & 1/2(1-a) \leq u \leq a \\[2ex]
K_o(u) - \pi a^2 + K_3(u) & 0 \leq u \leq 1/2(1-a)
\end{cases}
$$

ATTACHMENT 2

The evaluation of the function $\Psi(U1)$ with $U1 = D/r_0$ and obscuration ratio $a = 0.20$ is given by the program PHA. The program PHA in terms depend on F1, F2, F3, F4, FF, FK, FL, and FM.

```
∇PHA[□]∇
   ∇ X←PHA U1;X
[1]    S1←+/(F1 U1)×(FF 0.2×A)
[2]    S2←+/(F2 U1)×(FF 0.2+0.2×A)
[3]    S3←+/(F3 U1)×(FF 0.4+0.2×A)
[4]    S4←+/(F4 U1)×(FF 0.6+0.4×A)
[5]    X←(1÷201)×16×U1×U1×(1÷01)×(0.2×S1)+(0.2×S2)+(0.2×S3)+0.4×S4
   ∇
```

```
∇F1[□]∇
   ∇ X1←F1 U1;X1;U
[1]    U←0.2×A
[2]    X1←(FK U)+(FL U)-00.04
   ∇
```

```
∇F2[□]∇
   ∇ X2←F2 U1;X2;U
[1]    U←0.2+0.2×A
[2]    X2←(FK U)-00.04
   ∇
```

```
∇F3[□]∇
   ∇ X3←F3 U1;X3;U
[1]    U←0.4+0.2×A
[2]    X3←(FK U)-FL U
   ∇
```

```
∇F4[□]∇
   ∇ X4←F4 U1;X4;U
[1]    U←0.6+0.4×A
[2]    X4←FK U
   ∇
```

```
∇FK[□]∇
   ∇ Y←FK U;Y
[1]    Y←(¯2○U)-U×(1-U*2)*0.5
   ∇
```

```
∇FF[□]∇
   ∇ X←FF U;X
[1]    X←U×(*¯3.44×(U1×U)*5÷3)
   ∇
```

```
      ∇FL[□]∇
    ∇ Z2←FL U;Z2;T1;T2
[1]     T1←2×⁻2○((U+0.6)×(U+0.4)÷2×U)*0.5
[2]     T2←2×⁻2○((U+0.6)×(U-0.4)÷2×U×0.2)*0.5
[3]     Z2←(0.04×(T2-(2○T2)×(1○T2)))+T1-(2○T1)×1○T1
    ∇
```

```
      ∇PHI[□]∇
    ∇ Z1←PHI U;Z1
[1]     Z1←(0.04×(⁻2○(U÷0.2)))-U×(0.04-U×U)*0.5
    ∇
```

For comparison purpose, $\psi(U1)$, with obscuration ratio $a = 0$ (Fried's equation 5.16) is given by the program PHI. Indeed, by direction evaluations, PHI U1 PHA U1, as we would expect.

```
      ∇PHI[□]∇
    ∇ Z←PHI U1;A;A1;Z
[1]     A←(1÷200)×(⁻1+ι201)
[2]     A1←+/(FK A)×(FF A)
[3]     Z←(1÷200)×16×U1×U1×A1÷○1
    ∇
```